THE UNIVERSITY *of* EDINBURGH

The Influence of Cosmology on Long Term Star Formation

Boon Kiat Oh

Doctor of Philosophy
The University of Edinburgh
September 2019

Lay Summary

Our universe is not only expanding but also at an accelerated rate. The first evidence of this phenomenon came from Edwin Hubble in 1929. He observed that galaxies further away from us are moving away from us at a faster speed. Recent observational evidence of an accelerated expansion of the universe points towards the existence of a cosmological constant, Λ, associated with a negative pressure component that counteracts gravity. It was introduced by Albert Einstein in his theory of General Relativity.

Λ represents an unstable balance between vacuum repulsion and gravity. If its value is positive and excessively large, vacuum repulsion will overpower gravity, resulting in the inability of galaxies and stars to form. On the other hand, if it is of a large negative value, matter will collapse rapidly under gravity. Fortunately, Λ is of the right value for galaxies to form in our universe, and we are here to observe it. This explanation is known as the anthropic reasoning. In this thesis, I am using cosmological simulations to apply the anthropic reasoning and investigate what happens in universes if Λ deviates from the value we observe.

If we want to use simulations to answer this question, we have to make sure that the simulated universe is similar to observations. We explain the process of calibrating our star formation and feedback parameters in Chapter 3. We tune them so that we can reproduce a Milky Way galaxy that contains approximately the observed amount of gas and stars. It turns out that our set of parameters can achieve more than that. We are able to have galaxies up to two orders of magnitude less massive than the Milky Way galaxy to contain the right amount of gas and stars.

With the calibrated feedback prescription, we proceed to simulate a universe similar to ours into the future in Chapter 4. As Λ dominates our universe in the future, we are only able to quantify the effects of changing the value of Λ at late

times. Since simulation codes are usually used to simulate our universe up to the present, we need to make some modifications to the code so that the future evolution of the universe appears realistic. We also test the convergence of our results by varying the resolution of the simulations. We find that the cosmic star formation rate density evolves in a similar way as predicted from our current observations: it rises and reaches a peak before the present and then declines as the universe evolves into the future. We also find that gas in the diffuse environment cools rapidly under the influence of the expansion of the universe

Finally, in Chapter 5, with the feedback prescription and resolution from previous chapters, we test how changing the value of Λ will affect the counter-factual universes. We assume the presence of observers is directly proportional to the total amount of stars formed. We then fit the cosmic star formation history of each universe with a double power-law fit. It is similar to the analytic fit of our observed cosmic star formation history. By integrating the obtained fit to infinite time, we calculate the total stellar mass formed in each counter-factual universe. We find that this mass is higher for lower values of Λ with an exponential decay to higher values of Λ, suggesting that observers are more likely to exist in universes with a value of Λ comparable to ours.

Abstract

This dissertation explores cosmological simulations of galaxy formation, focusing on the asymptotic efficiency of conversion of baryons into stars and asking how this quantity varies in different cosmological models. By exploring the behaviour into the future and in counter-factual universes with altered cosmological parameters, I hope to gain insight into the robustness of galaxy formation codes for their behaviour in different parameter regimes, addressing the concern that the models may be fine-tuned to fit observations, rather than being genuinely predictive.

Through the calibration of multiple star formation and feedback parameters within zoom simulations using the Enzo code, I obtain a set of parameter values able to reproduce the observational constraint of baryon makeup of haloes of masses between 10^{10} and 10^{12} $M_{\odot}$. Comparing two different star formation setups, I show that feedback is self-consistent with a higher feedback energy injection associated with a low star formation efficiency, and vice versa. I also explore the reproducibility of the simulation results and conclude that operational differences in the implementation of the numerical code can create approximately 10% – 25% deviation in the stellar and baryon mass respectively.

Using the best star formation and feedback prescription from the zoom simulations, I attempt a cosmological box simulation in a standard cold dark matter cosmology beyond $z = 0$. Comparing with previous work, I find a similar elongation in the general evolution of the distribution of temperature and density of the gas into the future. I then extend the analysis to the evolution of the halo mass function, the equation of state of the intergalactic medium and star formation rate into the future to determine the level of convergence with various resolutions. Interestingly, I identify a turn-around in the cosmic star formation, deviating from the extrapolation obtained from observations. There is also a cross over in the fraction of baryon in the form of stars and in gas around the

period of 'freeze out' in both the zoom and box simulations.

Lastly, I present results from simulations of counter-factual simulations, exploring the effects of different values of Λ on structure formation and evolution. These simulations allow the study of anthropic explanations for the small observed value of Λ, considering the relative frequency of observers within a multiverse. It appears that a distinct peak in the star formation rate may be due to the presence of Λ. For a higher value of Λ, the peak in star formation is of a lower value, and it occurs earlier in the evolution of the universe. Given these differences in the star formation rate, the UV background must be calculated self consistently in these models. This corrected UV background will provide a more realistic representation of the counter-factual universe. I show that almost 54% of possible observers reside in universes with a value of Λ similar to ours, implying that anthropic principle can explain why Λ is of such a small value.

Declaration

I declare that this thesis was composed by myself, that the work contained herein is my own except where explicitly stated otherwise in the text, and that this work has not been submitted for any other degree or professional qualification except as specified.

(*Boon Kiat Oh, September 2019*)

Acknowledgements

To the pillars of my life, my lovely wife, Jie Yi Tan and my wonderful son, Kai Le Xavier Oh: Thank you for coming into my life!

My forever supportive family, my mother, father, mother-in-law, father-in-law and brother-in-law: I am grateful for your help in every little aspect along this journey. My encouraging brother and his family: They are always keen to find out how my family and I was doing! My brother never hesitates to offer his words of wisdom even though he is younger! Also, I want to thank my aunt and grandmother for their constant reminders to finish my PhD as fast as possible.

My heartfelt gratitude to my supervisors: Professor John Peacock, Professor Sadegh Khochfar and Dr Britton Smith. They gave me the precious opportunity to pursue my dreams 4 years ago. Thank you, John, for accepting me as your student, your constant support, advice and understanding along every step of the way and selfless sharing of your limitless knowledge. Thank you, Sadegh, for recommending me to John for this project and sharing all your insights about research! Simulations are always right! Thank you, Britton, for all the discussion on and beyond the project and giving me the confidence in what I was doing.

Special mention to Daniel Eastwood, Ben Morton, Jose Oñorbe and the rest of the TMOX group for all the insightful discussion and comments. Especially Jose, thank you for reading through the countless research proposals I wrote for my job applications and keeping me focused on the important stuff. Not to forget, Thomas Kemp for being my buddy since we started our Masters 5 years ago. I am also grateful to the other students and staff whom I have the honour of knowing. They have contributed one way or another through the conversations we had along the way.

Finally, last but by no means least, to my friends in Edinburgh outside of my PhD life, Ian, Joe, Sean, Oisín, Siri, Chris, Peter and everyone in King's Buildings: Thank you for your generous hospitality in the lovely city of Edinburgh!

To all my family and friends, past, present and future: Thank you!

Contents

List of Figures

List of Tables

Chapter 1

Introduction

1.1 Overview

In 1929, Edwin Hubble revolutionised our understanding of the universe. Through the determination of a linear relation between the recession velocities of galaxies and their distances, Hubble showed that the universe is expanding (Hubble, 1929). Two independent measurements of the distance-redshift relation of Type Ia supernovae in the late 1990s (Riess et al., 1998; Perlmutter et al., 1999) confirmed that the universe is not only expanding but the expansion is accelerating.

The mathematical fundamentals of the expansion of the universe were laid down earlier by Albert Einstein in 1915 through his theory of general relativity. The theory described a set of equations that related the geometry of space-time to the distribution of matter/energy. Adhering to his belief that the universe is static, Einstein added the cosmological constant, Λ to his field equations in his 1917 model of the cosmos (Einstein, 1917). Although this constant created a static solution, it was an unstable one.

As the volume of evidence supporting an expanding universe grew, Λ was slowly removed from the limelight in the 1930s. However, it was not entirely forgotten as it was still required to explain puzzles such as the age of the universe and the redshifts of quasars. In the coming years, other problems such as cosmic inflation, anisotropies in the cosmic microwave background (CMB) also invoked Λ. When the present universe was determined to be undergoing a phase of accelerated expansion and spatially flat, the cosmological constant made a

comeback as the main focus of modern cosmology.

The incorporation of the cosmological constant in the theory of general relativity naturally predicts an unstable balance between vacuum repulsion and matter attraction (Eddington, 1930, 1933). Therefore, the value of this constant is of immense importance. In order to calculate this value, we require both the theoretical and observed values of vacuum energy density. The former can be derived by invoking the concept of zero-point energy introduced by Max Planck in 1911. The scientific community only became convinced this effect was real following the successful demonstration of the Casimir effect in the late 1950s. By summing up the zero-point energies of the vacuum up to 1 GeV, Yakov Zel'dovich derived a lower bound of $10^{20}\,\mathrm{kg\,m^{-3}}$ for the energy density of vacuum. This value is much larger than the value of $10^{-26}\,\mathrm{kg\,m^{-3}}$ set by observations (Zel'Dovich, 1967; Zel'dovich, 1968).

If a cutoff is applied at the Planck scale instead, this 46 orders of magnitude difference balloons to 120 orders of magnitude between the observed and the theoretical value of the energy density of Λ. This huge difference was referred to as the 'cosmological constant problem', setting the basis for this thesis. Λ must take a small positive value to counteract the forces of gravity while permitting a universe suitable to harbour life. In 1987, Steven Weinberg applied anthropic reasoning to the 'cosmological constant problem' and derived a much more restrictive bound on the possible values of Λ. If it had been much more positive, the formation of cosmic structures would have been suppressed, reducing the expected number of observers. Similarly, if it had been a substantial negative value, i.e., working together with gravity, the rapid collapse will lead to the same fate (Weinberg, 1987).

The work presented throughout the main body of this thesis aims to explore the impact of the dominance of Λ on structure formation and evolution. We will quantify its effects using simulations of our universe and counter-factual universes with different values of Λ into the future when Λ is dominant. The remainder of this chapter will provide a summary of the key concepts and ideas about the cosmological model. We will follow up with the necessary components to set up and run the intended cosmological simulations to explore the evolution of counter-factual universes, together with our ΛCDM universe in the following chapter.

1.2 Cosmological model

The widely accepted cosmological framework of the universe is known as the ΛCDM model. Λ is the cosmological constant and CDM stands for cold dark matter (Blumenthal et al., 1984). The model is represented by six parameters, and tight constraints have been placed on the values of these parameters with various observational probes (Voit, 2005; Allen et al., 2011; Hamilton, 2014). The values determined by the Nine-Year Wilkinson Microwave Anisotropy Probe (WMAP9) are $\Omega_m = 0.285$. $\Omega_\Lambda = 0.715$, $\Omega_b = 0.0461$, $h = 0.695$, $\sigma_8 = 0.828$ and $n_s = 0.9632$ with $\Omega = \rho/\rho_c$ where ρ_c is the critical density discussed in Section 1.2.2, h is the dimensionless Hubble parameter, σ_8 is the present root-mean-square matter fluctuations on a scale of $8\,h^{-1}$Mpc, and n_s is the scalar spectral index. At present times, our universe is dominated by Λ and dark matter whose fundamental nature is still an open question. Despite our lack of understanding, the presence and impact of these components manifest in the observations of the universe. We will provide a historical introduction to cold dark matter and Λ in Sections 1.2.1 and 1.2.2 respectively.

1.2.1 Cold dark matter

One significant component of our universe is in the form of invisible matter known as dark matter. Unlike gas and stars, it is not detectable via electromagnetic emission or absorption and manifests itself only through gravity. In 1922, Jacobus Kapteyn suggested the existence of dark matter with measurements of stellar velocities in his work "First attempt at a theory of the arrangement and motion of the sidereal system" (Kapteyn, 1922). His theoretical work implied the possibility of determining the amount of dark matter from its gravitational effect.

The first evidence for dark matter was presented in 1933. When studying the velocities of galaxies in the Coma Cluster, Zwicky concluded the stellar mass alone is insufficient to hold the cluster together. Instead, the total mass requirement is 400 times larger, indicating the presence of other forms of mass (Zwicky, 1933). Smith (1936) supplemented this work with his own on the Virgo Cluster where it also appeared to contain an unexpectedly large amount of mass. He suggested that this mass is in the form of internebular material. In 1939, Babcock also showed an unexpectedly high velocity in the outskirts of M31 (Babcock, 1939)

with the long-slit spectra of the Andromeda galaxy. Collectively, these works hinted at the presence of a previously unknown component that is common among them. However, individual work did not establish any links to each other, evident from the lack of citations between them.

40 years passed before the presence of dark matter was widely accepted through the works of Ostriker et al. (1974) and Einasto et al. (1974). They showed that the presence of massive haloes around our Milky Way galaxy and other nearby galaxies is required to explain the motion of their satellites. Furthermore, measurements of spiral galaxy rotation curves showed no signs of a velocity decrease at large radii. This observation is in contrast to the decrease in visible stars and gas should these masses be the only component in the galaxy (Roberts & Rots, 1973; Roberts & Whitehurst, 1975; Rubin et al., 1978, 1980). Ostriker & Peebles (1973) suggested these flat rotation curves at large radii were a result of the presence of dark matter stabilising the thin disk of stars.

Using X-rays as an independent measure of mass through the relation of temperature and rotational velocity, Mathews (1978) calculated the amount of invisible matter mass required to hold the hot gas together in M87. He concluded that the majority of the mass is of low luminosity and distributed differently in comparison to luminous matter. Measurements of 21-cm emission from neutral hydrogen allowed velocity data to be obtained at even greater radii. (van Albada et al., 1985) applied this technique to infer velocity data to 11 disk scale radii as seen in Figure 1.1, well beyond the extent of stars in the disk (van Albada et al., 1985). Together with the postulation of the presence of an unseen form of matter in 1922, these pieces of observational evidence convinced the majority of the astronomy community of the presence of dark matter in our universe.

After the establishment of its existence, the immediate follow-up question is the nature of dark matter. The title of this section already gave away the answer that dark matter is cold. However, dark matter was initially thought to be hot. Cowsik & McClelland (1973) linked dark matter to light neutrinos with masses less than 100 eV, also known as hot dark matter (HDM). Having a low mass means that particles will only become non-relativistic at low z. The velocity of the particles today ($v_{\rm now}$) is given by

$$v_{\rm now} = \frac{c}{1 + z_{\rm nr}}, \tag{1.1}$$

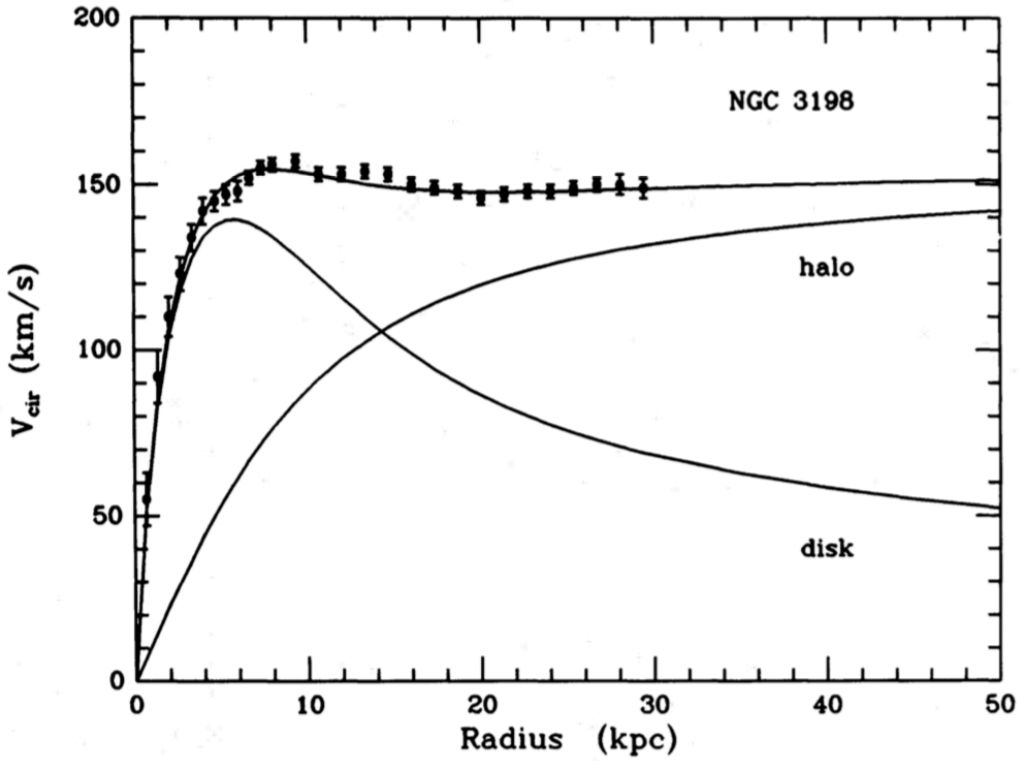

Figure 1.1 The model rotation curves for different components of NGC 3198 from van Albada et al. (1985). The black dots are measurements obtained from 21-cm emission from neutral hydrogen with the best fitting model derived from the superposition of the disk and halo rotation curves. The contribution of the luminous disk dominates in the inner region of the halo, followed by a flat outer rotation curve due to the dark matter halo

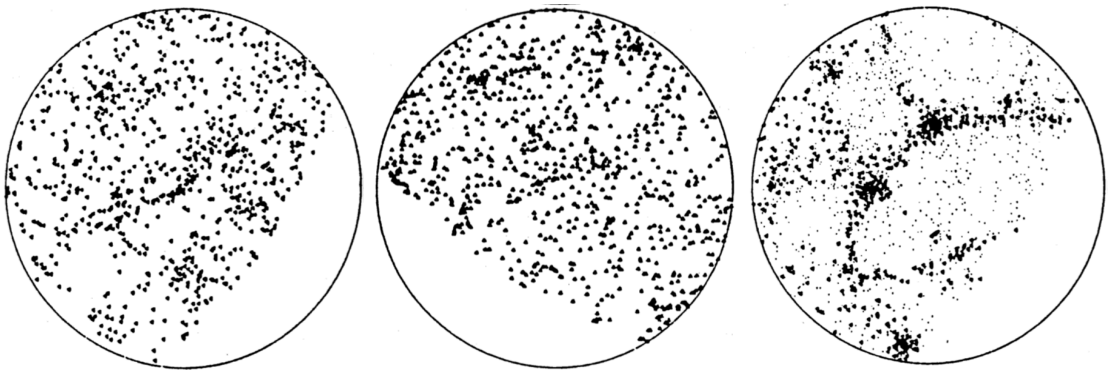

(a) Observation **(b)** CDM simulation **(c)** HDM simulation

Figure 1.2 Comparison of the observed galaxy distribution on the northern sky (a), mock halo catalogue generated with a CDM model (b) and a HDM model (c) adapted from White (1986). According to these equal area projections, HDM is ruled out because of the excessively inhomogeneous distribution of galaxies.

where c is the speed of light in vacuum and $z_{\rm nr}$ is the redshift when the particles become non-relativistic. Assuming that $z_{\rm nr} < 300$, $v_{now} \approx 1000$ km s^{-1}, making it impossible for haloes to capture these particles. This idea was, however, pursued by Zel'dovich and his group in the 1980s (Doroshkevich et al., 1981; Zeldovich et al., 1982; Bond & Szalay, 1983). In this paradigm, the small-scale fluctuations are damped because of the free streaming of neutrinos, allowing dark matter to congregate on larger scales. The minimum mass of a hot dark matter halo is determined to be $\sim 10^{15}\,{\rm M}_{\odot}$, corresponding to the mass of a super cluster. Since there are observations of lower mass galaxies. such a high value of the minimum halo mass thus suggests that structure formation occurs in a top-down order. These superclusters will form and later fragment to form smaller galaxies, which meant that galaxy distribution will be highly inhomogeneous as shown in Figure 1.2. Prior to this comparison in Figure 1.2, White et al. (1983) already ruled out neutrino-dominated universe or HDM through N-body simulations. They found that the coherence length of the neutrino distribution from HDM is too large to be consistent with the observed clustering scale of the galaxies.

Peebles (1982) then assumed a large mass for dark matter particles and first mentioned weakly interacting massive particles (WIMP) as a potential dark matter candidate. The term 'cold dark matter' was coined and presented by Blumenthal et al. (1984). They showed that the CDM model could reproduce

several observational evidence, such as the observed mass range of galaxies, Faber-Jackson (Faber & Jackson, 1976) and Tully-Fisher (Tully et al., 1975) relations, and the large scale clustering. The Faber-Jackson relation describes a empirical power-law relation between the mass and central stellar velocity dispersion of an elliptical galaxy and the Tully-Fisher relation refers to a similar relation between the mass and maximum rotation velocity of a spiral galaxy. It was also concluded that CDM favours $\Omega = 0.2$ but could not rule out the possibility of $\Omega = 1$. In 1992, results from Cosmic Background Explorer (COBE) indicated CMB temperature fluctuations of $\Delta T/T \approx 10^{-5}$ and a scale-invariant spectrum of inhomogeneities in the temperature (Smoot et al., 1992). These results were consistent with the CDM model of structure formation. In combination with measurements of large scale structures, this result also hinted at the inclusion of a cosmological constant, Λ in the standard model of cosmology (Efstathiou et al., 1992; Padmanabhan & Narasimha, 1992).

1.2.2 Cosmological constant, Λ

The existence of Λ

The cosmological constant has been weaving in and out of our description of the universe since its introduction by Einstein. He was trying to obtain a static solution for his equations in the theory of general relativity. However, he was not the first to introduce the addition of a cosmological constant in order to obtain a consistent model of the universe. Near the end of the 19th century, Hugo von Seeliger added a constant in his work that was small enough that the Newtonian potential only significantly changes at vast distances. It was proposed to correct for the undefined Newtonian gravitational force at any point in an assumed infinite universe, and a deterministic uniform large scale matter density (Seeliger, 1898a,b).

In his 1917 model of the universe, Einstein made a few assumptions. Firstly, he assumed that the cosmos is static as the insignificant velocities of the stars to that of light meant that matter could be regarded as permanently at rest (Einstein, 1917). This assumption is subsequently disproved due to the observed relation of the recession of distant galaxies and their distances (Hubble, 1929). Einstein made a second assumption that the universe obeys the 'Cosmological Principle' (Milne, 1935) or that the universe is isotropic and homogeneous. He

also assumed that the universe is spatially closed geometrically to generate the appropriate boundary conditions for his model. These assumptions were coupled with the addition of a new term, $-\Lambda g_{\mu\nu}$, to his field equations of general relativity,

$$R_{\mu\nu} - \Lambda g_{\mu\nu} = -\kappa \left(T_{\mu\nu} - \frac{1}{2} g_{\mu\nu} T \right) \tag{1.2}$$

where T is a scalar, $\kappa = 8\pi \mathrm{G}/c^2$ is the Einstein constant, (Einstein, 1915), $G_{\mu\nu}$, $R_{\mu\nu}$ and $T_{\mu\nu}$ is a four-dimensional tensor corresponding to the curvature of space-time (Ricci curvature tensor), energy and momentum respectively. $g_{\mu\nu}$ represents elements in the space-time tensor determined by the distribution and flux of matter/energy and Λ is a universal constant, which is later known as the cosmological constant (Einstein, 1917). Similar to Seeliger's constraints, the constant must be so small that any modification to the equations is only significant at considerable distances.

In 1922, Alexander Friedmann derived two differential equations with an appropriate form of the metric tensor

$$\left(\frac{\dot{R}}{R} \right)^2 + \frac{kc^2}{R^2} = \frac{8\pi G}{3} \rho + \frac{\Lambda}{3}, \tag{1.3}$$

$$\frac{\ddot{R}}{R} = -\frac{4\pi G}{3} \left(\rho + \frac{3p}{c^2} \right) + \frac{\Lambda}{3}, \tag{1.4}$$

from the 00 component and trace of Equation 1.2 respectively. In these equations. R represents the cosmic radius, ρ is the density, p is the pressure, G is the Newton's gravitational constant, c is the speed of light in vacuum and k is the spatial geometry of the universe. $k = 1, k = -1$ and $k = 0$ indicates a closed, open and flat universe respectively. Similar to Einstein, Friedmann assumed a closed geometry initially (Friedmann, 1922) before realising that an open geometry was also possible (Friedmann, 1924). Georges Lemaître derived these differential equations assuming $k = 1$ independently a few years later. These equations related the evolution of R with ρ and Λ, suggesting a time-varying cosmology.

Since Einstein believed in a static universe, he dismissed this idea when it was mentioned by Lemaître. Einstein's stance changed following the evidence of a time-varying universe was published by Hubble in 1929. Through the linear relation between the z and radial distance of spiral nebulae (Hubble, 1929), Hubble showed that the further away an extra-galactic nebula is, the faster it is moving away from us as indicated in Figure 1.3. This observation prompted

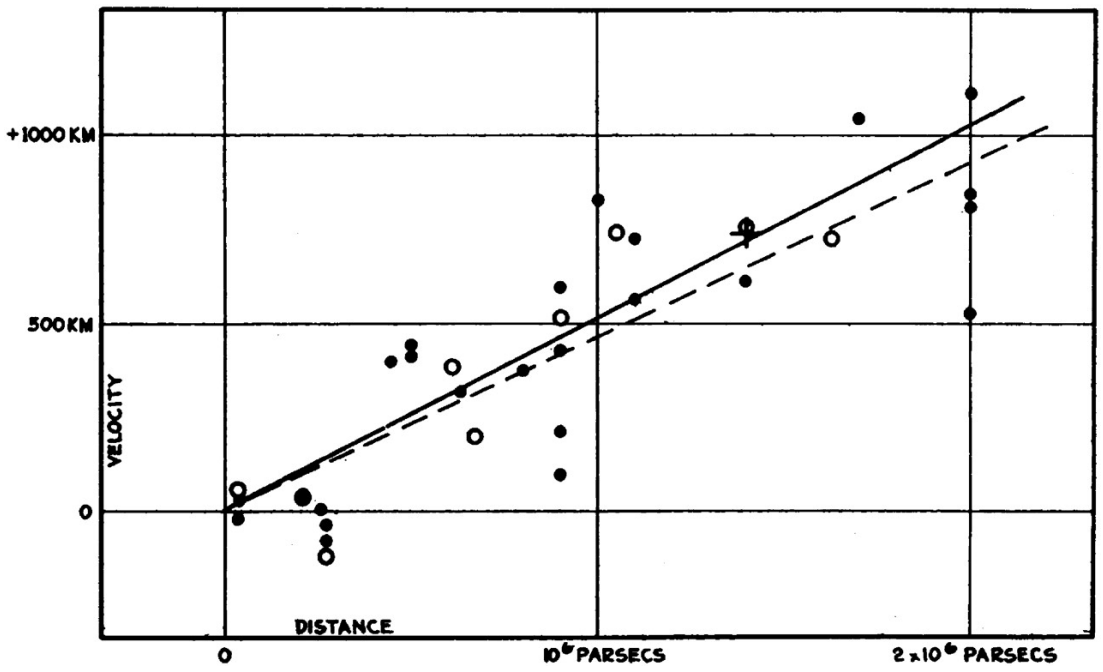

Figure 1.3 Relation of radial velocity against distance. The full and empty circles represent individual nebula and groups of nebulae respectively. The solid and dashed lines correspond to the fit to the filled and empty circles. Lastly, the cross indicates the mean velocity calculated from the mean distance of 22 nebulae whose individual distances could not be determined. Adapted from Figure 1 of Hubble (1929).

Einstein to discard the cosmological constant. Not only did Λ not provide a stable solution, the universe was observed to be time-varying, rendering it pointless to be included. In the following years, observations by Otto Heckmann showed that a non-static universe having matter does not indicate a positive curvature of space (Heckmann, 1931, 1932). Coupled with the lack of proof for any spatial curvature, Einstein and de Sitter came up with the famous Einstein-de Sitter (EdS) model by setting both the cosmological constant and spatial curvature to zero (Einstein & de Sitter, 1932).

By setting k and Λ in Equation 1.3 to zero, and equating $\dot{R}/R$ to H, the EdS model predicts a critical density,

$$\rho_c = \frac{3H^2}{8\pi G}, \tag{1.5}$$

that balances the expansion of universe. With a density higher than this critical value, the universe will be spherical in geometry and collapse eventually. On the

other hand, a universe with a density less than that will be spatially open and expand at an ever increasing rate. This allows us to define a density parameter

$$\Omega = \frac{\rho}{\rho_c}, \tag{1.6}$$

explaining the values determined by WMAP9 in Section 1.1. By introducing the scale factor, $a = R/R_0$, and separating ρ into the matter (ρ_m) and radiation contribution (ρ_r), Equation 1.3 becomes

$$\left(\frac{\dot{a}}{a}\right)^2 = \frac{8\pi G}{3}\left(\rho_r + \rho_m\right) - \frac{kc^2}{R^2} + \frac{\Lambda}{3}. \tag{1.7}$$

Solving the fluid equation for matter and radiation separately yielded $\rho_m = \rho_{m,0}a^{-3}$ and $\rho_r = \rho_{r,0}a^{-4}$ where the subscript, 0 corresponds its present day value. Substituting these expressions, Equation 1.7 can be expressed as

$$H^2(a) = H_0^2\left(\Omega_{\mathrm{r},0}a^{-4} + \Omega_{\mathrm{m},0}a^{-3} + (1-\Omega_0) + \Omega_{\Lambda,0}\right), \tag{1.8}$$

where

$$\Omega_m = \frac{\rho_m}{\rho_c},\ \Omega_r = \frac{\rho_r}{\rho_c} \text{ and } \Omega_\Lambda = \frac{\Lambda}{3H^2}. \tag{1.9}$$

The EdS model enjoyed success for many years but there are two fundamental problems associated with it. Firstly, the age of the universe predicted from the EdS model, $t = 2/(3H_0)$ is shorter than the estimates of the age of stars and Earth. Secondly, the observed mean density of matter in the universe is smaller than the critical density predicted by the model.

To account for this discrepancy in age, Lemaître hypothesised that the universe began as a 'primaeval atom' (Lemaître, 1931b). His model described the expansion of the universe in three stages. The first stage is one where gravity overpowers and slows down the expansion. In the next stage, the effect of the cosmological constant kicks in and counteracts the effect of gravity. This stage is known as the 'loitering' phase. The last stage occurs when the repulsion is dominant over gravity (Lemaître, 1931a). In this 'loitering' universe, Λ in Equation 1.2 is modified to $\Lambda(1+\epsilon)$ where ϵ is a free parameter that determines the length of the 'loitering'. This phase provided a stable period in which perturbations in the matter density can grow (Lemaitre, 1934). It results in a mechanism for structure formation, answering one of the questions that the discovery of cosmic expansion brought about (Kragh, 1996). Also, since the length of the 'loitering' phase is arbitrary, it solves the age problem of the

EdS model. This model gained traction in the 1960s and 1970s as evidence for structure formation during the 'loitering' phase mounted (Petrosian et al., 1967; Shklovsky, 1967; Kardashev, 1967; Rowan-Robinson, 1968; Petrostan & Salpeter, 1970). However, redshifts of quasars eventually became sufficiently high that this model could be conclusively ruled out (Petrosian, 1974).

After the opening of the 200-inch Hale telescope at the Palomar Observatory in California in 1949, the focus shifted to a more accurate determination of the cosmological parameters. Baade (1952) and Sandage (1958) re-derived the Hubble parameter after recalibrating the distances to the galaxies. From an original estimate of $H_0 = 500\,\mathrm{km\,s^{-1}\,Mpc^{-1}}$, it shrunk to $H_0 = 75 \pm 25\,\mathrm{km\,s^{-1}\,Mpc^{-1}}$, improving the estimate of the age of the universe to approximately 8 Gyr according to the EdS model. However, this is still much younger than the oldest stars (~ 15 Gyr) in the Milky Way (MW). Sandage (1961) saw this result as an indication of the need to include a positive cosmological constant in the time-varying universe. Also, measurements of the mean density of matter yielded an estimated value that is lower than the ρ_c predicted by the EdS model.

An indirect approach towards measuring the matter density was proposed in the 1950s (Robertson, 1955; Humason et al., 1956; Hoyle & Sandage, 1956) For a matter-filled universe where $\Lambda = p = 0$, Equation 1.4 is reduced to

$$\frac{\ddot{R}}{R} = -\frac{4\pi G}{3}\rho, \tag{1.10}$$

where it indicates that the expansion of the universe is always slowing down. A de-acceleration parameter

$$q_0 = -\frac{1}{H_0^2}\frac{\ddot{R}_0}{R_0} = -\frac{\ddot{R}_0 R_0}{\dot{R_0}^2}, \tag{1.11}$$

is introduced where $\dot{R}_0/R_0 = H_0$. Substituting Equation 1.10 into Equation 1.11,

$$q_0 = \Omega_{\mathrm{m},0}/2, \tag{1.12}$$

for cosmologies with $\Lambda = 0$ or

$$q_0 = \Omega_{\mathrm{m},0}/2 - \Omega_{\Lambda,0}, \tag{1.13}$$

for cosmologies with non-zero Λ. The value of q_0 contains much information about the universe. For a cosmology without Λ, if $q_0 > 1/2$, the universe is spatially

closed and vice versa. For $q_0 = 1/2$, the universe is flat. By taking the time derivative of the Hubble parameter,

$$\frac{\dot{H}_0}{H_0^2} = -(1 + q_0), \tag{1.14}$$

the value of q_0 can differentiate between the steady-state cosmological model in which the Hubble parameter does not change with time ($q_0 = -1$) or time-varying ones ($q_0 \neq -1$). Comparing redshift-distance relations for far away galaxies and local galaxies, Humason et al. (1956) and Sandage (1961) concluded a deacceleration in the expansion was indeed observed and assigned $q_0 \sim 1.2 \pm 0.4$. However, the result was derived based on galaxies with $z < 0.5$ and failed to account for galactic evolution, rendering it debatable.

The universe was determined to be extremely homogeneous even on the largest scales by studying the CMB. However, any two regions of the present-day universe would have been too far apart to be in causal contact at sufficiently early times (Misner, 1968), violating the implied presence of similar regions across the universe required by the isotropy of the CMB. This issue is known as the 'horizon problem'. To resolve this problem, It was proposed that the universe has undergone a period of exponential expansion from its hot and dense initial state (Starobinsky, 1980; Guth, 1981; Linde, 1982; Albrecht & Steinhardt, 1982). This process of inflation is driven by the vacuum energy of some quantum field. It proves the causal contact of different patches of the universe, allowing physical processes to establish homogeneity and isotropy of the universe. Also, due to the amount of expansion during the inflation period, its curvature radius grew beyond the presently observed universe, indicating that the universe is flat ($\Omega = 1$). Since observations suggest $\Omega_m \leq 0.3$, the remainder of the energy density contribution will come from the cosmological constant, i.e., $\Omega_\Lambda = 0.7$. From the mid-1980s onward, observational data increasingly tended to be in better agreement with a model that contains Λ than with the EdS model (Turner et al., 1984; Peebles, 1984; Fujii & Nishioka, 1991).

We then pick up from where we left off in Section 1.2.1. The data from COBE are consistent with either a matter dominated universe with a low value of $H_0 < 50\,\mathrm{km\,s^{-1}\,Mpc^{-1}}$ or a flat universe with a larger H_0 dominated by a positive cosmological constant (Wright et al., 1992). Better data from the Hubble Space Telescope (HST) and other ground telescopes in 1994 constrained $H_0 = 80 \pm 17\,\mathrm{km\,s^{-1}\,Mpc^{-1}}$ (Freedman et al., 1994; Pierce et al., 1994). This

value clearly favoured the latter model of the universe. Compiling all available observational data and theoretical models, ΛCDM model of the universe (Carroll et al., 1992; Krauss & Turner, 1995; Ostriker & Steinhardt, 1995) began to gain support and interest from the community (Chaboyer et al., 1996; Turner & White, 1997; Krauss, 1998), marking the return of the cosmological constant, Λ.

A class of supernovae known as SNe Ia is capable of providing reliable estimates of the Hubble parameter to great distances. They are thought to originate from exploding white dwarfs made up of carbon and oxygen in binary systems. As a result, there is a lack of hydrogen absorption lines in their spectrum. Using the Phillips relationship (Phillips, 1993), distances to the supernovae can be determined to 7% accuracy (Hamuy et al., 1996). The Phillips relationship tells us the faster the supernova dimmed from its maximum luminosity, the lower is the peak luminosity of the supernova. With such high accuracy in distance measurements, SNe Ia are used as standard candles. The Supernova Cosmology Project (SCP) at the Lawrence Berkeley Laboratory in California and the High-Z Supernova Search Team (HZT) undertook the task of measuring distances by surveying type Ia SNe in the 1990s. Both teams reported a negative q_0, highlighting that the universe is currently undergoing a phase of accelerated expansion (Riess et al., 1998; Perlmutter et al., 1999). The results from the SCP (red circles) and HZT (blue circles) are shown in Figure 1.4. The upper panel in this figure showed the relation of the distance modulus of the supernova against z and the lower panel indicated the magnitude residual against z. Different lines in Figure 1.4 represents the various cosmological models with dashed, thin solid and thick solid lines corresponding to the EdS, matter-dominated, and ΛCDM model.

While the results from HZT and SCP in Figure 1.4 ruled out the EdS model definitively, we still require observations of the geometry of the universe to distinguish between a matter dominated, i.e., ($\Omega < 1$) and a ΛCDM universe. This information came from the Balloon Observations of Millimetric Extragalactic Radiation and Geophysics (BOOMERanG) collaboration (de Bernardis et al., 2000). They studied the CMB with balloon-borne instruments, and their results found that the universe was flat with the angular power spectrum of the CMB shown in Figure 1.5. The measured spectrum (red dots) showed excellent agreement with the prediction of the inflationary CDM model (solid line). There is a low level of deviation between the model and the measurements, indicated by the value of the green dots particularly around the peak at $\ell \approx 200$. Combined

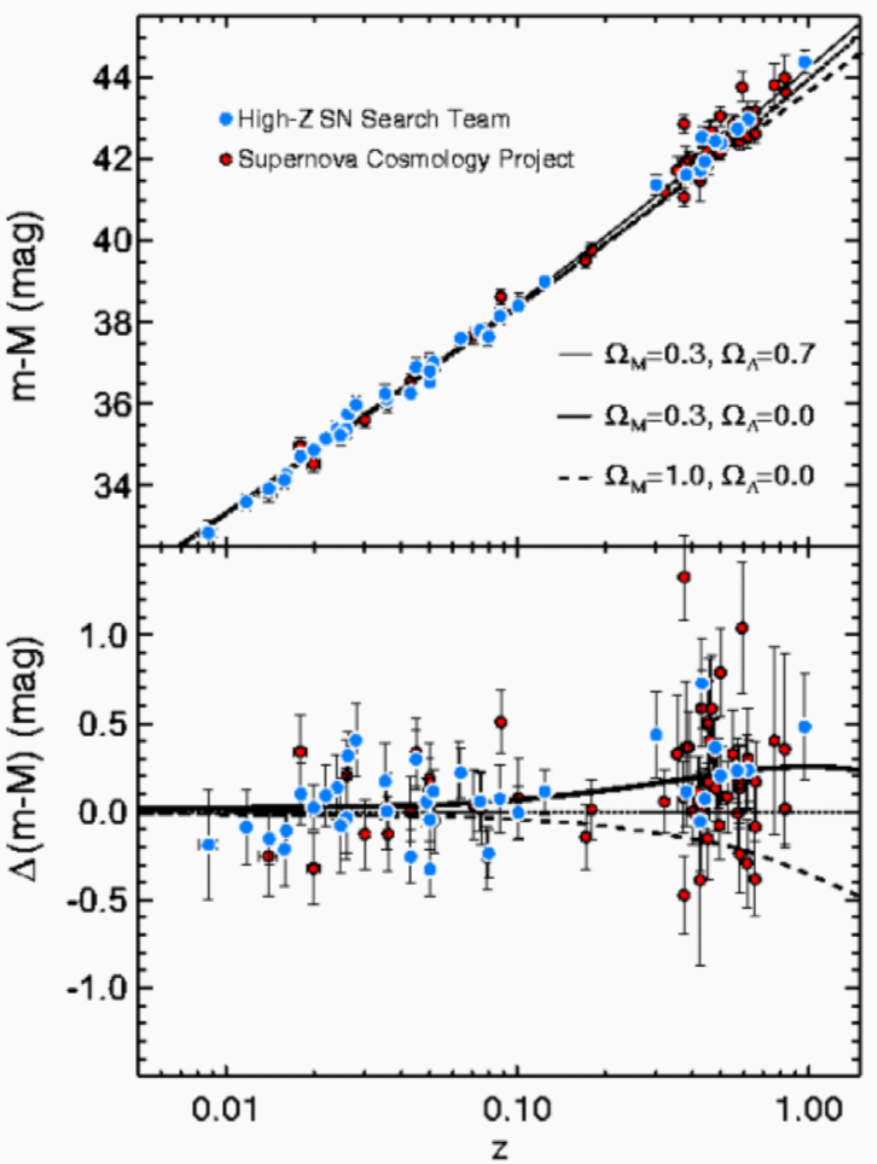

Figure 1.4 Plots of the distance modulus of the supernova against redshift (upper panel) and the magnitude residual against redshift (lower panel). The blue and red circles represent results from HZT and SCP respectively. The thin and thick solid, and dashed lines correspond to various combinations of cosmological parameters indicated in the legend. It is clear that these data can no longer support the EdS model. When combined with other observations about the flatness of the universe, we can distinguish between the cosmology represented by the thin and thick solid lines. Adapted from Figure 4 of O'Raifeartaigh et al. (2018).

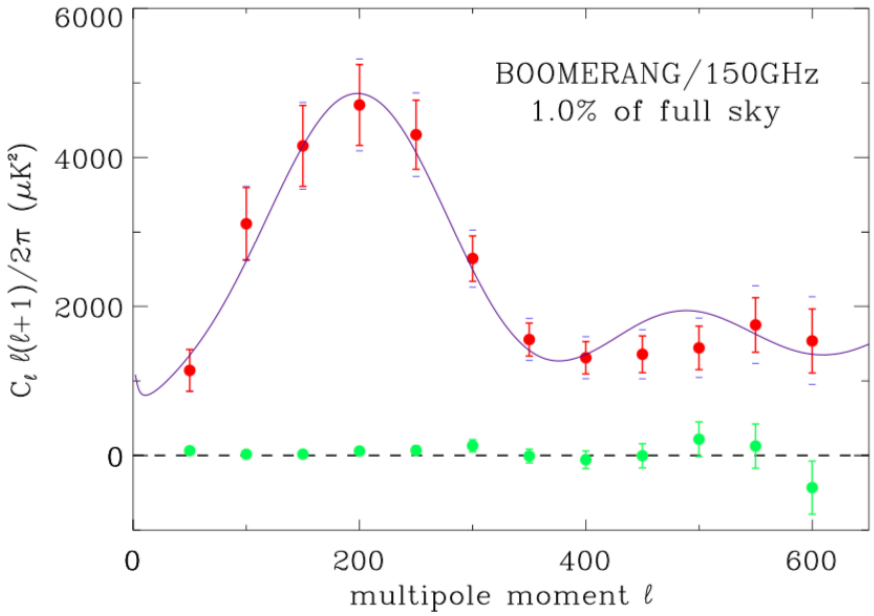

Figure 1.5 Angular power spectrum measured by BOOMERanG indicated by the red dots. The solid line represents the prediction from the inflationary model. The green dots are the differences between the prediction and measurement at each multipole moment, ℓ. The peak at $\ell \approx 200$ is consistent with the prediction from inflationary CDM models. Adapted from Figure 2 of de Bernardis et al. (2000).

with a similar result from the Millimeter Anisotropy Experiment Imaging Array (MAXIMA) collaboration (Balbi et al., 2000; Hanany et al., 2000), the spatial geometry of the universe is constrained to $\Omega \sim 1.0 \pm 0.04$, highly favouring a flat universe (Jaffe et al., 2001).

Over the years, the existence and inclusion of Λ in the cosmological model has been driven largely by observations. With ever-improving observations, Λ withstood the test of time. Its presence has been verified by large scale experiments including the Sloan Digital Sky Survey, WMAP and Planck. We summarise the parameter space of the cosmological parameters in Figure 1.6. The various lines separate the different universes that we have discussed thus far. For a universe with a negative Ω_Λ, the expansion will decelerate and eventually re-collapse. The speed of re-collapse will be accelerated with a significant matter density. On the contrary, the universe will expand forever with a positive Ω_Λ unless its value is very small with a corresponding large value of Ω_m. We illustrate this type of universe with a slightly increasing, nearly horizontal line at $\Omega_\Lambda = 0$ in the figure. The diagonal line refers to a combination of Ω_m and Ω_Λ that results in $\Omega = 1$ i.e., a spatially flat universe. The region of parameter space to the left and right of the diagonal line thus, refers to universe with $\Omega < 1$ (spatially open)

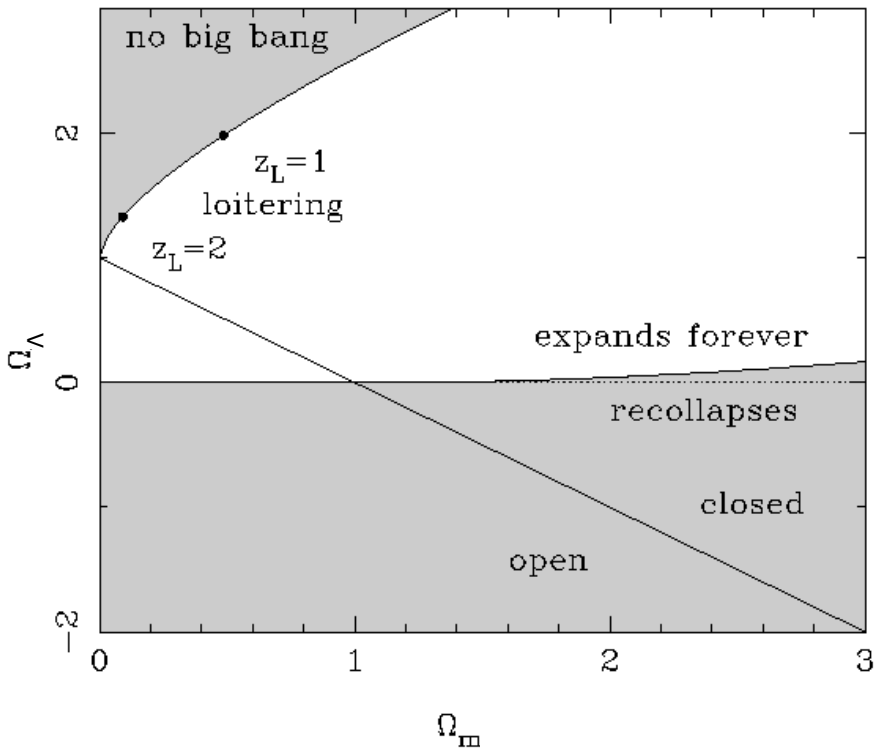

Figure 1.6 Possible scenarios for the universe, which are dependent on the combination of Ω_m and Ω_Λ. The various lines differentiate between the possible outcome of the universe. Any universe with negative Ω_Λ will re-collapse. On the other hand, if Ω_Λ is positive, the universe will expand forever except for a universe with a tiny positive Ω_Λ and an extremely large Ω_m. The diagonal line refers to $\Omega = 1$, corresponding to a spatially flat universe. To the left and right of this line, the universe is spatially open and closed respectively. Lastly, the curve line on the upper left of the figure refers to the bounds of a bouncing cosmology model. Adapted from Figure 3.5 of Peacock (1999).

and $\Omega > 1$ (spatially closed) respectively. The latter universe can expand forever given that $\Omega_\Lambda \neq 0$. We have also included the once popular 'loitering' model, on the top left of the parameter space. It has a small value of Ω_m, accompanied by $\Omega_\Lambda > 1$. If the value of Ω_Λ is increased beyond the limit of the 'loitering' model indicated by the curved line, it will constitute a universe with no hot big bang. These universes have an expansion history that bounces, i.e, the universe will collapse to a minimum size and then expands again.

The value of Λ

The starting point of determining the value of Λ came from the concept of zero-point energy. It was proposed by Max Planck in 1911 that the lowest amount of energy of an oscillator of frequency ν is $h\nu/2$ instead of zero Planck (1911).

h refers to the Planck's constant. Although vacuum is usually associated with a region of empty space, in quantum physical point of view, it consists of energies and particles pairs. These particles are known as the quantum vacuum. Since the introduction of the zero-point energy, Max Planck and Walter Nernst actively developed this concept between 1911 and 1916.

Since the vacuum is not completely empty, it has a zero point energy. In 1916, Nernst suggested that this energy could prevent the heat death of the universe (Nernst, 1916). Heat death refers to a state of the universe where there is no thermodynamic free energy and can no longer sustain entropy increasing processes. From his calculations, he estimated a value of $\rho_{\text{vac}} = 1.5 \times 10^5\,\text{kg}\,\text{m}^{-3}$ for the energy density of vacuum from the Rayleigh-Jeans law of radiation with a cut-off for frequencies above $10^{20}\,\text{Hz}$. Applying this concept to the static universe model proposed by Einstein, Wilhelm Lenz and Wolfgang Pauli concluded that the contradiction with observation meant that the zero-point energy of the vacuum was not a real effect (Lenz, 1926; Jordan & Pauli, 1928). This view changed in the late 1950s because of the successful demonstration of the Casimir effect (Casimir, 1948).

We can sum up the zero-point energies of all normal modes of the associated quantum fields in vacuum to yield

$$\sum_{k}^{k_{\text{max}}} \frac{1}{2}\hbar\omega_k \approx \frac{k_{\text{max}}^4}{16\pi^2} \tag{1.15}$$

where $\hbar$ is the reduced Planck constant, $\omega = 2\pi\nu$ and the final expression makes the common 'natural units' assumption: $c = \hbar = 1$. If we believe general relativity up to the Planck scale, then $k_{\text{max}} \approx (8\pi G)^{-1/2} \approx 10^{19}\,\text{GeV}$, resulting in $\rho_{\text{vac}} \approx 10^{92}\ \text{kg}\ \text{m}^{-3}$. For observations, we know from Peacock (1999),

$$\rho_{\text{vac}} = 1.8791 \times 10^{-26}\ \Omega\ h^2\ \text{kg}\ \text{m}^{-3} \tag{1.16}$$

where $\Omega = 1$ and $h = H_0\ /\ 100\,\text{km}\,\text{s}^{-1}\,\text{Mpc}^{-1}$. With the estimates of H_0, $\rho_{\text{vac}} \approx 10^{-26}\,\text{kg}\,\text{m}^{-3}$, which is about 120 orders of magnitude smaller than the theoretical value. Zel'Dovich (1967) did a similar calculation but with an unknown cutoff of 1 GeV, yielding a value that is closer to observations but still about 10 orders of magnitude larger. In general, ρ_{vac} is proportional to the cutoff scale raised to the fourth power. The cutoff will have to correspond to some piece of new physics. Since it is not observed at the Large Hadron Collider energies ($\sim 10\,\text{TeV}$), there

is inevitably a colossal mismatch between the theoretical and observed value of $\rho_{\rm vac}$. Anthropic reasoning (see Section 1.4 below) can be invoked to explain this difference.

1.3 Star formation within the ΛCDM paradigm

The ΛCDM model sets the stage for structure formation, subsequently star formation and ultimately the emergence of intelligent life in our universe. In this paradigm, structure formation occurs in a 'bottom-up' manner, where primordial density fluctuations grow by gravitational instability as a result of the CDM (Peebles, 1982). This method of structure formation meant that small haloes first form before mergers and accretions grow them into more massive ones (Blumenthal et al., 1984) over time. This formation scenario is in stark contrast to HDM, where structure formation occurs in a 'top-down' method, discussed in Section 1.2.1. Once the dark matter gravitational instability creates the potential wells, baryonic matter reacts and falls into these wells where star formation and feedback processes can occur (White & Rees, 1978). From these processes, galaxy formation and evolution happen in our universe that we would like to quantify and understand.

To fully comprehend galaxy evolution, a method focusing on the overall emission properties of the entire galaxy zoo has been developed. This method employs the analysis of data from the far-UV (FUV) to the far-infrared (FIR) spectrum. One advantage of this method is the empirical determination of the star formation history, independent of the complicated evolution of galaxy sub-population. Different components of the electromagnetic spectrum are analysed for the various components of star formation. The UV emission is dominated by short-lived massive stars and provides a direct measurement of instantaneous star-formation rate density (SFRD). The near-infrared (NIR) emission is dominated by stars comparable in mass to our Sun. These are proxies for stellar mass density (SMD). Lastly, interstellar dust absorbs UV light and emits in the FIR regime, making this emission a determinant for young stars and the SFRD. Combining all of the above, the emission history of the stars in the universe at the above mentioned and optical wavelengths is shown in Figure 1.7. It paints the picture of star formation history in the universe from $z \approx 8$ to present day by combining the measurements from both UV and IR.

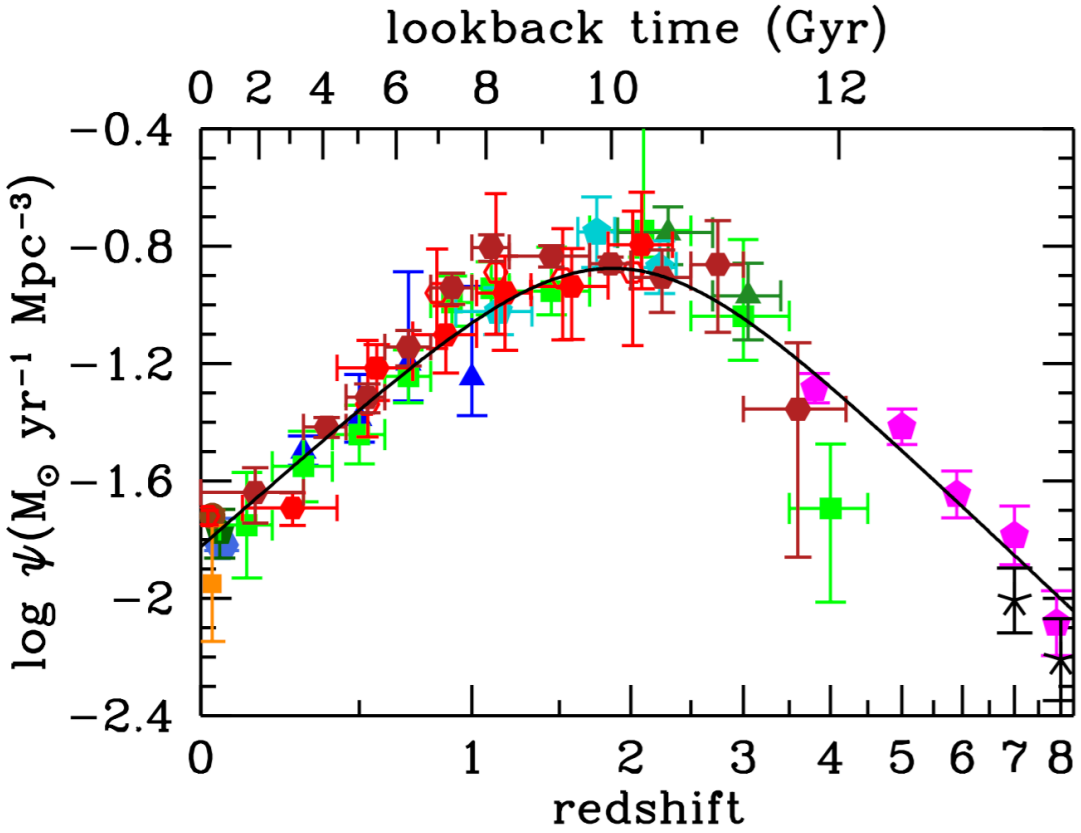

Figure 1.7 Cosmic star formation history based on UV and IR measurements. The star formation rates are determined in a given comoving volume. The various symbols correspond to different measurements in UV and IR spectrum. They are as follows: UV: Wyder et al. (2005) (blue-gray hexagon), Schiminovich et al. (2005) (blue triangles), Robotham & Driver (2011) (dark green pentagon), Cucciati et al. (2012) (green squares), Dahlen et al. (2007) (turquoise pentagons), Reddy & Steidel (2009) (dark green triangles), Bouwens et al. (2012a,b) (magenta pentagons), Schenker et al. (2013) (black crosses). IR: Sanders et al. (2003) (brown circle), Takeuchi et al. (2003) (dark orange square), Magnelli et al. (2011) (red open hexagons), Magnelli et al. (2013) (red filled hexagons), Gruppioni et al. (2013) (dark red filled hexagons). Adapted from Figure 9 of (Madau & Dickinson, 2014).

In Figure 1.7, the UV and FIR luminosities have been converted to instantaneous star formation rate using

$$\mathrm{SFR}_{\mathrm{FUV}} = \kappa_{\mathrm{FUV}} \times L_{\nu}(\mathrm{FUV}), \tag{1.17}$$

$$\mathrm{SFR}_{\mathrm{IR}} = \kappa_{\mathrm{IR}} \times L_{\mathrm{IR}}, \tag{1.18}$$

where $\kappa_{\mathrm{FUV}} = 2.5 \times 10^{-10}$ and $\kappa_{\mathrm{IR}} = 1.73 \times 10^{-10}$, assuming a Salpeter initial mass function (IMF) in Equation 1.17 and Equation 1.18 respectively. For the

values of Chabrier or Kroupa IMFs, refer to Figure 4 of Madau & Dickinson (2014). These factors have the units of $M_\odot\,year^{-1}\,L_\odot^{-1}$ and they are sensitive to recent star formation history, metal enrichment history and the IMF. The purpose of these factors is to translate observed luminosity to SFR and they are calibrated based on the value proposed by Kennicutt (1998a). L_ν(FUV) and L_{IR} refers to the intrinsic FUV-specific luminosity and the integrated IR luminosity from 8 to 1000 μm in Equation 1.17 and Equation 1.18 respectively. The total star formation rate is then calculated from the summation of these two equations.

As pointed out in Figure 1.7, the cosmic star formation rate ψ(z) experiences a turnover. This behaviour can be fitted by

$$\psi(z) = 0.015\frac{(1+z)^{2.7}}{1+[(1+z)/2.9]^{5.6}}\ M_\odot\ year^{-1}\ Mpc^{-3}. \tag{1.19}$$

Between $z = 3$ to $z = 8$, $\psi(z)$ scales proportionally as $(1+z)^{-2.9}$ which slows down and reaches a maximum at roughly $1.5 < z < 2$. Beyond which, the star formation rate decreases proportionally as $(1+z)^{2.7}$. The increase in $\psi(z)$ from $z \approx 8$ to 3 appears to be constant without any steep drop. However, there is active discussions as to whether this trend continues beyond $z = 8$ (Ellis et al., 2013; Oesch et al., 2013).

If we were to extrapolate Equation 1.19 into the future, the SFRD is expected to decrease. Such a behaviour was found by Salcido et al. (2018) with the continuation of the EAGLE (Schaye et al., 2015) simulation into the future. They conclude that this decrease is due to the feedback from active galactic nuclei (AGN). When such feedback is switched off in the simulations, the SFRD starts to increase again. This trend was consistent for both a ΛCDM and a EdS universe simulation as indicated in Figure 8 of Salcido et al. (2018). Given infinite time into the future to cool, the gas which is not presently star forming may potentially turn into stars. However, Salcido et al. (2018) only traced star formation 6 billion years into the future, around 10 billion years prior to the predicted 'freeze-out' of structure formation at $z \sim -0.6$ (Nagamine & Loeb, 2004; Salcido et al., 2018). Future star formation may be boosted by the currently declining SFR, which corresponds to a decrease in feedback, thereby increasing the cold gas reservoir for star formation in the future. This potential turn-around in the star formation rate in the future will be explored in detail in this thesis.

1.4 Multiverse and the anthropic principle

The anthropic principle states that the universe is in its current state because it needs to be compatible with the observers in it (Carter, 1974). This principle is often quoted in an attempt to explain why the fundamental constants have their measured values. It can be differentiated into the weak and the strong anthropic reasoning as shown.

- Weak anthropic reasoning: The preferential presence of observers at a special time or location biases the observed properties of the universe.
- Strong anthropic reasoning: One or more universes within the multiverse scenario must be suitable for the existence of observers.

The explanation provided by Carter (1974) is a demonstration of the weak anthropic reasoning. On the other hand, the strong anthropic reasoning states that the universe will eventually have intelligent life and hence results in the universe as it is (Barrow & Tipler, 1986). The main difference between the weak and strong anthropic reasoning is where the focus lies. In the former, the existence of observers is a natural outcome of the current state of a single universe while the latter argues that observers are special because at least one of the universe within the multiverse must have these conditions to host observers. Both arguments serve to explain the current state of the universe. Observers are likely to exist at specific times because conditions have to be met. One of these conditions assume that observers can exists only after recombination. This assumption means that the temperature of the universe has to be less than 1000 K where it is thermodynamically favourable for the occurrence of recombination. If we also require the densities of baryons and dark matter to be relatively equal, and the photon to baryon ratio is roughly $137^2\,\mathrm{m_p/m_e}$, these conditions constrained the window of structure formation to be soon after matter-radiation equality (Peacock, 1999). If other ingredients such as metals are required for life to exist, the universe has to be of an age comparable to a typical stellar lifetime.

An example of a successful application of the anthropic reasoning is the prediction of the existence of a previously unknown energy state in the carbon atom. The energy state must exist because it is vital for the occurrence of stellar evolution and life (Barrow & Tipler, 1986; Hoyle, 1994). The anthropic reasoning can be extended to cosmology, particularly regarding the value of the cosmological

constant (see Section 1.2.2). There exists a vast discrepancy in the value of ρ_Λ predicted by quantum field theory and observations, 120 orders of magnitude to be exact. Through anthropic reasoning, Weinberg (1987) concluded that Λ could not be of a substantial negative nor positive value. In the case of a large negative Λ, the universe will re-collapse upon itself, allowing structure formation to be highly efficient. However, this scenario only happens for a short time before the 'big crunch', i.e., complete collapse of such a universe, heavily restricting the amount of time available for star formation. On the other hand, if Λ is of a large positive value, the universe will expand at such a fast rate that no structure formation and consequently, star formation can take place. Both of these scenarios will prevent the emergence of intelligent life.

The growth of density perturbations which leads to structure formation is dependent on the cosmological parameters. Within the Newtonian limit, we can obtain an equation for the time-varying amplitude of fractional density perturbation $\delta = \delta\rho/\rho_0$

$$\ddot{\delta} + 2\frac{\dot{a}}{a}\dot{\delta} = \delta(4\pi G\rho_0), \tag{1.20}$$

for a flat universe. Cosmological parameters influence the growth of density perturbation through both $\dot{a}/a$ and ρ_0. The $\dot{a}/a$ term is also known as the 'Hubble drag term', reflecting how cosmic expansion will slow down growth. The ρ_0 is the driving term that enhances the growth of density perturbation. This is a second-order differential equation for $\delta(\mathbf{x}, t)$ with a growing ($D_1(t)$) and decaying mode ($D_2(t)$)

$$\delta(\mathbf{x}, t) = A(\mathbf{x})D_1(t) + B(\mathbf{x})D_2(t), \tag{1.21}$$

where A($\mathbf{x}$) and B($\mathbf{x}$) are the corresponding spatial configurations of the cosmic primordial matter distribution. For an EdS universe, $D_1(t) \propto t^{2/3} \propto a$ and $D_2(t) \propto t^{-1} \propto a^{-3/2}$. Usually, the decaying mode solution is ignored because it will be negligible by present time. For a flat universe with Λ, we find $d\ln\delta/d\ln a \approx \Omega_m^{0.55}$ (Linder & Cahn, 2007). When $\Omega_m \approx 1$, we recover the same relation $\delta \propto a$ as the EdS universe. As Ω_m decreases below one, growth slows down and freezes when $\Omega_m = \Omega_\Lambda = 0.5$.

As previously mentioned, anthropic reasoning can potentially provide constraints for physical models. However, it does not provide a valid explanation or determination of the values of the parameters (Earman, 1987; Kolb & Turner, 1990; Deltete, 1993). Some would argue the anthropic reasoning for the value of the cosmological constant is sufficient, and no further explanation is required.

There have been several examples where great emphasis was placed on the value of a certain number but was later determined as an accident of nature. These include the number of planets in the solar system and distance between the Sun and Earth by Johannes Kepler and the Large Number Coincidence by Dirac (1937).

Based on the anthropic principle, one can consider the more abstract concept of a multiverse. Infinite copies of the universe with different values for the fundamental constants such as the cosmological constant constitutes the multiverse. This ensemble of universes is predicted by some models of inflation (Vilenkin, 1983; Linde, 1986). In this infinite possibility, universes can have a wide range of values for Λ. As mentioned previously, other conditions have to be fulfilled before intelligent life can emerge. Universes with too high values of the cosmological constant will inhibit the emergence of life. Therefore, observers will preferentially exist in models with a small value of cosmological constant, potentially answering the questions about the scale of vacuum energy and the existence of observers (Peacock, 2007). This argument, therefore, provides an upper limit on the value of cosmological constant and allowed Weinberg (1989) to predict Λ to be non-zero. Efstathiou (1995) calculated the expected value of the distribution of Ω_ν to be approximately 0.9, which is close to the current observed value.

A high value of Λ is in disagreement with the observations of galaxies formation at present day Weinberg (1989). The observed value is about 10^{120} smaller than the 'natural' value determined by Planck scale (Efstathiou, 1995). This small cosmological constant started to dominate the energy content of the universe at $z \sim 1$, coinciding with the period of decline in SFRD. This coincidence is interesting and we aim to find out why is this so. In this thesis, we quantify star formation into the future when Λ becomes dominant, attempting to determine if these two events are directly related. To probe their relation further, we invoke the idea of the multiverse. Through altering the value of Λ, it will affect structure and star formation. By quantifying the star formation rate in universes with different values of Λ, the relation of Λ domination and star formation can be verified. We aim to extend the work of Weinberg (1987), Efstathiou (1995) and Peacock (2007) by incorporating modern structure formation and the corresponding star formation knowledge in numerical simulations.

1.5 Thesis overview

The goal of this thesis is to use cosmological simulations to quantify star formation and other properties of a ΛCDM universe into the future, so that we can understand the asymptotic efficiency of conversion of baryons into stars. We will then use simulations of counter-factual universes to investigate the degree of impact of Λ on structure formation. These numerical experiments will explore the concepts of anthropic reasoning and the multiverse. The process of and results from running the simulations will address the concern of the predictive ability and robustness of galaxy formation codes through their behaviour in different parameter regimes. The content of each chapter is provided below.

- **Chapter 2**: The various components of cosmological simulations are described. These include the generation of initial conditions, the main simulation code, `Enzo` used to evolve the simulation, chemistry and cooling library, and analysis tools such as halo finding and analysis of results.

- **Chapter 3**: The calibration of feedback parameters used in simulations in this thesis. From a total of 71 zoom simulations of a Milky Way (MW) sized halo, we tune the feedback parameters to reproduce the baryon makeup of a MW sized halo. This work shows that the final feedback prescription can extend the match of baryon content down to halo masses of $10^{10}\,\mathrm{M}_{\odot}$. Also, comparisons to other observables are made, and we explore the reproducibility of results from identical initial conditions.

- **Chapter 4**: Using the feedback prescription from the previous chapter, we attempt a cosmological box simulation beyond $z = 0$. We choose a resolution that is comparable to a similar previous work with a different numerical method to establish the convergence of the obtained results. We then extend the analysis to other properties not explored in the previous work, such as the star formation rate density (SFRD) and the intergalactic medium (IGM). We also conduct a numerical convergence study on the results obtained. Lastly, we evolve the zoom simulation from the previous chapter beyond $z = 0$ and compare it to haloes with similar mass from the cosmological box simulation at $z = 0$.

- **Chapter 5**: We generate and evolve the initial conditions obtained by scaling the value of Λ at an early epoch of the universe. We investigate

the specific components of the simulation that has to be changed according to the counter-factual cosmological parameters. We also modify the value of clustering in a ΛCDM universe to mimic the effect of scaling Λ. These simulations will address and explore the concept of the multiverse.

- **Chapter 6**: In this final chapter, we summarise the results from the numerous simulations conducted across the previous chapters. We will address the limitation in the results obtained and suggest future extensions that will improve the accuracy and validity of the results. Together with these limitations, we will predict the evolution of the star formation rate and the likelihood of the presence of observers in a multiverse setting.

Chapter 2

Numerical simulation

Cosmological simulations solve equations of gravity for dark matter, with equations of hydrodynamics and thermodynamics on top of gravity for baryons. Dark matter is represented by particles while fluid elements can be represented by either particles or grid cells. The total number of fluid elements and dark matter particles is limited by the available computational resources. Within the limits of the simulation, dark matter and baryonic properties, such as density, velocity and temperature can be predicted, and their evolution traced over time. This information, in turn, sheds light on the structure and kinematics of galaxies, their corresponding properties and spatial distribution, which is the main advantage of this method. As mentioned, the dynamic range, defined by the ratio of the length of the simulation box to the smallest grid cell, that can be simulated is restricted. Physical processes taking place on scales below the resolution limit of the simulation are treated with subgrid models with free parameters. Also, limitations in computational resources increase the difficulty in testing different subgrid recipes or fully exploring the parameter space of the variables in these recipes.

In this Chapter, we will introduce the key components that are used in constructing, running and analysing a specific set of numerical simulation. We will start with the generation of initial conditions with emphasis on the code, MUlti-Scale Initial Conditions for cosmological simulation (`MUSIC`), before introducing the working principles of the main cosmological simulation code used, `Enzo` and its associated chemistry library, `Grackle`. Lastly, we look at halo finding using the code, Robust Overdensity Calculation using k-Space Topologically Adaptive

Refinement (ROCKSTAR) and the analysis tool, yt. In this work, we are focusing on a particle-mesh code, where the gas and dark matter are represented by grid cells and particles respectively. This methodology is different from a smooth particle hydrodynamics (SPH) code where both the gas and dark matter are particles in the simulation. SPH naturally increases the resolution in the dense regions where structure formation is occurring, maximizing the usage efficiency of computational resources. However, it does not resolve shocks as well as a particle-mesh code and fails to provide adequate resolution in the extremely underdense region, which is of interest in this work.

2.1 Initial conditions

The initial conditions of our cosmological simulations consist of initial positions and velocities for dark matter particles and initial densities, velocities and internal energies for baryons in grid cells, which must be generated separately for cosmological simulations. It requires a few general steps which are summarised as follows. Firstly, a linear matter power spectrum will be generated with a transfer function (Eisenstein & Hu, 1999). The next step involves Gaussian random sampling of the power spectrum for modes within the simulation volume. The modes are then evolved in the linear regime via the Zel'dovich approximation. This procedure creates initial particle positions and velocities and grid cell properties sampling the matter field within a volume for fixed cosmology parameters, at a high enough redshift before structure formation within the box volume enters the nonlinear regime (Hahn & Abel, 2011).

2.1.1 Density fluctuation field

Cosmological box

We assume that the power spectrum is completely described by a real space over-density field $\delta(\mathbf{r})$ in the form $P(k) \equiv \left\langle \tilde{\delta}(\mathbf{k})\tilde{\delta^*}(\mathbf{k}) \right\rangle$ where $\tilde{}$ represents the transformed function of a Fourier transform pair and $\tilde{\delta^*}(\mathbf{k})$ is the complex conjugate of $\tilde{\delta}(\mathbf{k})$ such that $\tilde{\delta^*}(\mathbf{k}) = \tilde{\delta}(-\mathbf{k})$. This property is necessary because $\delta(\mathbf{r})$ is a real physical quantity. The amplitudes of the over-density field, $P(k)$,

can then be expressed in the form

$$P(k) = \alpha k^{n_s} \mathcal{T}^2(k), \tag{2.1}$$

where α is a normalization constant, n_s is the constant power spectrum spectral index after inflation and $\mathcal{T}(k)$ is the transfer function. `MUSIC` generates the initial conditions by creating a white noise sample of random values, $\mu(\mathbf{r})$ from a Gaussian distribution with a zero mean and unit variance. By multiplying the Fourier transformed white noise $\tilde{\mu}(\mathbf{k})$, with the square root of the power spectrum

$$\tilde{\delta}(\mathbf{k}) = \sqrt{P(|\mathbf{k}|)}\tilde{\mu}(\mathbf{k}), \tag{2.2}$$

it ensures that their amplitudes follow $P(k)$ in Equation 2.1. This process is known as 'k-space sampling'.

As `MUSIC` requires the over-density in real space instead of k-space, $\delta(\mathbf{r})$ is obtained through inverse Fourier transforming Equation 2.2. This simplifies the mathematical operation to a convolution in real space, which is the counterpart to the product in k-space in Equation 2.2 (Efstathiou et al., 1985; Salmon, 1996),

$$\delta(\mathbf{r}) = T(|\mathbf{r}|) \star \mu(\mathbf{r}), \tag{2.3}$$

where $T(r)$ corresponds to $\tilde{T}(k) \equiv \alpha k^{n_s/2} \mathcal{T}(k)$ in real space and $\star$ denotes a convolution. Evaluating Equation 2.3 is one of the two methods commonly used by initial condition generators, e.g., Salmon (1996); Pen (1997); Sirko (2005); Hahn & Abel (2011). The other method works by inverse Fourier transforming Equation 2.2 directly since both methods are mathematically equivalent (Bertschinger, 2001). Despite this similarity, the two approaches can create significant differences in the discrete realizations of the density fields, a discussion of which is beyond the scope of this section. These differences are discussed extensively in Pen (1997); Sirko (2005); Hahn & Abel (2011).

Zoom simulations

The zoom simulation is a product of the advances in the multi-mass technique (Navarro & White, 1994) used to understand physical processes of galaxy formation and evolution in a cosmological context. The main idea is to select an area of interest from a low-resolution simulation and rerun it with improved resolution in this region, while keeping the rest of the volume at the original

resolution. This approach streamlines the usage of computational resources into this area while allowing accurate representation of the long-range gravitational forces (Hahn & Abel, 2011).

The region or object of interest, such as a cosmological halo, is first identified in a low resolution simulation. The particles identified in the halo are then traced back to their initial position at the starting redshift of the simulation, chosen to be $z = 99$ in this work. At this time, the particles occupy a region called the Lagrange volume (Oñorbe et al., 2014). Within this volume, the spatial and mass resolutions are increased while the rest of the simulation box remains at low resolution. A simplistic representation is shown in Figure 2.1. In the Lagrange volume, dark matter particles are refined by splitting up a single particle into multiple particles, effectively increasing the mass resolution. It is, however, not as simplistic as the depiction in Figure 2.1. The refinement must be able to reproduce perturbations of the distribution from the overdensity field, and the discrete distribution of mass through the convolution of the transfer function with white noise to obtain the appropriate over-density field (Oñorbe et al., 2014).

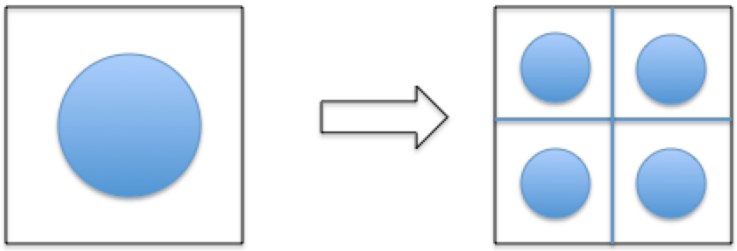

Figure 2.1 Simplistic diagram of zoom simulations. The box and circle represent the grid and dark matter particle respectively. We show one additional level of refinement in which the parent cell (left) is split up into 8 children cells in three dimensions (right). Further levels of refinement are repeats of the step illustrated.

It is a challenge to obtain the white noise for a zoom simulation containing cells that are at least of two different refinement levels. `MUSIC` addresses two key constraints: preservation of Fourier modes between grids and mass conservation in the simulation domain. A grid is defined as a collection of cells at the same resolution. To simplify the explanation, we consider only one additional level of refinement present, as illustrated in Figure 2.1. The steps described can be repeated in order to accommodate multiple levels. `MUSIC` first generates the unconstrained white noise field for the refined cells at eight times the variance of

the unrefined cells. The next step involves performing a fast Fourier transform (FFT) on both the refined and the overlapping portion of the unrefined grid. For a refined region, the boundary conditions are not periodic, which is a problem for FFT-based convolution. `MUSIC` introduces a padding that is twice the refined region and truncates the transfer function to overcome this problem. `MUSIC` then replaces all modes $\mathbf{k}$, up to the half the sampling wavenumber of the unrefined grid known as the Nyquist wavenumber by the corresponding Fourier coefficient from the unrefined grid, before inverse Fourier transforming, ensuring that the Fourier modes present in the unrefined grid are preserved.

To achieve mass conservation, `MUSIC` applies the Hoffman-Ribak algorithm (Hoffman & Ribak, 1991) in reverse. In other words, the white noise values of the unrefined grid are replaced by the average of the refined cells within the unrefined cell. Given that the mass of the subgrid is conserved through Fourier interpolation and the average of the refined cells, the global mass in the simulation box is conserved, too. Together with the previous step, `MUSIC` repeats this over multiple levels, achieving mass conservation and Fourier mode preservation across all refinement levels in the zoom initial conditions.

As discussed earlier, the other key component to generate the initial conditions is the convolution kernel, $T(r)$. `MUSIC` utilises Equation 2.3 and therefore focuses on the convolution step to generate the initial density field on grids of multiple levels of refinement. The primary concern is again to conserve mass across all levels. In contrast to the top-down approach where the coarse grid is used to constrain the finer grids, as in `GRAFIC2` (Bertschinger, 2001), `MUSIC` employs the bottom-up approach. This approach achieves a higher resolution sampling of the convolution kernel in Equation 2.3. The steps above generate the initial density field for the zoom simulation. For detailed steps and explanations, refer to Section 2 of Hahn & Abel (2011).

If a halo or any region of interest is chosen as the subject for zoom simulations, we identify a Lagrangian volume more extensive than the minimum size, e.g., the virial radius for the MW halo. This precautionary step is necessary to prevent contamination, which will adversely affect the properties of the central halo. Contamination in this context refers to the presence of low-resolution particles in the halo of interest in a zoom simulation. By having a particle with larger mass in the vicinity of the halo of interest, it will cause artificial mass concentration in a region of the halo. Therefore, it adversely affects the accuracy of the properties of the halo, which is highly undesirable (Oñorbe et al., 2014).

2.1.2 Initial particle position and velocity fields

After obtaining the initial density field, we need to generate the initial dark matter particle positions and velocity fields. They must be perturbed in a way that is consistent with the density fluctuation described in Section 2.1.1. `MUSIC` can apply either first or second order Lagrangian perturbation theory to obtain these fields based on the solutions of Poisson's equation. `MUSIC` opts for a multigrid based Poisson solver for its ease of extension for the generation of initial conditions for zoom simulations.

The dark matter particles are first uniformly deposited on a Cartesian grid and then displaced based on the Zel'dovich approximation (Zel'dovich, 1970). The comoving particle position, $\mathbf{x}$ at time, t is given by

$$\mathbf{x}(t) = \mathbf{q} + \mathbf{L}(\mathbf{q}, t), \tag{2.4}$$

where $\mathbf{q}$ is the initial unperturbed position and $\mathbf{L}(\mathbf{q})$ is the displacement field. At first order in a Friedmann-Robertson-Walker background, $\mathbf{L}$ can be expressed as the gradient of a potential Φ, proportional to the gravitational potential, ϕ,

$$\mathbf{L}(\mathbf{q}) = -\frac{2}{3H_0^2 a^2 D_+(t)} \boldsymbol{\nabla}_q \phi(\mathbf{q}, t) = \frac{\boldsymbol{\nabla}_q \Phi(\mathbf{q}, t)}{D_+(t)} \tag{2.5}$$

where H_0 is the Hubble constant, $D_+(t)$ is the growing mode of the linear density perturbation, a is the cosmological scale factor and ϕ is the gravitational potential according to Poisson's equation

$$\Delta_q \phi(\mathbf{q}, t) = \frac{3}{2} H_0^2 a^2 \delta(\mathbf{q}, t) \tag{2.6}$$

where δ is the Gaussian overdensity field. By taking the time derivative of Equation 2.4, we can obtain the velocity field

$$\dot{\mathbf{x}}(t) = \mathbf{v}(t) = \frac{d}{dt} \mathbf{L}(\mathbf{q}, t). \tag{2.7}$$

Since the velocities are derived from the gradient of a potential, they are irrotational, i.e., $\boldsymbol{\nabla} \times \dot{\mathbf{x}}(t) = 0$. As mentioned before, `MUSIC` choose to employ a multigrid based solver to naturally extend it to a nested adaptive grids. With first order Lagrangian perturbation, some argue that it can severely underestimate higher order moments of the density probability distribution functions at early

times (Munshi et al., 1994; Scoccimarro, 1998; Crocce et al., 2006; Tatekawa & Mizuno, 2007), which undermines its accuracy. Hence, second-order Lagrangian perturbation theory can often be used instead to generate more accurate initial conditions.

2.1.3 Baryon initial conditions

On top of the initial conditions for the dark matter particles, we have to initialise the baryon density fluctuations as well. At high z, the baryon density fluctuations are not yet tracing that of the dark matter exactly (Yamamoto et al., 1998). Also, the baryon fluctuations are exponentially suppressed beyond the photon diffusion scale (Silk, 1968). This combined effect means that the baryon transfer function differs from the pure dark matter transfer function, especially on scales below $\sim 10^{-2}\,h^{-1}$Mpc.

With the appropriate transfer functions, `MUSIC` can then replace the density transfer functions used for the computation of the initial velocities given in Section 2.1.2 (see Section 5.1 in Hahn & Abel (2011) for more detail). This formulation can be extended to second order Lagrangian perturbation theory because the transfer functions generate an "effective" source field. Since the difference in both the initial amplitudes of density perturbations and initial velocity is captured with this approach, `MUSIC` can accurately model the growth of density perturbations in the fluid composed of baryons and dark matter (Yoshida et al., 2003). At the Hubble radius, which is defined as the distance derived from the ratio of the velocity of light, c to the value of H_0, there is a large difference in the velocities of baryons and dark matter due to the coupling between photons and baryons. To prevent errors arising from this difference, we set the initial conditions to a time long after photon decoupling ($z \approx 1100$) (Valkenburg & Villaescusa-Navarro, 2017). Therefore, the starting redshift for the simulations in this work is set to $z = 99$.

2.2 The Enzo simulation code

`Enzo` is a publicly available simulation code that is widely used for many astrophysical and cosmological purposes. It started as the PhD thesis of Greg Bryan at the University of Illinois from 1994 to 1996 and has undergone

tremendous improvement through inputs from numerous contributors over the years (Bryan et al., 2014). It is an adaptive mesh-refinement (AMR) simulation code which solves the Euler equations for fluid dynamics on a Cartesian mesh and treats dark matter as a set of discrete, collisionless particles.

Building upon the application of structured AMR in shock hydrodynamics by Berger & Colella (1989), Bryan & Norman (1997) and Norman et al. (1999) adapted and applied this to cosmological simulations. The AMR machinery in `Enzo` will be discussed in further detail in Section 2.2.1. AMR focuses the usage of computational resources on the regions of interest by increasing spatial resolution around these regions, capturing the high dynamic range in gravitational physics and hydrodynamics in a cosmological simulation.

`Enzo` solves the hydrodynamical equations of an ideal gas in comoving coordinates consistent with that of an expanding background cosmology:

$$\frac{\delta \rho_b}{\delta t} + \frac{1}{a}\mathbf{v}_b \cdot \boldsymbol{\nabla}\rho_b = -\frac{1}{a}\rho_b \boldsymbol{\nabla} \cdot \mathbf{v}_b, \tag{2.8}$$

$$\frac{\delta \mathbf{v}_b}{\delta t} + \frac{1}{a}\left(\mathbf{v}_b \cdot \boldsymbol{\nabla}\right)\mathbf{v}_b = -\frac{\dot{a}}{a}\mathbf{v}_b - \frac{1}{a\rho_b}\boldsymbol{\nabla} p - \frac{1}{a}\boldsymbol{\nabla}\phi, \tag{2.9}$$

$$\frac{\delta E}{\delta t} + \frac{1}{a}\mathbf{v}_b \cdot \boldsymbol{\nabla} E = -\frac{\dot{a}}{a}\left(3\frac{p}{\rho_b} + \mathbf{v}_b^2\right) - \frac{1}{a\rho_b}\boldsymbol{\nabla} \cdot (\rho \mathbf{v}_b) - \frac{1}{a}\mathbf{v}_b \cdot \boldsymbol{\nabla}\phi + \Gamma - \Lambda_c, \tag{2.10}$$

where ρ_b is the comoving density of baryons, $\mathbf{v}_b$ is the peculiar velocity of baryons, p is the pressure, ϕ is the gravitational potential in comoving coordinates, a is the cosmic scale factor, E is the specific energy of the gas, and Γ and Λ_c are the heating and cooling rates respectively. All the derivatives in these equations are in comoving coordinates. Equations 2.8, 2.9 and 2.10 correspond to the conservation of mass, momentum and energy respectively.

`Enzo` completes the set of equations with:

$$E = p/\left[(\gamma - 1)\,\rho_b\right] + \mathbf{v}^2/2, \tag{2.11}$$

$$\boldsymbol{\nabla}^2\phi = \frac{4\pi G}{a}\left(\rho_b + \rho_{dm} - \rho_0\right), \tag{2.12}$$

$$\frac{\ddot{a}}{a} = -\frac{4\pi G}{3a^3}\left(\rho_0 + 3p_0/c^2\right) + \Lambda/3, \tag{2.13}$$

where ρ_{dm} is the comoving dark matter density, ρ_0 is the comoving background density, p_0 is the background pressure, γ is the ratio of specific heats and Λ is the cosmological constant. Equations 2.11, 2.12 and 2.13 are the equation of state, comoving form of Poisson's equation and one of the Friedmann equations which describes the evolution of the Universe in comoving coordinates.

The particles in the simulation are governed by Newtonian gravity in comoving coordinates. These equations are valid under a few assumptions. Firstly, the velocities of the baryons and dark matter are much smaller than the speed of light, i.e., relativistic effects are negligible. The next assumption is that cosmological curvature effects can be neglected, which translates into the simulation volume being much smaller than the radius of curvature of the universe.

`Enzo` offers several hydrodynamic methods with two being commonly used: the piecewise parabolic method (PPM) (Woodward & Colella, 1984) extended to cosmological simulations (Bryan et al., 1995) and the hydrodynamic method, `ZEUS` in the magnetohydrodynamics (MHD) code (Stone & Norman, 1992). Although PPM is of higher order accuracy and does not introduce artificial viscosity to resolve shocks, `ZEUS` is more robust and less intensive on computational resources. Therefore, `ZEUS` is the preferred hydrodynamic method for the aims of this work, and we will focus on the description of `ZEUS`. `Enzo` also comes with the capability to handle MHD simulations, but it is not within the scope of this work. We will discuss about the various components in the `Enzo` simulation code in the following sections: the AMR machinery in Section 2.2.1, the gravity solver in Section 2.2.2, the `ZEUS` hydrodynamic method in Section 2.2.3, the associated chemistry and radiative cooling/heating library, `Grackle` in Section 4.2.3 and star formation and feedback algorithms in Section 2.2.5.

2.2.1 AMR machinery

The main advantage of `Enzo` is in its AMR capability, focusing computational resources into regions of interest. It achieves this by an adaptive hierarchy of grid patches at varying levels of resolution. For a cosmological simulation, a root grid covers the entire computational domain initially. During the evolution of

the simulation, regions of interest depending on user-defined criteria can emerge, demanding better resolution. In this region of space, the coarse grid is now the parent grid of a more highly resolved child grid. As the simulation continues to evolve, such regions may appear in specific areas within the child grid, which calls for higher resolution. The child grid will then become a parent grid, hosting an even more highly resolved child grid. This process is allowed to repeat until the maximum level of refinement specified is reached. We visualise this with Figure 2.2 where we can identify multiple levels of refinement in response to the gas density. The gas density is indicated by the colour bar, and it is clear that the finer cells are concentrated around regions of high densities.

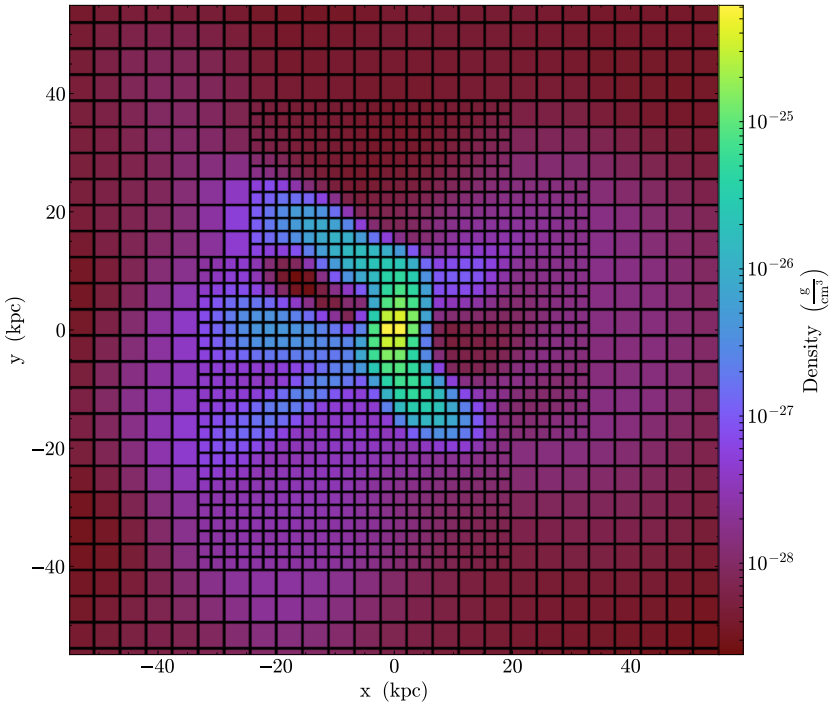

Figure 2.2 Density projection illustrating the AMR machinery in `Enzo` with grid cells overlaid. The gas densities are represented by the colour bar on the right. Although this projection plot only consists of two levels of AMR, it is clear that finer grid cells are concentrated around the region of high density.

Grids consist of active zones surrounded by a layer of ghost zones. The active zones store the properties of the baryons and particle properties while the ghost zones act as temporary storage for values obtained either from the neighbouring grids or interpolated from the parent grid. The ghost zones play an essential role in accommodating the computational calculations involving the hydrodynamic and gravity solvers, which requires three and six layers of ghost zones respectively.

AMR can occur in `Enzo` based on several criteria. These include but are not limited to gas, stellar and dark matter mass within the cell, local Jeans length, local density gradient, local pressure and energy gradients, cooling time and metallicity. These criteria work with the threshold values set for different scientific purposes. The AMR in `Enzo` allows the specification of any integer ratios of the parent and child grid resolution. However, a value of two is most commonly used due to efficiency. The effective resolution in the most refined region is, therefore, $N_{\rm root} \times 2^{\ell_{\rm max}}$ where $N_{\rm root}$ refers to the number of cells along one edge of the root grid and ℓ_{max} is the maximum level of refinement allowed. It is important to remember that this is only affecting the spatial resolution while keeping the dark matter particle mass of the simulation constant.

Assume that at some point of time in the simulation, there exist multiple levels of refinement. How does the simulation decide the size of the timestep it should take to evolve the entire simulation? At each level of refinement, several timesteps corresponding to different physical process are determined:

$$\Delta t_{\rm hydro} = \min\left(\kappa_{\rm hydro}\frac{a\Delta x}{c_s + |v_x|}\right), \tag{2.14}$$

$$\Delta t_{\rm dm} = \min\left(\kappa_{\rm dm}\frac{a\Delta x}{v_{{\rm dm},x}}\right), \tag{2.15}$$

$$\Delta t_{\rm accel} = \min\left(\sqrt{\frac{\Delta x}{|\mathbf{g}|}}\right), \tag{2.16}$$

$$\Delta t_{\rm rad} = \min\left(\sqrt{\frac{\Delta x}{|\mathbf{a}_{\rm rad}|}}\right), \tag{2.17}$$

$$\Delta t_{\rm cond} = \min\left(\frac{k_{\rm cond}}{f_{\rm sp}}\frac{\Delta x^2 n_b}{\kappa_{\rm sp}\left(T\right)}\right), \tag{2.18}$$

$$\Delta t_{\rm exp} = f_{\rm exp}\left(\frac{a}{\dot{a}}\right), \tag{2.19}$$

here shown for the one-dimensional case. These timesteps are calculated for individual cells at the same level for each of the coordinate axes and the minimum is taken as the representative timestep. This information is also passed to the chemistry and cooling library, `Grackle`, described in Section 2.2.4. κ in Equations 2.14 to 2.19 are dimensionless constants with typical values of 0.5 except $\kappa_{\rm sp}$ in Equation 2.18, which is the Spitzer thermal conductivity.

Equation 2.14 enforces the Courant-Friedrichs-Levy (CFL) condition for accuracy and stability of an explicit finite difference discretisation of the Euler equations. In other words, it ensures that the timestep is small enough to prevent any changes in the fluid spreading beyond a single cell spacing, Δx. c_s and v_x are the sound speed and peculiar baryon velocity in a given cell respectively. Equation 2.15 acts identically to Equation 2.14 to ensure accuracy in the N-body solver by limiting the movement of the particles to no more than a single cell. $v_{\mathrm{dm},x}$ is the peculiar dark matter particle velocity.

Equations 2.16 and 2.17 are supplementary to Equation 2.14. The purpose of these two equations is for the consideration of the possibility of large gravitational ($\mathbf{g}$ in Equation 2.16) or radiation pressure ($\mathbf{a}_{\mathrm{rad}}$ in Equation 2.17) driven accelerations in individual cells on each level of refinement. Equation 2.18 is the stability condition for an explicit solution to the equation of heat conduction where n_b is the baryon number density and f_{sp} is the user-defined conduction suppression factor. In contrast to the scaling in the equations discussed before ($\Delta x/\sqrt{T}$), this timestep scales as $\Delta x^2/T^{2.5}$. This means that in regions of high spatial resolution and temperature, this timestep can easily become the limiting timestep. Since thermal conduction models require a two-fluid MHD approach and have a insignificant impact on the star formation rate (Smith et al., 2013), we do not apply any such model nor consider this timestep in this work.

Lastly, Equation 2.19 is related to cosmology in that it limits the timestep in which a can change by f_{exp}. In other words, the expansion of the Universe is constrained by some fractional amount specified by f_{exp}. This criterion is important because the expansion of the Universe and its first derivative with respect to time appears in Equation 2.9 and 2.10. It is particularly crucial for the stability of the PPM algorithm in comoving coordinates. This timestep criterion is significant only during high redshifts, before the formation of a substantial amount of structures.

After the calculation of the minimum timestep for each refinement level, `Enzo` evolves the simulation starting with the coarsest level, L. For simplicity, let us assume that the simulation consists of three total refinement levels L, $L+1$ and $L+2$. At level L, all the cells at this level are advanced in time by Δt_L. `Enzo` then proceeds to the next refinement level, $L+1$ and advance all cells at this level by Δt_{L+1}, determined by the minimum of all the calculated timesteps from Equations 2.14 to 2.19, repeating for finest level $L+2$ with Δt_{L+2}. At this level, `Enzo` will evolve the cells by ω timesteps such that $\omega \times \Delta t_{L+2} = \Delta t_{L+1}$.

After achieving this, Enzo will evolve level $L+1$ by Δt_{L+1} again and return to level $L+2$ after to ensure $\omega \times \Delta t_{L+2} = \Delta t_{L+1}$. This process continues until all the refinement levels present advance by the same amount of time given by Δt_L. It can be extended to any arbitrary number of refinement levels in a simulation. A graphical representation of the time stepping is shown in Figure 2.3

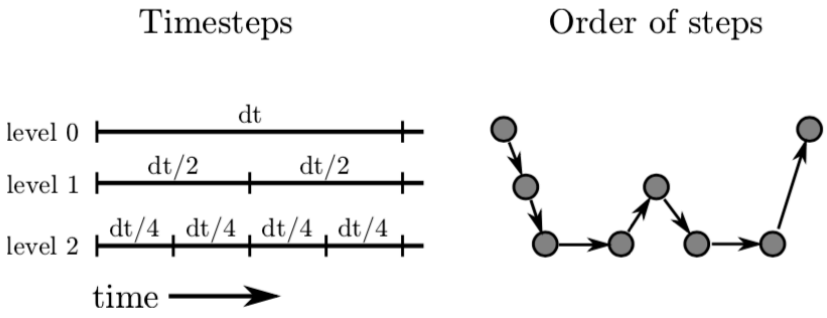

Figure 2.3 Time stepping process of Enzo. Level 0, 1 and 2 in the figure corresponds to $L, L+1$ and $L+2$ in the text description respectively. Adapted from Figure 2 of Bryan et al. (2014).

At the beginning of each timestep, cells at a given level fill the ghost zones by copying from neighbours on the same level and interpolating from the parent grid if they exist. When cells of two different levels evolved by the same amount of time, flux correction occurs at the interface boundary between the fine and coarse grids, improving the accuracy of the solution on the coarser level. At the end of every timestep on every level, the ghost zones are updated identically at the start of the timestep. Also, cells are examined in order to determine if they should be refined or de-refined and rebuild the entire grid hierarchy. This process of time stepping and hierarchy evolution is repeated recursively from the coarsest to the finest level of refinement in the simulation.

2.2.2 Gravity solver

The movement and acceleration of the gas and particles in the simulation as influenced by gravity are solved and evolved in three general steps. The total gravitating mass is first calculated, followed by the solution of the gravitational potential field in Equation 2.12 with the corresponding boundary conditions and lastly, using the difference of the potential to obtain the force on the mass. This force can be interpolated back to the particles for their evolution.

The calculation of the total gravitating mass begins with the deposit of the particles (dark matter and stars) onto the grids, which is accomplished with the second-order cloud-in-cell (CIC) interpolation technique (Hockney & Eastwood, 1988), yielding a spatially-discretised density field. Baryonic grid densities are then added to obtain the total matter densities. During the CIC interpolation, the baryonic cells are treated as virtual CIC particles placed at the grid centre. Together with the particles, the positions of both actual and virtual particles are temporarily advanced by $0.5v^n\Delta t$ where v^n is the particle velocity and n is the particle position in time, in order to obtain an estimate of the time-centred density field. The result is a total gravitating mass field $\rho_{\text{total}}^{n+1/2}$.

On the root grid, the potential field can be computed by applying a fast Fourier transform on $\rho_{\text{total}}^{n+1/2}$, in conjunction with the boundary conditions. Different methods are applied according to the type of boundary conditions present. `Enzo` then inverse Fourier transforms this potential field to obtain it in real space, giving potential values at the cell centres. `Enzo` interpolates these potential values of the cells on the root grid to generate the boundary conditions of the child grid via the tri-linear interpolation by default. `Enzo` requires the gravitating mass field to solve for the potential field in these child grids together with the boundary conditions. The particles in the child grids are deposited using the same CIC method as the root grid, with the only difference being the resolution of the grids. A multigrid relaxation technique is then applied to calculate the gravitational potential within each child grid (Falgout & Yang, 2002).

By finite-differencing the potential values, forces can be calculated and then interpolated to the particle positions. The position and velocity of a given particle are then updated accordingly. It is a recursive process within the child grids, and they are evolved with the respective timestep determined for each level of refinement as described in Section 2.2.1. Since the force is calculated from the gradient of the potential, i.e., the finite difference of two potential values, the effective force resolution in `Enzo` is equal to twice the cell size at a given refinement level.

This particle-mesh method is extended to solve a collisionless N-body problem in `Enzo`. By following the trajectories of a representative sample of individual particles, it is much more efficient than a direct computation of the collisionless Boltzmann equation. Updated particles that move out of a grid patch are sent to the adjacent volume with the highest spatial resolution. This

communication process occurs at the end of the corresponding timestep on each different refinement levels.

2.2.3 ZEUS hydrodynamic method

As mentioned before, the finite difference hydrodynamic algorithm in the compressible MHD code 'ZEUS' (Stone & Norman, 1992) is available as one of the many choices for hydrodynamic solvers in Enzo. The fluid transport is solved on a Cartesian grid with the upwind, monotonic advection scheme of van Leer (1977) within a multi-step (operator split) solution process which is entirely explicit in time. This method has a second-order and first-order accuracy in space and time, respectively, and conserves total energy.

As the name suggests, operator split methods divide the solution of Equations 2.8 to 2.10 into parts that represents a single term in the equations individually. Each part is evaluated based on the results before it. On top of operator splitting the expansion terms present in Equations 2.8 to 2.10, the remaining terms in these equations are split up into source and transport steps. In the source steps, ZEUS solves the terms on the right-hand side of Equations 2.8 to 2.10. On the other hand, the terms on the left-hand side of these equations are classified as those involved in the transport step as they are responsible for the movement of mass, momentum and energy across the grid.

One key feature of the ZEUS method is the introduction of a von Neumann-Richtmeyer artificial viscosity in order to smooth potential shock discontinuities in fluid flows. These discontinuities will lead to the break-down of the finite difference equations. The artificial viscosity proposed by Von Neumann & Richtmyer (1950), $\mathbf{Q}$ is inserted into the source terms as

$$\rho\frac{\partial \mathbf{v}}{\partial t} = -\boldsymbol{\nabla} p - \rho\boldsymbol{\nabla}\phi - \boldsymbol{\nabla}\cdot\mathbf{Q}, \tag{2.20}$$

$$\frac{\partial \mathbf{e}}{\partial t} = -p\boldsymbol{\nabla}\cdot\mathbf{v} - \mathbf{Q} : \boldsymbol{\nabla}\mathbf{v}, \tag{2.21}$$

where $\mathbf{v}$ is the baryon velocity, ρ is the mass density, p is the pressure, e is the internal energy density of the gas, : is the double dot product operator and $\mathbf{Q}$ is

the artificial stress tensor given by

$$Q_{ii} = \begin{cases} Q_{\mathrm{AV}} \rho_b \left(a\Delta v_i + \dot{a}\Delta x_i \right)^2, & \text{for } a\Delta v_i + \dot{a}\Delta x_i < 0 \\ 0, & \text{otherwise} \end{cases} \tag{2.22}$$

and

$$Q_{ij} = 0 \text{ for } i \neq j. \tag{2.23}$$

Δx_i and Δv_i corresponds to the comoving width of the grid cell and the difference in the peculiar velocity of gas across the grid cell in the i-th axis respectively, a is the cosmic scale factor, and Q_{AV} is a constant, typically of value 2 (Stone & Norman, 1992; Anninos & Norman, 1994).

Inserting the artificial viscosity ensures that the correct Rankine-Hugoniot jump conditions are achieved, but it results in the broadening of shocks over 3-4 cells. This broadening can potentially give rise to unphysical pre-heating of gas in the upstream of the shock wave (Anninos & Norman, 1994). However, it is much more robust than PPM, and it is more stable operationally, both in terms of the simulation completing successfully and the amount of time required for completion. Therefore, despite its shortcomings, it is more suited for this thesis.

2.2.4 The Grackle chemistry and cooling library

Chemistry and cooling are essential processes in various astrophysical scenarios, especially for star formation. Simple molecules created from gas- and dust-phase chemical reactions can significantly enhance cooling (Hollenbach & McKee, 1979; Omukai et al., 2005). Gas falling into a potential well of a dark matter halo can experience shock heating to the virial temperature and relies on radiative cooling processes to allow further collapse (Rees & Ostriker, 1977; White & Frenk, 1991). Specific elements can affect the ability of gas to cool and form stars (Raymond & Smith, 1977; Black, 1981; Sarazin & White, 1987; Cen, 1992; Sutherland & Dopita, 1993; Abel et al., 1997; Anninos et al., 1997). These will significantly influence the outcome of the simulation and therefore, should be modelled as accurately as possible.

`Grackle` is a multi-code chemistry and cooling library for astrophysical simulations (Smith et al., 2017). The primordial chemistry used in `Grackle` is based on the `Enzo` code but has more extensive coverage of processes. `Grackle`

offers the option of equilibrium and non-equilibrium chemistry networks. The timestep received from Section 2.2.1 is used to solve and update the network and the internal energy in both options of chemistry network. Since this timestep is often relatively large, it can possibly lead to significant errors. Therefore, `Grackle` limits the timestep used in its calculation such that the H and e^- abundances do not change by more than 10% in any sub-cycle step. However, we choose to focus on the usage of the equilibrium mode in this thesis. This mode only provides cooling rates, which is particularly helpful when disentangling the origin of any particular features in the results which we will discuss in more detail in Section 4.2.3.

The equilibrium mode in `Grackle` uses tables of pre-computed heating and cooling rates of primordial species (H & He) and metals under the assumption of ionisation equilibrium. In the absence of incident radiation, the cooling rates are functions of temperature only, which is known as collisional ionisation equilibrium. On the other hand, with incident radiation, the cooling rates are no longer just functions of temperature, but also of density. `Grackle` provides the cooling rate, Λ, heating rate, Γ, and the average molecular weight, μ in the form of a table of pre-computed values. For any values not in the table, interpolation is done linearly in log-space.

Rather than calculating the temperature directly, `Enzo` and other simulation codes solve for the internal energy of the gas. An equation relating one to the other is given by

$$e = \frac{kT}{(\gamma - 1)\,\mu m_{\mathrm{H}}}, \tag{2.24}$$

where k is the Boltzmann constant, e is the specific internal energy, T is the temperature of the gas, γ is the adiabatic index of an ideal gas, and m_{H} is the mass of a hydrogen atom. Given that μ is also a function of temperature, Equation 2.24 has to be solved iteratively. Initially, we assume that $\mu = 1$ and calculate the corresponding T from Equation 2.24. With T as input, we obtain a new value of μ through linear interpolation from the table of $\mu(T, ..)$. The average of this new value of μ and $\mu = 1$ will be the input for the next step in the iterative process. Generally, this is expressed as

$$\mu_i = \frac{1}{2}\left(\mu_{i-1} + \mu\left(T_{i-1}, ...\right)\right), \tag{2.25}$$

where i is a random iteration step in this iterative process. This acts as a dampener to prevent the solution of μ and T from oscillating.

With T calculated, `Grackle` interpolates over the table of pre-computed values for the primordial species to obtain the corresponding rates in the absence of a radiation background. However, for cosmological simulations, a radiation background is used to model heating from the stars and active galactic nuclei (AGN). Not only did this radiation reionise the Universe at $z \sim 6 - 10$, it heated the IGM to $\sim 2 \times 10^4\,\mathrm{K}$ (Schaye et al., 2000). This hot IGM means that gas within haloes of virial temperature less than that would not collapse, preventing star formation. However, it is impossible to reproduce these effects in simulations unless they are of large volume, significantly high resolution and performed with radiative transfer. Therefore, due to limitations in computational resources, it is assumed that the redshift-dependent UV background is spatially uniform. `Grackle` derives the photo-heating and photochemical reaction rates from the models by Faucher-Giguère et al. (2009) or Haardt & Madau (2012), which are the inputs to the photoionisation code, `CLOUDY` (Ferland et al., 2013). This UV background complicates the previous one-dimensional table with T into a multi-dimensional table which relates Λ, Γ and μ to z, ρ and T.

In the astrophysics context, metals are defined as elements heavier than He. For simulations with metals, an additional correction has to be considered in order to obtain $\mu_{i,Z}$ from μ_i from Equation 2.25,

$$\frac{\rho}{\mu_{i,Z}} = \frac{\rho}{\mu_i} + \frac{\rho_Z}{\mu_Z}, \tag{2.26}$$

where ρ_Z is the metal density and $\mu_Z \equiv 16$, consistent with a Solar abundance pattern. This iterative process converges to a solution for μ and T within 1% in a small number of iterations. Furthermore, the impacts of metals on cooling and heating rates have to be considered in these simulations. `Grackle` computes this in a similar way to that of the primordial species described above and was first discussed by Smith et al. (2008). The cooling rates of metals up to atomic number 30 (Zn) corresponding to Solar abundances are added to the table of rates of primordial species. When applying these to simulations, these are scaled according to local metallicity.

Lastly, the CMB acts as a temperature floor in cosmological simulations where no gas can cool radiatively below this temperature. This effect is modelled by

$$\Lambda_{\mathrm{final}}(T) = \Lambda(T) - \Lambda(T_{\mathrm{CMB}}), \tag{2.27}$$

where the final cooling rate used in the simulation is calculated by subtracting the cooling rate at the CMB temperature from the cooling rate obtained from the table look-up. With this formulation, cooling rates decrease smoothly to zero when the temperature approaches the CMB temperature. Also, for gas that drops below the temperature of the CMB, it will be heated by the CMB.

2.2.5 Star formation and feedback

Among the choices offered in `Enzo` in terms of star formation and feedback, we employ the model described by Cen & Ostriker (1992). Despite its age, this model is one of the most commonly used in `Enzo` to the present day. The conditions required for star formation in a cell include:

1. No further refinement of the cell
2. Gas density greater than a threshold density: $\rho_{\rm gas} > \rho_{\rm threshold}$
3. Convergent flow: $\boldsymbol{\nabla} \cdot \mathbf{v} < 0$
4. Cooling time less than a dynamical time: $\rm t_{cool} < t_{dyn}$
5. Gas mass larger than the Jeans mass: $\rm m_{gas} > m_{jean}$

If all the conditions are fulfilled, the algorithm generates a 'star particle' within the grid cell with a mass,

$$m_* = m_{\rm gas} \times \frac{\Delta t}{t_{\rm dyn}} \times f_*, \tag{2.28}$$

where $m_{\rm gas}$ is the gas mass in the cell, Δt is the timestep, $t_{\rm dyn}$ is the dynamical time and f_* is a dimensionless efficiency factor. The mass of the generated star particle is compared to a user-defined minimum star particle mass. If it is higher than the threshold, a star particle will be created. It will be positioned in the centre of the cell and possesses the same peculiar velocity as the gas in the cell. It will be treated dynamically as all other particles. An equivalent mass of gas to that of the star particle will then be removed from the cell to ensure mass conservation.

Although the creation of a star particle is immediate, feedback happens over a longer timescale, designed to mimic the gradual process of star formation. In

each timestep, the star forming mass is given by

$$m_{\rm form} = m_0 \left[\left(1 + \frac{t - t_0}{t_{\rm dyn}}\right) \exp\left(-\frac{t - t_0}{t_{\rm dyn}}\right) - \left(1 + \frac{t + dt - t_0}{t_{\rm dyn}}\right) \exp\left(-\frac{t + dt - t_0}{t_{\rm dyn}}\right) \right], \tag{2.29}$$

where m_0 is the star particle mass, t_0 and t are the creation time of the star particle and current time in the simulation respectively. Through this implementation, according to Equation 2.29, the rate of star formation increases linearly and peaks after one dynamical time before declining exponentially (Smith et al., 2011).

We adopt Smith et al. (2011)'s modification of the Cen & Ostriker (2006) thermal supernova feedback model. The star particles add thermal feedback to a set of neighbouring grids with size and geometry that can be tuned by the user, known as distributed stellar feedback. This feedback continues until 12 dynamical times after its creation. In each timestep, feedback in the form of mass, energy, and metals is deposited.

Mass is removed from the star particle and returned to the grid as gas, given by

$$\mathrm{m_{ej}} = \mathrm{m_{form}} \times \mathrm{f_{ej}}, \tag{2.30}$$

where $f_{\rm ej}$ is the fraction of mass removed. Momentum of gas,

$$\mathrm{p_{feedback}} = \mathrm{m_{ej}} \times \mathrm{v_{particle}}, \tag{2.31}$$

where $v_{\rm particle}$ is the velocity of the star particle and is conserved by addition into the grid cell hosting the star. Feedback energy,

$$\mathrm{E_{feedback}} = \mathrm{m_{form}} \times \mathrm{c}^2 \times \epsilon \tag{2.32}$$

where ϵ and c are the feedback efficiency and speed of light respectively, is deposited into the user defined cells. For an ϵ value of 10^{-5} (Cen & Ostriker, 1992), an energy of 10^{51} erg is injected for every $\sim$ 56 $\mathrm{M_\odot}$ of stars formed. Metals are returned to the grid cells and their corresponding metallicity is given by

$$\mathrm{Z_{feedback}} = \mathrm{m_{form}} \times ((1 - \mathrm{Z_{star}}) \times \eta + \mathrm{f_{ej}} \times \mathrm{Z_{star}}), \tag{2.33}$$

where Z_{star} and η are the star particle metallicity and the fraction of metals yielded from the star respectively, are returned to the grid cells.

2.3 Analysis

The completion of the simulation is not the end of the investigation. The results have to be analysed and presented in a fashion that is easy to understand and comprehend. We know that in galaxy formation, gas can reside in gravitationally bound structures and the diffuse intergalactic medium. Therefore, we have to be able to identify these different environments in the simulation, and we achieve this with the help of halo finders described in Section 2.3.1. To assist with the presentation and analysis of the results from the simulations and the halo finding process, we will describe the analysis tool, `yt`, briefly in Section 2.3.2

2.3.1 Halo finding

Identifying the dark matter haloes in simulations is a crucial step in differentiating the various environments in the Universe. Halo finding methods can be separated into two major categories, namely the Spherical Overdensity (SO) finders such as the Amiga's Halo Finder (AHF) (Knollmann & Knebe, 2009), HOP-based halo finders and the Adaptive Spherical Overdensity Halo Finder (ASOHF) (Planelles & Quilis, 2010), and friends-of-friends (FOF). SO finders employ a top-down approach by first locating density peaks based on the particle distribution before adding particles in the sphere of increasing radius until the enclosed density falls below a predetermined threshold. FOF methods use a bottom-up approach by grouping particles together that are within a given linking length.

We are using a new form of finder which includes particle velocity information in addition to their position, known as phase-space finders such as Robust Overdensity Calculation using k-Space Topologically Adaptive Refinement (`ROCKSTAR`) (Behroozi et al., 2013a) in this work. One key advantage of using `ROCKSTAR` instead of other finder methods is its strength in distinguishing major mergers and subhaloes close to the centres of their host haloes where the density contrast is insufficient to identify the halo to which the particles belongs (Behroozi et al., 2013a). For the remainder of this section, we will look at the working principle of `ROCKSTAR` summarised in Figure 2.4

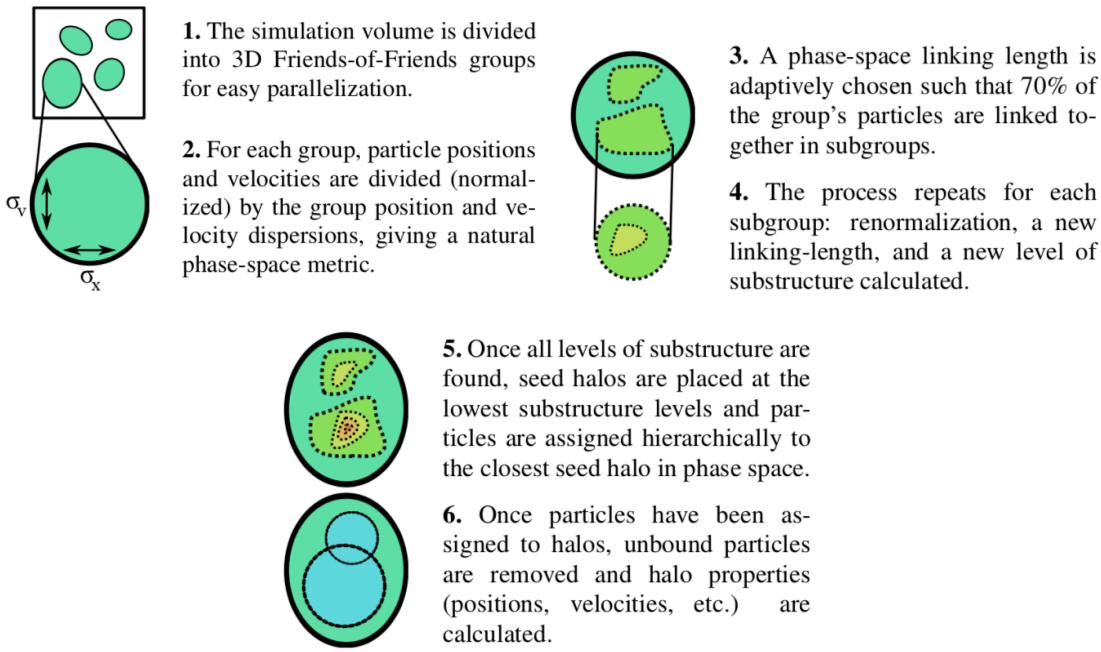

Figure 2.4 Summary of the working principle of ROCKSTAR supplemented by graphical representations of the various steps. Each step is explained in greater detail in subsequent paragraphs. Adapted from Figure 1 of Behroozi et al. (2013a).

When supplied with the particle information in a simulation box, ROCKSTAR first applies a rapid version of 3D FOF halo finding to locate over-dense regions. As compared to the standard FOF algorithm (Davis et al., 1985), the variant applied by ROCKSTAR focuses on the speed of analysis by simplifying specific steps. The critical parameter in a FOF halo finding algorithm is the linking length. It is expressed as a fraction of the mean inter-particle distance in ROCKSTAR or the cube root of mean particle volume for other halo finders. Any particles within this linking length are classified as members in the same group. This standard algorithm is time-consuming because the purpose of the FOF groups in ROCKSTAR is to be distributed to processors for more detailed analysis instead of high accuracy. Therefore, ROCKSTAR modifies this by setting a limit to the number of neighbours within the linking length of the particle. If the number exceeds this limit, ROCKSTAR skips the neighbour-finding process and instead, uses twice the original linking length to identify neighbours. If any of these particles is part of another FOF group, it is combined with that of the original particle. In other words, through this modification, the results from the original FOF algorithm will provide the minimum classification of a group of particles. This change allows the choice of a longer linking length of 0.28 (Behroozi et al., 2013a) instead of the usual range between 0.15 to 0.2 (More et al., 2011). These FOF groups are then distributed to processors with those that cross processor boundaries stitched

together, for further phase-space analysis.

After receiving the FOF group information, ROCKSTAR determines a phase-space distance metric identical to the metric used in Gottloeber (1998),

$$d\left(p_1, p_2\right) = \left(\frac{|\vec{x_1} - \vec{x_2}|^2}{\sigma_x^2} + \frac{|\vec{v_1} - \vec{v_2}|^2}{\sigma_v^2}\right)^{1/2}, \tag{2.34}$$

where σ_x and σ_v are the particle position and velocity dispersions for a given FOF group. The phase-space linking length is chosen based on the distance of each particle to their nearest neighbour. It ensures that a constant fraction of particles is linked together with at least one other particle. For large groups of more than 10,000 particles, a random subset of 10,000 particles is chosen to determine the phase-space linking length. Increasing this fraction of particles slows down the algorithm and causes spurious subgroups to be identified. Conversely, reducing this fraction will lead to the algorithm missing smaller substructures. ROCKSTAR uses an intermediate value of 0.7. Subsequent tests in the algorithm will remove any false positives of a subgroup. This process of determining subgroups in the base FOF group is repeated with the recalculation of the linking length each time, setting the hierarchy of the FOF groups.

Starting with the lowest level in the hierarchy, ROCKSTAR generates a seed halo. It then assigns particles to the seed haloes recursively through the higher levels until all the particles in the FOF group are assigned. Two seed haloes are merged if their positions and velocities are within 10σ of the variance. It is straightforward to assign all particles in a FOF group to a single seed halo if there is only one present. However, for groups with multiple seed haloes, the particles are assigned to different seed haloes based on their proximity in phase space. The properties of the seed halo set the phase-space metric used for particle assignment,

$$d\left(h, p\right) = \left(\frac{|\vec{x_h} - \vec{x_p}|^2}{r_{\mathrm{dyn,vir}}^2} + \frac{|\vec{v_h} - \vec{v_p}|^2}{\sigma_v^2}\right)^{1/2}, \tag{2.35}$$

where the subscripts h and p represents the halo and particle respectively, σ_v is the seed halo's velocity dispersion, 'vir' corresponds to the definition from Bryan & Norman (1998) (360 times the background density at $z = 0$) and $r_{\mathrm{dyn,vir}} = v_{\mathrm{max}}/\sqrt{4\pi G\rho_{\mathrm{vir}}/3}$. Instead of the virial radius, different radii representative of any density contrast can be used. This metric will remove particles too far from its corresponding subhalo density peaks even if they are close in velocity space. The main advantage of this method is that velocity is the dominant information

of differentiating particle memberships when two haloes are in close proximity. By this stage, ROCKSTAR has assigned the particles to their corresponding bound structures.

The next step in the algorithm is to determine haloes and subhaloes within these structures. The main difference between main and satellite haloes is that the latter is included in the mass of the former but not the other way around. Therefore, it is essential to differentiate them. Treating each halo as an individual particle, ROCKSTAR constructs the same phase-space metric as Equation 2.35 and calculates the distance to all other haloes that consists of more particles. If such a halo exists within the same 3D FOF group, the halo in question is designated as the subhalo. ROCKSTAR also includes temporal information from the previous data snapshot, if they are available to preserve the host-subhalo relationship across datasets.

Finally, before calculating all the properties of the haloes, ROCKSTAR carries out a single-pass unbinding procedure with a modified Barnes-Hut (Barnes & Hut, 1986) method. ROCKSTAR does not output haloes where less than 50% of the particles are bound (Behroozi et al., 2013a). This process is particularly tricky when dealing with major mergers. During mergers where the haloes possess large initial velocity offsets, it will be challenging to disentangle the membership of the particles on the outskirts of the merging haloes due to mixing in phase space. This process continues until the halo cores merge and will result in the unbinding of a large number of particles, leading to a significant loss in halo masses during the merger. In this circumstance, ROCKSTAR calculates the gravitational potential of the entire merging system for the unbinding procedure, which is triggered based on user definition but does not affect the mass function or clustering significantly.

2.3.2 yt

After the completion of halo finding, we analyse the simulation data with the publicly available simulation analysis toolkit, yt. Similarly to Enzo, yt is also open-source software, but it is designed as an analysis module, to examine data at a fast pace while not being constrained to any particular simulation code or project (Turk et al., 2011). The computing language used in the development of yt is primarily Python but consists of core routines written in Cython to allow fast computation. Notably, it makes use of the NumPy library extensively and is classified as one of the many Python modules. yt is made up of several sub-

packages which handle the data, analyse the data and plot graphs. The purpose of such a design is to facilitate multi-step analysis procedure, such that the code can be used on any simulation data that `yt` supports.

`yt` offers an extensive list of visualisation tools including slice plots, projection plots, 1D profile plots and 2D phase plots. These can be generated with as little as two lines of codes. Within each type of plot, there is a wide range of customisations available to users, such as the choice of colours and units of the axes. The unit system within `yt` is one of the most convenient features it offers, allowing easy conversion from one to the other. It acts as a consistency check when mathematical operations are carried out on the various properties derived from the simulations. Because of its ease and convenience, `yt` is used extensively to generate the wide range of figures presented in this thesis.

Chapter 3

Star formation and feedback calibration

3.1 Introduction

Dark matter only simulations are employed to study structure formation, and the modelling has been done with high accuracy and progressively with higher resolution and box size (Efstathiou et al., 1985; Moore et al., 1999; Springel et al., 2008; Diemand et al., 2008; Klypin et al., 2011). On the baryonic side, due to the limitation in numerical resolution, several baryonic processes are not simulated from first principles. These processes include fundamental phenomena of the transformation of cold gas to stars, feedback from the energy released by stars, supernovae and massive black holes and their effects on the dark matter distribution and the star formation rate (SFR). As a result, these processes are implemented using a subgrid approach in cosmological hydrodynamical simulations (Springel & Hernquist, 2003; Governato et al., 2010; Agertz et al., 2013). These analytical implementations are sensitive to poorly determined parameters and limited in their capability to make robust predictions ahead of observations (Madau & Dickinson, 2014).

Without the implementation of feedback, there are fundamental issues in numerical simulations such as the problem of "overcooling" (Cole, 1991; White & Frenk, 1991; Blanchard et al., 1992) and "angular momentum" (Katz & Gunn, 1991; Navarro & White, 1994). Overcooling results in the formation

of too massive galaxies particularly in high-resolution simulations (Davé et al., 2001). In addition to these issues of small-scale physics, cosmological simulations contain additional uncertainties. In the absence of feedback, Genel et al. (2018) highlighted differences in the properties of shadow galaxies arising from slight displacement of dark matter particles. The sensitivity of properties of galaxies in simulations can even be due to the difference in the functionality of numerical methods (Keller et al., 2019). The problem is alleviated by the self-regulation of feedback and points out the importance of implementation on the resulting properties of the galaxies in a simulation.

Feedback processes that inject energy into the gas are therefore integral to numerical simulations. For smaller mass haloes, the energy comes mainly from the supernova. In contrast, for more massive ones, the main energy sources are active galactic nuclei (AGN) (Sijacki et al., 2007; Booth & Schaye, 2009; Teyssier et al., 2011) and gravitational heating as a result of infalling clumps of matter (Dekel & Birnboim, 2006; Khochfar & Ostriker, 2008). However, it is unclear how the energy is distributed, either to generate motion or to heat the gas. For supernova implementation alone, various techniques have been employed across different simulation codes (Stinson et al., 2006; Cen & Ostriker, 2006; Dubois & Teyssier, 2008; Dalla Vecchia & Schaye, 2012; Smith et al., 2018). Given the huge diversity in the method of implementation, it is not unusual to expect significantly different outcomes (Thacker & Couchman, 2000; Springel & Hernquist, 2003; Oppenheimer & Davé, 2006). Since the resolution in cosmological simulation is finite but feedback occurs on all scales, the impact of feedback can only be modelled on the resolution scale of the simulation.

The implementation of subgrid physics differs from one numerical simulation code to the other, requiring exploration and adjustment of these routines. Therefore, these are the most significant source of uncertainty in a cosmological simulation. Differences between codes range from values used in parameters to actual implementation method, and it has drastic effects on results from the simulation (Okamoto et al., 2005; Schaye et al., 2010). Unless extremely high resolution can be achieved, certain aspects of running simulations have to be handled by subgrid routines. The accuracy of subgrid physics can be improved both via a better understanding of physical processes and identifying the limitations during its implementation.

To reproduce a realistic picture of the observed universe, there is a need to calibrate parameters of the appropriate subgrid routines (Schaye et al.,

2015). These are adjusted to obtain values of specific properties of the galaxy that can be compared to observations. By matching related properties, the simulation can then be used to answer a wide range of questions. For example, the feedback implementation in the "Evolution and Assembly of GaLaxies and their Environments" (EAGLE) simulation project is calibrated to reproduce the observed $z = 0.1$ galaxy stellar mass function (GSMF), the relation between the mass of galaxies and their central black holes and realistic galaxy sizes (Schaye et al., 2015). Illustris calibrate the parameters to match various observational scaling relations and galaxy properties at low and intermediate redshifts (Vogelsberger et al., 2014). Despite the calibrations, there are shortcomings in each simulation. For example, Illustris recognised that the decrease of their simulated cosmic star formation rate density was too slow, leading to an update in their feedback prescription, resulting in the introduction of IllustrisTNG (Pillepich et al., 2018). In general, feedback implementation is iterative and evolves as new and better constraints are added.

In contrast to these full cosmologically representative box simulations, there are also zoom simulations which focus computational resources on smaller volumes (Springel et al., 2008; Griffen et al., 2016; Wang et al., 2015). In particular, Wang et al. (2015) studied a halo mass range from dwarf masses ($5 \times 10^9\,\mathrm{M}_\odot$) to Milky Way (MW) masses ($2 \times 10^{12}\,\mathrm{M}_\odot$). They included baryonic processes and were able to match stellar to halo mass relation from abundance matching (Behroozi et al., 2013b; Moster et al., 2013; Kravtsov, 2013) across a wide range of redshift. However, they did not account for the mass of gas remaining in the haloes, and this is an important issue for the present analysis.

In this Chapter, we use zoom simulations of MW haloes in an attempt to quantify the stellar and gas mass present in such a halo at $z = 0$. We calibrate parameters governing star formation and the feedback used in this suite of simulations to the inventory of the baryonic and gravitating masses of cosmic structures spanning a dozen decades presented by McGaugh et al. (2010). These will be quantified using the mass fraction of baryons in the halo and the conversion efficiency of gas into stars. It is important to note that this is the first suite of simulations using these observables to calibrate the feedback implementation. In addition to abundance matching, we are interested in the baryon makeup of a MW halo at $z = 0$. This additional constraint on the baryonic properties of the halo will lay the foundation for subsequent chapters.

This Chapter is structured as follows. Section 3.2 will describe the generation of initial conditions used in the simulations, the code, and setup used to evolve them. Also, we will describe the parameters used for calibration and analysis tools used to extract and analyse the results. Section 3.3 will present the properties from McGaugh et al. (2010) that we are interested in, along with the observational fit of the Kennicutt-Schmidt relation (Kennicutt et al., 2007). Section 3.4 will describe the results from various simulations: effects of single parameter variation, calibration of parameters to results from McGaugh et al. (2010) and performance of the simulations to match other constraints. Lastly, the results are summarised and discussed in Section 3.5.

3.2 Simulations and analysis

This section provides an overview of the simulation setup and the associated subgrid physics. In particular, the focus is on MW-sized haloes, where AGN feedback is not prevalent (Storchi-Bergmann, 2014). We look at the main parameters related to star formation efficiency and supernova feedback. As described by Crain et al. (2015), the resulting properties of a halo are very sensitive to the variations of feedback parameter values. Therefore, a detailed explanation of the role of each parameter is necessary.

The cosmological parameters in this suite of simulations are obtained from WMAP-9 (Bennett et al., 2013). The key parameters are $\Omega_m = 0.285$, $\Omega_\Lambda = 0.715$, $\Omega_b = 0.0461$, $h = 0.695$ and $\sigma_8 = 0.828$ with the usual definitions. With these parameters, we generate initial conditions with MUlti-scale Initial Conditions (`MUSIC`) for cosmological simulations (Hahn & Abel, 2011). We derive all zoom simulations from the parent simulation with a volume of $L = 100\,h^{-1}$ cMpch with 256^3 particles.

The simulation is evolved using `Enzo`, an adaptive mesh refinement (AMR) code (Bryan et al., 2014). `Enzo` uses a block-structured AMR framework (Berger & Colella, 1989) to solve ideal Eulerian hydrodynamics equations using multiple solvers. In the simulations presented here, we use the `ZEUS` (Stone & Norman, 1992) hydro solver in combination with an N-body adaptive particle-mesh gravity solver (Efstathiou et al., 1985). Parameter space explorations are made mainly on the star formation and feedback routines. They will be outlined extensively in Section 3.2.1 and 3.2.2. Lastly, the chemistry and cooling processes are handled

by the `Grackle` library (Smith et al., 2017). We use the equilibrium cooling mode from `Grackle`, which utilises the tabulated cooling rates derived from the photoionisation code CLOUDY (Ferland et al., 2013) together with the UV background radiation given by Haardt & Madau (2012).

The MW-sized halo is initially identified from a dark matter only parent simulation through its merger history and final dark matter halo mass. It is isolated, has undergone a smooth merger history and a final mass of approximately $10^{12}\,\mathrm{M}_{\odot}$. The particles within a high-resolution region, typically larger than the virial radius, then undergo additional levels of refinement in mass while the region's spatial resolution is increased. Each nested level is equivalent to an increment in spatial and mass resolution by a factor of two and eight respectively. Contamination occurs if larger mass particles cross the region of interest (Oñorbe et al., 2014). In our simulations, we define a high-resolution region of three virial radii from the centre of the halo to carry out the refinement (Simpson et al., 2018) as a preventive measure. We use three nested levels, giving an effective resolution of 2048^3 particles or a nested dark matter particle mass of $1.104 \times 10^7\,\mathrm{M}_{\odot}$. This nested simulation is evolved with an additional five levels of AMR which is only allowed around particles within the high-resolution region, resulting in a maximum resolution of eight levels of spatial refinement or 2.196 comoving kpc (ckpc). This simulation setup is similar to that presented by Peeples et al. (2019) and Hummels et al. (2018).

From the high-resolution region of the MW halo, a smaller halo with a mass of approximately $10^{10}\,\mathrm{M}_{\odot}$ is identified. The purpose of this smaller halo is to test the universality of the optimal feedback parameters from the MW zoom simulation. We use approximately the same number of dark matter particles in the dwarf as in the MW halo. The increased mass resolution translates into an effective resolution of 8192^3 particles or a nested dark matter particle mass of $1.715 \times 10^5\,\mathrm{M}_{\odot}$. Because of the additional nested levels, we reduce the number of AMR levels to three, maintaining a constant maximum spatial resolution of 2.196 ckpc.

3.2.1 Star formation parameters

We modify certain aspects of the star formation criteria in Section 2.2.5 to calibrate the simulations. These include the Jeans instability check, timestep dependence of star formation, threshold star particle mass and the value of f_*

(see Equation 2.28). The following sections will explain in detail the role each parameter plays, and they are organised in the order within the source code that each factor is used in the star formation condition check.

Jeans instability check

In (v) of the list of conditions in Section 2.2.5, the creation of star particles is only allowed when the gas mass is more than the Jeans mass of the cell. When the spatial resolution of the simulation is high enough to resolve the Jeans length, this particular check in the star formation routine instead restricts star formation that can occur.

Minimum star particle mass

Once a cell fulfils all five conditions for star formation, the final barrier to star formation is the minimum mass of a star particle that will be inserted into the simulation. This threshold is explicitly designed to prevent the production of too many star particles, which can increase computational costs significantly. However, the inability to exceed this minimum star particle mass can lead to a build-up of potential star-forming gas in surrounding cells. This accumulation then reaches a point where a burst in star formation occurs, creating a spike in the amount of stellar mass.

Timestep dependence of star formation

Two factors affect the mass of the star particle to be compared to the threshold value as seen in Equation 2.28: $\Delta t/t_{dyn}$ and f_*. They correspond to the timestep dependence of star formation and a conversion factor respectively. By opting for a timestep independent star formation, the factor $\Delta t/t_{dyn}$ is removed from the calculation shown in Equation 2.28, resulting in a stellar mass,

$$m_* = m_{gas} \times f_*, \tag{3.1}$$

where the symbols have the same meaning as Equation 2.28. The purpose of the factor of dt/t_{dyn} is to explicitly satisfy the Kennicutt-Schmidt (KS) relation, which states that a fraction, f_* of gas will turn into stars over a dynamical time.

Table 3.1 List of star formation setups explored

Star formation setup list			
Setup	Jeans instability check	Minimum star particle mass $[M_\odot]$	Timestep dependence of star formation
1	✓	10^5	✓
2	✗	0	✗

However, since star formation is self-regulating, this does not actually guarantee that the KS relation will be fully satisfied at $t = t_{dyn}$. By removing this factor, the simulation is instantaneously converting f_* of gas into stars and the feedback associated will immediately start regulating further star formation.

As we show in Sections 3.4.2 and 3.4.3, the timestep independent star formation model generally leads to a smoother buildup of stellar mass, but not without some additional effects. When we contrast the performance of the simulation, a simulation employing timestep dependent star formation will take roughly a month to complete whereas a similar setup with timestep independent star formation completes in approximately two days, likely due to the production of fewer star particles. Shorter run times allow for more exploration of the parameter space. However, this choice has significant impact on the resulting KS relation. These effects will be quantified and discussed in Section 3.4. In summary, we calibrate the feedback in two different star formation setups as detailed in Table 3.1. The reasons for two setups and switching from Setup 1 to 2 will be discussed in Section 3.4.3.

Star formation efficiency factor, f_*

As mentioned, regardless of the timestep dependence of star formation, there exists an efficiency factor, f_* in both Equations 2.28 and 3.1. This parameter regulates the conversion efficiency of identified gas mass in a cell into star particles. f_* can vary from zero to unity but not including the limits where none or all the identified gas mass in the cell is converted to stellar mass respectively. The latter scenario will remove all the gas from the cell, resulting in a cell having a density of zero, crashing the simulation.

3.2.2 Feedback parameters

We adopt Smith et al. (2011)'s modification of Cen & Ostriker (2006) thermal supernova feedback model described extensively in Section 2.2.5. We assume that 25% of the mass is removed from the star particle and returned to the grid as gas ($f_{ej} = 0.25$) with 10% of this returned gas as metals ($\eta = 0.1$), consistent with Cen & Ostriker (1992). These values result in a total metal yield of 0.025 of the mass of the star particle, similar to the calculations by Madau et al. (1996). Also, this metal yield is consistent with average values in the MW, with a mean SFR of $\sim 3\,M_\odot\,yr^{-1}$, a core-collapse supernova rate of 1 per 40 years, and an IMF-averaged metal yield of $\sim 3\,M_\odot$ per supernova (Smith et al., 2011). Therefore, we do not alter values of both f_{ej} and η.

Instead, we focus on the factors that influence the energy injection, both in terms of the amount and the physical extent. We select three factors in the feedback implementation to be varied for the calibration of the simulations. They are ϵ, radius of feedback (r) and number of cells (s) within r. The first parameter is related to the amount of feedback energy emitted by the star particle (see Equation 2.32) while the remaining parameters work together to define the extent of energy injection. These will be described in more detail in the following sections.

Feedback efficiency, ϵ

The amount of feedback energy injected as thermal energy is calculated by Equation 2.32. It is dependent on both rest mass energy ($m_{form} \times c^2$) and a user-defined fraction, ϵ. The former relies on the amount of stellar mass created per timestep (see Equation 2.29), and the latter defines the percentage of the rest mass energy injected into the IGM. Together with Equation 2.30, this implementation is similar to the temporal release of Galactic Superwinds energy and ejected mass from stars into the IGM discussed in Cen & Ostriker (2006).

Feedback energy injection extent

In the original feedback method described by Cen & Ostriker (2006), all of the feedback energy is injected into the grid cell housing the star particle. However, Smith et al. (2011) modified this to allow the feedback to be spread across multiple

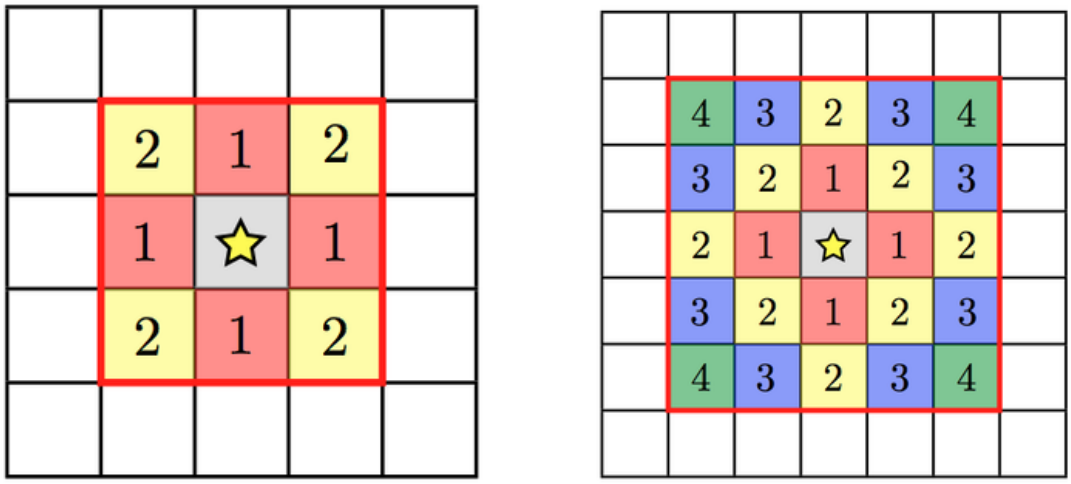

(a) $r = 1$ **(b)** $r = 2$

Figure 3.1 Distributed stellar feedback setup for $r = 1$ (left) and $r = 2$ (right) described in Section 3.2.2 (Enzo Collaboration, 2018). Different coloured cells illustrates the accessible s corresponding to the particular value of r.

zones as a means of bypassing overcooling issues, where too much energy injected into a single grid cell can result in unphysical short cooling times. This setup is known as distributed stellar feedback, and it is defined by r and s. These parameters work together to define the physical extent of the injection of feedback from the star particle. We can visualise it with a cube surrounding the star particle in the centre. r is the distance of the cell from the star particle. When $r = 1$, it refers to a 3×3 cube since all the cells are within one cell distance away from the star particle. Similarly, when $r = 2$, it refers to a 5×5 cube around the star particle. These are illustrated in two dimensions in the left and right panel of Figure 3.1 respectively.

s is the number of steps allowed to be taken from the star particle within the cube determined by r. Referring to the left panel of Figure 3.1, setting $s = 2$ corresponds to an allowable two steps of movement away from the star particle, specifying injection within the cells labelled 1 and 2 in the 3×3 cube. As the value of r increases, shown in the right panel of Figure 3.1, the larger is the maximum value of s accessible. These increased values translate to more flexibility in the usage of distributed stellar feedback.

In summary, we calibrate our simulations with ϵ, r and s, and f_* to match the observations. For the remainder of the paper, when discussing the combination of parameters in a simulation setup, they will be referred to as (ϵ, r_s, f_s), e.g., (1.0×10^{-5}, 1_3, 0.1).

Table 3.2 Methods of determining V_c for different gravitationally bound systems (see McGaugh (2005); Hoekstra et al. (2005); Gavazzi et al. (2007); Walker et al. (2007, 2009); Simon & Geha (2007); Giodini et al. (2009)).

Gravitationally bound systems	Methods
Star dominated spiral galaxies	Rotation velocities
Gas dominated galaxies	Baryonic Tully-Fisher relation
Elliptical galaxies	Gravitational lensing
Local group dwarfs	Direct measurement
Clusters of galaxies	Hot X-ray emitting gas

3.2.3 Analysis

Haloes are identified using the Robust Overdensity Calculation using k-Space Topologically Adaptive Refinement (`ROCKSTAR`) halo finder (Behroozi et al., 2013a) (see Section 2.3.1). It is a 6-dimensional phase-space finder, using both position and velocity of particles to locate and define a halo. In regions where the density contrast is insufficient to distinguish which halo hosts a given particle, `ROCKSTAR` can differentiate subhaloes and major mergers that are close to the centres of their host haloes. This feature is particularly useful in identifying main haloes when creating zoom simulations of lower mass haloes. Analysis of the simulation results is then carried out using the `yt` analysis toolkit (Turk et al., 2011).

3.3 Observations

3.3.1 Baryon Content of Cosmic Structures

The main observables matched in this suite of simulations are taken from the work of McGaugh et al. (2010). The authors attempted to account for the distribution of baryonic mass within cosmic structures. Galaxies are broadly categorised into rotationally, and pressure supported systems. These are further divided into star dominated spiral galaxies and gas dominated galaxies for the rotationally supported system, and elliptical galaxies, local group dwarfs and some clusters of galaxies for pressure supported systems. The primary method for determining the baryonic budget in different systems is their equivalent circular velocity (V_c) obtained through various methods described in detail in McGaugh et al. (2010) and summarised in Table 3.2.

In their analysis, McGaugh et al. (2010) choose to use r_{500}, a radius where the enclosed density is 500 times the critical density of the universe to derive their data. The main result presented in Figure 2 of McGaugh et al. (2010) relates the fraction of expected baryons that are detected,

$$f_d = \frac{m_b}{f_b \times m_{500}}, \tag{3.2}$$

and the conversion efficiency of baryons into stars,

$$f_s = \frac{m_*}{f_b \times m_{500}}, \tag{3.3}$$

where m_b and m_{500} refer to the baryonic and total mass within this radius respectively, and f_b is the universal baryon fraction determined to be 0.17 ± 0.01 (Komatsu et al., 2009). One important point to note is that these fractions are dependent on the choice of radius. To facilitate comparison of results to Figure 2 in McGaugh et al. (2010), we fit the data points with

$$f_d = \frac{1}{1 + e^{-x}}, \tag{3.4}$$

and

$$f_s = 0.91 \exp\left(\frac{-y^2}{2}\right) \times f_d, \tag{3.5}$$

where

$$x = \frac{\log_{10}(m_{500}/M_\odot) - 12.91}{1.12}, \tag{3.6}$$

and

$$y = \frac{\log_{10}(m_{500}/M_\odot) - 12.19}{1.18}, \tag{3.7}$$

shown in Figure 3.2. We aim to calibrate our suite of simulations to yield a good match to these fits. Also, we will compare our simulated galaxy properties to the KS relation, which serves as an additional constraint.

3.3.2 Kennicutt-Schmidt relation

The KS relation is a measure of the correlation between gas surface density and the SFR surface density. From the work of Schmidt (1959); Kennicutt (1989, 1998b); Kennicutt et al. (2007); Bigiel et al. (2008), there appears to be a tight correlation between these measured properties on galactic scales ($\sim$ kpc). This strong relation makes it one of the critical observations that simulations with star

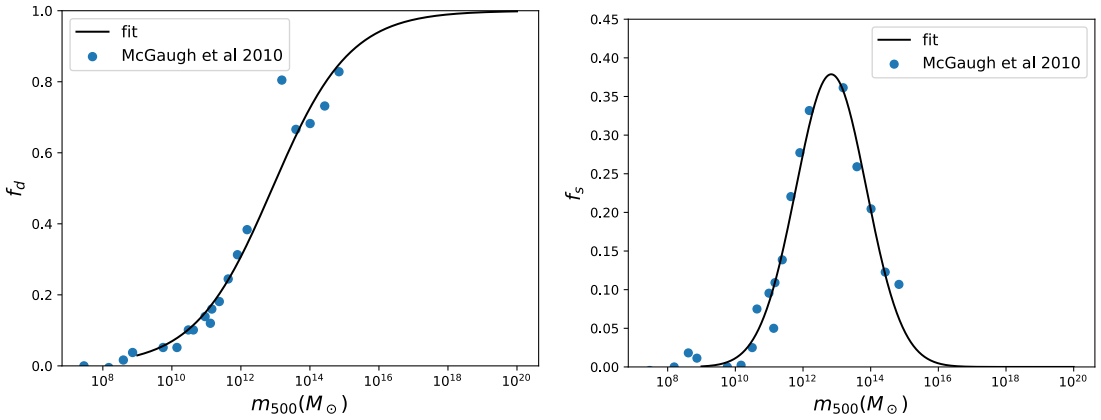

(a) f_d **(b)** f_s

Figure 3.2 Best fit of f_d (left) and f_s (right) from McGaugh et al. (2010) with equations described in Section 3.3.1.

formation attempt to match.

We adopt a similar methodology to the AGORA project (Kim et al., 2016). The SFRs are calculated using the mass of star particles and time-averaged over the past 20 Myrs of the simulation snapshot. Together with the gas density, they are then deposited onto a fixed resolution grid of 750 pc, consistent with the methodology of Bigiel et al. (2008) to derive the SFR and gas surface density required by the KS relation. In fact, we find that the conclusions drawn are insensitive to changes in the grid resolution. With non-zero SFR surface density patches, we will also compare our results to

$$\log \Sigma_{\rm SFR} = 1.37 \log \Sigma_{\rm gas} - 3.78, \tag{3.8}$$

which is obtained from the best observational fit given by Equation 8 in Kennicutt et al. (2007).

3.4 Results and discussion

3.4.1 MW galaxy zoom simulations with Setup 1

We explore the parameter space by switching on the Jeans instability check, applying timestep dependent star formation and setting a threshold star particle mass of $10^5\,\mathrm{M}_\odot$ (Setup 1) (see Table 3.1). With this setup, we run a total of 22

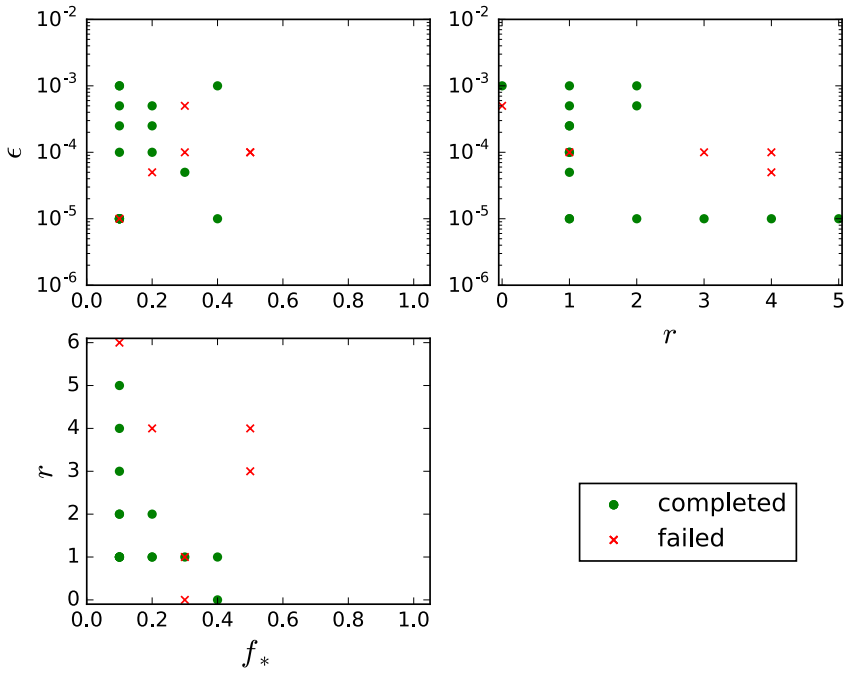

Figure 3.3 Overview of parameter space exploration using a total of 22 different combinations of f_*, ϵ and r with Setup 1, described in Section 3.4.1. The plots are ϵ against f_* (top left), ϵ against r (top right) and r against f_* (bottom left). The green dots and red crosses represent runs that reached and failed to reach $z = 0$ respectively.

simulations by modifying f_* (see Equation 2.28), ϵ (see Equation 2.32), r and s (see 'Feedback energy injection extent' under Section 3.2.2), as shown in Figure 3.3. This explored region of parameter space is motivated both physically and numerically. Cen & Ostriker (1992) applied a value of ϵ ($10^{-4.5}$), which is similar to other work (Ostriker & Cowie, 1981; Dekel & Rees, 1987). r and s is restricted by the maximum number of cells used to define a grid. Lastly, by taking the ratio of f_s to f_d, we obtain m_*/m_b that is similar to f_*. Hence, the limits of f_s can be easily determined with the data from McGaugh et al. (2010), ranging from 0.1 to 0.9 approximately.

Out of the 22 simulations, we classify the runs into those that reach $z = 0$ (completed) and those that did not (failed) since we are interested in the relevant properties at $z = 0$. The simulation can fail to reach $z = 0$ because of a variety of reasons such as the generation of non-physical property values, e.g., negative energy due to reasons such as interpolation errors across discontinuities or come to a grinding halt because of the increase demand in calculations caused by large values of feedback parameters. We can see overlapping points with conflicting conclusions in Figure 3.3 as a result of projecting a 3-dimensional plot onto a

2-dimensional plane. Although a 3D plot can be used to illustrate the same information, it is easier to identify regions where parameter space is inaccessible with `Enzo` using a 2D plot.

Comparison to baryonic properties from McGaugh et al. (2010) – Setup 1

Initially, we attempted to cover the parameter space optimally with minimal numbers of simulations using a technique known as Latin Hypercube Sampling (McKay et al., 1979). We wanted to minimise the maximal distance between various points in our feedback parameter space as described by Heitmann et al. (2009). However, due to the failure of several runs to reach $z = 0$ and the inaccessibility of certain parts of the parameter space, it is not possible to obtain a space-filling design. Therefore, we try a more fundamental approach to quantify how changing each parameter will affect the observables. This result is presented in Figure 3.4, showing a plot of $f_{\rm s}$ against $f_{\rm d}$ across a range of m_{500}.

From the initial values of (1.0×10^{-5}, 1_3, 0.1), we vary ϵ only, which corresponds to a change in the strength of feedback. Increasing the strength of feedback reduces both the f_s and f_d of the halo (see blue arrow in Figure 3.4). This evolution can be easily explained by the increased expulsion of gas due to stronger feedback, reducing the amount of fuel available to form stars, which leads to a decrease in f_s. The removal of gas also causes the amount of baryons within r_{500} or f_d to decrease.

We then try to increase f_*. This change has a direct impact on the total stellar mass as more gas mass is converted into stars. However, this increased star formation corresponds to a stronger feedback strength. Therefore, the net result of increasing f_* is similar to increasing ϵ, which decreases both f_s and f_d (see green arrow in Figure 3.4). This effect is, however, to a lesser extent, evident from the small transition of the cyan point to the purple point on the top right of the plot. To improve the clarity of an increase in f_*, we add another green arrow connecting another set of data points (grey and light green dots). This difference in the impact of f_* also suggests its sensitivity to other feedback parameters.

The last parameters to adjust are r and s. Essentially, we are increasing the size of the cube into which the feedback energy is injected (see Figure 3.1). By increasing r and correspondingly, s, f_s and f_d are reduced, similar to the effect of increasing ϵ and f_s. However, this phenomenon only persists until $r = 3$

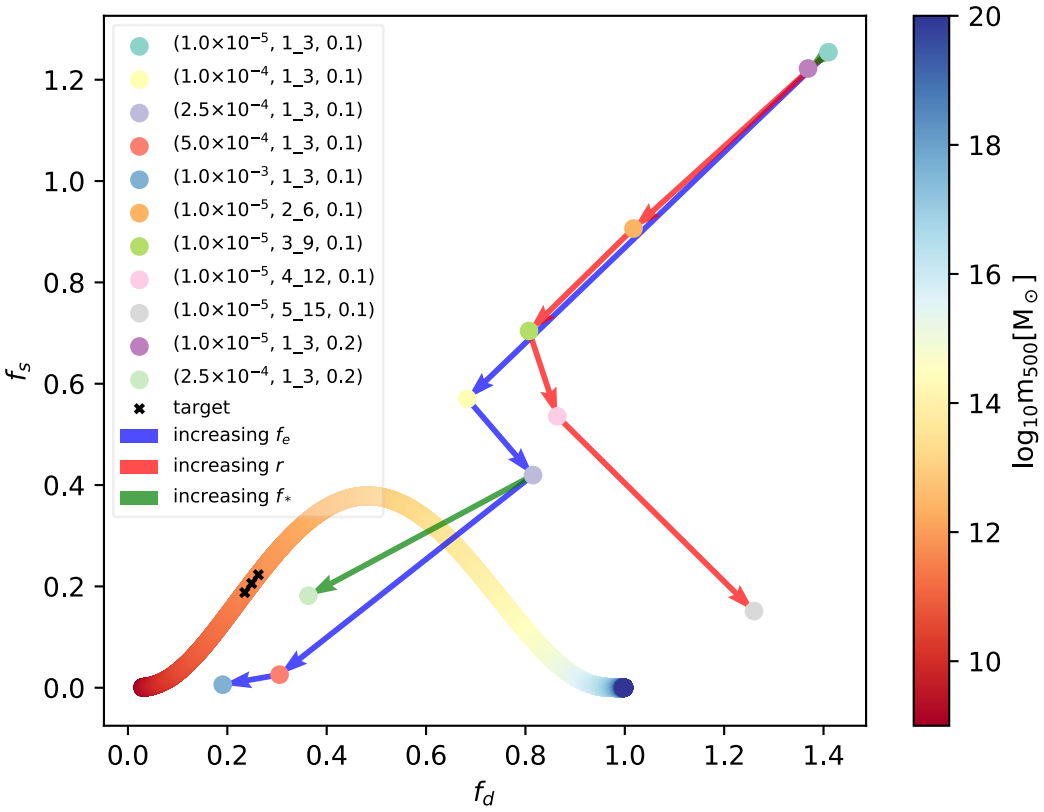

Figure 3.4 Graph of f_s against f_d across a range of m_{500}. The colour coded curve shows the values of f_s and f_d corresponding to the mass range indicated. Cross marks on this curve shows the values to be matched. It includes the mean of m_{500} with the upper and lower limits given by the maximum and minimum m_{500} from the simulations plotted. Dots represent simulation with different feedback parameters and contrasting coloured arrows show effects of increasing a particular parameter. For detailed description, refer to Section 3.4.1.

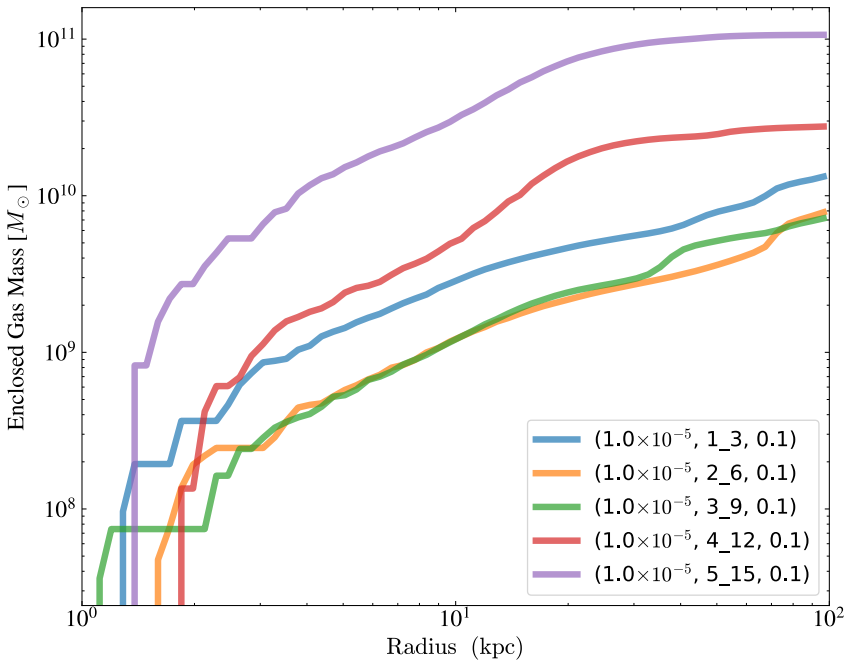

Figure 3.5 Cumulative plot of m_{gas} against halo radius. The different coloured lines represent simulations of various r and s. As the extent of feedback injection is increased beyond $r = 3$ and $s = 9$, the amount of baryons in the outer region of the halo is significantly higher. This trend shows gas collapse being prevented to form stars as the extent increases, providing support for the explanation given in Section 3.4.1 for Figure 3.4.

and $s = 9$, which corresponds to a 7^3 box or 343 cells centred around the star particle. Beyond this point, the trend changes when a further extension of the feedback injection decreases f_s but increases f_d, indicating the presence of a turnaround point. As energy is deposited further from the star particle, the gas is kept away at a larger distance from the centre of the gravitational potential well as seen in Figure 3.5. As a result, m_* decreases as fewer stars form due to a deprivation of fuel for star formation while m_{gas} increases as more gas is now present. Increasing the physical extent of feedback injection beyond $r = 3$ and $s = 9$ only serves to dilute the amount of feedback energy per cell, leading to gas remaining in outskirts of the halo's r_{500}. Thus, it increases f_d while decreasing f_s. Furthermore, the average AMR grid size in an `Enzo` simulation is not likely to be much larger than about 7^3, so extending beyond $r = 3$ and $s = 9$ should be avoided as feedback is only deposited on the local grid.

From the 16 completed simulations, the combination of parameters that yielded the most MW like properties in the halo is (2.5×10^{-4}, 1_3, 0.2), which is represented by the pale green dot in Figure 3.4. The halo contains a stellar

mass comparable to the MW while having approximately 50% more baryon mass than the MW halo. This point is the closest match to the target for the region of parameter space that we sampled. The next best set of parameters that produce halo properties that matches the target is (5.0×10^{-4}, 1_3, 0.1). While it provides a better f_d agreement, the f_s is approximately zero. From the trends and the best match in Figure 3.4, further improvement in the agreement of halo properties will only be marginal. In order to achieve a better agreement, we suggest including other free parameters or even modify the star formation and feedback model. However, it is not within the scope of this work to design such modifications.

KS relation – Setup 1

The KS relation describes a tight relation of gas surface density and SFR surface density of a galaxy. It provides an additional constraint on top of the baryon makeup of a MW halo to the feedback calibration. Since the KS relation is frequently used to constrain the modelling of star formation, we apply the methodology described in Section 3.3.2 to compare and contrast with the observed KS relation (blue line) in Figure 3.6. We also include a rough approximation of observed values of nearby galaxies from Bigiel et al. (2008) in the form of blue hatched contours.

The results show that the simulation data intersect with observations and the fit given by Equation 3.8, but the slopes of the simulation data differ from the KS relation in every feedback prescription. Most of our simulations managed to reproduce the characteristic "threshold" gas density value of approximately $10\,\mathrm{M_\odot pc^{-2}}$, which signifies the transition point between high and low star formation efficiency and is apparent from the blue hatched contour. The slopes of the relations in the simulations do not appear to be significantly different from each other despite changes in the subgrid physics. However, they are consistently steeper than the gradient of the fit.

When increasing ϵ, we observe a shift towards lower SFR but higher gas density from the transition between the green circles (1.0×10^{-5}, 1_3, 0.1) and the red squares (5.0×10^{-4}, 1_3, 0.1). This shift can be explained by the higher feedback energy budget associated with a larger ϵ value, which inhibits further star formation. The simulation data points are insensitive to any increase in r until $r = 3$. Beyond this point, similar SFR densities patches are associated with a higher gas density, highlighted by green crosses (1.0×10^{-5}, 4_12, 0.1) and pink

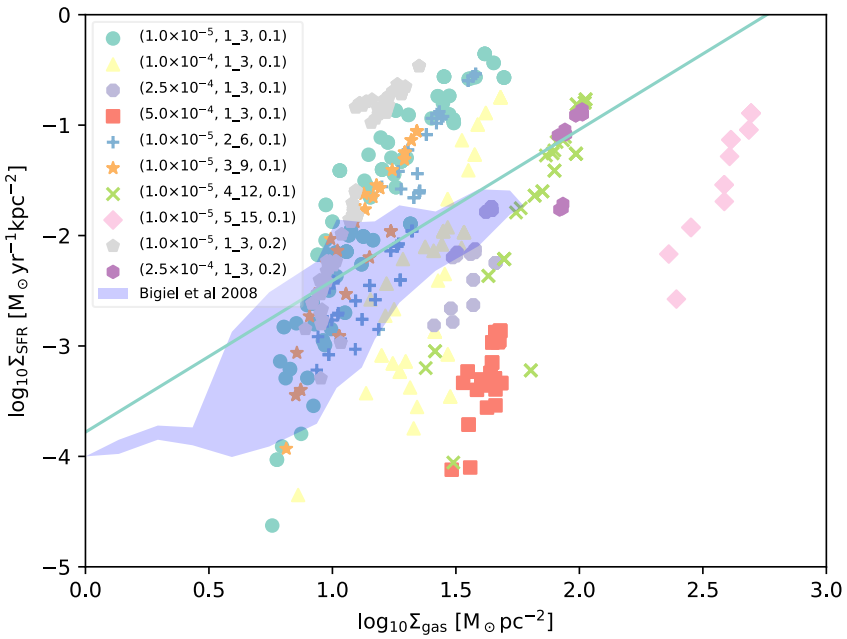

Figure 3.6 Graph of SFR surface density against gas surface density illustrating the KS relation. Different coloured points are simulation data from sub-kpc resolution consistent with rough approximation from the observations in nearby galaxies by Bigiel et al. (2008) represented by the blue hatched contours. The blue line is derived from the observational fit of Kennicutt et al. (2007). For further description of this figure, refer to Section 3.4.1.

diamonds (1.0×10^{-5}, 5_15, 0.1). This behaviour is consistent with the explanation provided for Figure 3.5. Lastly, from the data points of (1.0×10^{-5}, 1_3, 0.1) and (1.0×10^{-5}, 1_3, 0.2), it appears that increasing f_* does not affect the relation significantly.

Focusing on the best parameter values (purple hexagon), they lie along with the KS relation fit but deviate from observations as they are clustered around high gas densities. This discrepancy with Bigiel et al. (2008) suggests that this combination of ϵ and f_* is too weak to create patches of lower gas surface density. However, adjustment of either factor will, in turn, affect f_s and f_d, leading to a halo that reproduces the KS relation instead of the observations of McGaugh et al. (2010).

Morphology – Setup 1

Figure 3.7 illustrates the change in the appearance of our simulated galaxies as a result of adjustments in ϵ, r and s, and f_*. The four pairs of projections in the figure show a face on (left) and edge on (right) density projection plot

of the simulated galaxy within 25 kpc. The projection plane is based on the angular momentum vector of the gas within a sphere of 50 kpc. The pair in (a) corresponds to the simulation with (1.0×10^{-5}, 1_1, 0.1) which is the starting point of our study in Figure 3.4. Pairs (b), (c) and (d) are the density projection plot with maximum values of ϵ, r and s, and f_* in our simulations respectively. The transition from (a) to (b), (a) to (c), and (a) to (d) is identical to the blue, red and green arrow in Figure 3.4 respectively.

Due to the limitation in resolution, we are unable to replicate any fine structures of the MW disk as evident from all four pairs of figures. Among the panels, the feedback prescription in our suite of simulations in (d) best reproduce the features of a thin disk. When r and s are increased in (c), the disk looks puffed-up as a result of increasing feedback injection extent, which pushes the gas out to greater distances. An increment in ϵ causes significant disruption in the structure of the disk because of the larger feedback energy budget. This disturbance in the disk structure tells us that although the feedback prescription can replicate the baryonic properties and the KS relation reasonably, due to the limitations in resolution, the morphology of the simulated galaxy deviates from that of a realistic disk galaxy due to limitation in the resolution of our simulation.

Haloes in the high-resolution region – Setup 1

Since we specify a safety factor of three virial radii to prevent contamination of the MW halo in the zoom simulation, there are other central and satellite haloes of varying mass in this region. Figure 3.8 illustrates the properties of other central haloes in the simulation with the best feedback prescription of (2.5×10^{-4}, 1_3, 0.2). This plot is not presented in a similar way to Figure 3.4 because we are looking at a range of halo masses. Instead, we populate Figure 3.2 with the corresponding f_s and f_d of various central haloes in the high-resolution region of the MW galaxy zoom simulation.

We present the graph of $f_{\rm d}$ against m_{500} on the upper panel and $f_{\rm s}$ against m_{500} on the lower panel of Figure 3.8. The black lines are Equations 3.4 and 3.5 fitted to the observations (blue dots). From the graph of $f_{\rm s}$ on the lower panel, the properties either match observation well or do not form stars at all ($f_{\rm s} = 0$), which is represented by a red star and grey cross respectively. The same cannot be said for the $f_{\rm d}$ relation on the left where there are vastly different properties with no apparent relation to the $f_{\rm d}$ values. We see lower mass haloes with $f_{\rm d}$

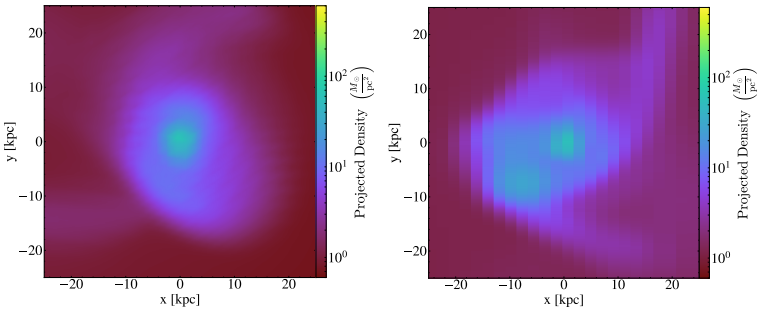

(a) $(1.0\times10^{-5}, 1\_3, 0.1)$

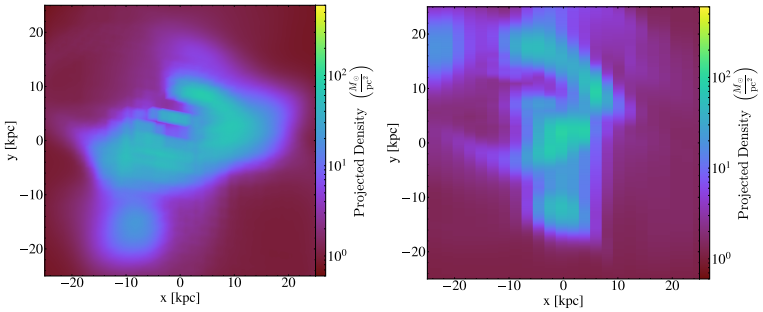

(b) $(1.0\times10^{-3}, 1\_3, 0.1)$

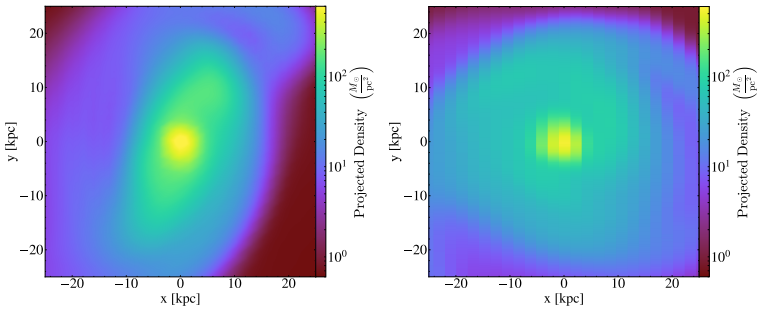

(c) $(1.0\times10^{-5}, 5\_15, 0.1)$

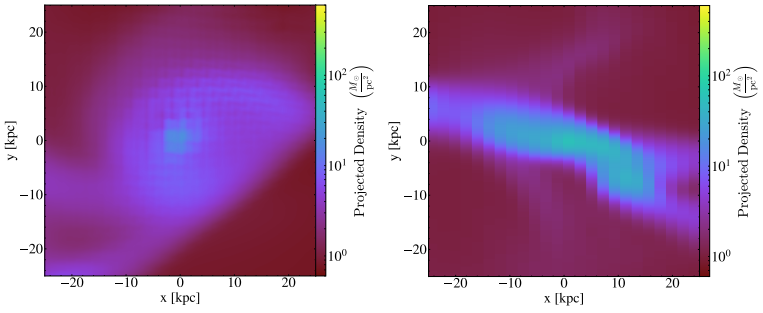

(d) $(1.0\times10^{-5}, 1\_3, 0.2)$

Figure 3.7 Pairs of density projection plots of the MW halo within 50 kpc. In each pair, the left and right panels show the face on and edge on projection respectively. (a), (b), (c) and (d) corresponds to simulation with baseline feedback prescription, feedback prescription with maximum ϵ of 1.0×10^{-3}, feedback prescription with maximum r of 5 and s of 15 and feedback prescription with maximum of f_* of 0.2 respectively. Transitioning from (a) to (b), (a) to (c) and (a) to (d) represents an increase in ϵ, an increase in r and s and an increase in f_* respectively. Refer to Section 3.4.1 for explanation of differences in the appearance of the simulated galaxy.

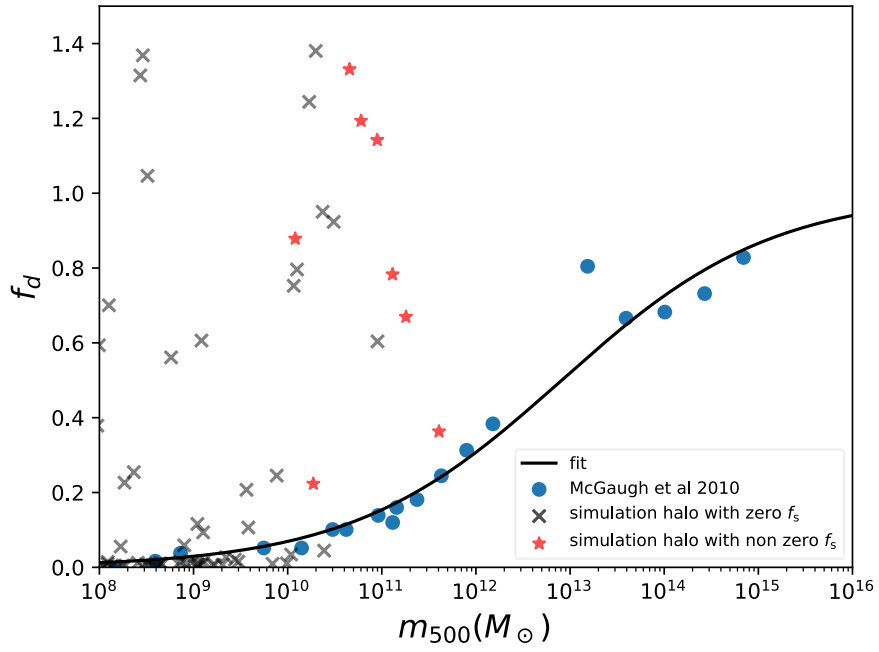

(a)

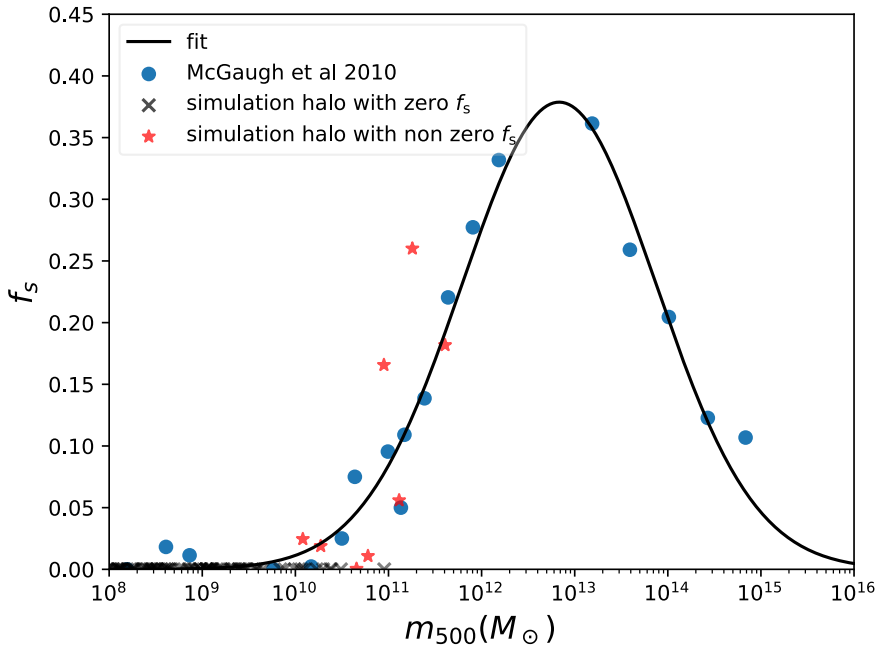

(b)

Figure 3.8 Graph of f_{d} against m_{500} (a) and f_{s} against m_{500} (b) with equations described in Section 3.3.1. The black line represents the fit given by Equation 3.4 and 3.5. The blue dots are points from McGaugh et al. (2010) and the crosses and stars are properties of haloes with various mass from the must refined region in the simulation. The black cross and red star refer to haloes in the must refine region with zero and non zero f_{s} respectively. Refer to Section 3.4.1 for a detailed description.

reaching 1.4, exceeding that of the universal baryon fraction while possessing f_s that is close to observations. These haloes are in contrast to the MW halo (right most red star), which hints at the need for additional work in order to understand and determine if this discrepancy is a numerical byproduct due to the fractional mass resolution of the lower mass halo. Therefore, we attempt a zoom simulation of a dwarf galaxy around $10^{10}\,M_\odot$ with a comparable mass resolution to the MW zoom to investigate if the conclusion from Figure 3.8 is due to resolution and whether this feedback prescription is universal.

3.4.2 Dwarf galaxy zoom simulations with Setup 1

Using the combination of parameters (2.5×10^{-4}, 1_3, 0.2), we implement the feedback prescription in a dwarf galaxy with a mass of approximately $10^{10}\,M_\odot$. However, the results indicate an absence of stars within the halo, consistent with Figure 3.8. Reviewing the star formation routine (see Section 2.2.5), we find that the Jeans instability check is the bottleneck of star formation. Due to the spatial resolution implemented in this dwarf galaxy, according to the discussion in Section 3.2.1, the Jeans instability check is restricting star formation that should occur. Therefore, to allow star formation, we switch off this check in the star formation routine. We label the runs with Jeans instability check switched off as NJ.

Figure 3.9 illustrates the virial (black) and stellar mass evolution (red) in the dwarf galaxy with different setups (solid vs dashed lines). As expected, removing the Jeans mass criterion allowed stars to form in the dwarf galaxy zoom simulation (solid red line). However, star formation starts around $z = 2$, which is late as compared to the MW zoom simulation, for which star formation commenced at $z \simeq 6.5$. Further investigations yielded the conclusion that the star formation threshold mass is the next limiting factor. Therefore, we reduce the threshold mass for star particle creation to zero, which relaxes the condition for star formation, allowing star particles to be created at $z = 8$ in the simulation. On top of these changes, we switch off the timestep dependence of star formation. This results in Setup 2 as shown in Table 3.1.

The purpose of $\Delta t/t_{dyn}$ in Equation 2.28 is to ensure the adherence of star formation to the KS relation. However, in Equation 2.29 where feedback is modelled to occur across time, there are additional factors of $\Delta t/t_{dyn}$ present to regulate these processes according to the KS relation. Hence, by switching to

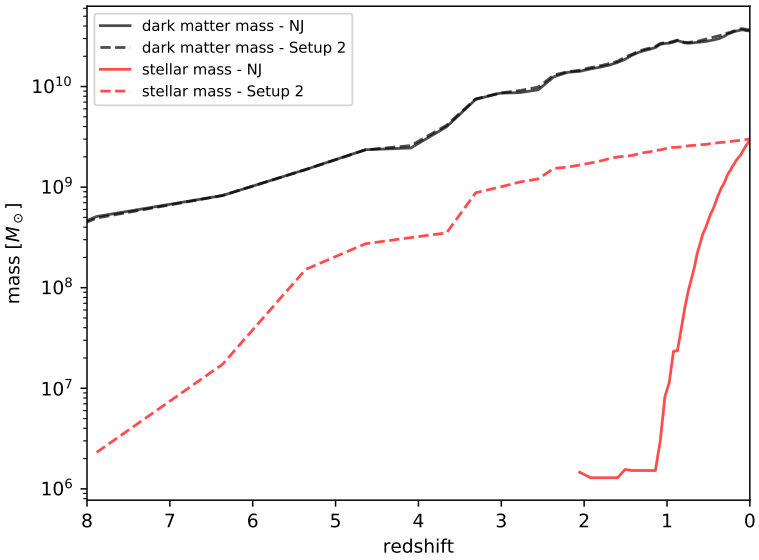

Figure 3.9 Redshift evolution of dark matter and stellar mass in the dwarf galaxy. Solid and dashed lines are mass evolution of NJ runs and Setup 2 runs respectively. Black lines refer to the dark matter mass evolution while red lines refer to the stellar mass evolution in the halo. Refer to Section 3.4.2 for discussion.

timestep independent star formation, we improve the promptness of the feedback. Lastly, since star formation is now instantaneous once conditions are met, high-density regions of gas are absent, reducing the hydrodynamical time scale of the simulation. This absence of high-density gas is evident from the number of timesteps required for the evolution to reach $z = 0$ and the time per timestep. For an identical feedback prescription, Setup 1 takes 1263 timesteps and $\sim 435s$ per timestep to reach $z = 0$, which is in stark contrast to Setup 2 where it takes 663 timesteps and $\sim 125s$ per timestep for the simulation to reach $z = 0$. The net result is an improvement in the speed of completion of simulations from weeks to days.

In summary, we modify the setup to switch off the Jeans instability check, turn off the timestep dependence of star formation and remove the requirement of a minimum star particle mass. This results in Setup 2 shown in Table 3.1. With this setup, we recover a more realistic star formation history beginning at $z \sim 8$ (see Figure 3.9). However, we do not compare the properties of the dwarf galaxy to observations for reasons that will be explained in Section 3.4.3.

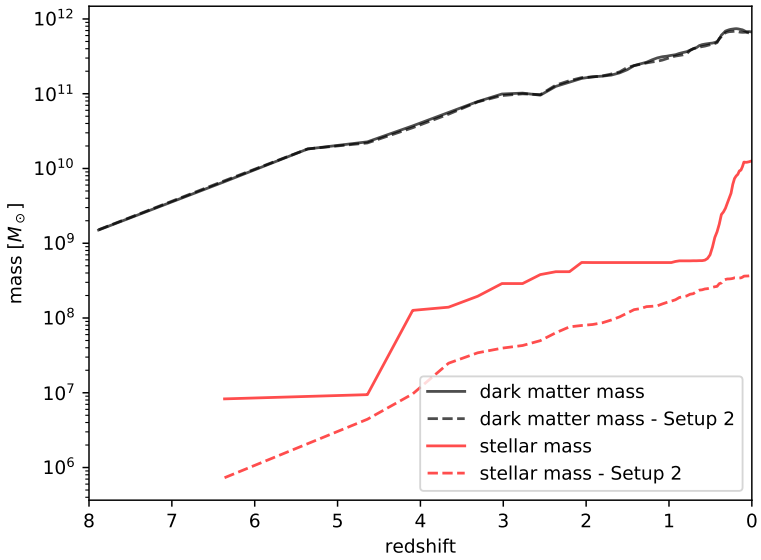

Figure 3.10 Redshift evolution of dark matter and stellar mass in the MW halo. Solid and dashed lines are mass evolution of NJ runs and runs with Setup 2 respectively. Black lines refer to the dark mass evolution while red lines looks at the stellar mass evolution in the halo. Refer to Section 3.4.3 for discussion.

3.4.3 Transitioning to Setup 2

Due to star formation issues in the dwarf galaxy zoom simulations, we make significant changes in the simulation setup. In Section 3.4.2, we show that the stellar mass of a dwarf galaxy at $z = 0$ changed from zero to $\sim 10^9\,\mathrm{M}_\odot$ by switching to Setup 2. We now have to review the results of the MW galaxy presented in Section 3.4.1. Figure 3.10 shows the evolution of the dark matter and stellar mass of the MW halo in different setups. The lines and labels are similar to Figure 3.9.

From the identical dark matter mass evolution in Figure 3.10 for different setups (black lines), we know that we are comparing the same halo across simulations. However, the stellar mass evolution paints a different picture. Comparing both setups, although the haloes start forming stars at the same time ($z \simeq 6.5$), the simulation using Setup 2 has a lower initial and final stellar mass as a result of its corresponding relaxed star formation conditions . With minimum mass of the star particles set to zero, the stars are allowed to form with a smaller mass, which explains a lower starting point in Setup 2. Between $z = 1$ and $z = 0$ in Setup 1, we note a spike in stellar mass due to the build up

of gas eligible for star formation (see Section 3.2.1). Despite these differences in the star formation history, the most significant one is the stellar mass of the halo at $z = 0$. The final stellar mass of the MW halo in Setup 1 is approximately $10^{10}\,\mathrm{M}_{\odot}$, which is two orders of magnitude higher than that in the new run with a value of roughly $10^{8}\,\mathrm{M}_{\odot}$. This difference means that these haloes have vastly different f_{d} and f_{s}.

Due to the non-linear coupling of the various processes, changing individual prescriptions always requires new parameter fitting (Crain et al., 2015). With a new star formation setup, we have to re-explore the feedback parameter space with Setup 2. However, we have two distinct advantages as compared to before. The first is that we understand the general effects changing the feedback parameters have on the f_s and f_d of the halo (see Figure 3.4). Secondly, the simulations will complete much faster, allowing us to obtain more data points, both in general feedback parameter space and in the region around the best match to observations. This improvement will help us narrow down the feedback prescription, and possibly identify more than one combination that yields a close match. Obtaining more than one set of parameters will open up the possibilities of testing the robustness of the feedback prescription in the MW halo zoom simulations, haloes in the high-resolution region and the dwarf galaxy zoom simulations.

3.4.4 MW galaxy zoom simulations with Setup 2

We perform the following parameter space exploration with Setup 2 in Table 3.1. With this setup, we run a total of 49 simulations in order to calibrate the feedback prescription, and we make a similar classification as before, shown in Figure 3.3. We summarise the various properties of the halo of interest of simulations with Setup 1 and 2 in Table 3.3. This table includes simulations that will be discussed in Sections 3.4.5 and 3.4.6.

From the 49 simulations, only one simulation with (3.0×10^{-5}, 1_1, 1.0) failed to reach $z = 0$ due to the complete removal of gas when stars form. The process of iteration started from the best combination of parameters found in Section 3.4.1, (2.5×10^{-4}, 1_3, 0.2) and progressed based on the trends found in Figure 3.4 to move the simulation data point closer to the target. This process will be explained later. We introduce a measure of closeness between the simulated and

Table 3.3 List of feedback prescriptions discussed in Sections 3.4.1, 3.4.4, 3.4.5 and 3.4.6 with the relevant properties of the halo of interest. These include m_{500}, $f_{\mathrm{d(obs)}}$, $f_{\mathrm{d(sim)}}$ and d as described in Section 3.4.4. The combination of feedback parameters that produces the lowest value of d, i.e., the most realistic galaxy in terms of its baryonic makeup is highlighted for each setup. We have included the sections which individual simulation is discussed in to guide the reader.

Feedback setup list							
MW galaxy zoom simulations – Setup 1							
Feedback parameters	$m_{500}\,[M_\odot]$	$f_{\mathrm{d(obs)}}$	$f_{\mathrm{d(sim)}}$	$f_{\mathrm{s(obs)}}$	$f_{\mathrm{s(sim)}}$	d	Discussed in Section
(1.0×10^{-5}, 1_3, 0.1)	5.59×10^{11}	0.26	1.41	0.22	1.25	1.54	3.4.1
(1.0×10^{-4}, 1_3, 0.1)	4.23×10^{11}	0.24	0.68	0.20	0.57	0.57	3.4.1
(2.5×10^{-4}, 1_3, 0.1)	4.92×10^{11}	0.25	0.82	0.21	0.42	0.60	3.4.1
(5.0×10^{-4}, 1_3, 0.1)	3.99×10^{11}	0.24	0.68	0.20	0.57	0.57	3.4.1
(1.0×10^{-3}, 1_3, 0.1)	3.88×10^{11}	0.24	0.19	0.19	6.01×10^{-3}	0.19	3.4.1
(1.0×10^{-5}, 2_6, 0.1)	4.65×10^{11}	0.25	1.02	0.20	0.91	1.04	3.4.1
(1.0×10^{-5}, 3_9, 0.1)	4.30×10^{11}	0.24	0.81	0.20	0.70	0.76	3.4.1
(1.0×10^{-5}, 4_12, 0.1)	5.05×10^{11}	0.25	0.86	0.21	0.54	0.69	3.4.1
(1.0×10^{-5}, 5_15, 0.1)	5.66×10^{11}	0.26	1.26	0.22	0.15	1.00	3.4.1
(1.0×10^{-5}, 1_3, 0.2)	5.53×10^{11}	0.26	1.37	0.22	1.22	1.49	3.4.1
(2.5×10^{-4}, 1_3, 0.2)	4.05×10^{11}	0.24	0.36	0.19	0.18	0.13	3.4.1
MW galaxy zoom simulations – Setup 2							
Feedback parameters	$m_{500}\,[M_\odot]$	$f_{\mathrm{d(obs)}}$	$f_{\mathrm{d(sim)}}$	$f_{\mathrm{s(obs)}}$	$f_{\mathrm{s(sim)}}$	d	Discussed in Section
(2.5×10^{-4}, 1_3, 0.2)	3.67×10^{11}	0.23	0.23	0.18	5.64×10^{-3}	0.17	3.4.4
(2.5×10^{-4}, 1_3, 0.9)	3.65×10^{11}	0.23	0.12	0.18	2.76×10^{-3}	0.21	3.4.4
(5.0×10^{-5}, 1_3, 0.9)	3.46×10^{11}	0.23	0.33	0.18	4.87×10^{-2}	0.16	3.4.4
(4.0×10^{-5}, 1_3, 0.9)	3.47×10^{11}	0.23	0.28	0.18	9.08×10^{-2}	0.11	3.4.4
(3.0×10^{-5}, 1_3, 0.9)	3.69×10^{11}	0.23	0.44	0.18	0.13	0.22	3.4.4
(2.0×10^{-5}, 1_3, 0.9)	4.15×10^{11}	0.24	0.61	0.19	0.39	0.42	
(3.0×10^{-5}, 1_1, 0.9)	3.50×10^{11}	0.23	0.24	0.18	0.10	7.59×10^{-2}	3.4.4 and 3.4.6
(2.5×10^{-5}, 1_1, 0.9)	3.71×10^{11}	0.23	0.29	0.18	0.14	7.3×10^{-2}	3.4.4 and 3.4.6
(3.0×10^{-5}, 1_1, 0.9) run 2	3.78×10^{11}	0.23	0.32	0.18	8.34×10^{-2}	0.14	3.4.6
(2.5×10^{-5}, 1_1, 0.9) run 2	3.59×10^{11}	0.23	0.33	0.18	0.15	0.10	3.4.6
Dwarf galaxy zoom simulations – Setup 2							
Feedback parameters	$m_{500}\,[M_\odot]$	$f_{\mathrm{d(obs)}}$	$f_{\mathrm{d(sim)}}$	$f_{\mathrm{s(obs)}}$	$f_{\mathrm{s(sim)}}$	d	Discussed in Section
(3.0×10^{-5}, 1_1, 0.9)	2.34×10^{10}	9.38×10^{-2}	8.14×10^{-2}	2.60×10^{-2}	8.47×10^{-3}	2.15×10^{-2}	3.4.5
(2.5×10^{-5}, 1_1, 0.9)	2.33×10^{10}	9.36×10^{-2}	0.12	2.58×10^{-2}	9.46×10^{-3}	2.79×10^{-2}	3.4.5

the observed galaxy properties via the Cartesian distance to the target,

$$d = \sqrt{(f_{\mathrm{s(sim)}} - f_{\mathrm{s(obs)}})^2 + (f_{\mathrm{d(sim)}} - f_{\mathrm{d(obs)}})^2}, \tag{3.9}$$

where subscripts *sim* and *obs* refers to simulation and observation respectively. Lower values of d represent a more realistic simulated galaxy in terms of both f_s and f_d. For the goodness of fit of individual properties, we refer to Table 3.3.

Comparing the feedback parameter values covered in both Setup 1 and 2, it is clear that they do not cover an equal area of parameter space. The main differences lie in the usage of high f_* while having low values of r and ϵ in Setup 2 as compared to Setup 1. There are two significant volumes of parameter space not covered in Setup 2: large values of ϵ coupled with low r and f_* and large values of r with low values of ϵ and f_*. Also, there are regions (intermediate values of ϵ and f_*, high values of r and intermediate values of f_*) in the parameter space of Setup 2 that are not sampled. The reason why we do not have any simulations in these regions will be explained in the next section with Figure 3.11.

Comparison to Baryonic properties from McGaugh et al. (2010) – Setup 2

We will identify the best star formation and feedback parameters through an iterative process beginning from the initial point (2.5×10^{-4}, 1_3, 0.2) from before, applying the knowledge of trends from Figure 3.4. We use arrows to represent the general movement of data points due to the initial adjustments of f_* and ϵ before using r and s for the finer last adjustments on the f_{s} and f_{d} plane. We present this with a representative set of simulations in Figure 3.11, similar to Figure 3.4 by starting from the best combination of parameters (blue dot) in Setup 1. It is evident that identical feedback prescription in different settings produced a MW with disparate f_s and f_d. In Setup 2, the previously optimal values produced a MW galaxy with minimal stellar mass. This small amount of stars at $z = 0$ is a result of the relaxed star formation conditions producing numerous small star formation events, which instantly yield feedback and reduces future star formation.

From the starting point, we increase f_* from 0.2 to 0.9 (see green arrow in Figure 3.11). This trend indicates that as f_* increases, f_{d} decreases while f_{s} stays constant, which is in agreement with the combination of effects of the green and blue arrows shown in Figure 3.4. Despite only having two data points, we

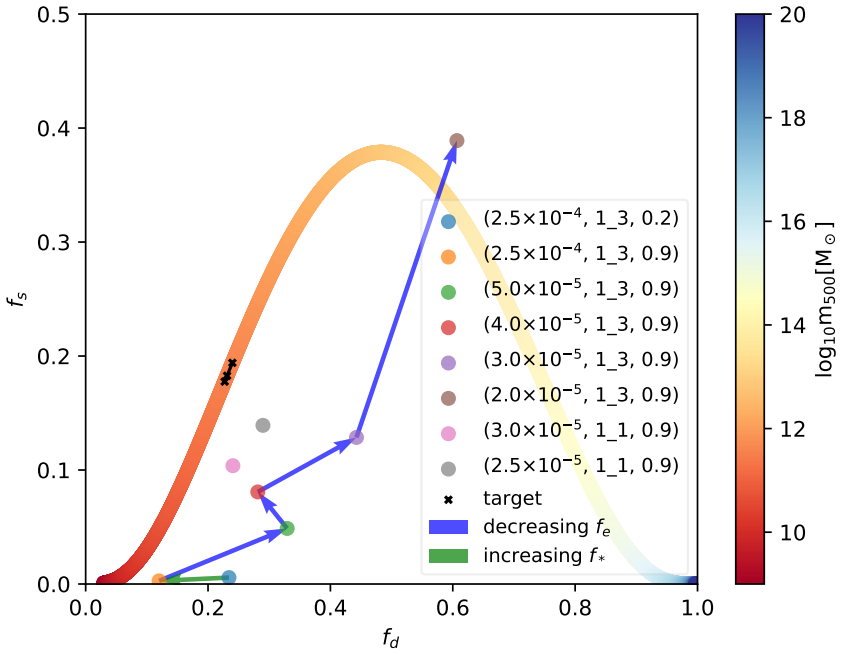

Figure 3.11 Graph of f_s against f_d across a range of m_{500} for Setup 2. The symbols and colourbar have the same meaning as those shown in Figure 3.4. For detailed description, we refer to Section 3.4.4.

know from the direction given by the green arrow in Figure 3.4 that it will have the same effect on the properties as increasing ϵ (blue arrow). Therefore, if we increase f_* further in Figure 3.4, we can expect it to follow the last blue arrow, which is a horizontal motion of decreasing f_d with constant f_s. Together with the immediate feedback from stars, increasing f_* converts more gas into stars, which reduces the amount of gas, leading to the decline in f_d. Although more stars form initially, the feedback is stronger, reducing the amount of gas available to form more stars as the halo aged, resulting in a constant f_s. Therefore, we increase f_* in an attempt to move the data point as far left as possible in Figure 3.11 in preparation for the next step. The simulation with $f_* = 1.0$ does not produce a MW galaxy with significantly different f_s and f_d. Furthermore, this value of f_* caused the only failed run from 49 simulations. Hence, we settle on a f_* value of 0.9 (orange dot) as the starting point for the next phase of iteration.

After obtaining the minimal f_d with (2.5×10^{-4}, 1_3, 0.9), we attempt to increase f_s and f_d in the next iteration to move closer to the target. From what we learned from Figure 3.4, we can achieve this by either decreasing ϵ or r. Since r is already at a minimum, lowering ϵ is the only option. We present only a

representative set of data points connected by the blue arrows to illustrate the general change in $f_{\rm s}$ and $f_{\rm d}$ due to smaller ϵ values. This increase in $f_{\rm s}$ and $f_{\rm d}$ is in agreement with Figure 3.4, explained by the less efficient baryon expulsion, which leads to higher star formation and retention of gas within r_{500}.

The final step is to adjust r and s to improve the match to the observed $f_{\rm s}$ and $f_{\rm d}$. Initially, we maintain the injection of feedback energy in a cube and increase the size, i.e, from $r = 1$ and $s = 3$ to $r = 2$ and $s = 6$. The aim is to obtain a point to the top right of the target and increase r and s correspondingly to move it towards the target as predicted by Figure 3.4. However, we do not obtain any good fit. Coupled with an upper limit to the extent of feedback injection where $f_{\rm d}$ increases instead beyond $r = 3$ and $s = 9$ (see Figure 3.4), we decide to change the shape of energy injection from a cube to just the adjacent cells centred around the star particle. In parameters terms, we change $r = 1$ and $s = 3$ to $r = 1$ and $s = 1$. As a result, the feedback energy is injected into four instead of 27 cells, effectively increasing the energy concentration per cell by approximately an order of magnitude. This increased energy density causes a larger decrease in $f_{\rm d}$ than in $f_{\rm s}$. In contrast, increasing the extent of feedback injection maintained in a cube region generates a comparable change in both $f_{\rm s}$ and $f_{\rm d}$.

We determine (2.5×10^{-5}, 1_1, 0.9) and (3.0×10^{-5}, 1_1, 0.9) as the two sets of parameters able to produce the smallest d value (see Table 3.3). Given the vast area of unexplored parameter space and the starting point of the iterative process, we are going to justify that the steps taken constitute the most reasonable route through parameter space that can produce a close match to observations. The starting values of (2.5×10^{-4}, 1_3, 0.2) define the boundaries where values can be adjusted. r and f_* are almost at the minimum, meaning they can only increase while ϵ can either decrease or increase. Furthermore, the low $f_{\rm s}$ of the starting point of properties in Figure 3.11 suggests that the current feedback is too strong that it restricts star formation.

Together with the trends of changing parameters, the possible motions of the data point are a horizontal movement to the left or right, and diagonally right. The worst possible option is to increase ϵ, moving the data point to the left. This choice leaves us stranded because we cannot create further motion since r and f_* are already close to their minimum values. The next possible option is to increase r above 3, causing the data to move horizontally right. The next steps associated with this first movement will be decreasing ϵ to iterate data points towards the

top right before increasing f_* to reduce the data to match the target. However, given the initial movement away from the target, we believe that this will not produce a better match than what is presented. The most plausible option is to decrease ϵ, moving the data point along the blue arrows indicated in Figure 3.11. f_* can then be increased to move it down diagonally left towards the target while fine-tuning r and s. This change is preferred over increasing r because of the turn around expected beyond $r = 4$, which limits the degrees of freedom. However, following this option will generate a combination of parameters similar to what we have found. Out of the possible options to move the initial point in parameter space, we have chosen the path that will produce the best match to fit the observational data from McGaugh et al. (2010). Since the argument put forth does not mention the possibility of an ideal set of parameters lying in the region of parameter space consisting of intermediate values of ϵ and f_* and high values, they are not investigated.

Comparing the values of the feedback parameters that reproduce the MW baryonic makeup from both setups, we can identify the self-consistency of our feedback implementation. Setup 1 yielded an optimal combination of (2.5×10^{-4}, 1_3, 0.2) but in Setup 2, we conclude that (2.5×10^{-5}, 1_1, 0.9) and (3.0×10^{-5}, 1_1, 0.9) reproduced the most realistic MW galaxy. In Setup 2, the simulation forms more star particles but they are of lower masses than in Setup 1. Therefore, in order to produce a similar amount of stars observed in a MW galaxy at $z = 0$, Setup 2 requires a higher gas to star conversion efficiency, 0.9 as compared to 0.2 in Setup 1. In response to this larger conversion efficiency, Setup 2 require a lower ϵ. The value of ϵ differs significantly between the setups as a result.

KS relation – Setup 2

In this section, we will present the agreement of star formation in the simulation with the KS relation described in Section 3.3.2. Similar to Figure 3.6, we choose non-zero SFR patches within r_{500} at $z = 0$ and compare it to the fit given by Equation 3.8 and observations of nearby galaxies by Bigiel et al. (2008), shown in Figure 3.12. There is a clustering of points around the fit but no slope can be deduced from the points. Also, the simulated gas density is too low for comparison to observational data. We believe the concentration of points around low surface gas density is due to the relaxed star formation criteria and the higher f_*. These conditions result in a more efficient conversion of gas into stars, leading to more

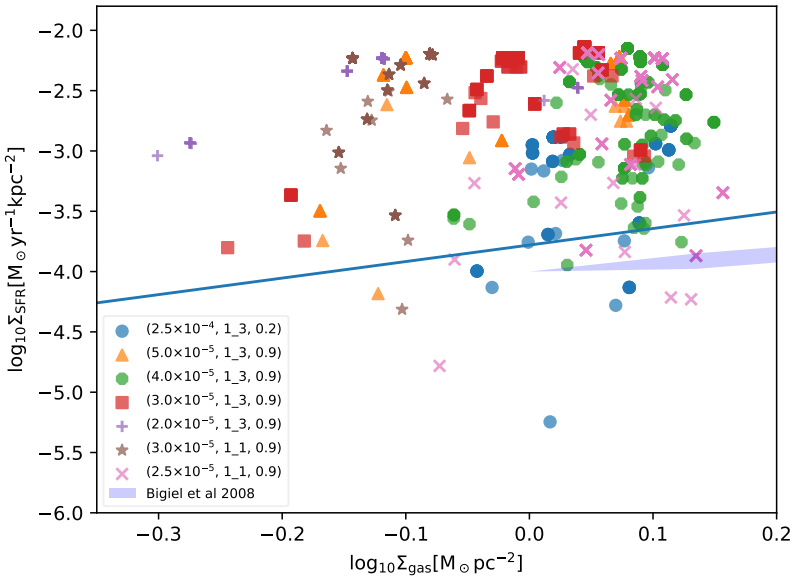

Figure 3.12 Graph of SFR surface density against gas surface density illustrating the KS relation similar to Figure 3.6. Different coloured points are simulation data with sub-kpc resolution consistent with rough approximation from the observations in nearby galaxies by Bigiel et al. (2008) represented by the blue hatched contours. The blue line is derived from the observational fit of Kennicutt et al. (2007). For further description of this figure, we refer to Section 3.4.4.

feedback energy injection that lowers the gas density.

While (3.0×10^{-5}, 1_1, 0.9) and (2.5×10^{-5}, 1_1, 0.9) recovers $f_{\rm s}$ and $f_{\rm d}$ well, there is an absence of patches with high gas surface density, restricting our ability to probe the KS relation in that regime. This absence also suggests that feedback might have been too efficient in driving gas out of the central region of the galaxy. Comparing Setup 2 to Setup 1, the former is not as good in recovering the KS relation due to the intrinsic nature of star formation in Setup 2 where it is more instantaneous, driving gas surface density to lower values. As discussed earlier, a larger quantity of stars is formed in Setup 2, which begins feeding back into the IGM immediately. Coupled with the high conversion efficiency of gas to stars, it empties the central region of the galaxy of gas, explaining why gas surface density is low.

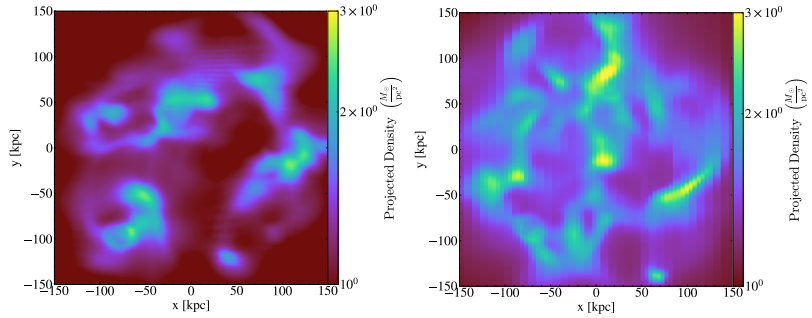

(a) (3.0×10^{-5}, 1_1, 0.9)

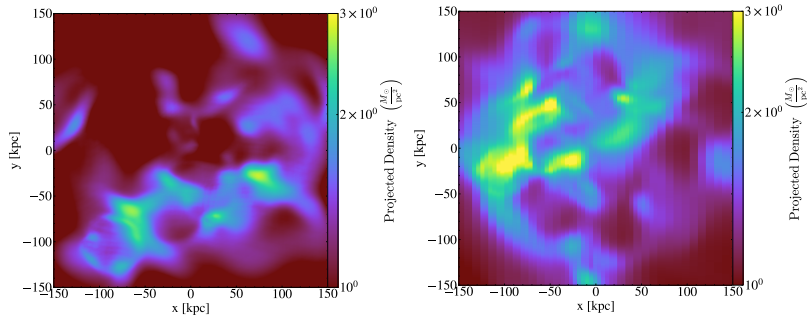

(b) (2.5×10^{-5}, 1_1, 0.9)

Figure 3.13 Pairs of face on and edge on density plots of the MW halo within the virial radius with (3.0×10^{-5}, 1_1, 0.9) (a) and (2.5×10^{-5}, 1_1, 0.9) (b) described in Section 3.4.4. The left and right panel of each pair correspond to the face on and edge on plot respectively.

Morphology – Setup 2

We present the projection plot for the best feedback prescription in Figure 3.13. The face and edge on orientation are determined by the angular momentum calculated from the cells within 50 kpc. (a) and (b) correspond to the simulation with (3.0×10^{-5}, 1_1, 0.9) and (2.5×10^{-5}, 1_1, 0.9) respectively. While we see considerably more substructures and disruption as compared to Figure 3.7, it is important to note two key differences. The first is the much lower projected gas density, and the second is the much larger distance scale as compared to that in Setup 1. Due to the same reasons accounting for the differences in the KS relation, the feedback from this relatively large amount of stars creates multiple low-density pockets across the structure. These pockets explain the lower overall gas density seen in Figure 3.12. Also, since feedback is pushing gas out more efficiently, it spreads the structure over a larger distance, resulting in a lack of a disk-like structure.

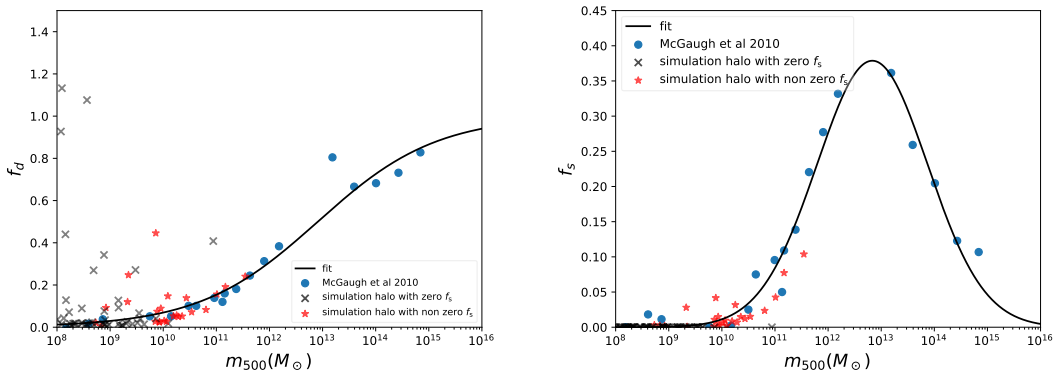

(a)

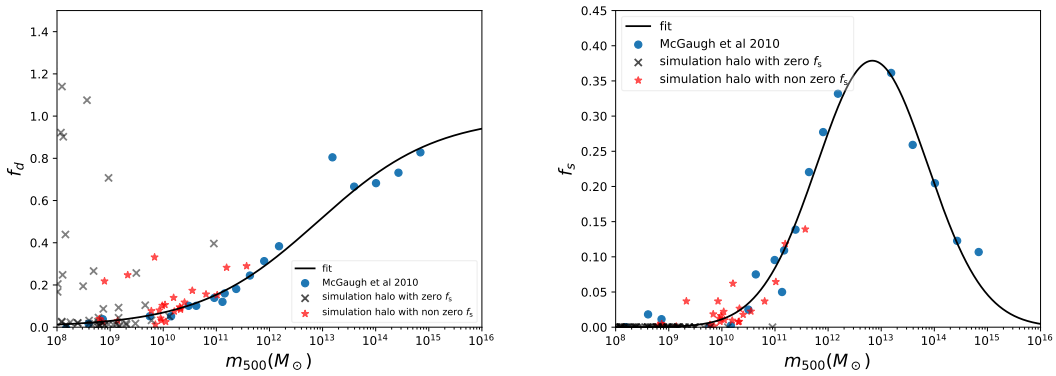

(b)

Figure 3.14 Graph of $f_{\rm d}$ against m_{500} (left) and $f_{\rm s}$ against m_{500} (right) with equations described in Section 3.3.1. The black line represents the fit given by Equation 3.4 and 3.5. The blue dots are data from McGaugh et al. (2010) while the crosses and stars are properties of haloes with various mass from the high-resolution region in the simulation. The black cross and red star refer to haloes in the must refine region with zero and non zero $f_{\rm s}$ respectively. Top row figures are from (3.0×10^{-5}, 1_1, 0.9) while the bottom row figures are from (2.5×10^{-5}, 1_1, 0.9). Refer to Section 3.4.4 for a detailed description.

Haloes in the high-resolution region – Setup 2

Similar to Section 3.4.1, we look at the $f_{\rm s}$ and $f_{\rm d}$ of the other haloes within the high-resolution region of three virial radii from the MW halo. We plot $f_{\rm d}$ against m_{500} on the left column, $f_{\rm s}$ against m_{500} on the right column, and simulations with (3.0×10^{-5}, 1_1, 0.9) and (2.5×10^{-5}, 1_1, 0.9) on the top and bottom rows in Figure 3.14 respectively.

With the exception of one and two haloes from the runs with (3.0×10^{-5}, 1_1, 0.9) and (2.5×10^{-5}, 1_1, 0.9) respectively, we show very good agreement for

both $f_{\rm s}$ and $f_{\rm d}$ of haloes between $10^{10}\,{\rm M}_{\odot}$ and $10^{12}\,{\rm M}_{\odot}$. This agreement is in contrast to Figure 3.8 where agreement is only achieved for $f_{\rm s}$ and not $f_{\rm d}$. On top of that, the level of agreement with observations is much better in Figure 3.14 than Figure 3.8 as points lie closer to the fit. For haloes below $10^{10}\,{\rm M}_{\odot}$, it is plausible that the lack of mass and spatial resolution is the cause of their inability to form stars. On the other hand, the larger mass haloes that suffer the same problem, require future zoom simulations to be carried out in order to identify the root of the issue.

3.4.5 Dwarf galaxy zoom simulation with Setup 2

We conduct zoom simulations of a dwarf galaxy with $m_{\rm vir}$ of approximately $10^{10}\,{\rm M}_{\odot}$ as an additional test of the universality of the feedback parameters in different halo mass bins. We described how we pick this dwarf galaxy from the high-resolution region of the MW zoom simulation in Section 3.2. Similarly, we increase the number of nested levels to keep the number of particles defining the halo constant with that of the MW while keeping the spatial resolution constant. We then compare the $f_{\rm s}$ and $f_{\rm d}$ of the halo to McGaugh et al. (2010) in Figure 3.15.

We present a close-up view of the parameter space in Figure 3.15 because we are showing results from zoom simulations of the dwarf galaxy using the two best sets of parameters only. It is clear that the $f_{\rm s}$ and $f_{\rm d}$ of the simulated galaxy in both feedback prescriptions are comparable to the target. We expect good agreement based on the results of Figure 3.14. Therefore, we argue that this feedback prescription is insensitive to mass resolution with a smaller mass halo having a lower and higher resolution in Figures 3.14 and 3.15 respectively. However, it is also essential to investigate the dependence of the feedback prescription on spatial resolution in future work.

It is remarkable that there is such a small error associated with the data presented by McGaugh et al. (2010). This is the main reason why we strive to improve the agreement between our simulation results and observations as much as possible. However, it is also important to note the possibility of underestimates in the errors and unaccounted systematics. The method of determining the mass of the halo from observations affects the amount of scatter too. If abundance matching is used, m_* will have a lot more scatter than m_b in the Tully-Fisher plane at low mass, leading a corresponding amount of scatter in f_s* and f_d. Since

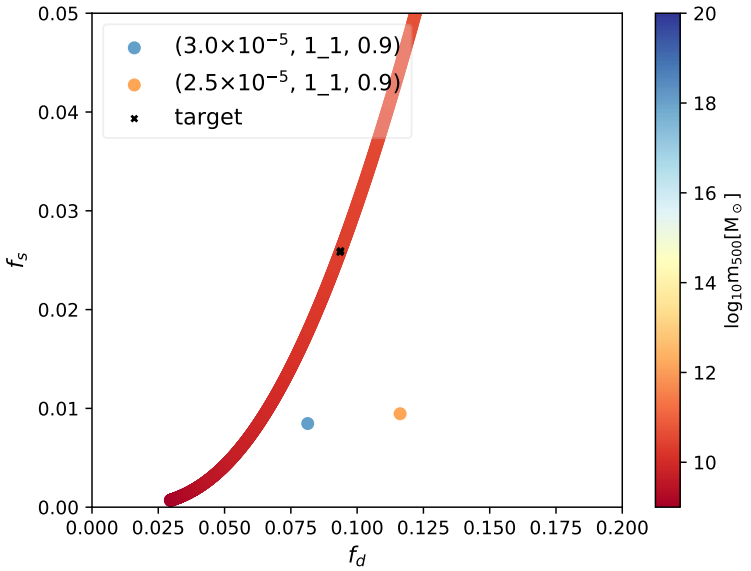

Figure 3.15 Plot of f_s against f_d for the zoom dwarf galaxy simulations. Various coloured dots represent runs with different set of feedback parameters with the colourbar having the usual meaning. It is focused on a small area near the target due to closeness of simulation results with the observed properties. See Section 3.4.5 for a detailed description.

most of the mass in low mass rotating galaxies is gas and not stars, one can also question the applicability of extrapolating abundance matching relations to such low masses.

3.4.6 Chaos and variance

Recognising the argument put forth by Keller et al. (2019) for chaotic variance in numerical simulations, we conduct our zoom simulations twice on different processors. They have identical initial conditions and feedback prescriptions but evolved on different combinations of processors in the same computing cluster. The aim is to find out how much the halo properties would differ from each other due to the usage of a different set of processors. We quantify this difference in Figure 3.16.

Dots and stars in Figure 3.16 represent the pair of simulations with (3.0×10^{-5}, 1_1, 0.9) (blue) and (2.5×10^{-5}, 1_1, 0.9) (red) respectively. Despite both of them being close to the target, f_s and f_d for each pair can differ as much as running a simulation with a different set of feedback parameters. Comparing

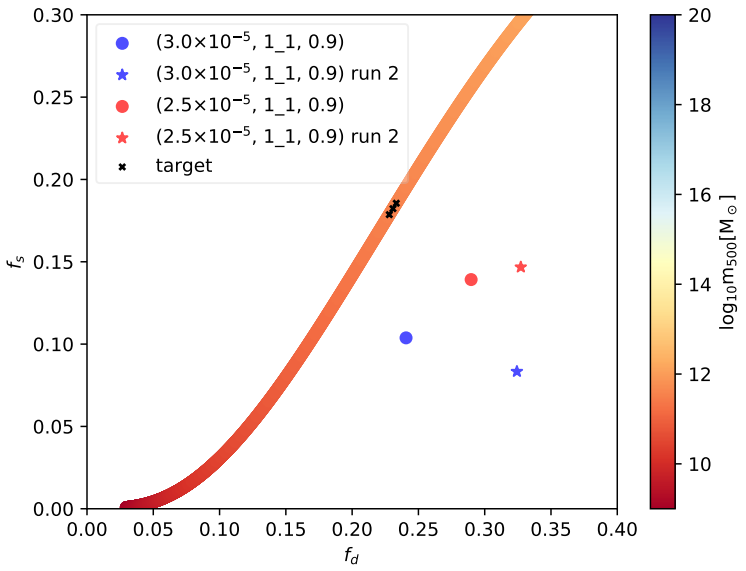

Figure 3.16 Plot of f_s against f_d for pairs on zoom MW simulation with identical initial conditions and feedback prescriptions evolved with different processors. Same coloured symbols refer to the simulations with identical setup while dots and stars represent identical simulations with two different sets of processors. The colour bar has its usual meaning. It is again focused in a small area near the target due to the level of agreement of simulation results with the properties. See Section 3.4.6 for a detailed description.

(3.0×10^{-5}, 1_1, 0.9) run 2 to (4.0×10^{-5}, 1_1, 0.9) in Figure 3.11, the simulated galaxies have similar values of $f_{\rm s}$ and $f_{\rm d}$. This variance is also apparent from the values of m_{500} where the maximum, minimum and the mean values are shown by the black crosses.

Looking at Figure 3.16, the deviation in $f_{\rm s}$ from the pair of simulations is comparable to the 10% difference in stellar mass concluded in Keller et al. (2019) despite not using identical processors. However, the deviation in total baryon mass is as high as 33%, possibly arising from the coupling of star formation and feedback where a 10% difference in stellar mass affects the feedback significantly. As a result, gas distribution in the halo is changed drastically. In conclusion, more computational resources have to be devoted to quantify any deviation of results due to coding of numerical codes.

3.5 Summary and conclusions

We present results from a large number of zoom simulations of both a MW and a dwarf galaxy. This suite of simulations is the first application of numerical simulations calibrated to match the f_s and f_d properties presented by McGaugh et al. (2010). Using the star formation routine of Cen & Ostriker (1992) and the thermal supernova feedback of Cen & Ostriker (2006), we select factors such as f_* to tune the conversion efficiency of gas to stars, ϵ for the feedback energy budget, and lastly, both r and s to calibrate the extent of feedback injection in the simulations. We also identify additional parameters that require adjustments in order to achieve realistic star formation histories. They are the Jeans instability check, the star particle threshold mass and the timestep dependence of star formation. These directly influence the criteria used to determine the occurrence of star formation.

With these parameters, we produce a MW galaxy with realistic baryon and stellar fraction when compared to the observations of McGaugh et al. (2010) with our suite of simulations. We achieve this agreement with two different setups shown in Table 3.1. Setup 1 utilises a timestep dependent star formation with Jeans instability check and a star formation threshold mass of $10^5\,{\rm M}_\odot$. We attempt a total of 22 simulations with this setup and find that (2.5×10^{-4}, 1_3, 0.2) managed to reproduce the observed $f_{\rm s}$ and $f_{\rm d}$. However, the simulated MW galaxy in this feedback prescription does not match the observed KS relation

and morphology perfectly. By applying this feedback prescription to a zoom simulation of a dwarf in this setup, we find star formation starting too late as compared to the simulated MW galaxy. To resolve this issue, we propose switching to a timestep independent star formation setup with no Jeans instability check and threshold mass (Setup 2). However, due to the non-linear coupling of the various processes in the simulation, a new prescription requires re-exploration of subgrid parameters.

We begin an iterative process from (2.5×10^{-4}, 1_3, 0.2) in Setup 2, concluding with two sets of parameters that produced a close fit to the $f_{\rm s}$ and $f_{\rm d}$ with the use of 49 simulations. They are (2.5×10^{-5}, 1_1, 0.9) and (3.0×10^{-5}, 1_1, 0.9). Similar to Setup 1, there are issues with the KS relation and morphology of the simulated galaxy. However, these feedback prescriptions performed remarkably well in matching the baryonic makeup of haloes between $10^{10}\,{\rm M}_\odot$ and $10^{12}\,{\rm M}_\odot$ in the high-resolution region to observations. A perfect feedback prescription that is able to replicate all the observables in the universe does not exist. If the prescription is tuned to certain observables, it might fail to reproduce others, which then requires further iterations to the feedback implementation (e.g. Pillepich et al. (2018)).

The main difference between setups is the conditions for star formation, and this is reflected in the best values of the feedback parameters we find. In Setup 2, with more relaxed star formation criteria, f_* is high, and ϵ is low as compared to Setup 1. These values in different setups show that feedback is self-consistent. In Setup 2, star particles form with ease, of lower mass but have a larger quantity. In order to match the same observed value of $f_{\rm s}$ with Setup 1, we use a higher value of f_*, creating star particles with higher mass. However, since we demand a good agreement with the observed $f_{\rm d}$, we have to lower the feedback energy efficiency from these higher mass star particles. This adjustment results in a lower ϵ as compared to Setup 1. Therefore, combining the values of feedback parameters with the star formation criteria, we show the self-consistent characteristics of the feedback processes.

In Setup 2, the points coalesce around low gas surface density, with more gas being converted to stars due to the higher value of f_* and the relaxed star formation criteria. As a result, in the recovery of the KS relation in both simulation setups, Setup 2 did not perform as well as Setup 1. Given the inability to reproduce a disk-like structure in the MW haloes, we understand that this feedback prescription performs well only for reproducing $f_{\rm s}$ and $f_{\rm d}$. In terms

of matching other observed properties, this feedback prescription requires more tuning.

Looking at the other haloes in the high-resolution region in Setup 2, all but three of the haloes within $10^{10}\,\mathrm{M}_{\odot}$ and $10^{12}\,\mathrm{M}_{\odot}$ with the calibrated star formation and feedback prescription are an excellent fit to f_{s} and f_{d} observed by McGaugh et al. (2010). In comparison to the results from Setup 1, the feedback prescriptions in Setup 2 perhaps suggest universality for haloes within the mass range described. We verify this claim with the zoom simulations of a dwarf galaxy of $10^{10}\,\mathrm{M}_{\odot}$ with these feedback prescriptions. Through the haloes in the high-resolution region of the MW zoom simulation and the halo in the dwarf galaxy zoom simulation, we demonstrate the insensitivity of our feedback prescription on the mass resolution. However, we have to conduct the same test with much lower mass haloes as well as with different spatial resolutions. On top of the resolution, the universality and robustness of the feedback prescription should also be extended to galaxies with various star formation and merger history.

As we demonstrate variance introduced by the numerical code is a cause for concern, more computational resources need to be invested in order to understand, quantify and minimise these effects. Since we do not reproduce all the observational constraints mentioned, there exists the possibility of including more parameters in the feedback model or developing a different model. These should be the focus of future work to improve the feedback prescription in order for the simulated galaxies to better match observations.

In conclusion, we have obtained sets of parameters that can produce a close match to the observed MW properties with two different star formation setups of the popular Cen & Ostriker (1992) model within the `Enzo` code. We can match the KS relation relatively well as compared to the ability to reproduce the disk structure we observe in the MW galaxy with our feedback prescription. Although demonstrating a potential for universality across mass ranges, more resources have to be devoted to understanding the resolution dependence of the feedback implementation and the inherent variance in the application of `Enzo`. Given the success of the star formation and feedback prescription, we are now ready to begin testing other aspects of the simulation. With a realistic baryon content in haloes as the starting point, we can investigate how future star formation evolves as gas continues to flow from the intergalactic medium into the haloes coupled with feedback processes regulating the star formation. These will be studied in great detail in Chapter 4.

Chapter 4

The fate of baryons in the future

4.1 Introduction

When haloes form through gravitational collapse, dark matter is the dominant component (White & Rees, 1978). As baryons fall into the gravitational potential wells, they become pressure supported until they are able to cool and condense to form stars. Once stars form, they immediately start to provide feedback by injecting energy into the interstellar medium (ISM). When massive stars reach the end of their main-sequence lifetimes, they explode as supernovae, enriching the ISM by injecting a large amount of energy (10^{51} erg per supernova) (Woltjer, 1972) and metals. The metals will provide an additional source of cooling, especially for cold gas (Smith et al., 2008).

We have studied these processes in Chapter 3 by exploring the parameter space of the subgrid physics extensively. After calibrating the subgrid physics parameters with haloes of specific masses, we now wish to apply this prescription to simulations of much larger volumes with haloes of a variety of masses with the aim of studying the long-term evolution of baryons. The gas that will fuel further star formation comes from the interstellar, circumgalactic and intergalactic medium. The infall begins on the outskirts of the halo, beyond the virial radius, in a region known as the intergalactic medium (IGM). The gas then enters the halo into the intersection between the galaxy and the IGM, referred to as the circumgalactic medium (CGM). The CGM contains gas that originate from the metal-poor IGM inflows, metal-rich supernova and feedback outflows, and

recycled gas from various sources such as those stripped from in-falling satellite galaxies (Peeples et al., 2019), making it a unique region. Finally, gas reaches the innermost of the galaxy among the stars known as the interstellar medium (ISM). According to this categorisation, the IGM contains the bulk of cosmic matter (McQuinn, 2016). Therefore, the IGM is vital across astrophysical scales, ranging from tests on the models of structure formation (Viel et al., 2005; Seljak et al., 2005) to anisotropies in the CMB (Ostriker & Vishniac, 1986; Hu, 2000) to cosmological parameter inferences (Pritchard et al., 2007; Wyithe & Dijkstra, 2011). Cooling timescales in the IGM are too long to have any significant impact on star formation at $z = 0$. However, as we are interested in the long-term evolution in this work, these timescales are now relevant.

Together with the star formation, the UV emission from active galactic nuclei maintains the ionisation of the IGM. However, the exact contributions from each of these sources are relatively unknown. At $z > 3$, decreasing population of bright quasars leads to a corresponding declining contribution to the UV background, suggesting that stars provide the majority of ionizing flux at early times (Madau et al., 1999; Gnedin, 2000; Wyithe & Loeb, 2003; Meiksin, 2005; Robertson et al., 2010). The bottom line is star formation is an important driver for the strength of the UV background. The transfer of energy from this diffuse background flux is most apparent in the IGM. There is a tight power law relation between the temperature and density of the gas in the IGM at high z (Hui & Gnedin, 1997). This relation results from the balance of the background UV photoheating and the adiabatic cooling due to the expansion of the universe (McQuinn & Upton Sanderbeck, 2016) amongst other processes.

An extrapolation of an analytic fit of the cosmic SFRD (Madau & Dickinson, 2014) into the future predicts a continuation of the decline seen between $z \approx 2$ and present times. Potential causes include the slowing of growth of large scale structure due to the accelerating expansion of the universe and efficient stellar and AGN feedback (Salcido et al., 2018). These authors demonstrated that the decline in the star formation rate can be avoided by switching off the AGN feedback in their simulations, suggesting that the future of star formation is heavily dependent on feedback processes. They ended their simulations at 20 Gyr, before the onset of 'freeze out' ($z \approx -0.6$ or $t \approx 30$ Gyr) when haloes undergo isolated evolution. Also, IGM gas which becomes relevant when provided with infinite amount of time, can potentially cool and form stars. Here, we aim to extend the analysis beyond 20 Gyr in order to examine the robustness of the conclusions drawn about

future star formation. We will investigate the evolution of the IGM into the future, expanding on the work of Nagamine & Loeb (2004) by using more methods and higher resolution.

In this Chapter, we start with a cosmological box simulation with comparable resolution to Nagamine & Loeb (2004). We aim to verify the level of convergence in that previous work. We use the calibrated star formation and feedback prescriptions discussed extensively in Chapter 3. Building on this simulation, we vary the mass and maximum spatial resolution to test for convergence. We also apply the feedback prescription associated with Setup 1 from Chapter 3 as a test of the sensitivity of the results to different star formation and feedback prescriptions. Lastly, we continue the zoom simulation in Chapter 3 into the future, quantifying the impact of vastly different resolutions. Comparing these seven simulations, we look at the evolution of the dark matter haloes, gas properties and star formation.

This Chapter is structured as follows. Section 4.2 describes the cosmological parameters used in the generation of the initial conditions, the code, and setup for evolving them into the future. As mentioned, we replicate the resolution of the simulation of Nagamine & Loeb (2004). This will be the first application of `Enzo`, `Grackle` and `ROCKSTAR` to galaxy formation simulations going to the future, i.e., negative redshifts. Since they were not designed for such a purpose, we explore the necessary changes to the codes to carry out the simulations. Section 4.3 will first present the iteration of results from these changes to the simulation code. We also verify the capability of the `ROCKSTAR` halo finder to accurately identify and trace haloes into the future. This will be followed up by the comparison of our results to Nagamine & Loeb (2004) and establishing the convergence of these results. Lastly, we present and discuss the results from simulations of various resolutions and, star formation and feedback prescriptions. The halo mass functions, phase distribution of temperature and density of gas, equation of state of the IGM and star formation history of these simulations will be compared. Section 4.4 provides a summary and conclusion of the results obtained.

4.2 Simulation setup and analysis

In this section, we provide an overview of the simulation setups. As mentioned, the codes used are not optimised for evolving galaxy formation into the future.

As such, we include a critical assessment of the `Enzo` and `Grackle` code to fulfill such a requirement. It is therefore not surprising to find that certain components of the code require modifications. Changes to specific parts of the `Enzo` and `Grackle` will be discussed in subsequent sections. Other than the resolution, all simulations are initialised and set up identically.

Cosmological parameters obtained from WMAP-9 (Bennett et al., 2013), $\Omega_m = 0.285$, $\Omega_\Lambda = 0.715$, $\Omega_b = 0.0461$, $h = 0.695$ and $\sigma_8 = 0.828$ with their usual definitions are assumed across all simulations. We generate the initial conditions of our simulations using MUlti-Scale Initial Conditions for cosmological simulations (`MUSIC`) (Hahn & Abel, 2011) from these parameters. We evolve the simulation using the AMR code, `Enzo`, using the hydrodynamic solver that originated from `ZEUS` (Stone & Norman, 1992) and N-body adaptive particle-mesh gravity solver (Efstathiou et al., 1985). The cooling and chemistry processes are handled by the equilibrium cooling mode of the `Grackle` library (Smith et al., 2017). It makes use of the tabulated cooling rates derived from the photoionisation code, `CLOUDY` (Ferland et al., 2013). Lastly, we apply and evolve the UV background radiation given by Haardt & Madau (2012) up to and beyond $z = 0$. We will discuss the extrapolation of the UV background in Section 4.2.3.

For the star formation and thermal feedback, we adopt the model by Cen & Ostriker (1992) and Smith et al. (2011)'s modified version of the Cen & Ostriker (2006) thermal supernova feedback. As the parameter space was explored extensively in Chapter 3, we apply the outcome of the study here. In this Chapter, we use both Setup 1 and 2 outlined in Table 3.1. When evolving a simulation with Setup 1, we apply the corresponding set of feedback parameter values of (2.5×10^{-4}, 1_3, 0.2), consistent with the definition of (ϵ, r_s, f_s) given in Section 3.2.2. On the other hand, when we evolve the simulation with Setup 2, the feedback parameter values are set to (3.0×10^{-5}, 1_1, 0.9). Setup 2 will be the main star formation and feedback prescription in this Chapter. We run a total of seven simulations to investigate the convergence of the properties of baryons as they evolve into the future. The list of simulations is summarised in Table 4.1.

The names of the simulations indicate their resolutions and feedback prescriptions. For example, the baseline simulation named *NL* indicates a simulation with resolution comparable to Nagamine & Loeb (2004) and contains the feedback prescription associated with Setup 2 described before. These resolution choices will be discussed in Section 4.2.1. For simulations named *NL*$\pm x$ and *NLm*$\pm x$, they refer to a simulation similar to *NL* but with x levels added

Table 4.1 List of simulations discussed in this Chapter with their corresponding reference name. This table includes the number of particles, cosmological box size, the maximum number of AMR level, the maximum spatial and mass resolution, and the star formation setup and its corresponding feedback prescription in each simulation. Refer to Section 4.2 for more information about the naming convention and specifics of each simulation.

Simulation setup list							
Reference name	Particle number	Box size $[h^{-1}\,\mathrm{cMpc}]$	AMR level	Spatial resolution [ckpc]	Mass resolution $[M_\odot]$	Star formation setup	Feedback prescription
NL	128^3	50	4	35.13	6.79×10^9	2	(3.0×10^{-5}, 1_1, 0.9)
NL-1	128^3	50	3	70.26	6.79×10^9	2	(3.0×10^{-5}, 1_1, 0.9)
NL+1	128^3	50	5	17.56	6.79×10^9	2	(3.0×10^{-5}, 1_1, 0.9)
NLm-1	64^3	50	5	35.13	5.43×10^{10}	2	(3.0×10^{-5}, 1_1, 0.9)
NLm+1	256^3	50	3	35.13	8.48×10^8	2	(3.0×10^{-5}, 1_1, 0.9)
NLfb	128^3	50	4	35.13	6.79×10^9	1	(2.5×10^{-4}, 1_3, 0.2)
zoom	256^3	100	8	2.196	1.72×10^5	2	(3.0×10^{-5}, 1_1, 0.9)

or removed from the AMR and root grid resolution respectively. In *NLm*$\pm x$ simulations, it affects both the spatial and mass resolution of the initial conditions while the maximum AMR is adjusted to keep the maximum spatial resolution constant. Only spatial resolution is changed for *NL*$\pm x$ simulations. Also, we have two other simulations named *NLfb* and *zoom*. *NLfb* refers to the simulation with Setup 1 and its corresponding feedback prescription and *zoom* is a continuation of the zoom simulations described in Chapter 3 beyond $z = 0$. The results obtained from these simulations will be discussed in Section 4.3.

4.2.1 Resolution

Nagamine & Loeb (2004) presented the future evolution of the IGM with a version of the parallel tree SPH code `GADGET` (Springel et al., 2001). Their simulation consisted of 64^3 particles each for dark matter and gas, translating into a mass resolution of $3.4 \times 10^{10}\,h^{-1}\mathrm{M}_\odot$ and $5.3 \times 10^{9}\,h^{-1}\mathrm{M}_\odot$ for the dark matter and gas respectively. In contrast, we are using the particle-mesh code, `Enzo` for a simulation into the future for the first time. To allow a fair comparison of results, we implement a comparable mass resolution in our simulation.

The resolution conversion between `GADGET` and `Enzo` is simplified by the work of O'Shea et al. (2005). The authors demonstrated the halo mass functions (HMF) from a `GADGET` and `Enzo` dark matter only simulation in a $12\,h^{-1}$Mpc cosmological box are in good agreement with the Sheth-Tormen mass function (Sheth & Tormen, 2002) at $z = 3$ in Figure 3 of their paper. Although this agreement is encouraging for our purposes, we are more interested in the agreement between `GADGET` and `Enzo` simulations of varying resolutions. There was a significant deviation in the low-mass end despite the general agreement of the HMFs. The 64^3 root grid `Enzo` simulation failed to produce similar number of low-mass haloes as a 64^3 `GADGET` simulation. Improving the resolution of the `Enzo` simulation to 128^3 resolved this discrepancy.

For Eulerian codes using the particle-mesh technique such as `Enzo`, the force resolution is twice the mean grid cell size; see Chapter 2. This definition of force resolution is particularly important at early times when overdensities are low. The lack of force resolution leads to a loss of small-scale power, preventing the formation of low mass haloes. Therefore, the 64^3 resolution of the `GADGET` simulations in Nagamine & Loeb (2004) requires a 128^3 root grid `Enzo` simulation for an equivalent comparison.

The situation of force resolution improves at late times when AMR occurs in Enzo. Grid refinement in dense regions increases the spatial and in turn, force resolution between particles. With five total refinement levels, O'Shea et al. (2005) found that late time power spectrum of Enzo agrees with that of GADGET simulations. The authors also mentioned that it is common to run simulations with gravitational softening of approximately $1/2^5$ of the mean inter-particle distance. Therefore, for a 64^3 Enzo simulation, we require five total levels of spatial refinement. Since we are already increasing the root grid resolution to 128^3 as mentioned previously, we implement four levels of AMR additionally. This setup should eliminate any discrepancies due to differences in resolution when we compare the results to Nagamine & Loeb (2004).

In summary, for a direct comparison to a 64^3 dark matter and gas particles each in a $50\,h^{-1}$Mpc cosmological box in a GADGET simulation, we require a 128^3 root grid with four AMR levels Enzo simulation in a box of equal size. This setup translates to a maximum spatial resolution of 35.13 ckpc and a mass resolution of $6.79 \times 10^9\,\mathrm{M}_\odot$. Generally, these numbers are indicative of a low-resolution simulation. Hence, we look to quantify and establish results convergence by increasing and decreasing the number of AMR and root grid resolution. As mentioned, a summary of these runs is presented in Table 4.1.

4.2.2 Final redshift

To compare with Nagamine & Loeb (2004), we have to evolve our simulations for an equivalent or longer period of time. The cosmological parameters assumed in their simulation ($\Omega_m = 0.3$, $\Omega_\Lambda = 0.7$, $\Omega_b = 0.04$, $h = 0.7$ and $\sigma_8 = 0.9$) are different from ours. Therefore, we need to know the evolution of t with z in our cosmology. The age of the Universe, t can be calculated from

$$H_0 t = \frac{2}{3\sqrt{1-\Omega_m}} \sinh^{-1} \sqrt{\frac{1-\Omega_m}{\Omega_m (1+z)^3}}, \tag{4.1}$$

where H_0 and Ω_m is the Hubble parameter and matter density parameter at $z = 0$ (Peebles, 1993). This is related to the scale factor

$$a = \frac{a_0}{1+z}, \tag{4.2}$$

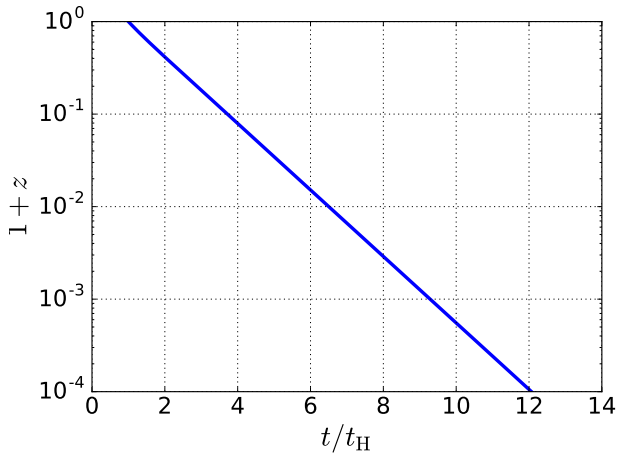

Figure 4.1 Co-evolution of t with z into the future

where a_0 is the scale factor at $z = 0$. We illustrate the relation of $(1 + z)$ with t normalized by the Hubble time, $t_{\rm H}$ (13.759 Gyr) in Figure 4.1, assuming cosmological parameters described in Section 4.2. We decide on a final redshift of -0.995 in our simulations, corresponding to $t \approx 7\, t_{\rm H}$ or $a = 200$.

4.2.3 Modifications to Enzo and Grackle

Armed with the resolution and the final redshift required of the simulation, we attempt to evolve a simulation into the far future. However, initial results contained some peculiarities, particularly in the distribution of the temperature and density of the gas. As a result, we re-evaluated the ability of various components in `Enzo` and `Grackle` to evolve properly in the simulations. The choice of certain methods or values in the machinery proves to be insignificant for evolution up to $z = 0$, but their effects amplify in conditions experienced in the future. These include the interpolation of the UV background, values in the `CLOUDY` table and fail-safe features in `Grackle`.

UV background interpolation

The reionisation of the IGM is an essential event in cosmic structure formation and evolution. The IGM remains ionised because of the UV emission from AGN and stars. One of the most popular UV background models is the Haardt and Madau model obtained with `CUBA`. It is a radiative transfer code that

quantifies the propagation of Lyman-continuum photons through a partially ionised inhomogeneous IGM (Haardt & Madau, 1996). This UV background model has undergone several iterations as a result of the improvements in the quantity and quality of observations, and a better understanding of the relevant physics over the years.

Nagamine & Loeb (2004) implemented a uniform UV background radiation of a modified Haardt & Madau (1996) spectrum with complete reionization at $z \sim 6$ (Davé et al., 1999; Becker et al., 2001) in their simulation. Beyond $z = 0$, the authors linearly extrapolated the UV background in z, consistent with the extrapolated decline of cosmic star formation. This methodology ensures that the UV background approaches zero quickly. Similarly, any interpolation or extrapolation of the UV background is done linearly in `Enzo` by default. We choose to use an updated Haardt & Madau (2012) UV background model for our simulations. If we continue to use a linear extrapolation in z for this model, it reverses the photoheating rates for neutral atomic hydrogen (HI), neutral helium (HeI) and singly ionised helium (HeII) from a positive to a negative value at $z = -0.195$, $z = -0.201$ and $z = -0.232$ respectively. This transition means that instead of heating the IGM, the UV background will be cooling the IGM at the mentioned z for the various species. To avoid such a scenario, we modify the extrapolation scheme of the photoheating rates from linear to logarithmic in `Enzo`.

CLOUDY table

In our simulations, we apply the equilibrium cooling mode from `Grackle` (Smith et al., 2017), which uses the tabulated rates derived from the photoionisation code, `CLOUDY` (Ferland et al., 2013). It consists of heating and cooling rates as a function of density, temperature and redshift. When evolving a simulation into the future, the available `CLOUDY` table fails to account for two factors: heating and cooling rates into the future and significantly lower densities due to the expansion of the universe. Therefore, there is a need to revise and modify the `CLOUDY` table.

It is impossible in practice to obtain the cooling and heating rates in the future because the data from Haardt & Madau (2012) UV background model does not extend beyond $z = 0$. The only available approach is to extrapolate from the last two data points of heating and cooling rates in redshifts. However, this extrapolation assumes that it encompasses all behaviour beyond these data

points, leading to an increased likelihood of unphysical values as we extrapolate further into the future. Therefore, we assume that the heating rates reach zero at some arbitrary point time in the distant future ($z = -0.99999999$), allowing the cooling and heating rates to be interpolated between two defined points ($z = 0$ and $z = -0.99999999$). As discussed before, the intensity of the UV background is expected to decrease to zero in the far future because of the extrapolated decline in the global star formation rate (see Figure 1.7). However, we will show in Section 4.3.7 that our simulated cosmic star formation rate density (SFRD) does not match the analytic fit from Madau & Dickinson (2014) exactly. This discrepancy prompts the need for an iterative process between the SFRD and implemented UV background in order for them to match in the simulations. We will discuss this process in detail in Chapter 5.

There is another unrelated issue that we have to address illustrated by Figure 4.2 where we plot the original heating rates (Γ) with respect to temperature (T) at a fixed density and redshift in the `CLOUDY` table (blue line). Although the heating rates are stored as Γ, they are calculated from $\Gamma \times n_{\rm H}^2$ where $n_{\rm H}$ is the number density of H. In the far future when $n_{\rm H}$ is very low, this quantity is low enough that it suffers from underflow due to limited floating point precision. Since $n_{\rm H}$ does not reach such a small value at $z = 0$, the problem was not raised before. Using the lowest temperature deemed to not be significantly affected by round-off error, T_α in a density ρ_0 slice, we carry out a second order interpolation in logarithmic space to correct the heating rates for $T \geq T_\alpha$,

$$\begin{aligned}\Gamma(\rho_0, z, T \geq T_\alpha) = {\rm L0} \times \Gamma(\rho_1, z, T \geq T_\alpha) + {\rm L1} \times \Gamma(\rho_2, z, T \geq T_\alpha) \\ + {\rm L2} \times \Gamma(\rho_3, z, T \geq T_\alpha),\end{aligned} \tag{4.3}$$

where L0, L1 and L2 are Lagrange basis functions given by

$$\begin{aligned}{\rm L0} &= (\rho_0 - \rho_2)(\rho_0 - \rho_3)/(\rho_1 - \rho_2)(\rho_1 - \rho_3), \\ {\rm L1} &= (\rho_0 - \rho_1)(\rho_0 - \rho_3)/(\rho_2 - \rho_1)(\rho_2 - \rho_3), \\ {\rm L2} &= (\rho_0 - \rho_1)(\rho_0 - \rho_2)/(\rho_3 - \rho_1)(\rho_3 - \rho_2),\end{aligned}$$

with subscripts 1, 2 and 3 referring to the first, second and third sequentially higher density. This process corrects regions affected by underflow in a manner that preserves the density dependence of the rates as shown by the green line in Figure 4.2.

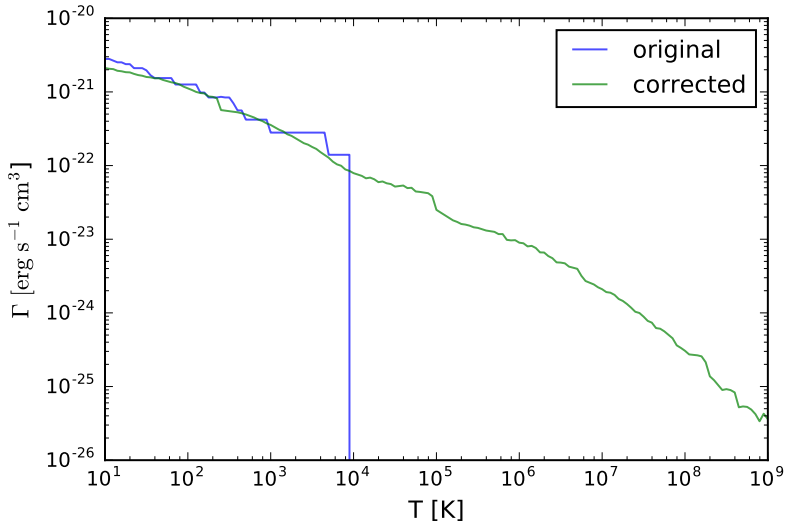

Figure 4.2 Graph of Γ with respect to T at a fixed density and z. The blue and green lines represent the heating rate with and without corrections respectively. The temperature range is much more extended with the corrections. In addition, the flat portions of the heating rate curve are removed, allowing for a more realistic interpolation. Refer to `CLOUDY` table under Section 4.2.3 for details about the corrections.

We carry out this correction iteratively starting from density slices of heating rates at a fixed redshift with the least amount of missing data points, i.e., from high to low density. Once we resolve the problem within the ρ_0 slice; we employ a slightly different process for the next density ρ_{-1} slice. We make use of the gradient

$$m = 0.5 \times \frac{\Gamma(\rho_1, z, T \geq T_\beta) - \Gamma(\rho_0, z, T \geq T_\beta)}{\rho_1 - \rho_0}, \tag{4.4}$$

where 0.5 is a factor to dampen the solution in order to better match the apparent density dependence, resulting in

$$\Gamma(\rho_{-1}, z, T \geq T_\beta) = m \times (\rho_{-1} - \rho_0) + \Gamma(\rho_0, z, T \geq T_\beta). \tag{4.5}$$

As mentioned previously, the temperature associated with the flat portion varies between density slices Therefore, we use T_β for the ρ_{-1} slice to differentiate it from the ρ_0 slice. The solution first fixes the slice with fewest missing data points, before moving to progressively harder cases. This entire process then repeats for different redshifts.

Grackle

There are measures in `Grackle` to prevent arithmetic underflow and round-off error, similar to other codes. In particular, round-off error occurs when the net change in internal energy is too small to be captured by the number of decimals of a floating point variable. For example, if X is recorded to 6 decimal places and $Y/X < 1 \times 10^{-6}$, then $X + Y$ will be equal to X. In the default setup, when the absolute change in internal energy is less than 10^{-20}, `Grackle` replaces this small change in internal energy with a small heating value, regardless of whether or not it was cooling or heating in the first instance. In typical simulations that complete at $z = 0$, this artificial heating is insignificant, and it was not appreciated at the outset that this small numerical patch could eventually come to dominate the results. However, the longer cooling times encountered in extremely low density gas in the future results in the conditions where this issue becomes important as we will discuss in Section 4.3.1.

We experiment with reducing the threshold value from 10^{-20} to 10^{-40} and setting the heating/cooling rate to zero instead of inserting the small heating value. We will elaborate in Section 4.3.1 that this solution is not perfect. While it resolves the issues associated with artificial heating, it introduces other numerical artefacts. In our follow-up attempt, we allow the gas to cool or heat accordingly, even if the absolute value is below the threshold. The effect of these changes on the gas in the simulations will be discussed in Section 4.3.1. In short, we simply remove the threshold and any corrections introduced because we did not find any occurrence of the round-off error.

In addition to the issues discussed above, `Grackle` also inserts a small heating value when gas in the cell is less than 1 K and still cooling. In the far future, 1 K is very close to the CMB temperature floor set in the simulations

$$T_{\rm CMB} = T_{\rm CMB,0}(1 + z), \tag{4.6}$$

where $T_{\rm CMB,0}$ is the CMB temperature at $z = 0$ ($\approx 2.725\,{\rm K}$). Therefore, to prevent the introduction of the heating term, we switch off the cooling and force the cold gas to remain at the CMB temperature according to Equation 4.6. Collectively, the modifications discussed thus far affect the evolution of the IGM most significantly. We will quantify and discuss how the different iterations of the suggested modifications influences the phase distribution in Section 4.3.1.

4.2.4 Analysis

Similar to Chapter 3, we identify haloes in the simulations with ROCKSTAR halo finder (Behroozi et al., 2013a). However, its capability to find haloes in simulations into the future has not been explored before. In the future, the 'freeze out' of the growth of large scale structures leads to a shut-down of merging processes, so that each halo evolves independently in isolation. This scenario means that the proper size of the halo remains constant, translating to a shrinking comoving size that poses a challenge to halo finding.

We show dark matter density projection plots of a 256^3 dark matter only run in a $100\,h^{-1}$Mpc with eight levels of AMR at $z = 5.0, 0.0, -0.5, -0.9$ in Figure 4.3. We annotate each projection plot with white circles to represent the haloes identified by ROCKSTAR. The number and comoving size of the haloes shrinks as the simulation evolves into the future. However, they are clustered around distinct regions, evident in Figure 4.3d. ROCKSTAR uses a minimum distance to classify haloes with centres less than this separation as noise or not. Should this threshold distance remain in the setup, ROCKSTAR will be tagging more haloes as noise in the far future, subjecting them to stricter removal tests than other haloes (Behroozi et al., 2013a). This minimum distance can, therefore, cause a discrepancy in the number of haloes located by ROCKSTAR, prompting us to set this distance to zero.

We explained in Chapter 2 that the force resolution in Enzo is twice the local spatial resolution. As the universe expands, the spatial resolution in the simulation is deteriorating as the grid cells are increasing to be of similar size to the haloes. The outcome is the loss of haloes as we see fewer circles in Figure 4.3 in the future and it will be further quantified with the evolution of the HMF in Section 4.3.5. As the simulation struggles to resolve the haloes, the ability of ROCKSTAR to identify and differentiate such haloes will be tested.

Parallelisation is a possible option in ROCKSTAR. It splits up the entire computational domain into smaller ones according to the number of processors assigned. To preserve accuracy, ROCKSTAR introduces buffer zones between the domains. In the future, the accelerating expansion of the universe causes the buffer zone size to be comparable to the halo's comoving size, leading to potential errors in the identification and tracking of the halo merger history. Whenever a halo crosses this buffer zone, the merger history becomes disjointed because it

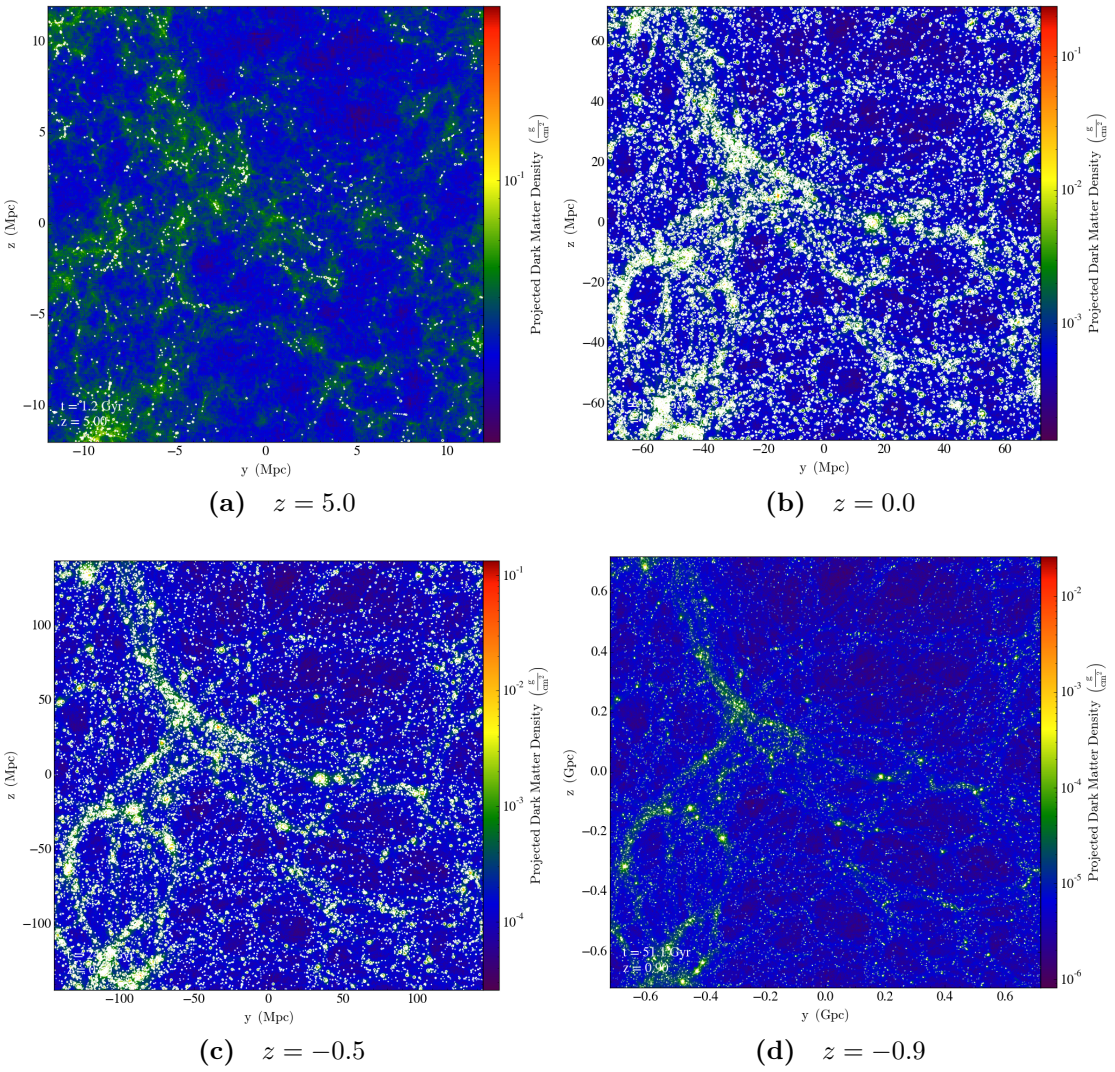

(a) $z = 5.0$ **(b)** $z = 0.0$

(c) $z = -0.5$ **(d)** $z = -0.9$

Figure 4.3 Dark matter density projection plot with annotated haloes (white circles) at redshifts indicated by the captions. As the simulation evolves further into the future, the circles get smaller because the comoving sizes of the haloes are decreasing. The force resolution in the simulation is also deteriorating into the future, affecting the ability to resolve a halo. The poor resolution causes the loss of haloes, explaining the diminishing number of white circles into the future. These physical and numerical issues pose a challenge for halo finding into the future.

does not transfer across domains. To ROCKSTAR, the halo appears out of nowhere in the 'new' domain, starting a new merger record. Zoom simulations complicate the issue because they positions the halo of interest in the centre of the simulation box, coinciding with the location of the buffer zone. Hence, we choose to use one processor to identify haloes in the entire cosmological box, eliminating the use of a buffer zone. We will support this choice with quantitative results in Section 4.3.2. The use of one processor for the entire simulation domain is a necessary

trade-off between speed and accuracy. We then carry out analysis of the results from the simulations and halo finding with the `yt` analysis toolkit (Turk et al., 2011).

4.3 Results and discussion

From the tests and comparison discussed in previous sections, we have completed the setup to simulate into the future. In the following sections, we will present and discuss the evolution of various properties of the gas and dark matter in the simulations. These include iterations of the changes described in Section 4.2 and comparisons to previous works. We will first focus on the simulation referenced *NL* before extending the study to six other simulations of varying spatial and mass resolution and feedback prescription. The specifications of these simulations can be found in Table 4.1. Lastly, we compare the results from the large box simulations with the zoom simulation described in Chapter 3 into the future.

4.3.1 Gas phase changes due to modifications to Grackle

In Section 4.2.3, we described the sequence of modifications to the simulation necessary for evolving into the future. In this section, we justify this series of changes by analysing the distribution of gas temperature and density at each stage of iteration. Primarily, we look at these phase distributions at $z = -0.99$ or $t \approx 7\,t_{\rm H}$. It is important to note that we have already implemented the changes to the UV background extrapolation and `CLOUDY` table.

The original behaviour of `Grackle` specifies the insertion of a small heating value whenever the absolute change in internal energy is less than 10^{-20}. Although insignificant at $z = 0$, this small artificial heating value can become significant in the far future. In Figure 4.4, which shows the distribution of gas mass in bins of density and temperature at $z = -0.99$, we can identify an unphysical relation on the left of the plot. At this point in time in the simulation, this inverse relation affects gas to relatively high overdensity. Therefore, we use this z as a reference point for comparison for subsequent modifications that we make to code, Prior to this redshift, especially at $z > 0$, the phase distributions are identical regardless of modifications to the code. This inverse relation arises from the heating term associated with the measures to prevent the round-off error.

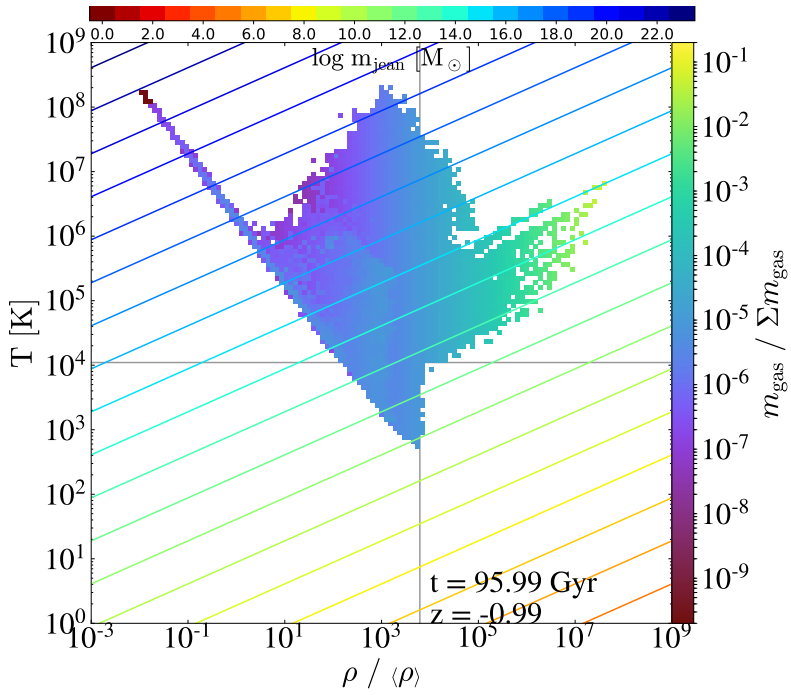

Figure 4.4 Gas mass in bins of overdensity and temperature in the simulation volume at $z = -0.99$. We have included diagonal lines of constant Jeans mass of the gas according to its temperature and baryon overdensity. The colour of these lines corresponds to a value indicated by the colour bar at the top of the figure. The horizontal and vertical lines are the specified threshold baryon overdensity and temperature required for star formation in the simulations. In other words, gas in the bottom right region can potentially form stars if all other criteria described in Section 3.2.1 are fulfilled. We identify an unphysical inverse relation of temperature to baryon overdensity (left region) and attribute it to the artificial heating inserted by `Grackle`. For more discussion, refer to Section 4.3.1.

Based on this relation, the most underdense gas in the IGM of the simulation heats up to 10^8 K. There is no physical explanation for this value because the fast expansion rate and practically zero UV background at this time should result in a much colder IGM. Hence, we looked at `Grackle` in more detail and identified this artificial heating as the root of the problem.

To obtain a more realistic evolution, we remove this heat source and instead, set the heating/cooling value to zero when the change in internal energy drops below the threshold. We also lower the threshold value that triggers it from 10^{-20} to 10^{-40}. The outcome of these changes is illustrated in Figure 4.5, plotted in an identical way to Figure 4.4. Since we remove the source of heating, the inverse relation is now absent. However, multiple horizontal lines of constant temperature ($T \approx 1.01,\ 2 \times 10^2,\ 10^5$ K) are introduced in the phase distribution.

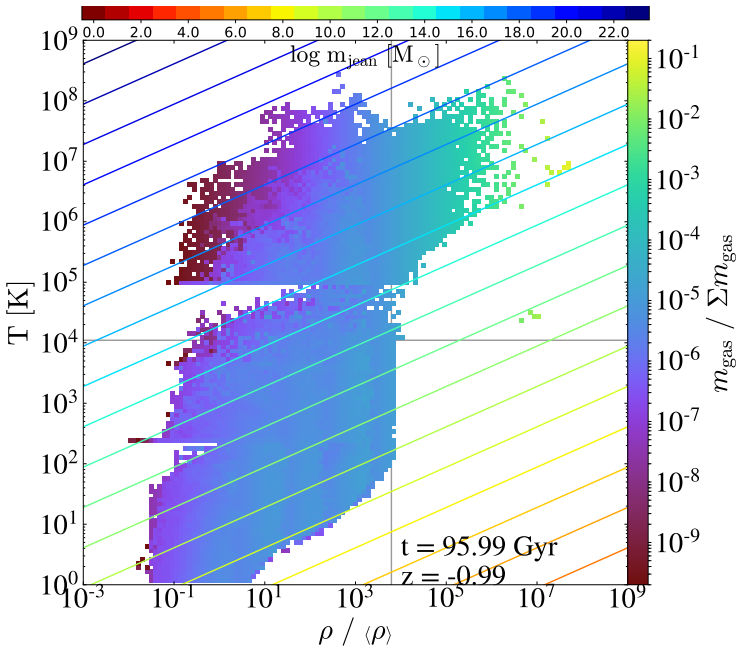

Figure 4.5 Similar to Figure 4.4 but instead of inserting a small heating value, we set the heating/cooling rate to zero when the absolute change in internal energy is less than 10^{-40}. This threshold value is lowered from the previous value of 10^{-20}. We get unphysical horizontal lines of constant temperature and unfilled region of phase space below these lines with these modifications, indicating the incompleteness of this approach.

These lines indicate a zero change in internal energy. The line at 1.01 K can be easily explained by the CMB temperature floor set in the simulations. When the gas temperature hits the floor, we force `Grackle` to set the change in internal energy to zero as described in Section 4.2.3. The other horizontal lines are the result of preventing any cooling or heating of the gas when the absolute change in internal energy is less than 10^{-40}. For gas just above or below the plateaus, it can heat up and cool down according to its change in internal energy, allowing it to either move away or towards and get stuck on the plateau. In the time evolution of the phase distribution, we see that the space below the horizontal lines opens up from low to high overdensity, from higher to lower temperature. This evolution suggests that the gas is cooling before it hits the threshold value. While it is an interesting feature, the most important conclusion drawn from Figure 4.5 is that the implemented solution still contains flaws.

Since setting the change in internal energy to zero results in these horizontal lines, we remove this condition altogether. In this iteration, we remove any notion of a threshold entirely. From Figure 4.6, we see that this solution does not create

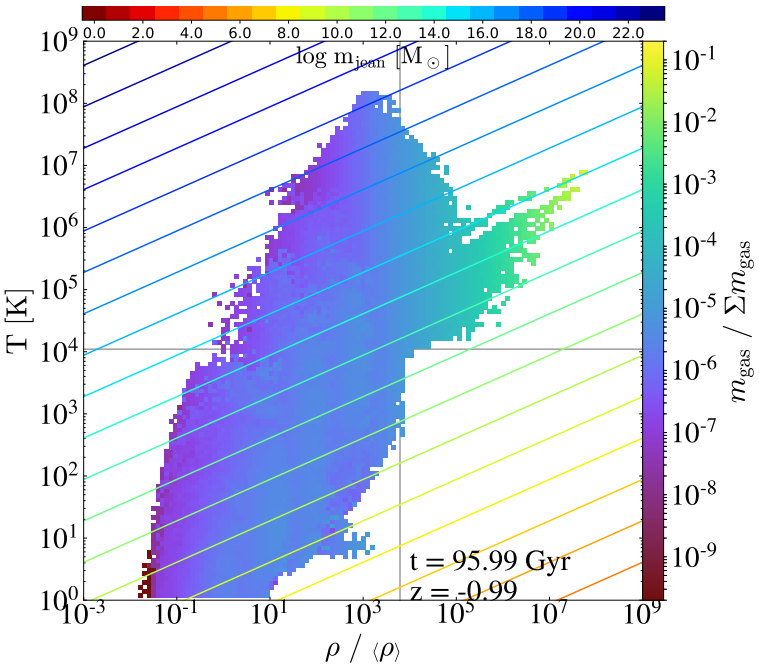

Figure 4.6 Similar to Figures 4.4 and 4.5 but with no attempt to catch round-off errors. This final iteration of the modifications results in a reasonable looking phase distribution at $z = -0.99$.

any obvious numerical artefacts. Through a couple of iterations, we have results that we believe to contain minimal unphysical features. We will present further details of the evolution of the IGM into the future and make comparisons with Nagamine & Loeb (2004) in the following sections.

4.3.2 ROCKSTAR halo finding into the future

The main goal of this Chapter is to understand the evolution of a universe into the future. To achieve this aim, we have verified that we can simulate the properties of the gas in the diffuse environment into the future realistically. We will now look at the other critical component: haloes. If we want to be able to continue distinguishing between IGM and halo material, we need to know where the haloes are, and hence the halo finder needs to be capable of identifying haloes.

In order to test the capability of `ROCKSTAR`, we created an idealised halo catalogue by placing isolated haloes on a uniform grid. They are sampled from the Sheth-Tormen halo mass function (HMF) (Sheth & Tormen, 2002). Each halo is endowed with a truncated Navarro-White-Frenk (NFW) density profile (Navarro et al., 1996), sampled randomly by particles, down to a mass limit of two particles

at three different redshifts ($z = 0, -0.5, -0.9$), resolving the haloes by at least two particles. This number is much lower than the minimum number of particles required by ROCKSTAR to classify them as gravitationally bound haloes. We thus expect a cut-off in the number of haloes identified because of this limitation of ROCKSTAR. Each redshift contains the same distribution of haloes. However, we shrink the comoving virial radii of the haloes to replicate the effect of the expanding universe explained in Section 4.2.4. We then input the positions and velocities of these dark matter particles into ROCKSTAR, experimenting with both single and multiple processors setup. We also repeat the halo finding with each setup five times to quantify the variation between each run, as ROCKSTAR has some explicitly non-deterministic features.

Figure 4.7 illustrates a comparison between the HMF from the ROCKSTAR halo catalogues (blue) and the mock catalogues (orange) at different redshifts. The agreement is remarkable across all redshifts. On the high mass end, we can recover a one to one mapping of the 40 most massive haloes, above a virial mass of $1.4 \times 10^{13}\, h^{-1}\mathrm{M}_{\odot}$ at $z = -0.9$ with similar numbers at other redshifts. However, in the intermediate mass range ($1.5 \times 10^{11}\, h^{-1}\mathrm{M}_{\odot} < m_{\mathrm{vir}} < 10^{12}\, h^{-1}\mathrm{M}_{\odot}$), ROCKSTAR slightly overestimates the number of haloes, most apparent in panels (b) and (c). This result is surprising considering that the haloes are isolated, eliminating the possibility of the clutering of the haloes in the future causing ROCKSTAR to combine two or more low mass haloes close to each other into one larger mass halo. This discrepancy requires further exploring but the level of agreement displayed in Figure 4.7 shows that ROCKSTAR is capable of accurately identifying haloes in the far future.

We also repeat the halo finding five times using the single and multiple processors setup. For the latter, We split the simulation box into two and assign two processors to each computational domain to locate and identify haloes. This setup involves a total of seven processors with six of them finding haloes and one master processor. A single processor setup is straightforward with one processor handling all processes. We consistently obtain an identical total number of haloes across all five runs with a single processor. However, we get two different numbers within the five repeats at each redshift with multiple processors. One of these numbers is consistent with the single processor setup while the other is always smaller. We repeat the exercise again at a different time but obtain results that are consistent across the different setups. This anomaly led us to believe it is a hardware related issue. Even though we cannot replicate the issue consistently,

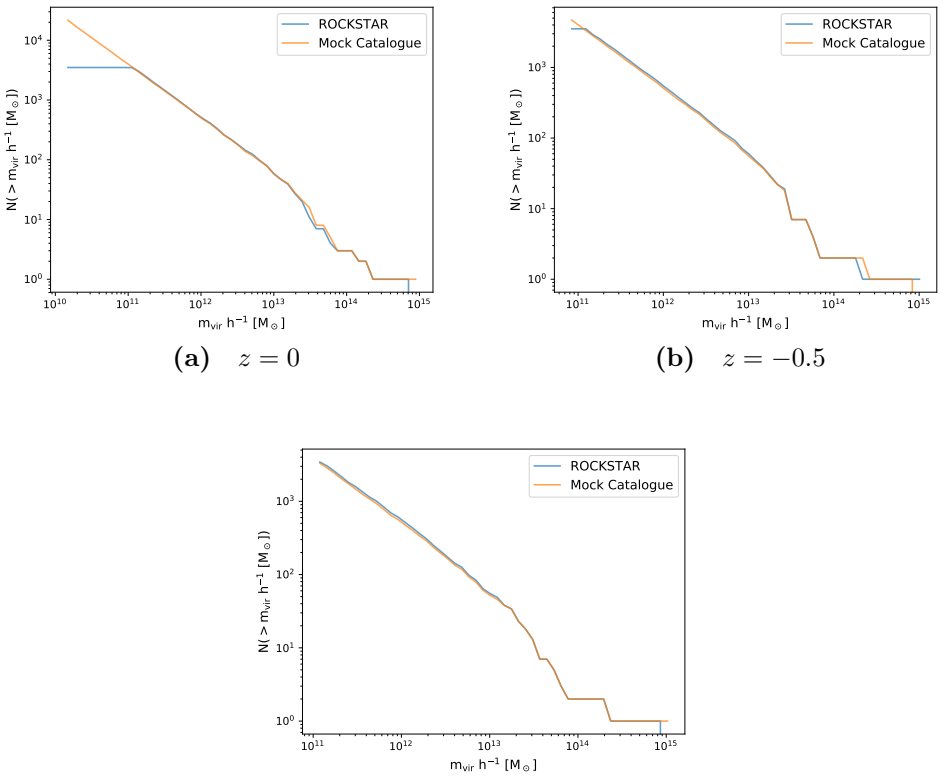

(a) $z = 0$ **(b)** $z = -0.5$

(c) $z = -0.9$

Figure 4.7 Cumulative number of haloes above a specified virial mass at three different z indicated in the captions. The blue and orange lines represent the numbers obtained from `ROCKSTAR` and our mock catalogue respectively. There is a consistent deviation on the low mass end and agreement on the high mass end across the redshifts. Refer to Section 4.3.2 for more detail.

we will use a single processor for halo finding in our simulations to prevent any potential error. The cause of the differences described in this section should be explored in greater detail in future work. Moving forward, we will investigate how the HMF within our simulation evolves into the future in Section 4.3.5.

4.3.3 Evolution of the gas phase distribution into the future

Convinced that the modifications to `Grackle` corrected the code for the evolution into the future, we can begin analysing various aspects of the simulation. We first look at the gas density projection plot of a slice with a comoving thickness of $10\,h^{-1}$Mpc and a comoving width of $50\,h^{-1}$Mpc in Figure 4.8. Starting from panel (b), we notice a lack of large scale structure evolution that is consistent with the prediction of 'freeze out' within $2\,t_{\rm H}$ past $z = 0$ (Nagamine & Loeb,

2004; Salcido et al., 2018). From this point of time, haloes evolve in isolation.

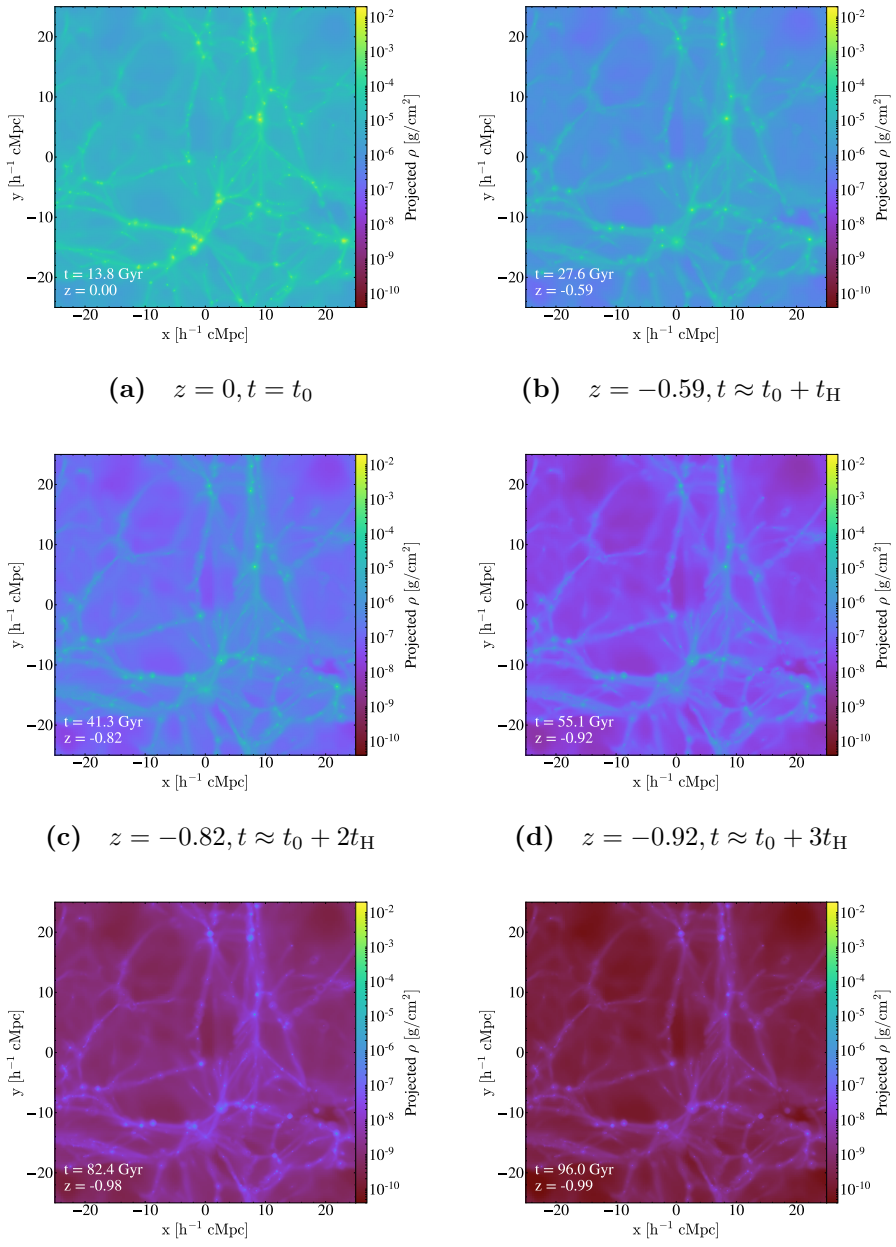

(a) $z = 0, t = t_0$ **(b)** $z = -0.59, t \approx t_0 + t_\mathrm{H}$

(c) $z = -0.82, t \approx t_0 + 2t_\mathrm{H}$ **(d)** $z = -0.92, t \approx t_0 + 3t_\mathrm{H}$

(e) $z = -0.98, t \approx t_0 + 5t_\mathrm{H}$ **(f)** $z = -0.99, t \approx t_0 + 6t_\mathrm{H}$

Figure 4.8 Density projection plots of a slice with a comoving thickness of $10\,h^{-1}$Mpc and a comoving width of $50\,h^{-1}$Mpc at the z and t indicated in the captions. As the simulation evolves into the future, large scale structures growth 'freezes out'. This phenomenon explains the high level of similarity of the plots, especially at late times. As the universe evolves, the filaments lose mass to the haloes. This mass transfer causes the density of filaments to become comparable to the background while the haloes can maintain their density contrast.

We then look at the mass-weighted temperature projection plot of an identical slice in Figure 4.9. The filaments cool from $T \approx 10^7\,\mathrm{K}$ at $z = 0$ to $T \approx 10^4\,\mathrm{K}$ at $z = -0.92$ before reaching the background temperature of $T \approx 10^2\,\mathrm{K}$ at $z = -0.99$. This temperature drop is most likely due to the adiabatic cooling from the expansion of the universe. The virialised dark matter haloes with $T > 10^4\,\mathrm{K}$ become increasingly isolated within the cold IGM. They are represented by small, brightly coloured dots, particularly in panels (e) and (f). These dots are a physical representation of their shrinking comoving size as the universe evolves into the future.

Lastly, we look at the combined evolution of these gas properties with the phase distribution in Figure 4.10. Similar to before, each panel corresponds to the same panel in Figures 4.8 and 4.9 at an identical time. We can split up the phase distribution into four quadrants with the lines of threshold density and temperature for star formation in the simulation. The bottom left quadrant contains gas of low overdensity and low temperature, which constitutes the IGM. We will investigate its evolution in greater detail in Section 4.3.6. The gas that has cooled radiatively inside dark matter haloes occupies the bottom right quadrant. However, there is an absence of gas in this region because it has been converted to stars according to the star formation criteria specified in the simulation. Lastly, we combine the upper left and right quadrant and classify gas in this region as hot gas. It consists of the warm-hot intergalactic medium (Cen & Ostriker, 1999) and hot dense gas in massive haloes. This separation of the phase space is consistent with the definitions used in Davé et al. (2001).

As the universe evolves into the future, the phase distribution elongates diagonally. The extremely long cooling time of the hot gas with $\mathrm{T} = 10^{7.5}\,\mathrm{K}$ and overdensity of 200 at $z = 0$ is the cause of this elongation. In this regime, the dominant cooling mechanism is Bremsstrahlung, which has a long cooling time that keeps the gas hot in the future (Nagamine & Loeb, 2004). It is important to note that gas at a constant overdensity corresponds to a lower ρ because $\langle\rho\rangle$ decreases into the future. Therefore, the feedback from galaxies is injected into gas of decreasing density as the simulation evolves into the future. If the same amount of thermal energy is injected into lower density gas, the resulting temperature will be higher, resulting in a second temperature peak ($\mathrm{T} \approx 10^8\,\mathrm{K}$) in gas of intermediate overdensity around 10^3. At $z = -0.98$, adiabatic cooling due to the expansion of the universe begins to cause some gas to hit the temperature floor given by Equation 4.6. Gas of higher density is able to reach the CMB

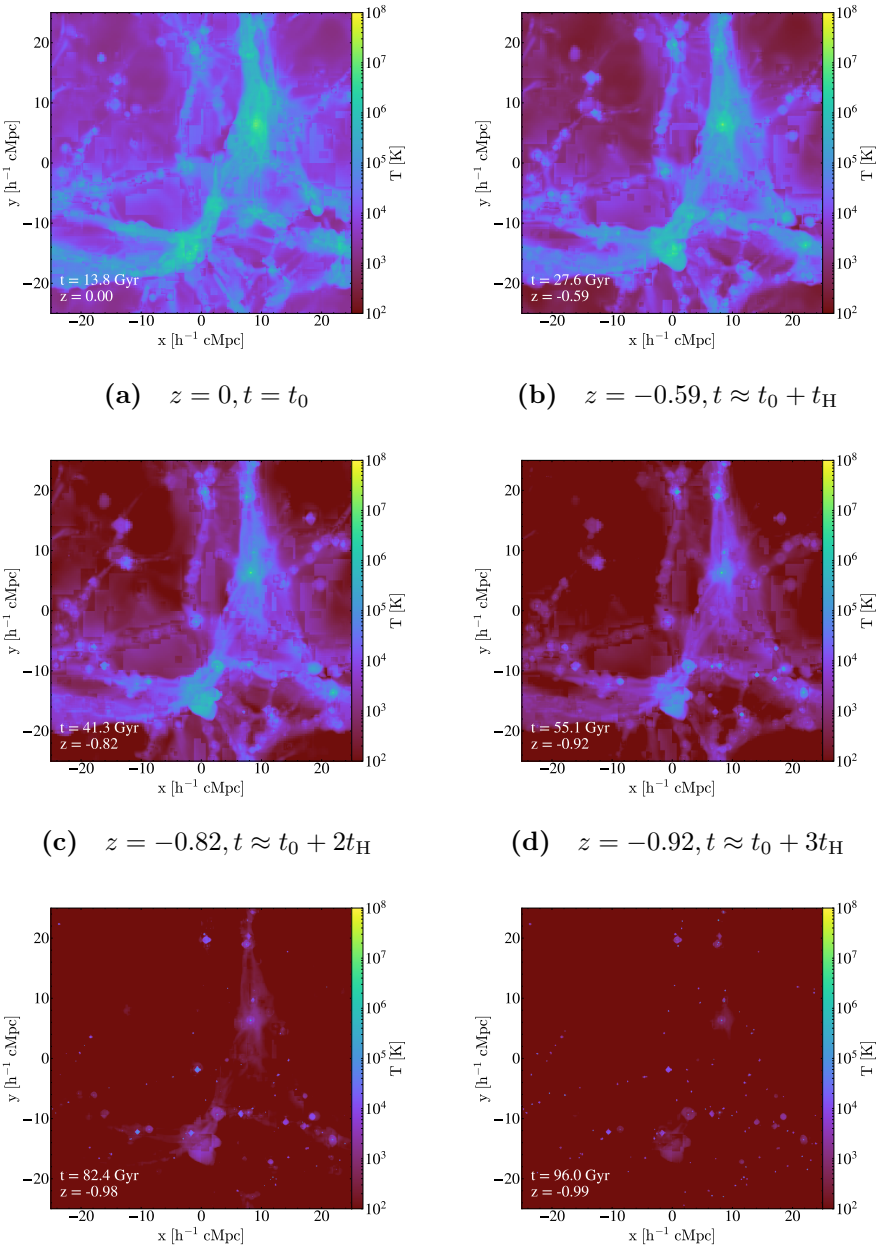

(a) $z = 0, t = t_0$ **(b)** $z = -0.59, t \approx t_0 + t_{\rm H}$

(c) $z = -0.82, t \approx t_0 + 2t_{\rm H}$ **(d)** $z = -0.92, t \approx t_0 + 3t_{\rm H}$

(e) $z = -0.98, t \approx t_0 + 5t_{\rm H}$ **(f)** $z = -0.99, t \approx t_0 + 6t_{\rm H}$

Figure 4.9 Mass-weighted temperature projection plot of an identical slice as Figure 4.8. As the simulation evolves into the future, the gas in the filaments cools and reaches an equilibrium with the background temperature. On the other hand, the haloes become hotter and their sizes shrink to small dots in the plots.

temperature, affecting the equation of state of the IGM, which we will discuss in Section 4.3.6.

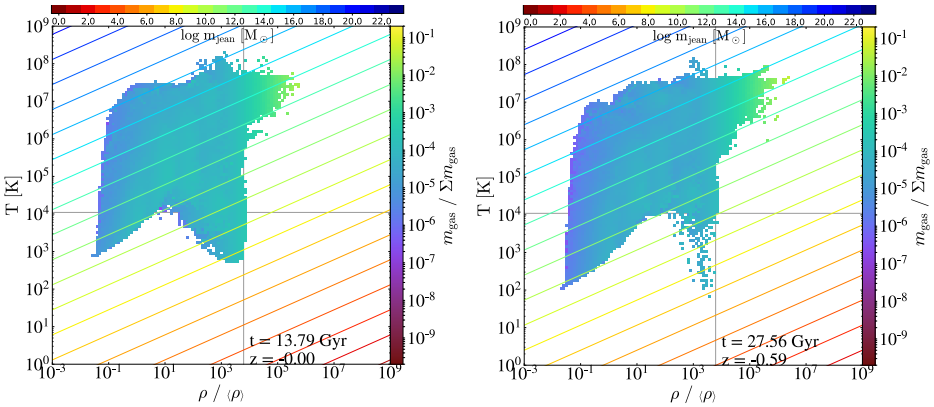

(a) $z = 0, t = t_0$

(b) $z = -0.59, t \approx t_0 + t_\mathrm{H}$

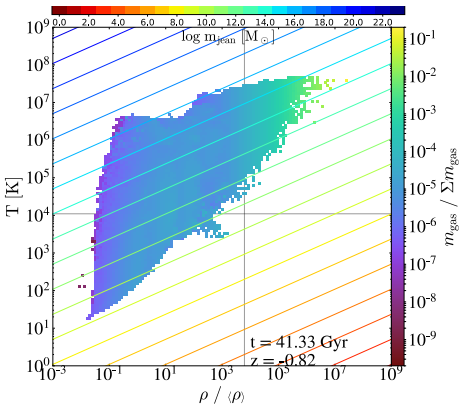

(c) $z = -0.82, t \approx t_0 + 2t_\mathrm{H}$

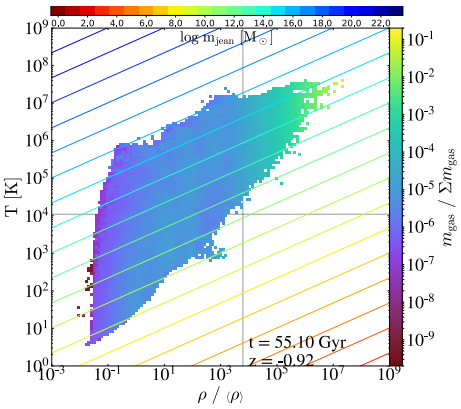

(d) $z = -0.92, t \approx t_0 + 3t_\mathrm{H}$

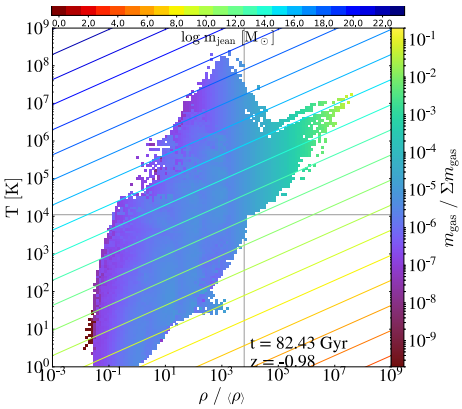

(e) $z = -0.98, t \approx t_0 + 5t_\mathrm{H}$

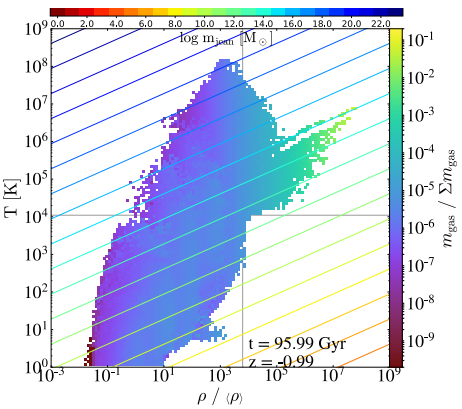

(f) $z = -0.99, t \approx t_0 + 6t_\mathrm{H}$

Figure 4.10 Gas mass in bins of overdensity and temperature of the gas at the z and t indicated in the captions. Individual panels include features such as the lines of constant Jeans mass that are identical to Figures 4.4, 4.5 and 4.6. Refer to Section 4.3.3 for description.

4.3.4 Comparison to previous work

Nagamine & Loeb (2004) performed an analysis similar to the one in Section 4.3.3 with a `GADGET` simulation into the future. We explained in Section 4.2.1

that the resolution of our simulation is comparable to this GADGET simulation. This similarity allows the exclusion of resolution disparities as the cause for any discrepancies in the results. The main differences between the simulations lie in the methodology of the simulation code and implementation of the baryonic processes. Taking these factors into account, we will compare the evolution of the phase distribution in Figure 4.10 to Figure 3 of Nagamine & Loeb (2004) shown in Figure 4.11.

There is a similar elongation in phase space occupied by the gas into the future in both simulations. We have discussed the reasons for this evolution in Section 4.3.3. We also observe a similar peak in gas mass at high overdensities ($> 10^5$) and temperature ($> 10^6\,\mathrm{K}$) in both figures. Despite the general agreement, there are specific differences present in the figures. They arise mainly due to the star formation and feedback prescriptions in the simulations. See Nagamine et al. (2004) for detailed descriptions of the star formation and feedback prescription used in Nagamine & Loeb (2004). An island of gas in haloes with $T \approx 10^4\,\mathrm{K}$ and $\log \rho / \langle \rho \rangle > 6$ in Figure 3 of Nagamine & Loeb (2004) is absent in Figure 4.10. This disparity arises because of the difference in the star formation criteria. In our simulation, gas is converted into stars when $\log \rho / \langle \rho \rangle > 4$, indicated by the vertical line in each panel of Figure 4.10. This threshold is lower than the comoving baryon overdensity of 7.7×10^5 at $z = 0$ used by Nagamine & Loeb (2004). Therefore, all the gas supposedly inhabiting this island in phase space is turned into stars in our simulation.

On top of the star formation criteria, the feedback prescription also differs between the simulations. The amount of feedback energy injected per solar mass of stars in our simulation is approximately an order of magnitude higher than $4 \times 10^{48}\,\mathrm{ergs\,M_\odot^{-1}}$ in Nagamine & Loeb (2004). This difference means that the gas in the haloes of our simulation is heated to a higher temperature and likely propagates further into the IGM. We note the overdensity corresponding to gas in haloes in our simulation is lower because the feedback is stronger and pushes the gas away from the centre of the haloes.

Although there are differences in the specific details of the evolution of the phase distribution, the general trend agrees between both simulations. Nagamine & Loeb (2004) claimed that the results obtained are dominated by gravitationally-induced shocks and insensitive to the exact UV background, star formation and feedback model. The comparison we have made thus far supports it to a certain extent, dependent on the scale that is of interest. We are now going to expand

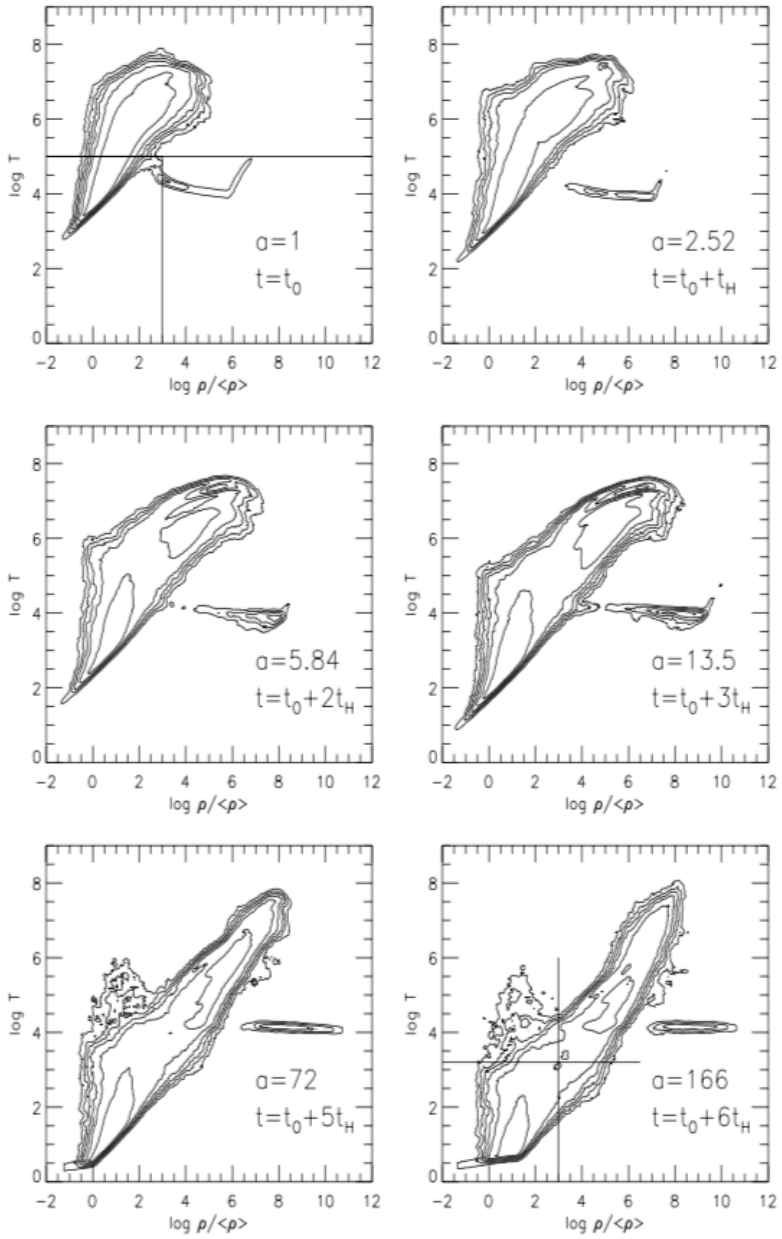

Figure 4.11 Evolution of the phase distribution with z into the future adapated from Figure 3 of Nagamine & Loeb (2004). The time and redshift in each panel correspond to those in Figure 4.10 and the six contours represent equally spaced mass bins between the minimum and maximum value of the gas mass distribution in logarithmic intervals. The vertical and horizontal lines are used to separate the gas according to the definitions used in Davé et al. (2001). See Section 4.3.4 for comparisons with our results.

on the convergence of the results obtained by analysing other aspects that is previously unexplored in Nagamine & Loeb (2004). These include the halo mass function (HMF), equation of state of the IGM, star formation rate density (SFRD) and resolution convergence of these properties.

4.3.5 The future of the halo mass function

We have investigated the ability of ROCKSTAR to locate haloes in an ideal environment where they are isolated (see Section 4.3.2). In this section, we wish to extend this study to a realistic cosmological simulation. We illustrate this evolution out to $z = -0.99$ in Figure 4.12. From $z = 0$ to $z = -0.92$, we believe that ROCKSTAR is locating and identifying haloes reliably over the entire halo mass range. The previously discussed period of 'freeze out' occurs within this period at $z \approx -0.6$. As a consequence, the HMF in the figure displays a lack of significant evolution from $z = -0.59$ to $z = -0.92$ between $8\times10^{13}\,M_{\odot} \leq \mathrm{m_{vir}} \leq 5\times10^{14}\,M_{\odot}$, giving us confidence in the results within this range. We also find an increasing deviation on the low mass end of the HMF due to worsening force resolution of the simulation as it progresses into the future. The impact is most apparent at low masses because these haloes are comparable in radius to the grid cell size.

At $z = -0.98$, there is a drastic drop in the number of haloes across the whole mass range. At the same time, the most massive halo in the simulation decrease in mass down to $\sim 2\times10^{14}\,M_{\odot}$. This trend continues to $z = -0.99$ where the effect is so significant that it causes orders of magnitude difference over the full mass range. We view this as a propagation of the poor force resolution from the low to high mass haloes. By comparing the position of the most massive halo at each redshift, we find the halo is in close proximity to its previously known location. However, it is losing mass, starting at $z = -0.92$ because of the loss of subhaloes in the main halo. The number of subhaloes within the most massive halo decreases from 18 to zero between 'freeze out' and $z = -0.99$ This explanation can be further verified by the virial radius of the most massive halo at different times. If we compare the size of the most massive halo, it is approximately an order of magnitude smaller at $z = -0.99$ ($2.964\,h^{-1}$ ckpc) than at $z = -0.98$ ($21.826\,h^{-1}$ ckpc). We have thus shown that caution should be taken when examining the state of the simulation in the distant future. Despite the overall reasonable appearance of the large-scale structure, the simulation loses its ability to properly resolve haloes. The experiment in Section 4.3.2 does not

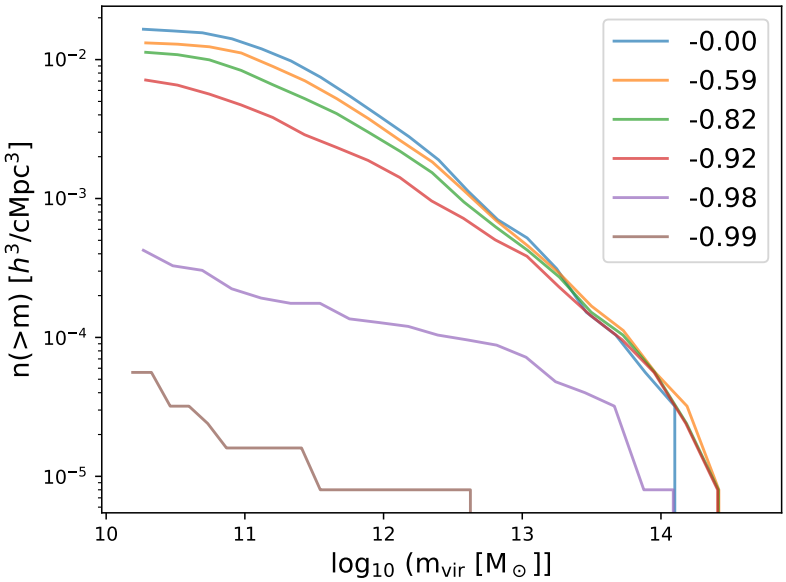

Figure 4.12 Evolution of the HMF with z into the future. The lines are coloured according to their respective z shown in the legend. The time interval between the lines is approximately one Hubble time, $t_H \approx 13.7\,\mathrm{Gyr}$. Refer to Section 4.3.5 for discussion.

capture this effect because the haloes were generated artificially.

4.3.6 The future of the intergalactic medium

In this section, we turn our attention to the evolution of the IGM itself. We focus mainly on the phase distribution of gas, defining IGM material as having an overdensity less than 10^3 (Davé et al., 2001). Hui & Gnedin (1997) found that low density gas (overdensity < 5) in the IGM could be characterised by

$$T = T_0(1+\delta)^{\gamma-1}, \tag{4.7}$$

where T_0 is the temperature at cosmic mean density, $\delta = \rho/\langle\rho\rangle - 1$ is the gas overdensity and γ is the sensitivity of the gas temperature to its overdensity. This fitted power law is added in the form of a diagonal black line at low overdensities to Figure 4.10, resulting in Figure 4.13. Also, we remove all gas within r_{vir} of any halo in the latter figure.

Before we look at how the IGM evolves into the future, it is interesting to note that the phase distribution at late times contains gas with overdensity

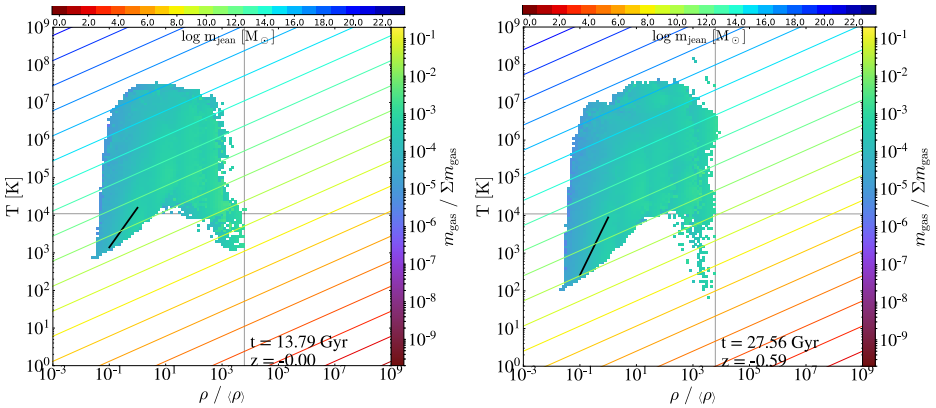

(a) $z = 0, t = t_0$

(b) $z = -0.59, t \approx t_0 + t_\mathrm{H}$

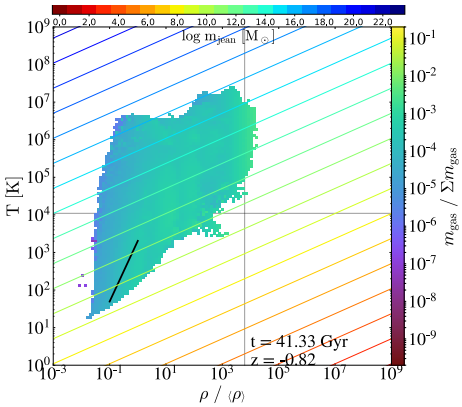

(c) $z = -0.82, t \approx t_0 + 2t_\mathrm{H}$

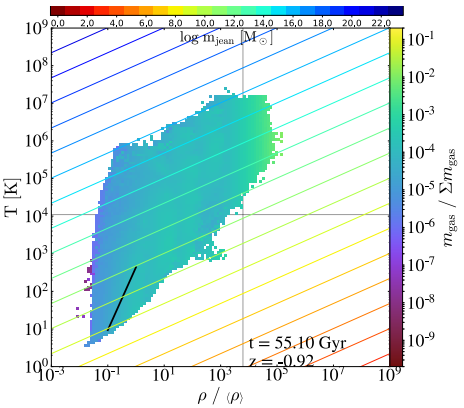

(d) $z = -0.92, t \approx t_0 + 3t_\mathrm{H}$

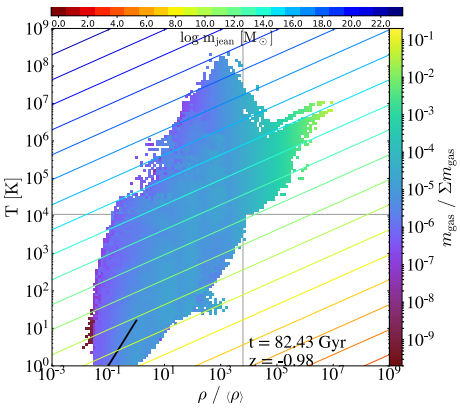

(e) $z = -0.98, t \approx t_0 + 5t_\mathrm{H}$

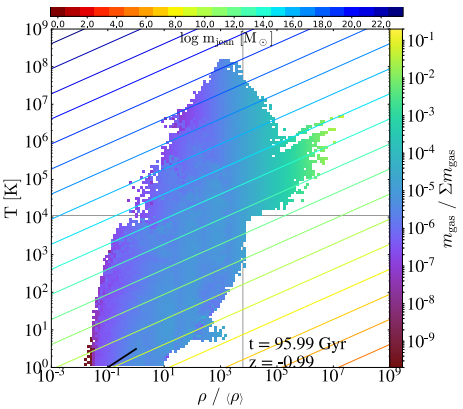

(f) $z = -0.99, t \approx t_0 + 6t_\mathrm{H}$

Figure 4.13 Similar to Figure 4.10 but considering only gas outside haloes. We add a black diagonal line to represent the best-fit equation of state of the IGM given by Equation 4.7. The black lines do not appear to be very good fits because I am plotting the mass instead of the volume of the gas. However, as we will see in Figure 4.15, the fits are better with the gas volume. Refer to Section 4.3.6 for discussion on the evolution of the IGM.

above 6×10^3. Such gas should reside within the haloes and should be excluded

from the plot. This is additional evidence that `Enzo` is failing to resolve low mass haloes. Since we fit the power law to much lower overdensity, these issues do not impact the evolution of the equation of state of this component of the IGM. We fit Equation 4.7 using two bins of grid cells with a width of 5% centred around gas overdensities of 10^{-1} and 10^{0}, consistent with previous work (Puchwein et al., 2015; Sorini et al., 2018). We then calculate the volume-weighted median temperature around these values and construct the best-fit power law.

We first compare our fit with previous results at $z \approx 2.5$ from Sorini et al. (2018). The authors presented results from both a Nyx simulation (Almgren et al., 2013; Lukić et al., 2015) and the Illustris simulation (Vogelsberger et al., 2014). The paramters obtained from fitting Equation 4.7 are $\log_{10} T_0 = 4.01$ and $\gamma = 1.57$ at $z = 2.4$ for Nyx and $\log_{10} T_0 = 4.12$ and $\gamma = 1.6$ at $z = 2.44$ for Illustris. These agree well with the values from our simulation, which are $\log_{10} T_0 = 4.21$ and $\gamma = 1.58$ at $z = 2.55$. They are also consistent with observational constraints from Schaye et al. (2000), where $\log_{10} T_0 \approx 4.20$ and $\gamma \approx 1.2$ at $z = 2.5$. Deviations in these values can arise due to the differences in the assumed UV background assumed (Oñorbe et al., 2017). However, for the purpose of this section, we have established the general agreement with other works.

The next step involves investigating how the values of $\log_{10} T_0$ and γ change into the future. We show the evolution of these parameters in Figure 4.14. We have included a visual fit to Figure 3 in Nagamine & Loeb (2004) as dots in Figure 4.14. The median temperatures and the resulting $\log_{10} T_0$ and γ from our simulation are insensitive to whether we use a volume-weighted or mass-weighted median. The evolution suggests a consistent drop in $\log_{10} T_0$ beyond $z = 0$ across both simulations. As discussed before, the expansion of the universe drives an increasing amount of gas towards the CMB temperature. Figure 4.13 points out the overdensity associated with this gas increasing with time, eventually encompassing the values used to derive γ by $1 + z \approx 0.01$. At this time, γ approaches a value of unity because the median temperatures of the gas within the overdensity bins are at the CMB temperature.

Before γ decreases drastically to a value of unity, Figure 4.14 shows that γ is slowly increasing between $4.0 \leq 1 + z \leq 0.02$. McQuinn & Upton Sanderbeck (2016) pointed out that the balance of the photoheating from the UV background and the cooling due to the cosmological expansion creates a tight relation between the temperature and density of the IGM at early times. Other processes such as Compton cooling off the CMB also shaped this relation, albeit in a minor

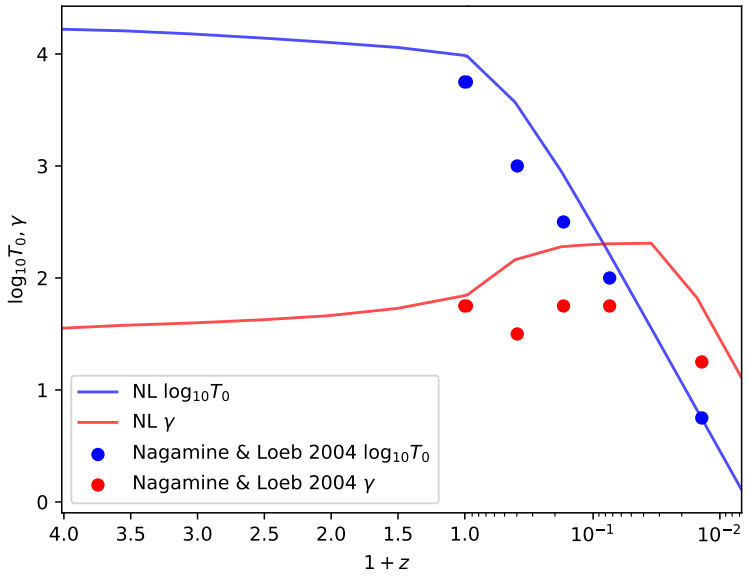

Figure 4.14 Evolution of the properties of the IGM, linearly for $z \geq 0$ and logarithmically for $z < 0$. The lines and dots are results from our and Nagamine & Loeb (2004)'s simulation respectively. Blue and red colour refers to $\log_{10} T_0$ and γ from Equation 4.7 respectively. Refer to Section 4.3.6 for discussion.

role. What happens in the future? Following our assumptions, the extrapolated heating from the UV background decreases to zero and the adiabatic cooling rate is increased due to the expansion of the universe. Together with the increase in the shocked fraction of gas with decreasing z (McQuinn & Upton Sanderbeck, 2016), these factors create deviations in the previously tight relation. We also show that the variance in temperature distribution of the gas within these overdensity bins is increased into the future in Figure 4.15.

Lastly, we note that the decline of T_0 begins at $z \approx 0$. It suggests that the IGM is currently at a delicate balance with just enough photons to remain ionised. Radiation from stars and AGNs that contribute to the UV background are no longer sufficient to keep the universe ionised. If this is the case, it adds another case study to the cosmological 'coincidence problem' of why is the present a unique point in the evolution of the universe. Since the star formation rate peaked at $z \approx 2$ and has declined since then, the strength of the UV background is dropping. The accelerating expansion of the universe balances this radiation. Consider scenarios that star formation rates peak at different times; this decrease in T_0 might not begin at $z \approx 0$.

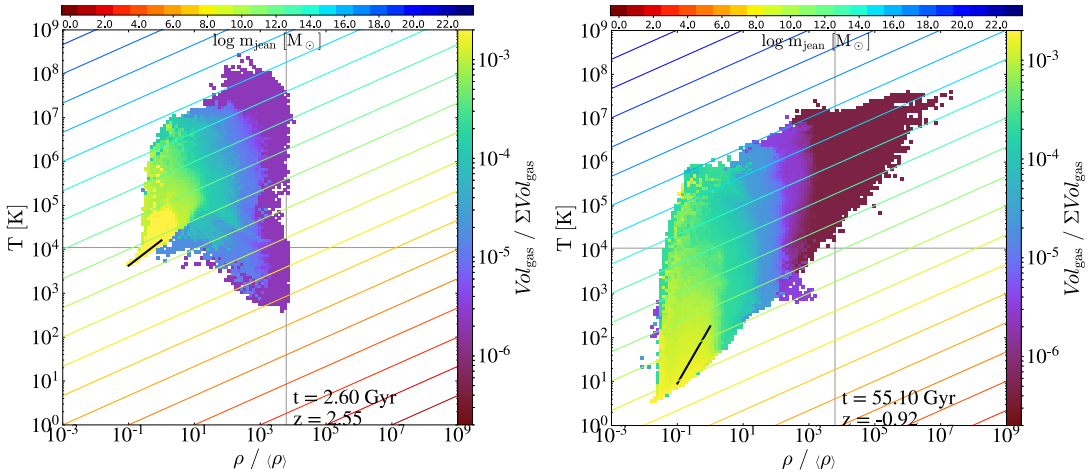

(a) $z = 2.55$ **(b)** $z = -0.92$

Figure 4.15 Phase distribution by volume, instead of by mass as in Figure 4.10. We are only showing the temperature-gas overdensity distribution at $z = 2.55$ (left) and $z = -0.92$ (right) for comparison. With the black line as a guide, we notice that the distribution of gas around the line has a higher variance at $z = -0.92$ than at $z = 2.55$. Refer to Section 4.3.6 for discussion.

4.3.7 Convergence

Halo mass function

In Sections 4.3.5 and 4.3.6, we discussed the evolution of the HMF and the IGM into the future using simulation *NL*, which has comparable resolution to the simulation of Nagamine & Loeb (2004). We have shown that our results are in reasonable agreement. However, it is not clear whether the results are converged in terms of resolution. Therefore, we introduce six other simulations that are summarised in Table 4.1. We will be using simulation *NL* as the baseline, *NL* $\pm$ *1* for spatial resolution comparison, *NLm* $\pm$ *1* for mass resolution comparison, and *NLfb* for a feedback sensitivity study. Each simulation contains only one parameter that is different from *NL* described in Section 4.2.

In Figure 4.16, we show that changing the root grid resolution in *NLm-1* (purple) and *NLm+1* (pink) affects the low mass end of the HMFs most significantly. The difference in the mass of the dark matter particles between *NLm-1* and *NLm+1* is 64. Since `ROCKSTAR` uses the same minimum number of particles to define a halo, this difference is carried forward to the minimum mass of a resolved halo in both simulations. On the high mass end, there is excellent agreement between all simulations at $z > -0.92$. However, this conclusion does

not hold for all times. In panels (e) and (f) of Figure 4.16, the HMFs of *NLm-1*, *NL* and *NLm+1* with identical spatial resolutions are clustered around each other but separated from the rest. Therefore, we do not have convergence at these times, and this separation hints at the sensitivity of the HMFs to spatial resolution.

The simulation with the worst spatial resolution is *NL-1* (blue). It starts to show signs of deviation earlier than the other simulations on the low mass end of the HMF at $z = -0.82$. From Section 2.2, we know that the force resolution of the simulation is dependent on its spatial resolution. As a consequence of this limitation, `Enzo` adversely impacts `ROCKSTAR`'s ability to classify these particles as haloes. This effect occurs on the low mass end first but eventually comes to affect the entire mass range (see Section 4.3.5). When the simulation is far enough into the future, the increase in grid cell size due to the expansion of the universe will affect even the best spatial resolution simulation (*NL+1*). By $z = -0.98$, the HMFs of the simulations are separated into three distinct bands according to their maximum spatial resolution. In future work, we can relate the redshift at which a simulation's HMF breaks down to its minimum grid cell size, so as to predict the onset and avoid such a scenario. Lastly, we do not notice any significant disparity between *NLfb* (orange) and *NL* (green) with an identical resolution confirming that baryonic processes have little influence over their host haloes.

Properties of the intergalactic medium

In this section, we shift the focus to the IGM, expanding the results in Section 4.3.6 and looking at the convergence achieved. Although we have shown a high degree of variance within the defined density of the IGM in the future, it is still one of the most prevalent methods to characterise the IGM. Therefore, we continue to use the power law fit in Equation 4.7 in our convergence study. We show the evolution of the $\log_{10} T_0$ (solid lines) and γ (dashed lines) from our suite of simulations in Figure 4.17. Generally, we find the evolution to be consistent regardless of resolution and star formation and feedback prescription. They exhibit a trend identical to Figure 4.14 (see Section 4.3.6) with some differences between the simulations.

We notice that the initial redshift when Equation 4.7 can be fitted to the simulations is different due to absence of gas with overdensity of 10^{-1}. It varies

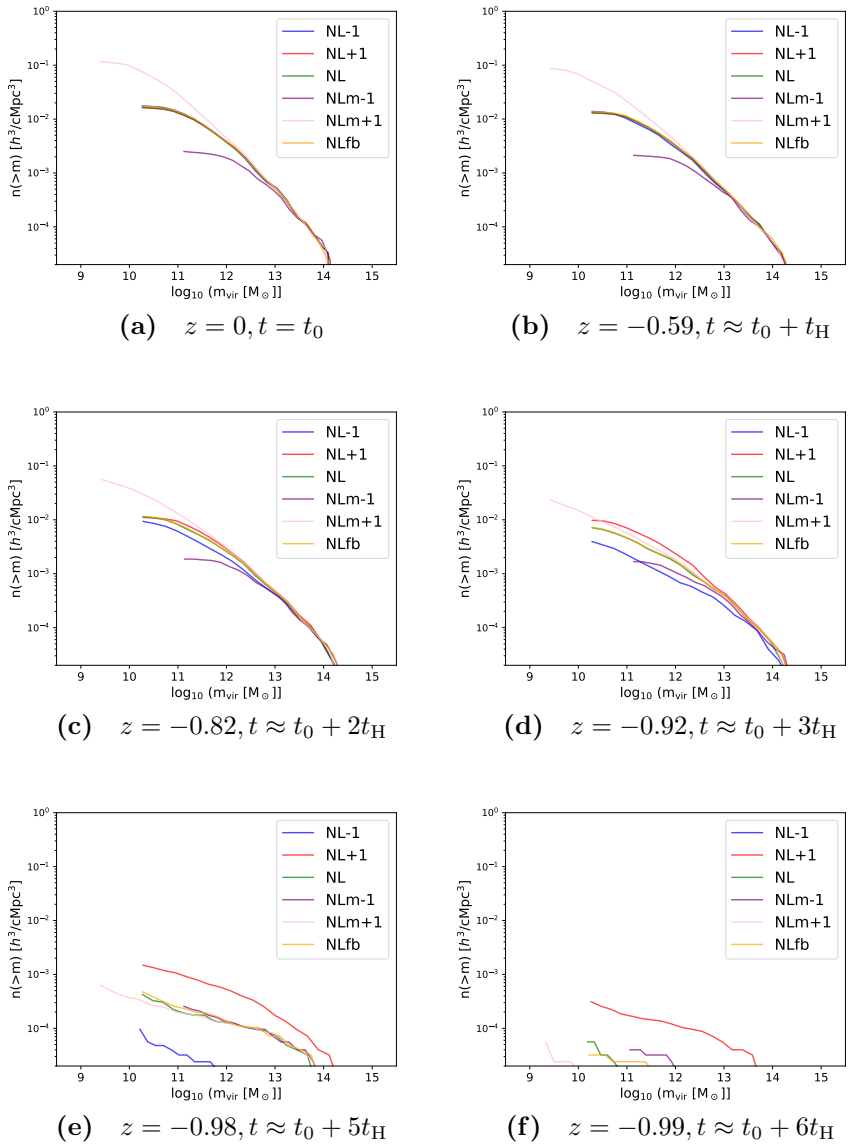

(a) $z = 0, t = t_0$ **(b)** $z = -0.59, t \approx t_0 + t_\mathrm{H}$

(c) $z = -0.82, t \approx t_0 + 2t_\mathrm{H}$ **(d)** $z = -0.92, t \approx t_0 + 3t_\mathrm{H}$

(e) $z = -0.98, t \approx t_0 + 5t_\mathrm{H}$ **(f)** $z = -0.99, t \approx t_0 + 6t_\mathrm{H}$

Figure 4.16 Evolution of the HMFs of simulations with varying specifications summarised in Table 4.1 into the future. The time interval between each panel is approximately t_H. The blue, red, green, purple, pink and orange lines correspond to *NL-1*, *NL+1*, *NL*, *NLm-1*, *NLm+1* and *NLfb* respectively. Across time, simulations with different root grid resolutions (NLm+1, NLm-1) have a correspondingly better or worse resolution, affecting its ability to resolve the smaller mass haloes. On the other hand, simulations with different maximum spatial resolutions (*NL-1*, *NL+1*) deviate more significantly further into the future. Lastly, different feedback implementations in simulations (*NLfb*) do not appear to influence the HMF as expected. Refer to 'Halo mass function' under Section 4.3.7 for discussion about the convergence of these results.

significantly between $2 < 1 + z < 8$ for *NLm-1*, *NLm+1* and the rest of the simulations except *NLfb*. This difference is a consequence of the disparity in the

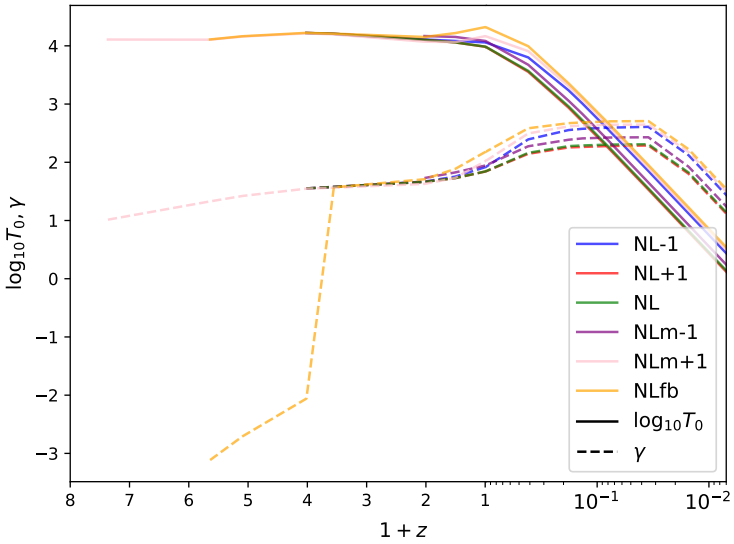

Figure 4.17 Evolution of the properties of the IGM linearly for $z \geq 0$ and logarithmically for $z < 0$ from our suite of simulations summarised in Table 4.1. The lines are coloured in the same way as Figure 4.16, indicated by the legend. The solid and dashed lines represents the evolution of $\log_{10} T_0$ and γ from Equation 4.7 respectively. The main difference between the simulations occurs at early times due to disparaties in spatial resolution and star formation criteria specifically for *NLm+1* and *NLfb*. Refer to 'Properties of the intergalactic medium' under Section 4.3.7 for detailed discussion.

root grid resolution. Note that AMR is not in full effect at this early time. With an improved root grid resolution, we can resolve the cosmic web better at an earlier time, illustrated in the upper panels of Figure 4.18. The better resolution means we are able to resolve lower mass haloes, which are shallower potential wells that allow gas to reach overdensity of 10^{-1}.

On the other hand, *NLfb* which uses a different subgrid prescription can resolve the IGM at early times because the difference in the conversion efficiency of gas into stars (see Section 3.2.1) leaves behind a significant amount of gas. This gas is heavily influenced by the feedback from the stars in the simulation, forming pockets of hot underdense gas seen in the lower panels of Figure 4.18. This hot, diffuse gas also explains the inverse relation (negative values) observed at very early times for *NLfb* in Figure 4.17.

What about the scatter observed in the late time evolution of the properties of the IGM in Figure 4.17? We mentioned in Section 4.3.6 that photo-heating from the UV background, adiabatic cooling due to the expansion of the Universe and shocks (McQuinn & Upton Sanderbeck, 2016) are the main drivers for the

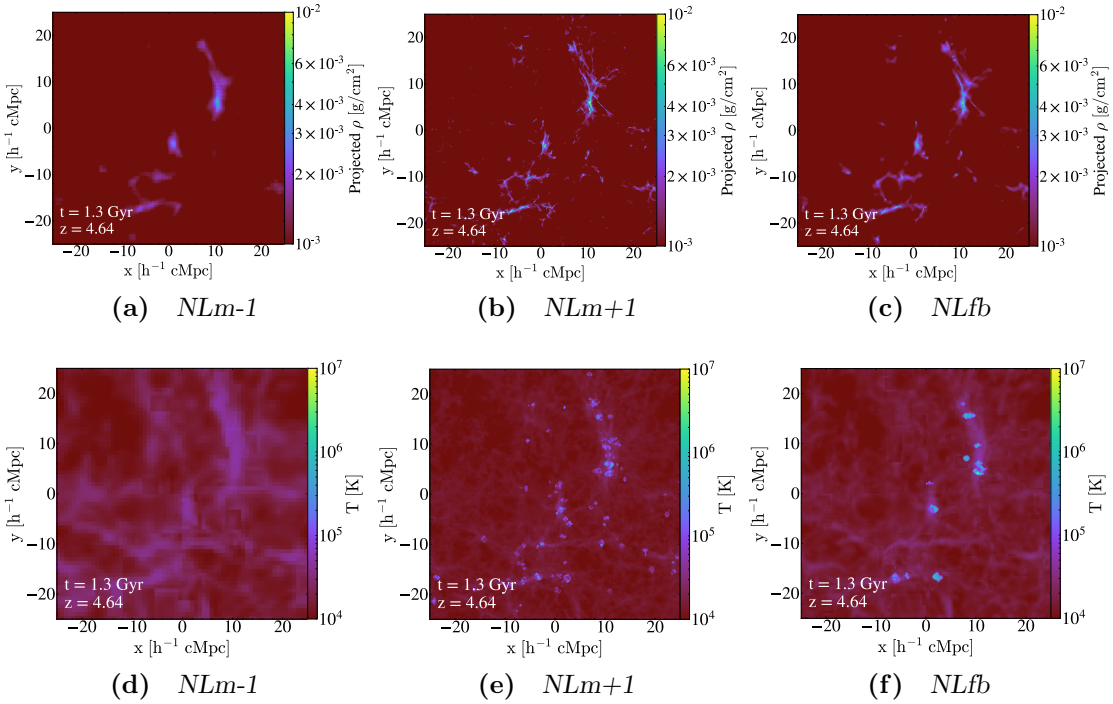

(a) *NLm-1* **(b)** *NLm+1* **(c)** *NLfb*

(d) *NLm-1* **(e)** *NLm+1* **(f)** *NLfb*

Figure 4.18 Density projection plots (upper panels) and mass-weighted temperature projection plots of a slice at $z = 4.64$, $t = 1.3$ Gyr, similar to Figures 4.8 and 4.9. The left, middle and right column corresponds to *NLm-1*, *NLm+1* and *NLfb* respectively. We can resolve the cosmic web better with a higher root grid resolution simulation (*NLm+1*), allowing gas to reach IGM densities. In *NLfb*, we have a different star formation and feedback prescription, somewhat improving our resolution of the IGM at early times as well. Refer to 'Properties of the intergalactic medium' under Section 4.3.7 for detailed explanations.

formation of the power-law fit to the IGM. Since the first two factors are consistent across the simulations, the last is the most likely cause. We showed that the HMFs are sensitive to the mass and spatial resolution of the simulations (see Section 4.3.5), which in turn affects the amount of shocked gas. In *NLfb*, using Setup 1 with a lower conversion efficiency leaves behind a larger gas reservoir as compared to Setup 2. Also, we showed in Figure 3.5 that this gas is pushed out to different radii because of the different extent of feedback energy injection, affecting its ability to fall back onto the halo. These reasons can affect the fraction of shocked gas, leading to slight deviations from each other.

Gas phase distribution

In Figures 4.19, 4.20 and 4.21, we compare the phase distribution at $z = 0$, $z = -0.98$ and $z = -0.99$ because the HMFs in Figure 4.16 highlighted significant

differences between each simulation at these times. Figure 4.19 illustrates the phase distribution for the simulations *NL-1*, *NL+1*, *NL*, *NLm-1*, *NLm+1* and *NLfb* at $z = 0$ from panels (a) to (f) respectively. As always, we will use NL in panel (c) as the baseline for comparison.

When we change the maximum allowed AMR levels, there is minimal difference between panels (a), (b) and (c) in Figure 4.19. This result agrees with the level of convergence demonstrated by Figures 4.16 and 4.17. Contrasting panels (c) and (d), we find a large portion of gas with overdensities between 10 and $\sim 10^4$ and $10^3\,\mathrm{K} < T < 10^6\,\mathrm{K}$ missing. The cause of this disappearance is the absence of small mass haloes due to poorer mass resolution. On the contrary, with better mass resolution, the cold gas spreads across to lower overdensity ($\sim 10^{-2}$) as we see in panel (e). This behaviour is attributed to the better resolution of the cosmic web at late times, similar to what Figure 4.18 showed. These are the changes to the phase distributions, possibly arising from the differences in the HMFs shown in Figure 4.16. More work has to be done in order to prove the causality of these differences. Also, hot underdense gas with a temperature above $10^5\,\mathrm{K}$ that is consistent with the extended hot pockets in the lower panels of Figure 4.18 is observed in Figure 4.20f. This difference is caused by Setup 1 having a lower star formation efficiency and a higher feedback energy budget than Setup 2 and explained with Figure 4.18 previously.

Fast forwarding to $z = -0.98$, we look at the degree of convergence achieved through Figure 4.20. We know from Figure 4.16 that the HMFs diverge and are grouped according to the maximum spatial resolution in the simulation at this moment, making it an interesting point in time. Figure 4.20 includes all previous differences in Figure 4.19 with some new additions.

NL-1 suffers a loss of haloes across the entire mass range. These factors lead to a correspondingly reduced maximum gas overdensity and an excess of hot gas around the overdensity value of 10^0 in the simulation in Figure 4.20a as compared to Figure 4.20c. Since *NL-1* has a poorer spatial resolution, hot gas previously in haloes unbound and enters the diffuse environment. The inverse is true for *NL+1* where the better resolution of the HMF keeps the hot gas in haloes in Figure 4.20b. This gas is removed from a region with an overdensity of 10^0 and resides in well-resolved haloes, reaching a higher maximum overdensity.

The remaining simulations, *NLm-1*, *NLm+1*, *NLfb* have the same maximum spatial resolution setup as *NL*. The impact of the different extent of the low

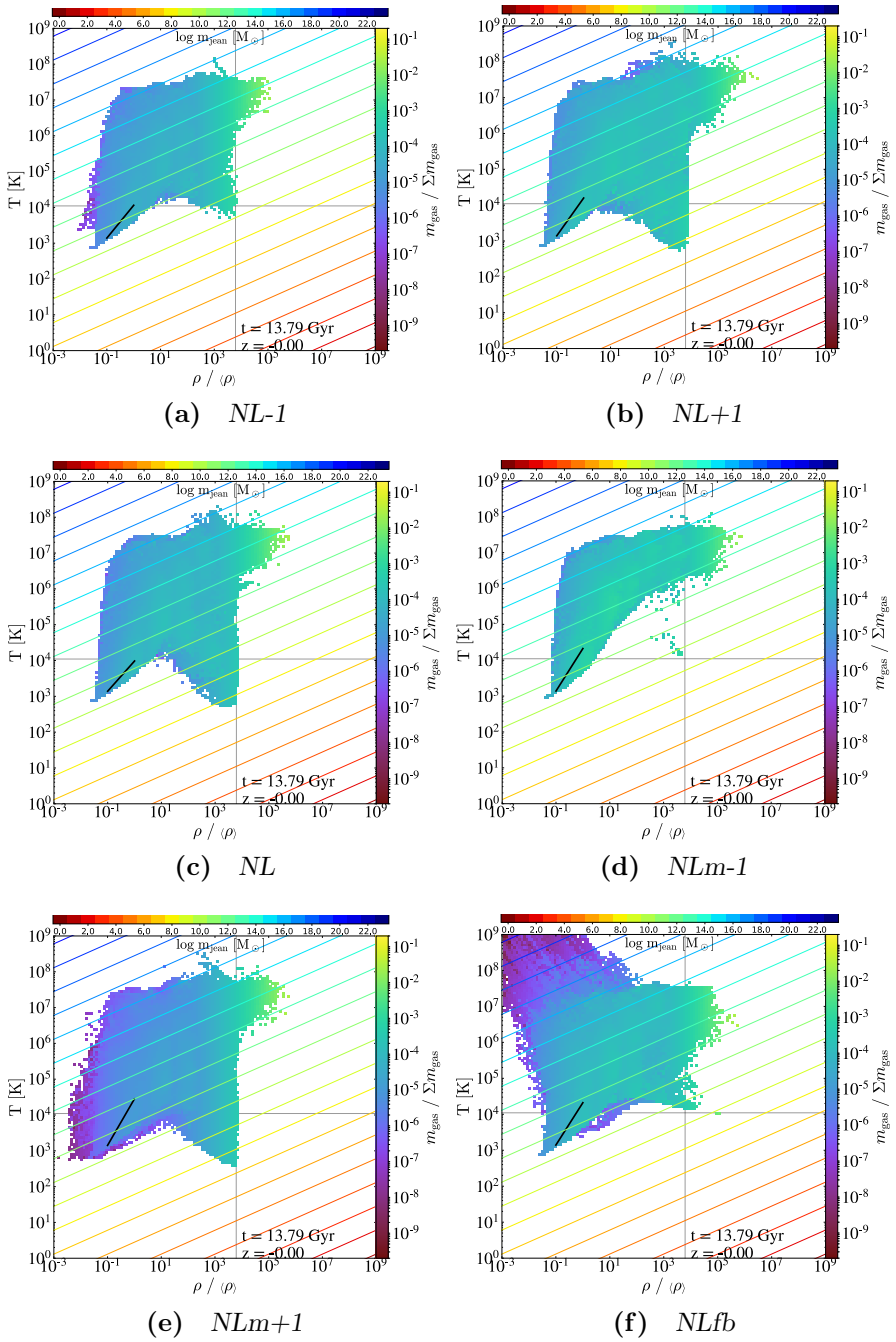

(a) *NL-1* **(b)** *NL+1*

(c) *NL* **(d)** *NLm-1*

(e) *NLm+1* **(f)** *NLfb*

Figure 4.19 Gas mass in bins of overdensity and temperature of the gas in different simulations at $z = 0$ indicated in the captions of panels (a) to (f). Other features such as the colour bars, vertical, horizontal and diagonal lines, and the power-law fit to the IGM are identical to Figure 4.10. Differences arising from the HMFs in Figure 4.16 are expressed very clearly in their respective panels. Refer to 'Gas phase distribution' under Section 4.3.7 for discussion on these differences.

mass end was noted in Figure 4.19, becoming more apparent at $z = -0.98$. Similar to $z = 0$, there is an absence of cold gas between gas overdensity of approximately 10^0 and 10^4 between *NLm-1* and *NL*. The opposite is true for

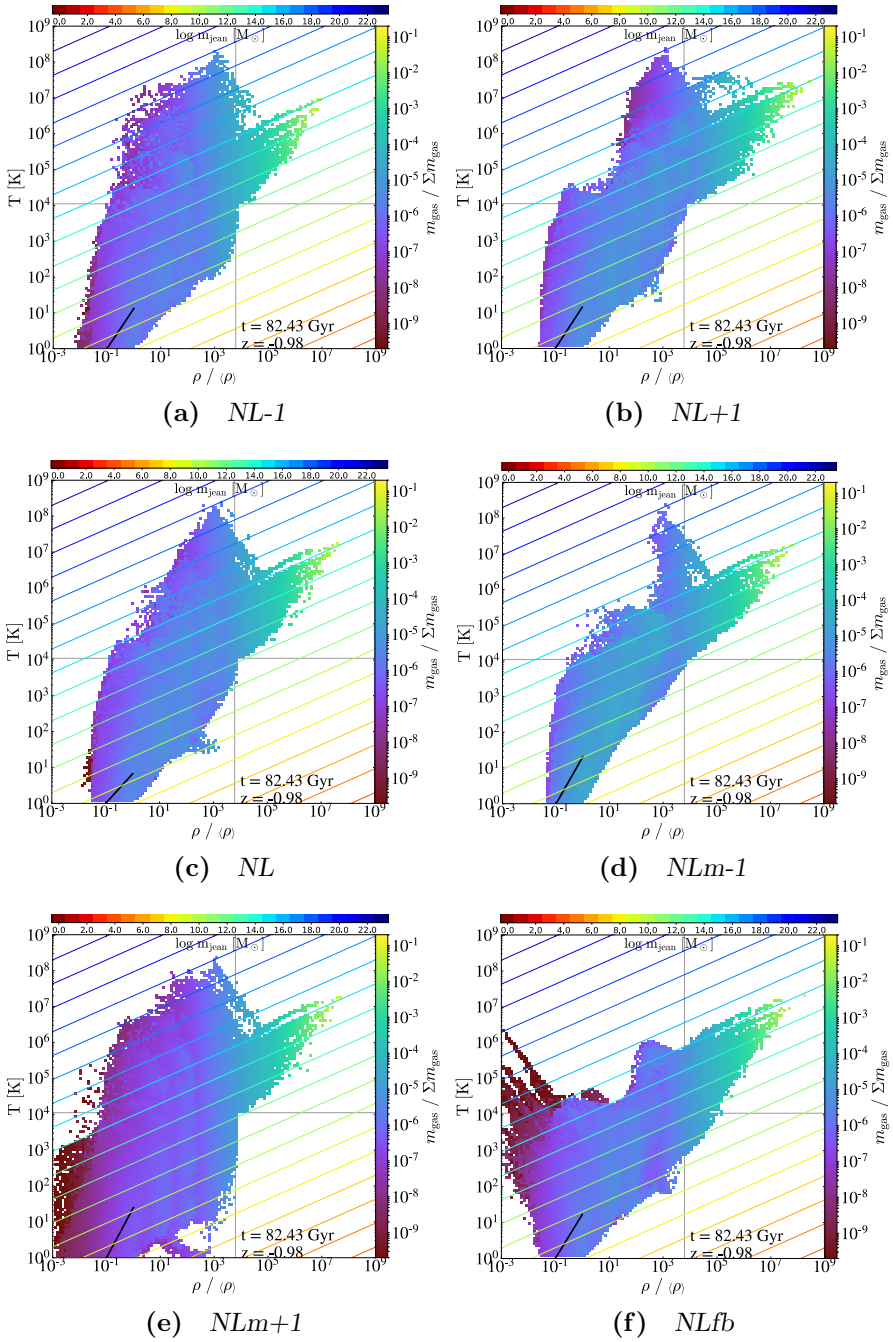

(a) *NL-1* **(b)** *NL+1*

(c) *NL* **(d)** *NLm-1*

(e) *NLm+1* **(f)** *NLfb*

Figure 4.20 Similar to Figure 4.19 but at $z = -0.98$. In general, more and more gas are hitting the temperature floor set by the CMB temperature. Distinct features as a result of the differences in the HMF are discussed in 'Gas phase distribution' under Section 4.3.7.

NLm+1. As explained before, these small haloes trace the resolution of the cosmic web, improving the distribution of gas. Collectively, these explain the differences in the amount of hot and cold gas in the intermediate overdensity regime.

Lastly, we compare *NLfb* to *NL* in Figure 4.20. There are two main differences between them: relatively hotter gas with an overdensity less than 10^{-1} and cooler gas around overdensity of 10^3. The latter arises because of the cooling of the previously hot gas at these overdensities in Figure 4.19f and the low star formation efficiency in *NLfb* while the former is due to wider extent of feedback energy injection in *NLfb*. As a result of the feedback prescription, more gas is swept out of haloes.

The last redshift that we look at is $z = -0.99$. Figure 4.16f indicates that all HMFs except for *NL+1* have broken down. However, there is no significant difference between the corresponding panels in Figures 4.20 and 4.21. This similarity suggests that the gravitational potential wells of the baryons in haloes are present even though `ROCKSTAR` no longer identifies a given collection of dark matter particles as a halo, which we will show in Figures 4.24 and 4.26. At this point of time in the simulation, we believe that `Enzo` is at its operational limits with the given force resolution, which affects `ROCKSTAR`'s ability to locate haloes. In conclusion, we find that the evolution of the phase distribution is sensitive to the feedback implementation.

Star formation history

Now that we have established the degree of convergence of the results, we are confident about the distribution of haloes that hosts star formation and the evolution of the IGM that provides the fuel for star formation into the future. These results allow us to study of how the simulated SFRD evolves into the future and its corresponding behaviour as $t \to \infty$. The trend and values will be compared with the observational fit from Madau & Dickinson (2014) in this section. We start by showing the evolution of the SFRD in Figure 4.22 with different coloured lines corresponding to the simulations and observations as indicated in the legend. If we compare all of our simulations as a whole with the analytic fit to observations, we immediately recognise that the peak of the SFRDs from the simulation is lower and occurs at a later time. This difference is due to the finite resolution of our simulations. Because of this limitation, structure formation is delayed in the simulation, leading to a later onset of star formation. The peak in SFRD is also lower because we do not have the resolution for all star-forming haloes.

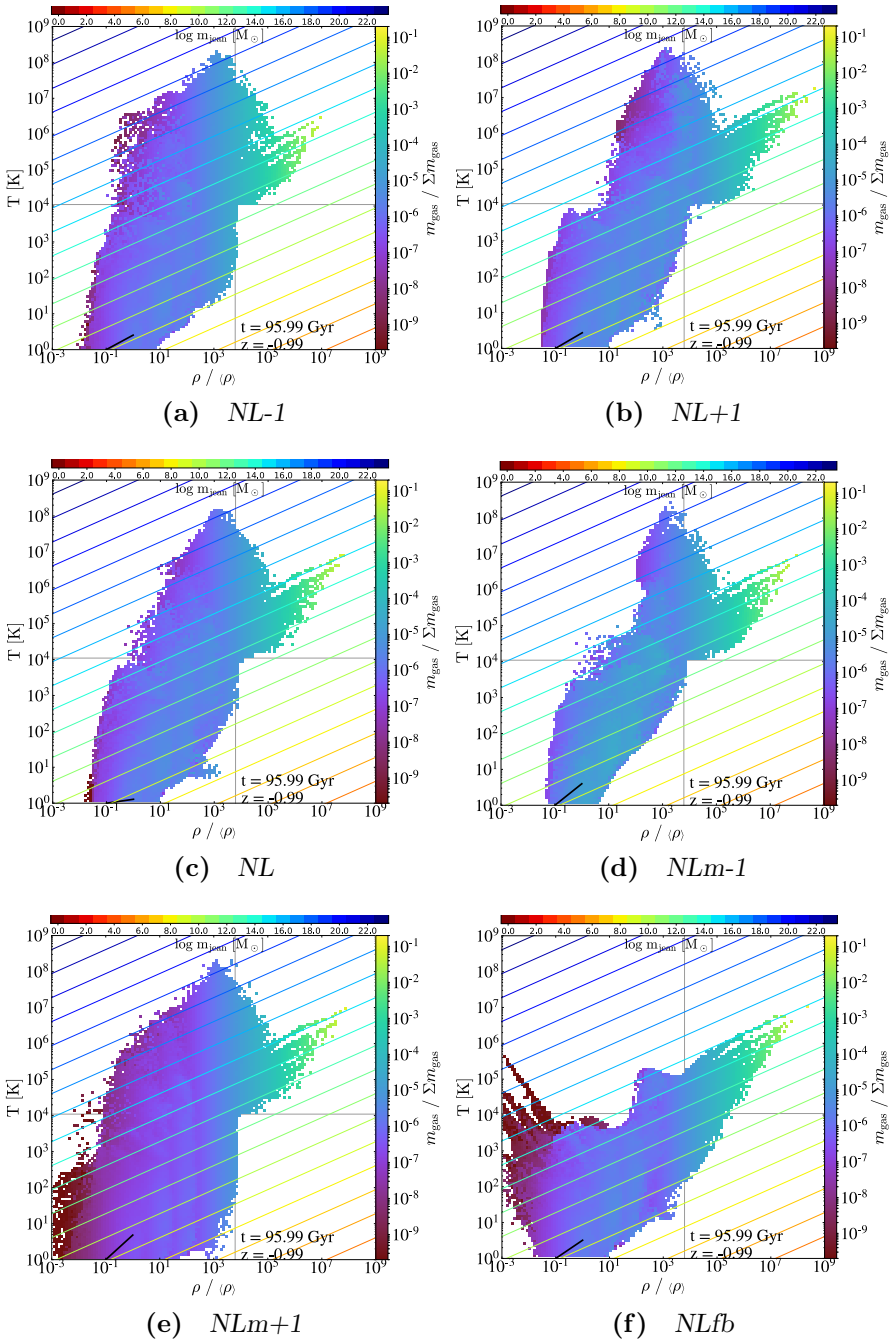

(a) *NL-1* **(b)** *NL+1*

(c) *NL* **(d)** *NLm-1*

(e) *NLm+1* **(f)** *NLfb*

Figure 4.21 Similar to Figure 4.19 but at $z = -0.99$. There is minimal change to the phase distributions in comparison to Figure 4.20. The presence of high gas overdensity is not justified by the HMFs in Figure 4.16f and we will discuss this in 'Gas phase distribution' under Section 4.3.7.

The peaks in the SFRD are very sensitive to the star formation and feedback prescription, evident from the significant difference between *NLfb* and the rest of the simulations. *NLm-1* and *NL-1* both have a lower SFR peak because of their poorer resolution. Specifically, *NLm-1* has the worst root grid resolution, which

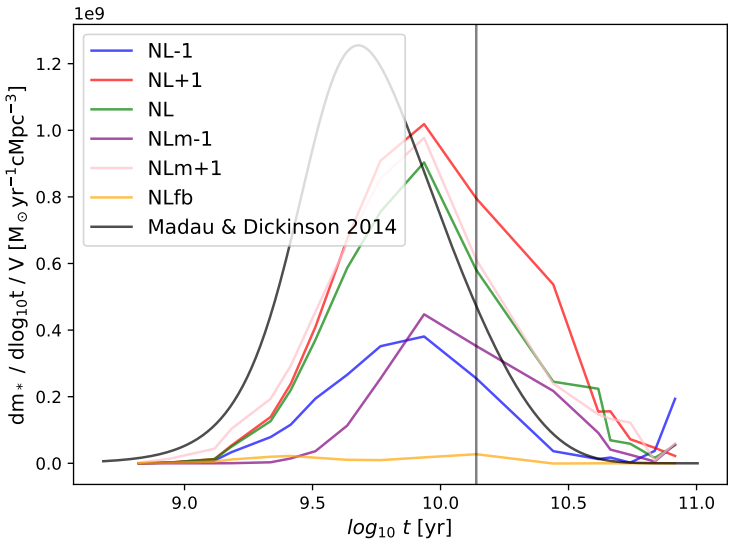

Figure 4.22 Evolution of SFRD across cosmic time in our suite of simulations. The blue, red, green, purple, pink and orange lines correspond to *NL-1*, *NL+1*, *NL*, *NLm-1*, *NLm+1* and *NLfb* respectively. The black curve represents a modified Equation 1.19 to match the axis labels. We have also added a vertical grey line to indicate the point of time where $z = 0$. Across all simulations, we obtain a similar peak in SFRD of different peak values, albeit at a later time than the black line. The impact of varying resolutions on the SFRD will be discussed in 'SFR' under Section 4.3.7.

means that the mass and spatial resolution is the lowest before AMR kicks in. The deficiency in the number of low mass haloes in *NLm-1* results in delayed structure formation, explaining why it has a lower peak in SFRD. *NL-1* suffers from a different problem that escalates with time. Since *NL-1* has the worst force resolution, gas is prevented from reaching high densities, thus limiting star formation. The other simulations, *NL*, *NLm+1*, *NL+1* exhibit a similar evolution in SFRD to each other, which shows that they are consistent with each other even if not in agreement with the observational fit.

To further illustrate the issue with resolution, we separate the SFRD into different halo mass bins and compare between *NL-1* and *NL+1* in Figure 4.23. We can track the evolution of the SFRD based on halo mass over a longer time in *NL+1* than in *NL-1*. This difference is consistent with the complete loss of the HMF in *NL-1* by $7\,t_{\rm H}$ (see Figure 4.16f). The decrease in stellar mass is happening because the star particles are losing mass due to the feedback prescription and no further star formation is occurring in the haloes. However, as we will explain later, these stars now formed in the environment not within the virial radius of any halo, which hints that haloes dissolve at late times. This scenario is also

unphysical and can be avoided if we can improve the spatial resolution to such an extent that we continue to resolve these haloes.

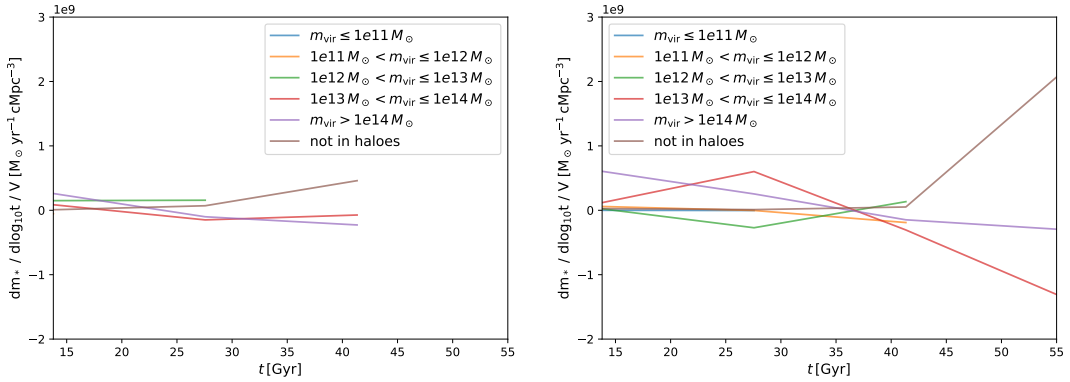

(a) *NL-1* **(b)** *NL+1*

Figure 4.23 Evolution of SFRD in haloes of different mass for *NL-1* (a) and *NL+1* (b) beyond $z = 0$. The blue, orange, green, red and purple lines correspond to haloes with mass below $10^{11}\,M_\odot$, between $10^{11}\,M_\odot$ and $10^{12}\,M_\odot$, between $10^{12}\,M_\odot$ and $10^{13}\,M_\odot$, between $10^{13}\,M_\odot$ and $10^{14}\,M_\odot$ and above $10^{14}\,M_\odot$ respectively. The brown line refers to stars formed beyond the virial radius of any halo identified by `ROCKSTAR`. The evolution further supports the presence of a halo-like structure due to baryons while the dark matter halo is absent. Refer to 'SFR' under Section 4.3.7 for discussion.

Let us now look into the future beyond $z = 0$, focusing on $t \approx 50\,\mathrm{Gyr}$ in Figure 4.22. There is a turnaround in cosmic SFRD, deviating from the extrapolated SFRD of the analytic fit to observations. This onset of a reversal in SFRD occurs at two different times that is dependent on the spatial resolution of the simulations. The SFRD begin to increase earlier for *NL-1*, followed by *NL*, *NLm-1*, *NLm+1* and *NLfb*. Within the timescale in Figure 4.22, we do not yet see a SFRD turnaround for *NL+1*. This trend suggests that the cause is of a numerical origin: a lower spatial resolution in the simulations results in earlier turnaround time in SFRD. Therefore, we expect the SFRD of *NL+1* to increase again further into the future.

In the simulations, star formation occurs above a fixed overdensity threshold. Since this value is constant with time, the decrease of the mean matter density into the future translates to a lowered physical density requirement. We illustrate in Figure 4.24 that star formation can occur at increasing distances from the centre. We separate stars formed within and beyond 500 Myr of the projection plot as young (red dots) and old stars (black dots) respectively. The young stars are further away from the centre of the 'halo'. It is not a halo by the definition of

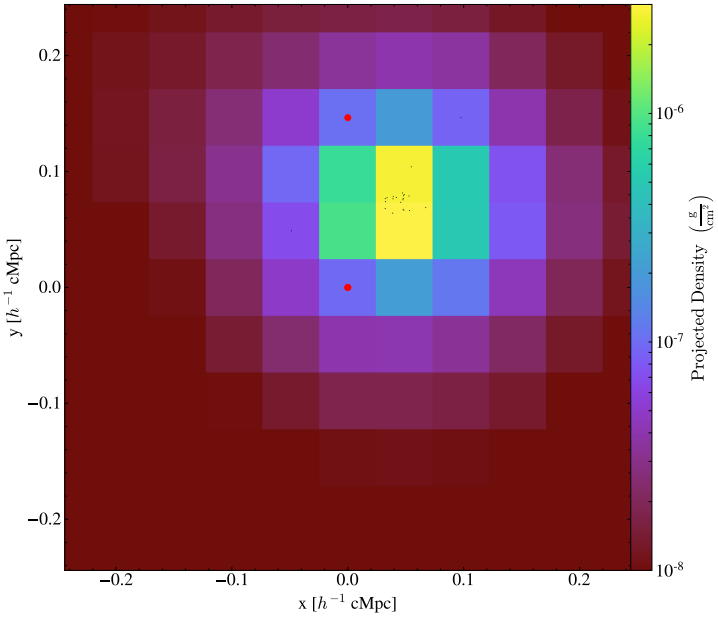

Figure 4.24 Density projection plot of *NL-1* at $z = -0.99, t = t_0 + 6t_H$ centred around a star particle formed within 500 Myr (young stars). Young stars and previously formed stars are indicated by red and black dots respectively. The site of active star formation is extending outwards for the reasons discussed in 'SFR' under Section 4.3.7.

`ROCKSTAR` because at $z = -0.99$, the HMF of *NL-1* (blue line) in Figure 4.16f is missing. However, the features of Figure 4.24 resembles that of a halo, consistent with the previously mentioned limitations of `Enzo` and its impact on `ROCKSTAR` in the far future and the individual evolution of SFRD by halo mass (see Figure 4.23).

The scenario in Figure 4.24 is delayed when the maximum level of refinement is increased. As a result, even though *NL+1* in Figure 4.22 did not turn around, we expect it to happen at a time later than in current simulations. Figure 4.25 validates the claim with an extension of *NL+1* (red line) further into the future. We have also added a simulation named *NL+3* (green line) with a maximum spatial resolution of 4.39 ckpc. The turnaround in SFRD occurs later for *NL+1* and should continue to be delayed for *NL+3*. Contrary to expectations, it happens at the same time for both *NL+1* and *NL+3*.

The first explanation is the coarseness of the temporal resolution applied to obtain Figure 4.25. With a time interval of $t_H = 13.7$ Gyr between each point, the exact time where the turnaround occurs may be slightly different between *NL+1* and *NL+3*, but nonetheless breaks with the expected trend. We therefore look

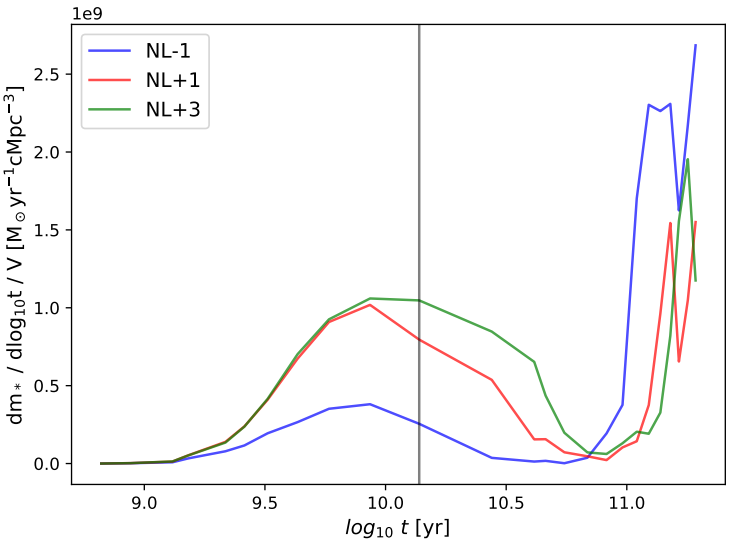

Figure 4.25 Evolution of SFRD beyond the timescale in Figure 4.22. The blue, red and green lines correspond to *NL-1*, *NL+1* and *NL+3* respectively. The vertical black line indicate the point of time where $z = 0$. As predicted, the SFRD for *NL+1* turns around at a later time. However, the turnaround time for *NL+1* coincides with *NL+3*, suggesting some level of convergence. We will provide some possible explanations in 'SFR' under Section 4.3.7.

at the environments where the young stars form in both simulations with Figure 4.26. It appears that star formation can occur in cells with lower density and at a refinement level that is two levels lower than the maximum level in *NL+3* (bottom region of Figure 4.26b), i.e., equivalent to the maximum level in *NL+1*. In the *NL+3* simulation, cells that satisfy these requirements are at a spatial resolution identical to the maximum resolution of *NL+1*, concluding that the refinement levels beyond *NL+1* is unnecessarily high for star formation. Therefore, the star formation in *NL+3* will be comparable to *NL+1*, resulting in the similarity of turnaround time.

The turnaround in SFRD does not appear to be physical because of the density at which this late-time star formation occurs. Looking at Figure 4.26, the young stars form in an environment with a density that is approximately two orders of magnitude lower than the old stars at the density peak. This difference arises because of the constant star formation overdensity threshold discussed earlier. We should investigate how to modify this parameter in future work for a realistic star formation scenario in the universe of the far future. Similar to us, Salcido et al. (2018) also found a turnaround in star formation rate in their simulations. However, the turnaround in their work happens much earlier and the origin is also very different. The authors attributed the turnaround to

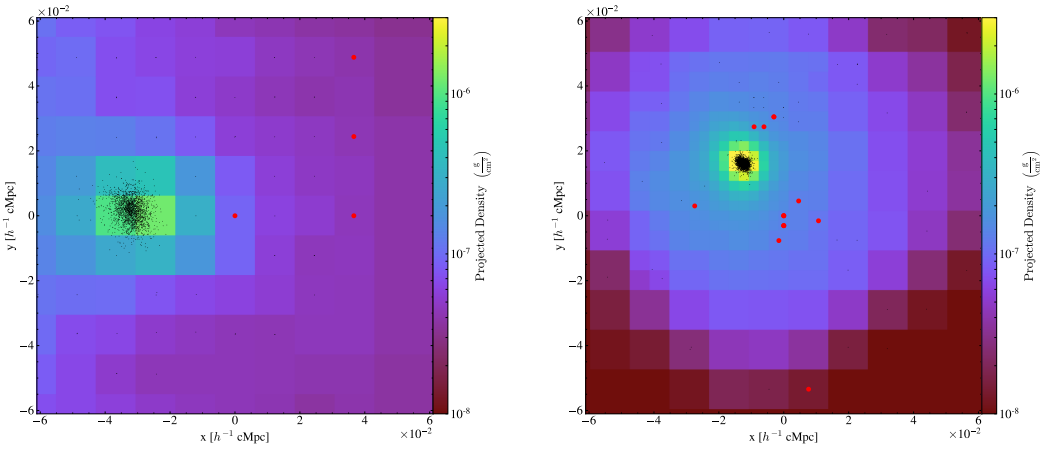

(a) *NL+1* **(b)** *NL+3*

Figure 4.26 Comparison of density projection plot between *NL+1* and *NL+3* at $z = -0.997$. The dots have identical meanings to those in Figure 4.24. Star formation happens further away from the density peak and in cells not at the maximum level of refinement in the simulation in *NL+3* in comparison to *NL+1*. Refer to 'SFR' under Section 4.3.7 for discussion.

the switching off of AGN feedback in their simulations. Since our simulation do not contain this form of feedback, it is possible that our stellar feedback is strong enough to encompass the effects from AGN and suppress a turnaround in SFRD.

Since star formation beyond the time scale of Figure 4.22 is questionable, we limit further analysis to $8 \geq z \geq -0.993$. Although the exact evolution of SFRD is different among the simulations, we are interested in finding out if the total amount of stellar mass formed is the same. Therefore, we integrate the SFRDs in Figure 4.22 between the specified redshifts and summarise the results in Table 4.2. Other than *NLfb*, the total stellar mass density within each of the remaining simulations agrees with each other and more importantly, with the value obtained from integrating Equation 1.19. The values are of the same order of magnitude with *NL+1* matching within 1% of the total predicted stellar mass density. In contrast, *NLfb* differs by nearly two orders of magnitude, proving again that the SFRD is highly sensitive to feedback and Setup 1 is not appropriate for our purposes.

Lastly, we look at the amount of stellar mass formed at different time, t as a fraction of the total stellar mass formed at $t \approx t_0 + 6\,t_{\mathrm{H}}$, which is the final redshift of all the results we have presented thus far. The time evolution of this ratio is shown in Figure 4.27. At $z = 0$, the observed stellar mass given by Equation 1.19 is 90% of the total stellar mass while the simulations are only

Table 4.2 List of simulations with their corresponding total stellar mass density formed between $z = 8$ and $z = -0.993$. Refer to Table 4.1 for specifications of individual simulations. Except *NLfb*, we obtain a good agreement within the same order of magnitude with the total predicted stellar mass based on the fit to observations provided by Madau & Dickinson (2014).

Simulation	Total stellar mass density $[M_\odot\, h^3\, \mathrm{cMpc}^{-3}]$
NL	2.06×10^9
NL-1	8.72×10^8
NL+1	2.62×10^9
NLm-1	9.04×10^8
NLm+1	2.30×10^9
NLfb	6.19×10^7
Madau & Dickinson (2014)	2.66×10^9

forming 40% – 60% of their respective total stellar mass. This difference is due to the delay in the star formation peak. As a result, the predicted stellar mass reaches a ratio of unity at an earlier time in contrast to the simulations except for *NLfb*. Although *NLfb* exhibits a comparable stagnation time to the analytic fit, we know from Table 4.2 that the total stellar mass formed is much less than predicted. For the other simulations except for *NL+1*, they stagnate at a ratio less than one before increasing again. *NL-1* illustrates this trend clearly with a plateau at roughly 90% for a significant amount of time before increasing again. This evolution is consistent with the late time turnaround in star formation rate discussed extensively before. The discrepancies between the simulated and predicted SFRD by Madau & Dickinson (2014) are outcomes of the finite resolution in the simulations. Despite the limitation, the agreement between simulations and predictions is remarkable, especially in the total stellar mass formed in *NL+1*, the simulation with the best resolution that we have.

It may be surprising that we are able to get such a good agreement with the predicted total stellar mass density given that we have a turnaround in the SFRD (see Figure 4.22). Since the analytic fit to observations naturally does not predict a turnaround and is declining to zero SFRD, we find that the total stellar mass density derived from this fit does not differ much if we change the upper limit assuming that $z < -0.99$. Within the limits in which we calculate the total stellar mass ($z = 8$ and $z = -0.993$), there is no turnaround in *NL+1*. Even in *NL-1* where the turnaround is relatively more severe than the other simulations, it only produced 32% of the predicted total stellar mass, suggesting that the general evolution of the SFRD that is affected by the resolution is more

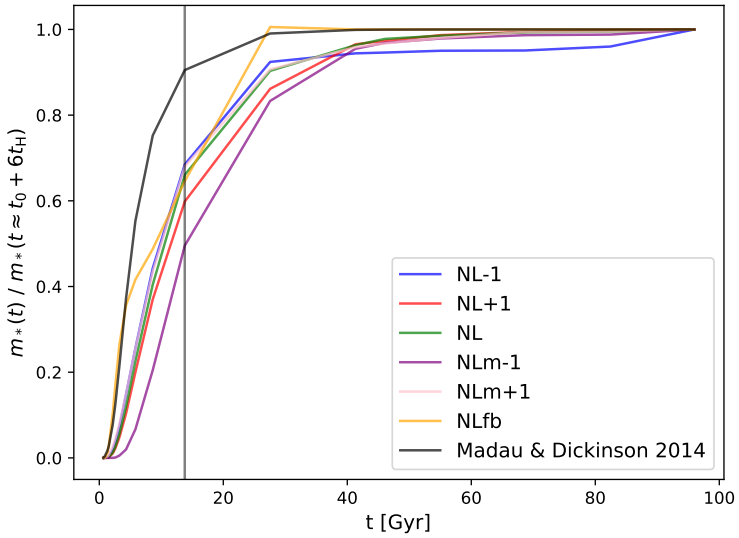

Figure 4.27 Evolution of the ratio of stellar mass formed at time, t to that at $t \approx t_0 + 6t_{\rm H}$. The blue, red, green, purple, pink and orange lines correspond to *NL-1*, *NL+1*, *NL*, *NLm-1*, *NLm+1* and *NLfb* respectively. The black curve represents the same ratio obtained from Equation 1.19. Across all simulations, at $z = 0$ (vertical black line), the percentage of stellar mass formed in simulations is 40% – 60% as compared to 90% predicted by the black line. Refer to SFR under Section 4.3.7 for further discussion.

significant than the additional stellar mass from the turnaround. If we continue the simulations even further, we can expect a divergence in the total stellar mass. Since we have established that this turnaround is not physical and we obtain a similar evolution in SFRD to observations with our simulations, we can restrict the calculation of the total stellar mass to before the turnaround by fitting a similar double power-law to Madau & Dickinson (2014) to the star formation history from the simulations. This methodology will be discussed in more detail in Chapter 5.

4.3.8 Zoom vs cosmological box simulations

Finally, we extend the zoom simulation discussed in Chapter 3 to $z = -0.995$, labelled *zoom* in this Chapter. Since the zoom simulation is of a much higher resolution, we want to investigate the significance of this resolution discrepancy on the baryon content within a halo. Using the virial mass of the MW-sized halo in *zoom* at $z = 0$, we identify haloes within 10% of this mass in *NL* at $z = 0$. We then trace and present the evolution of several properties of these haloes in Figure 4.28. The most obvious difference between *NL* and *zoom* is the vastly different

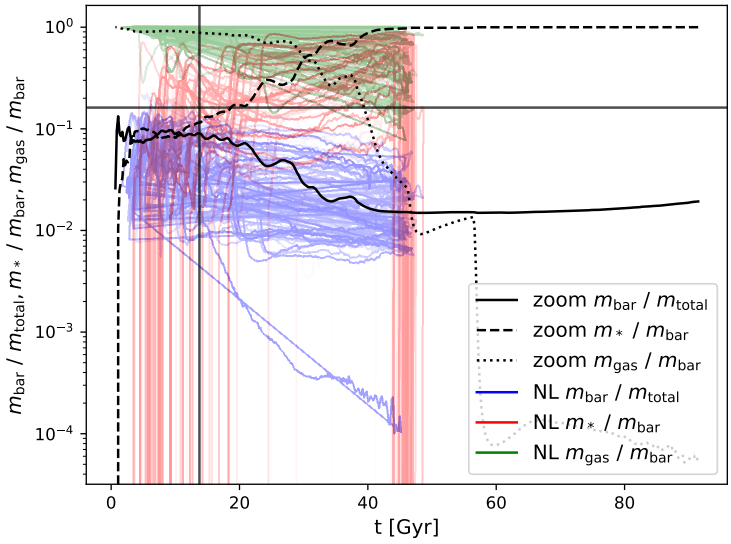

Figure 4.28 Evolution of various mass fractions in haloes with time. The black and coloured lines in this figure are from *zoom* and *NL* respectively. We can group several pairs of lines for comparison: solid black and blue lines, dashed black and red lines, and dotted blacked and green lines. They correspond to the baryon fraction ($m_{\rm bar}/m_{\rm total}$), $m_*/m_{\rm bar}$ and $m_{\rm gas}/m_{\rm bar}$ of the haloes respectively. Also, we included a horizontal and vertical line which correspond to the universal baryon fraction in the simulation (0.1618) and $z = 0$ respectively. Other than resolution affecting the starting and ending time when the halo can be traced, the MW-sized halo in the *zoom* exhibits a typical evolution as other haloes within the specified mass range in *NL*. Refer to Section 4.3.8 for a detailed discussion.

mass and spatial resolution, allowing the halo to be tracked over a longer time. However, the general evolution of the various properties show that the MW halo in *zoom* is typical of haloes in this mass range in *NL*.

If we focus on at the baryon fraction of the haloes from both *zoom* (black line) and *NL* (blue line), it is always below the universal baryon fraction specified in the initial conditions of the simulations (grey horizontal line). This difference implies that haloes of other masses or the IGM will contain more baryons than dark matter mass. The equivalence of $m_*/m_{\rm bar}$ and $m_{\rm gas}/m_{\rm bar}$ happens for both *zoom* and *NL* at $t \approx 30\,$Gyr, coinciding roughly with the period of 'freeze out'. Since 'freeze out' reduces the supply of gas from the large scale environment and feedback from stars drives the gas out of halo, it causes $m_{\rm gas}$ in the haloes to decrease. On the other hand, m_* remains relatively constant because of the decreasing SFRD. These lead to an increasing $m_*/m_{\rm bar}$ and a corresponding decreasing $m_{\rm gas}/m_{\rm bar}$.

4.4 Summary and conclusion

In summary, we study the first suite of simulations using `Enzo` to simulate the evolution of the universe into the future. We modify certain aspects of the cooling and chemistry library, `Grackle` and the extrapolation of the UV background to mimic star formation into the future. We start with a simulation of resolution consistent with Nagamine & Loeb (2004) in order to establish the convergence. We then examine the effects of resolution on the evolution of a range of properties including stellar masses, SFRDs, HMFs, tight power law fit of the IGM, and gas phase distribution. We survey these properties spanning from $z = 99$ to $z = -0.995$, which translates to a final age of more than 7 $t_{\rm H}$. We summarise our conclusions as follows:

- We convert the resolution of the `GADGET` simulation presented by Nagamine & Loeb (2004) to the corresponding parameters available in our `Enzo` simulation, namely the root grid resolution and the maximum allowed levels of AMR. Since the force resolution in `Enzo` is twice the mean inter-particle separation, we use a 128^3 root grid `Enzo` simulation, equivalent to the 64^3 used in the mentioned previous work. From comparisons made by O'Shea et al. (2005), we implement four additional levels of AMR to eliminate any discrepancies of the results due to resolution. We also decide a final redshift of -0.995 based on the WMAP9 cosmological parameters to produce a universe of a similar age to that of Nagamine & Loeb (2004). These are described and discussed in Section 4.2.1.

- We change the method of extrapolation of the UV background beyond $z = 0$ from linear to logarithmic. Using the former method, at $z \approx -0.2$, the photoheating rates from HI, HeI and HeII become negative. In other words, the UV background will begin to cool the gas in the IGM unphysically. Also, we modify the `CLOUDY` table to extend its capability to handle the low densities present in the far future. Furthermore, we remove the preventive measures against round-off error in `Grackle` so that it does not inject an artificial heating value that causes significant effects into the future. These modifications and results are presented in Section 4.2.3 and Section 4.3.1 respectively. We also validate the capability of `ROCKSTAR` to locate and track haloes into the future with a mock halo catalogue in Section 4.3.2.

- The results from *NL* show an excellent agreement of the evolution of

the distribution of gas on the temperature – gas overdensity plane with Nagamine & Loeb (2004) in Section 4.3.4. We observe the same elongation in the shape of the phase distribution due to the long Bremsstrahlung cooling time at high temperature and similar peaks in gas mass in haloes. Also, the equation of state of the IGM evolves similarly for both, with a consistent drop beyond the present time. This drop occurs around $z = 0$, fueling the argument of the 'coincidence' problem. Despite this agreement, we also observe differences arising from the disparities in subgrid physics implemented in both simulations. We then build upon this convergence and analyse various other aspects of the simulation that is previously unexplored in Nagamine & Loeb (2004).

- We obtain useful insights about the limitation of the results by changing the mass and maximum allowed spatial resolution in our suite of simulations. The lack of evolution at the high mass end of the HMF in Figure 4.12 is consistent with the prediction of 'freeze out' happening at $z = -0.6$. By adjusting the mass resolution, we alter the extent of the HMF at the low mass end, evident in Figure 4.16. On the other hand, the maximum spatial resolution of the simulation has a more drastic impact on the HMF at late times. Since the force resolution is twice the spatial resolution in `Enzo`, the expansion of the universe translates to a deteriorating force resolution. It leads to the loss of low mass haloes from the HMF. Eventually, the loss of these haloes affects the entire HMF. We, therefore, conclude that the maximum level of AMR is the most critical factor to extend the period in which we can trust the simulation results. From our simulation with the best spatial resolution, *NL+1*, its HMF is valid up to $z = -0.92$ or $t \approx 4t_{\rm H}$.

- We show in Figure 4.17 that these resolution changes do not affect the evolution of the IGM significantly. The balance of the photoheating rate from the UV background and the adiabatic cooling due to the expansion of the universe creates a tight relation between temperature and density of gas in the IGM. This balance is disrupted into the future because the photoheating rate decreases due to the falling star formation rate while the adiabatic cooling rate increases because of the accelerated expansion of the universe. In the far future, the majority of gas in the IGM cools to the CMB temperature floor causing the gas temperature to be insensitive to its density and the mean density to be exactly the temperature floor across all simulations.

- In Figure 4.22, we show that our simulations reproduce a peak in SFRD. This peak is, however, lowered and delayed as compared to the fit by Madau & Dickinson (2014). The limited resolution in the simulations causes this difference because it restricts the onset of structure formation. Differences in star formation and feedback prescription also results in a significantly lower star formation rate and total stellar mass formed. We observe a turnaround in cosmic star formation rate at late times, which seems to depend on the spatial resolution of the simulation, making it a numerical artefact rather than physical. Integrating between $z = 8$ and $z = -0.993$, we obtain a good agreement between the simulated and predicted total stellar mass within the same order of magnitude except *NLfb*. The ratio of simulated to predicted total stellar mass reaches as high as 99% in *NL+1* which did not exhibit a turnaround within the timescale of integration.

- Lastly, we select haloes within 10% of the virial mass of the MW-halo in *zoom* and compare the evolution of various properties of these haloes from *NL* in Figure 4.28. Although the resolution differs by a large margin, the general evolution of a MW halo in *zoom* is similar haloes of similar mass in *NL*. There is also a crossover of $m_*/m_{\rm bar}$ and $m_{\rm gas}/m_{\rm bar}$ at $t \approx 30\,{\rm Gyr}$ which coincides with the period of 'freeze out' in both *zoom* and *NL*.

We have studied the evolution of the IGM extensively and compared our results to those from Nagamine & Loeb (2004). Despite differences in the methodology of the simulation code, star formation and feedback prescription, we obtain a general agreement of the results. The aim of this study of the IGM is to understand the long-term supply of gas into the haloes, fueling future star formation. With this purpose in mind, we consider the significance of the presence of an isolated island of cold dense gas in Nagamine & Loeb (2004)'s simulated universe. Unlike our simulation, this gas is not converted to stars, causing possible disparities in the late-time star formation rates, leading to deviations of the asymptotic stellar mass formed.

This discrepancy is especially concerning for the purposes of this thesis, which includes using the asymptotic star formation efficiency as weights for counter-factual universes in a multiverse setting. Before the unphysical turnaround in SFRD, our simulations reproduce an evolution of the cosmic SFRD that is similar to the analytic fit of the observed SFRD from Madau & Dickinson (2014). Although limited resolution of our simulations means the

exact time and value of the SFRD peak is different from that predicted from the fit, we obtain a remarkable convergence of the asymptotic stellar mass from the analytic fit and our simulations. This agreement means that our simulation is calibrated to predict a realistic asymptotic star formation efficiency for our ΛCDM universe. We can then use these parameters to simulate counter-factual universes in Chapter 5 and quantify how cosmology influences the asymptotic star formation efficiency.

Chapter 5

Fates of baryons in counter-factual universes

In Chapter 4, we explored the usage of galaxy formation models through cosmological simulation to account for the evolution of the cosmic SFRD in a ΛCDM universe. We studied the impact of resolution and subgrid physics on the star formation history by comparing various simulations and the analytical fit to the cosmic star formation history beginning from $z \approx 8$ from Madau & Dickinson (2014). The observed star formation rate density (SFRD) peaked around $z = 2$ before starting to decline exponentially. In this Chapter, we want to understand how the cosmological parameters affect this evolution through simulations of counter-factual universes.

In the future, the expansion of the universe results in the 'freeze out' of the growth of large scale structures. It represents a point in time where the haloes are highly isolated, allowing for only internal evolution. This process causes a deprivation of gas that is required to fuel star formation, making it one of the reasons for the exponential decline of the cosmic SFRD at late times (Salcido et al., 2018). If 'freeze out' is crucial to explain the decline in star formation, then it is also essential to consider the cause of this phenomenon: the cosmological constant Λ. Because of its small positive value, vacuum repulsion can overcome gravity, causing our universe to expand. However, as we saw in Chapter 1, the value of Λ does not seem to converge between calculations and observations. From quantum field theory, the minimum energy density of Λ is estimated to be $10^{27}\,\mathrm{kg\,m^{-3}}$ (Zel'Dovich, 1967; Zel'dovich, 1968). This value is 46 orders of

magnitude larger than the maximum observational value of $10^{-26}\,\mathrm{kg\,m^{-3}}$. This discrepancy is known as the 'cosmological constant problem' (Weinberg, 1989; Carroll, 2001). The anthropic principle is an alternate explanation invoked to explain the small value of Λ. It can be classified into weak and strong anthropic reasoning. The former states that the presence of observers biases the observed properties of the universe (Carter, 1974) while the latter argues that one of the universes in a multiverse setting has to be in this condition for observers to exist (Barrow & Tipler, 1986).

We have shown in Chapter 4 that we have the ability to carry out a simulation of a realistic ΛCDM universe. Not only were we able to replicate a similar evolution of cosmic SFRD, we derived an asymptotic stellar mass that is in excellent agreement with the predicted value from the analytic fit to the observations. Therefore, we are now ready to apply these tools in the context of a multiverse to simulate counter-factual universes. The concept of a multiverse is suggested by many models of inflation where the universe as a whole consists of multiple bubbles, which are equivalent to inflationary patches or sub-universes (Vilenkin, 1983; Linde, 1986). The values of the physical constants and cosmic parameters can differ drastically from one to the other if we subscribe to the idea of an enormous number of vacuum states (10^{500}) (Woit, 2006). These states are sufficiently diverse to include all possible universes.

In this infinite number of possible universes, applying the anthropic principle already rules several of these universes out as not conducive to harbouring observers. For a universe with a large positive Λ, it will experience an expansion so rapid that structure formation will be limited. Similarly, for a recollapsing universe with large negative Λ, structures form so late that it is close to the end of the universe's lifetime. Without meaningful structure formation, the resultant lack of galaxies and stars will inhibit the presence of observers. As a result, the cosmological constant must be of a small value in universes that host observers, providing the solutions to questions about the scale of vacuum energy and existence of observers (Peacock, 2007). With the anthropic principle, one can therefore deduce an upper limit on the value of Λ (Weinberg, 1989). Efstathiou (1995) calculated the expected value of the distribution of Ω_Λ and approximated it to be 0.9, which is close to the observed value of approximately 0.7. Weinberg (2000) did a similar study, estimating an upper limit on Λ to allow for the formation of galaxies that is roughly 200 times the present mass density.

In this Chapter, we apply cosmological box simulations of counter-factual universes to refine and extend the work of Weinberg (1989), Efstathiou (1995) and Peacock (2007). We utilise these hydrodynamical simulations to explore the sensitivity to Λ of structure formation and, subsequently, galaxy formation and evolution. We assume a flat universe and scale the cosmological parameters within the ΛCDM cosmology. Also, we modify the value of σ_8 in the observed cosmological parameters (Bennett et al., 2013) because raising Λ produces the same effect as lowering σ_8 in terms of reducing the final post-freezeout inhomogeneity. Therefore, by comparing the two approaches, we can diagnose the importance of when 'freeze out' happens as opposed to the level of inhomogeneity at that time. Furthermore, we scale the UV background according to the ratio of star formation rates in each of these counter-factual universes to that of ΛCDM. This approach allows us to explore the extent of influence the UV background has on the properties of baryons in the counter-factual universes.

This Chapter is structured as follows. Section 5.1 will describe the method used to scale counter-factual cosmological parameters from the ΛCDM model. These will be inputs for the generation of the initial conditions. Also, we will mention the code and setup used to evolve and analyse the simulation results. Section 5.3 will present and discuss various quantities such as the cosmic SFRD, equation of state of the IGM and the sensitivity of these results on the UV background applied in each simulation. We will also compare and contrast the results with analytical approximations from Efstathiou (1995) and Peacock (2007), as well as other simulation studies Barnes et al. (2018). Lastly, Section 5.5 will summarise the results and provide a conclusion to this Chapter.

5.1 Initial conditions

The simplest anthropic ensemble is a subset within the multiverse in which only the value of Λ varies between the universes. All other dimensionless numbers such as the photon-to-baryon ratio remains constant at the values in our ΛCDM universe. Imagine making multiple copies of the universe at high redshifts when Λ is so small that its effect is non-existent. We can then scale Λ up or down in these universes, which will have negligible effect until Λ dominates. It will modify the cosmological parameters at $z = 0$, defined as the time when the temperature of the CMB is 2.725 K. To determine the cosmological parameters with the scaling of Λ, we employ the separate universe technique discussed in Wagner et al. (2015).

We modify the mean background density of a counter-factual cosmology with the overdensity δ_ρ of the ΛCDM cosmology (Sirko, 2005; Baldauf et al., 2011; Sherwin & Zaldarriaga, 2012; Li et al., 2014; Schmidt et al., 2018; Barreira et al., 2019) in the form

$$\rho(t)[1 + \delta_\rho(t)] = \tilde{\rho}(t), \tag{5.1}$$

where $\tilde{}$ refers to the modified cosmology that we are interested in. This methodology extracts a region in ΛCDM with overdensity δ_ρ and considers it as a different universe with an appropriately modified cosmology.

At an early enough time in the Universe, t_i, δ_ρ is so small that the scale factor of these different cosmologies are identical, i.e., $a(t_i) = \tilde{a}(t_i)$. With the definition of $\rho(a = 1) = \Omega_m \rho_c$ where $\rho_c = 3H_0^2/8\pi G$ and $H_0 = 100\,\mathrm{km\,s^{-1}\,Mpc^{-1}}$, we can express Equation 5.1 as

$$\frac{\Omega_m h^2}{a^3(t)}[1 + \delta_\rho(t)] = \frac{\tilde{\Omega}_m \tilde{h}^2}{\tilde{a}^3(t)}, \tag{5.2}$$

which simplifies to

$$\Omega_m h^2 = \tilde{\Omega}_m \tilde{h}^2, \tag{5.3}$$

at early times.

Suppose we scale Λ by a factor α at some early time when the scale factor is a_i, the subsequent evolution of the Hubble parameter is

$$H^2 = H_i^2[(1 - \alpha\epsilon)(a_i/a)^3 + \alpha\epsilon)], \tag{5.4}$$

where $\epsilon = \rho_v/\rho_{\mathrm{tot}}$ at a_i. We assume that spatial flatness is maintained in Equation 5.4. At early times, ϵ is small enough that we can neglect the $(1 - \alpha\epsilon)$ factor. Equating to the reference ΛCDM model, $H^2 = H_0^2(\Omega_m a^{-3} + 1 - \Omega_m)$, this allows $H_i^2 a_i^3$ and $H_i^2 \epsilon$ to be re-expressed in terms of the usual parameters by taking $\alpha = 1$. This results in the evolution of H as

$$H^2 = H_0^2[\Omega_m a^{-3} + \alpha(1 - \Omega_m)]. \tag{5.5}$$

To translate into the modified cosmology parameters, we equate Equation 5.5 to $\tilde{H}_0^2[\tilde{\Omega}_m \tilde{a}^{-3} + (1 - \tilde{\Omega_m})]$. In this case, $\tilde{a}$ and a are equivalent because they refer to the scale factor of the same modified cosmology. At $\tilde{a} = a = 1$, we can

express $\tilde{H}_0$ in terms of our reference parameters,

$$\tilde{H}_0 = H_0[\Omega_m + \alpha(1 - \Omega_m)]^{1/2}, \tag{5.6}$$

and from Equation 5.2, the new density parameter must satisfy

$$(1 - 1/\tilde{\Omega}_m) = \alpha(1 - 1/\Omega_m). \tag{5.7}$$

After the determination of the modified cosmological parameters, we have to define $\tilde{\sigma}_8$ in this modified cosmology. If the comoving length in the reference ΛCDM model R is $8\,h^{-1}$ Mpc, then $\sigma(R)$ is unchanged at high redshift. However, $\sigma(R)$ at $z = 0$ is now altered because the modification of the value of Ω_m will change the linear growth factor (see Equation 1.21). Finally, because R is no longer $8\,h^{-1}$Mpc in terms of $\tilde{h}$, we need to scale $\sigma(R)$ by a factor that depends on the shape of the power spectrum. The value of $\tilde{\sigma}_8$ can then be obtained with $\tilde{\sigma}$ at $8\,\tilde{h}^{-1}$Mpc.

On top of simulating universes by modifying the entire suite of cosmological parameters, we also attempt a set of simulations that retain the values of the ΛCDM universe with changes to σ_8 only. Since σ_8 provides a measure of mass inhomogeneity, i.e., the density field averaged in spheres of radius $8\,h^{-1}$Mpc, it can be altered independently to mimic one aspect of the effect of changing Λ. In general, a modified universe with a higher value of Λ corresponds to a ΛCDM universe with a lower asymptotic value of σ_8 at late times. This matching attempts to obtain the same degree of collapse, yielding the same number of objects of a given mass. However, this degeneracy only applies at a single redshift and we are most concerned with the value of σ_8 in the far future. To what degree will the results change due to this single number as opposed to the evolutionary track by which it was attained? This question motivates us to scale σ_8 in order to obtain an equivalent combination of the cosmological parameters to one where Λ is changed. We know that $d\ln\delta/d\ln a \approx \Omega_m^{0.55}$ (Linder & Cahn, 2007) and growth freezes when $\Omega_m = \Omega_\Lambda = 0.5$ (see Equation 1.21). Suppose we take a universe where we increase ρ_Λ by two orders of magnitude, the scale factor where $\rho_\Lambda = \rho_m$ is reduced to $\sqrt[3]{100}$. Since we are in the linear regime of the power spectrum, we reduce the value of σ_8 in the reference ΛCDM universe by $\sqrt[3]{100}$ accordingly.

Table 5.1 List of simulations in this Chapter with their corresponding reference name from this point onwards. We have included Ω_m, Ω_Λ, Ω_b, σ_8, h, cosmological box size of the simulations and starting z of the simulations. Refer to Section 5.2 for more information about the naming convention and specifics of each simulation.

Simulation setup list							
Reference name	Ω_m	Ω_Λ	Ω_b	σ_8	h	Box size [h^{-1}cMpc]	starting z
LCDM	0.285	0.715	0.0461	0.828	0.695	50	99
EDS	1.000	0.000	0.1618	0.6786	0.371	26.69	25.69
10x	0.0383	0.9617	0.0062	0.8742	1.895	136.34	99.027
100x	0.004	0.996	0.00065	0.7217	5.8885	423.63	98.748
s5x	0.285	0.715	0.0461	0.484	0.695	50	99
s10x	0.285	0.715	0.0461	0.384	0.695	50	99
s20x	0.285	0.715	0.0461	0.305	0.695	50	99
s100x	0.285	0.715	0.0461	0.178	0.695	50	99

5.2 Simulation setup

The scaling relations from Section 5.1 allow us to produce sets of cosmological parameters to either change the values of Λ or σ_8 from a reference ΛCDM universe. These are summarised in Table 5.1. The reference ΛCDM cosmological parameters are obtained from WMAP-9 (Bennett et al., 2013). They are $\Omega_m = 0.285$, $\Omega_\Lambda = 0.715$, $\Omega_b = 0.0461$, $h = 0.695$ and $\sigma_8 = 0.828$ with their usual definitions. We generate the initial conditions for these universes with MUlti-Scale Initial Conditions (`MUSIC`) for cosmological simulations (Hahn & Abel, 2011) and evolve them with Enzo (Bryan et al., 2014) using the hydrodynamic solver, `ZEUS` (Stone & Norman, 1992) and N-body adaptive particle-mesh gravity solver (Efstathiou et al., 1985). We also couple the simulation with `Grackle` and all the modifications detailed in Section 4.2.3. As in previous chapters, we adopt the model described by Cen & Ostriker (1992) and Smith et al. (2011)'s modified version of the Cen & Ostriker (2006) thermal supernova feedback for star formation and feedback respectively. The values of these parameters are obtained from the calibration made in Chapter 3.

From the reference cosmological parameters, we choose a value of α to scale Λ in order to derive $\tilde{\Omega}_m$ using Equation 5.2, which can then be used to calculate the remaining cosmological parameters. Evident from Table 5.1, we decide on $\alpha = 0, 10, 100$ that corresponds to simulations labelled as *EDS*, *10x* and *100x* respectively. For $\alpha = 0$, it refers to a universe fully dominated by

matter, equivalent to the EdS universe discussed in Chapter 1. We also scale σ_8 with $\alpha = 5, 10, 20, 100$. More values are included to provide better coverage since scaling σ_8 is more straightforward than scaling Λ. These simulations are named *sαx* with a 's' prefix to distinguish them from the simulations with scaled Λ.

In addition to cosmological parameters, Table 5.1 includes two additional columns of the comoving box size and starting z required to generate the initial conditions for the counter-factual universes. For *LCDM*, the mass and maximum spatial resolutions are identical to *NL* indicated in Table 4.1 in Chapter 4. Since the comoving box size is in h^{-1}Mpc, we have to change the box size according to h at $z = 0$ in different cosmologies to maintain a consistent spatial resolution across all simulations. Again, this process is relatively straightforward for simulations with scaled σ_8 since h is constant. For *EDS*, *10x* and *100x*, h is significantly different between the universes. Therefore, we adjust the box size accordingly (see Table 5.1).

The starting z of the simulations also has to be adjusted such that the universes are at the same starting age. We can convert the starting z of 99 in *LCDM* to a corresponding starting z of the counter-factual universes with Equation 4.1. Because of the lack of dependence of σ_8 in Equation 4.1, we do not need to change the starting redshifts for simulations with scaled σ_8. For *EDS*, *10x* and *100x*, the starting redshifts have been adjusted to 25.69, 99.03 and 98.78 respectively. These adjustments in the simulation box size and starting z maintain consistency across all counter-factual universes that we are simulating.

5.3 Results and discussion

In this section, we will make a similar comparison of various properties of both gas and dark matter in the simulations (see Chapter 4). Rather than the effect of resolutions, we look at how cosmology, specifically Λ, affects the picture of structure formation and evolution. With the asymptotic star formation efficiency in the different universes with this suite of simulations, we can extend the works of Weinberg (1987), Efstathiou (1995) and Peacock (2007). We will investigate the applicability of the anthropic reasoning on the cosmological constant and explore the idea of a multiverse.

5.3.1 Agreement at high redshifts

We first have to establish the validity of our simulations since there are no observations for counter-factual universes. Recall that α is applied at high z in Equation 5.4 when Λ is still relatively insignificant. At this epoch, the distribution of temperature and overdensity of the gas in the simulations should be very similar because the universe is matter-dominated. Assuming we have adjusted all relevant parameters correctly, the simulations should be identical to each other. We illustrate this test of our simulations in Figure 5.1. It is presented in the form of a phase distribution similar to Figure 4.10, where we investigate how the gas in different cosmologies is distributed in the temperature-baryon overdensity phase space. Panels (a), (b), (c) and (d) corresponds to *EDS*, *LCDM*, *10x* and *100x* respectively.

We illustrate this distribution at $t = 1.09\,\mathrm{Gyr}$ for all counter-factual universes except *EDS*. While the specific features of the phase distribution differ from one simulation to the next, the general distribution of gas in the temperature-overdensity plane is very similar at similar times. The reason why we did not obtain a higher level of agreement is that we are not looking at a high enough z. $t = 1.09\,\mathrm{Gyr}$ in *LCDM* translates to $z = 5.36$. At this point, even though Λ is not dominant, it is no longer insignificant. Therefore, its effect manifests in the phase distribution, accounting for the slight deviations between counter-factual universes at a similar time in Figure 5.1. This reason also explains why there is not a need to obtain these distributions at an identical time across all simulations. These were not taken at a higher z because of restriction of the starting z of *EDS* (see Table 5.1) and allocation of time for numerical calculations to stabilise.

5.3.2 Halo mass functions in counter-factual universes

We have tested the sensitivity of the HMF to resolution and feedback prescription under 'Halo mass function' in Section 4.3.7. In this section, we replace resolution with cosmology and explore how the latter affects the evolution of the HMF in Figure 5.2. We choose several snapshots at $t \approx 7,\ 14,\ 26,\ 51\,\mathrm{Gyr}$, which correspond roughly to $0.5\,t_\mathrm{H}$, t_H, $2\,t_\mathrm{H}$ and $4\,t_\mathrm{H}$ with $t_\mathrm{H} \approx 13.7\,\mathrm{Gyr}$ in panels (a) to (d) respectively. Each coloured line refers to the same cosmology consistently across the panels as indicated in the legend and caption.

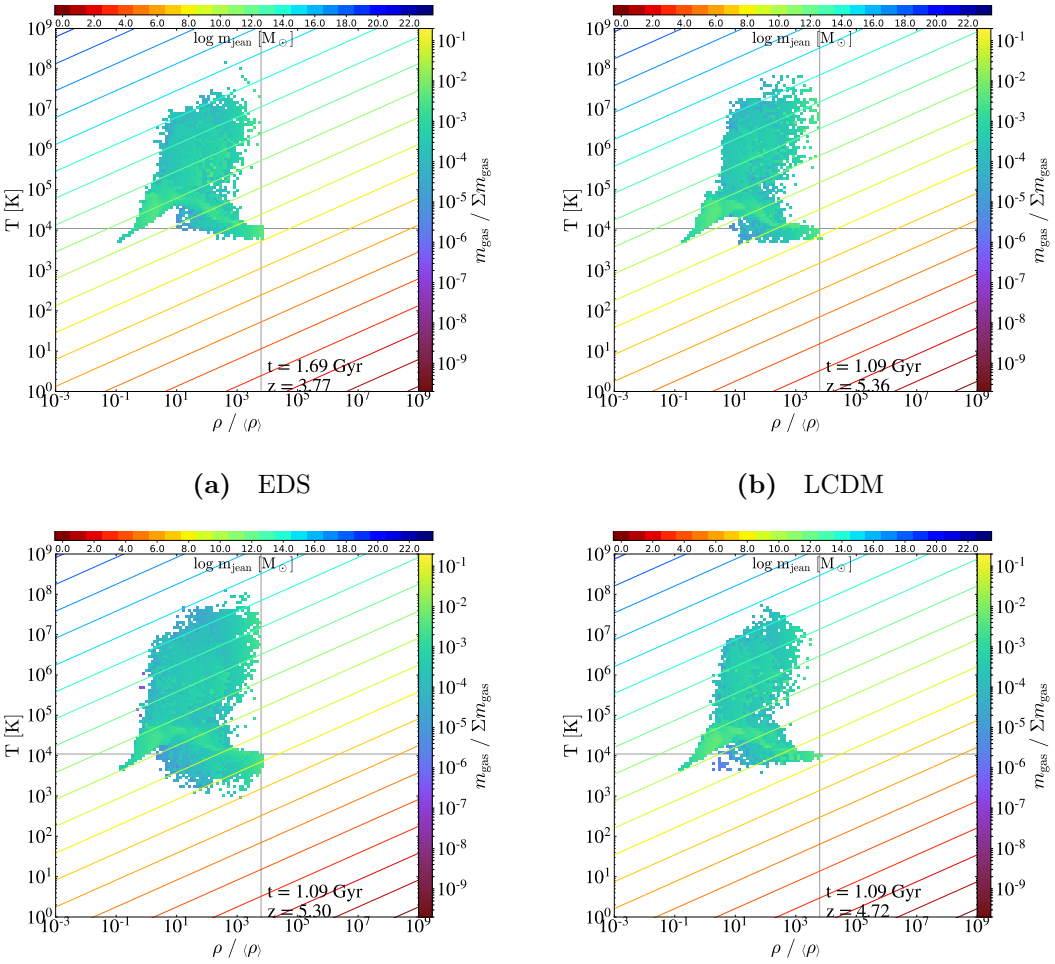

(a) EDS **(b)** LCDM

(c) 10x **(d)** 100x

Figure 5.1 Gas mass in bins of overdensity and temperature of the gas in simulations of different α indicated in the captions. Except *EDS* which is at $t = 1.69\,\mathrm{Gyr}$, the remaining simulations are at $t = 1.09\,\mathrm{Gyr}$. We want to show that the general features from the plots are similar to each other with some specific differences at similar times. This similarity is expected and provides a check to the accuracy of the setup of the simulation. Refer to Section 5.3.1 for further discussion.

Since structure formation in the CDM paradigm happens in a bottom-up manner, low mass haloes first form from the primordial density fluctuations before merging to form massive haloes. This process explains the general trend that the HMF 'enters' the plot in Figure 5.2 from the low mass end. The HMF then grows and move towards higher mass as the number and mass of the haloes increase. However, recall the evolution into the future (see Section 4.3.5), where the expansion of the universe causes a deterioration of the force resolution in the simulations. Without appropriate force resolution, the particles

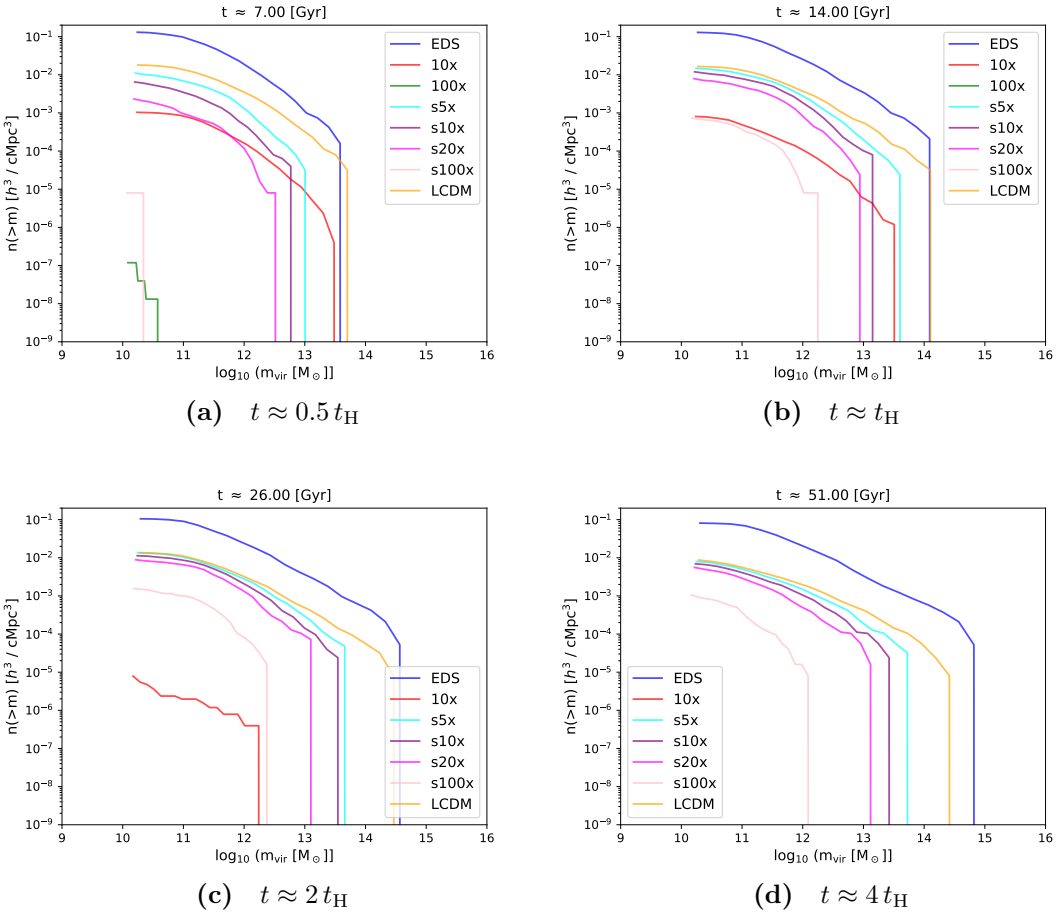

(a) $t \approx 0.5\,t_{\mathrm{H}}$ **(b)** $t \approx t_{\mathrm{H}}$

(c) $t \approx 2\,t_{\mathrm{H}}$ **(d)** $t \approx 4\,t_{\mathrm{H}}$

Figure 5.2 Time evolution of the HMF from the simulations of different cosmology. The blue, red, green, cyan, purple, magenta, pink and orange lines refer to *EDS*, *10x*, *100x*, *s5x*, *s10x*, *s20x*, *s100x* and *LCDM* respectively. These are presented at the times labelled in the captions. The general evolution is the HMF will 'enter' the plot from the left, before turning around at a certain point in time and 'exiting' the plot from the left again. We observe and explain a similar trend in Figure 4.12. Refer to Section 5.3.2 for a detailed description and comparison of the evolution of the HMFs in different cosmologies.

are unable to feel the gravitational force, causing the haloes to dissolve and fade into the background. The loss of haloes begins in the low mass end and eventually propagates to the high mass end where the massive haloes start to lose their subhaloes. This loss reduces the mass of the most massive haloes, causing the HMF to start moving towards the low mass end before eventually disappearing from the plots (see red line in Figure 5.2 and Section 4.3.5 for detailed explanation).

Even though the general evolution is consistent for different cosmologies, the turn around of the HMF occurs at different times. Considering that the

turnaround or loss of haloes is due to worsening force resolution, it will depend heavily on α. With a larger α, Λ dominates earlier in the universe. Not only does it accelerate the expansion, but it also leads to an earlier stagnation of the growth factor. In other words, 'freeze out' occurs earlier in a universe with a larger α. As a consequence, the number density of haloes across the mass range and the mass of the most massive halo decreases earlier with higher α. This difference is obvious when we compare *10x* (red), *100x* (green) and *LCDM* (orange) in Figure 5.2. Particularly, in panel (a) of Figure 5.2, *100x* is deviating significantly from *10x* and *LCDM* because *100x* is already at the point of time where the force resolution is so poor that it is losing the haloes. *10x* then starts to experience this between $t = 14.00\,\mathrm{Gyr}$ and $t = 26.00\,\mathrm{Gyr}$ while it is still not evident in *LCDM* yet. However, this phenomenon does not apply to *EDS* where $\alpha = 0$. If we trace the evolution of the blue line across time, we see that the most massive halo in the simulation continues to gain mass as structure formation proceeds. Because of the slower rate of expansion in *EDS*, the force resolution of the simulation remains adequate to hold dark matter particles together. Furthermore, haloes continue to grow because it has not encountered 'freeze out' in *EDS*.

What happens when we scale σ_8 within ΛCDM? As we decrease this value, it affects the clustering of haloes. If we compare the HMFs of *sαx* to *LCDM*, we can see differences in both number density and mass of the haloes across the entire range. If we cross-compare *10x* and *s10x*, and *100x* and *s100x* respectively, it is clear that simply reducing the value of σ_8 by the corresponding factor does not have the same effect on the HMF. For example, in panel (a) of Figure 5.2, the low number and mass of haloes associated with *100x* is due to the worsening of the force resolution whereas the haloes in *s100x* are in its early stage of formation and evolution. In summary, scaling Λ is not equivalent to scaling σ_8 in terms of their impact on the HMF. If we adjust Λ, we are modifying the rate of expansion of the universe, which influences both the force resolution and the clustering of matter. On the other hand, changing σ_8 does not affect the expansion of the universe, resulting in a significantly different HMF evolution.

Let us now assume that the simulations have infinite resolution such that the issue about force resolution does not occur. It will then reduce to a timing issue of when 'freeze out' occurs in each counter-factual universe. For universes with scaled Λ, e.g., *10x* and *100x*, 'freeze out' will happen at an earlier time which means HMF will remain constant earlier. The opposite is true for *EDS*. For universes with scaled σ_8, 'freeze out' will occur at an identical time. However,

the clustering associated with the value of σ_8 will cause the deviations in the HMFs that we observe in Figure 5.2 before force resolution becomes a problem. Since we have established convergence of the results at $t \approx 4\,t_{\rm H}$ (see 'Halo mass function' under Section 4.3.7), we would expect the differences between *sαx* and *LCDM* to remain constant from this point on, assuming infinite resolution.

5.3.3 Star formation histories in counter-factual universes

After we understand how the HMF evolves differently in each counter-factual universe, we investigate how the SFRD in these haloes is influenced by cosmology in this section. We trace the evolution of the SFRD to the maximum allowable time without the simulation crashing. In particular, we can trace the SFRD of *EDS* to approximately 1200 Gyr as compared to approximately 26 Gyr for *100x*. This considerable difference suggests that the simulation code is not fully optimised to handle a simulation with extremely rapid expansion. However, this time is sufficient to make comparisons since both the HMF (see Section 5.3.2) and cosmic SFRD discussed in this section of *100x* are significantly lesser than other counter-factual universes in terms of value and evolution with time. We illustrate the evolution of the SFRDs in these universes with Figure 5.3.

It is clear from Figure 5.3 that the SFRD differs significantly between counter-factual universes. Each cosmology leads to a different peak in SFR in terms of both the time it occurs and the value. For a universe with a higher α, the peak in SFRD happens earlier and reaches a lower maximum value. Such a relation is expected given the consistency of the subgrid physics across all simulations. With a higher value of α, Λ dominates earlier in the universe, leading to the loss of haloes seen in the HMF (see Section 5.3.2). Due to the decrease in both the number and strength of the gravitational potential wells, star formation is affected adversely (see Figure 4.23). Limited amounts of gas can fall into the haloes, thereby restricting the conversion of gas into stars, causing an earlier and lower SFRD peak. For counter-factual universes with scaled σ_8, structure formation is always hindered (see Figure 5.2). This stunted growth in structures translates to reduced star formation. Significant differences exist between the SFRD of corresponding pairs of αx and $s\alpha x$ universes, proving that the evolution is sensitive to the time when 'freeze out' occurs.

The general evolution of the SFRD in *EDS* is also different from the rest. It has an oscillatory instead of a well-defined SFRD peak in its evolution. The

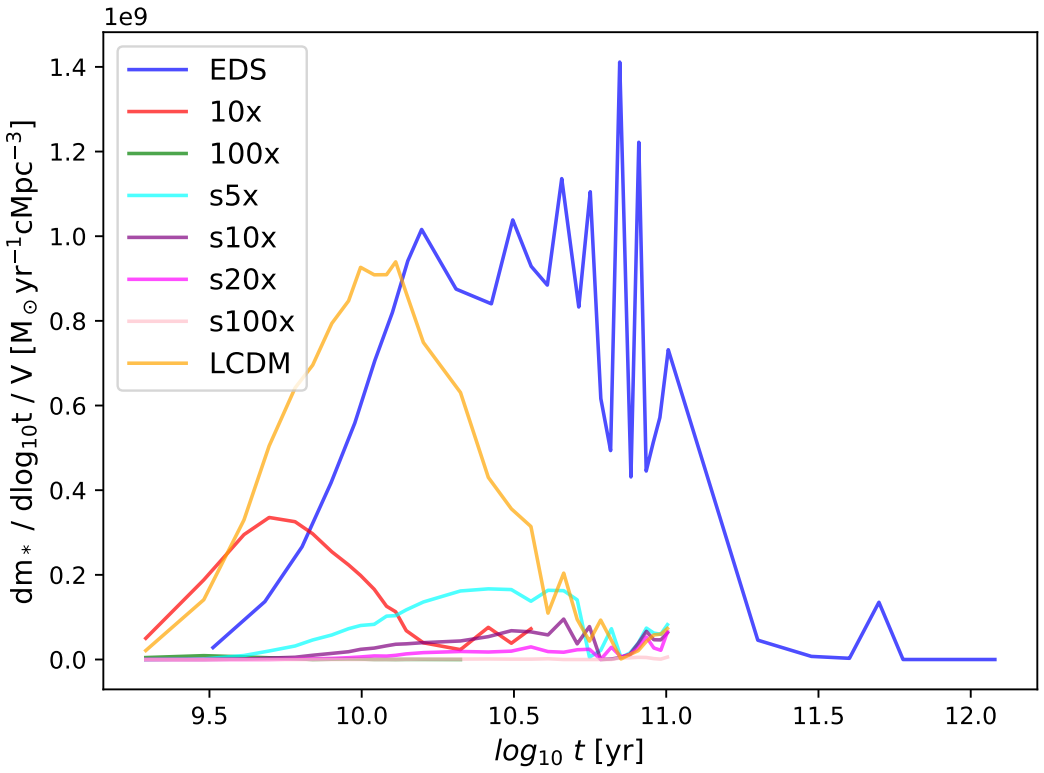

Figure 5.3 Evolution of the SFRD for counter-factual universes across cosmic time. We use identical colours as Figure 5.2 to represent the respective cosmology. The evolution of the cosmic SFRD differs significantly between the universes. We will discuss specific differences of the SFRD arising from the cosmology in Section 5.3.3.

reason behind these oscillations is the manifestation of feedback. When SFRD is high, more feedback energy is injected into the surrounding medium, prohibiting further star formation. When the SFRD is lowered, the corresponding feedback is also decreased, raising the ability of gas to cool and form stars again. We do not observe this prominent feature in other counter-factual universes, suggesting its possible association with the presence of a cosmological constant. Regardless, the true cause of the oscillations in *EDS* and a well-defined peak in SFRD is a topic for further explorations.

It is important to disentangle features in Figure 5.3 caused by numerical resolution or cosmology. Since we have established that the turnaround in SFRD is due to limitations in the resolution (see Section 'Star formation history' under 4.3.7), we can attribute any differences in the SFRD before this time to the different cosmologies. In summary, a larger α translates to a smaller σ_8, reducing the clustering of matter, which then leads to a lower peak in SFRD. A similar trend is observed when we scale Λ. However, the scalings are not equivalent, resulting in the obvious disparity between corresponding pairs of αx and $s\alpha x$ simulations. *EDS* is a special case because it has a lower expansion rate, which delays the onset of numerical resolution issues. It also exhibits an oscillatory behaviour at late times in stark comparison to the other counter-factual universes.

5.3.4 Tests of sensitivity to UV background

As a result of the differences in the SFRDs between different cosmologies, we expect the UV background in each counter-factual universe to vary as well. Since the UV background model of Haardt & Madau (2012) is derived from a fit to the evolution of the SFRD in Madau & Dickinson (2014), we should scale the UV background even in *LCDM* because our simulated SFRD in *LCDM* does not replicate the fit. However, since it is one of the observational constraints of *LCDM*, it should arguably not be altered. Of course, this is not so when we consider counter-factual universes, in which the UV background will have to be estimated in a self-consistent way. Before doing this, we look at the *LCDM* case in more detail, noting how our simulation reacts to different UV backgrounds, and how our SFRD discrepancy arises from the finite resolution of the simulations (see Section 4.3.7). In this section, we do a simple test of running pairs of similar simulations with and without a UV background to quantify its impact on both the evolution of the SFRD and IGM of the simulated universes. We begin with

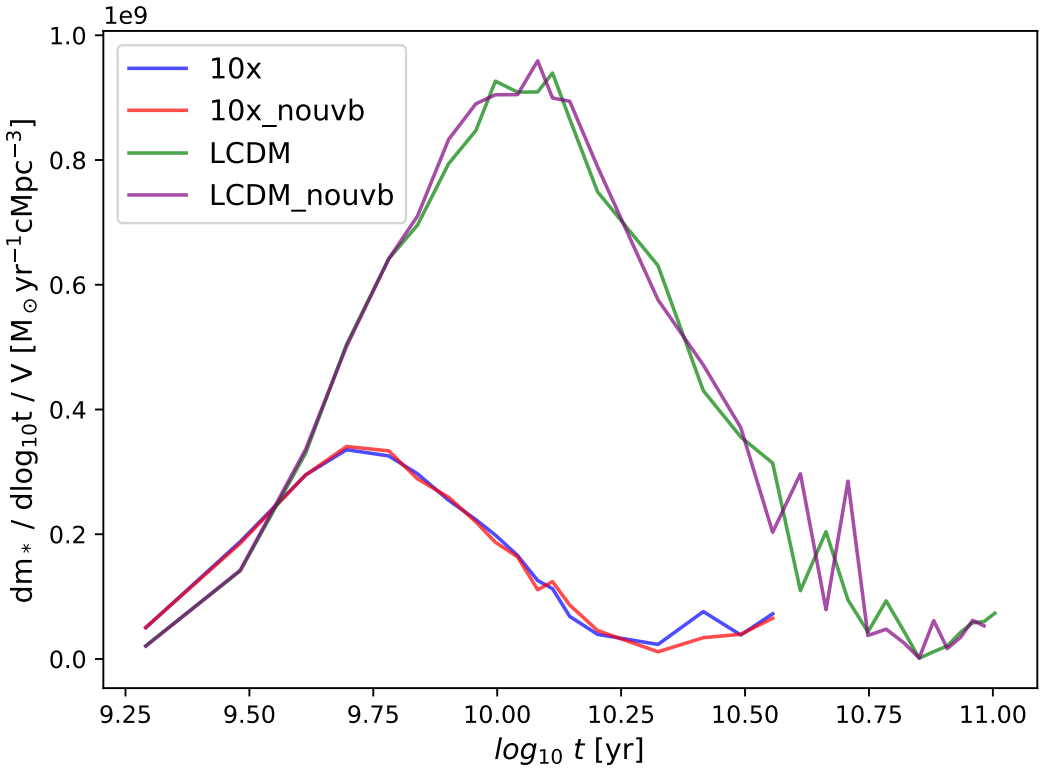

Figure 5.4 Comparison of cosmic SFRD of simulations with and without UV background. The blue, red, green and purple lines correspond to *10x*, *10x_nouvb*, *LCDM* and *LCDM_nouvb* respectively. The status of the UV background in these simulations is represented after the scaled cosmology in their names. The evolution of the cosmic SFRD is insensitive to the UV background and its the reasons will be discussed in Section 5.3.3.

the analysis of the SFRD in Figure 5.4.

It is evident from Figure 5.4 that the UV background does not influence the evolution of the SFRD in these simulations. Comparing *10x* (blue) and *10x_nouvb* (red), and *LCDM* (green) and *LCDM_nouvb* (purple), we see that the pairs of lines are indistinguishable. This agreement arises as a result of the mass resolution limit in our simulations. Previous work suggest that the UV radiation only suppresses star formation in haloes of mass below $10^7 M_\odot$ (Dawoodbhoy et al., 2018; Katz et al., 2019). Since this mass is well below the resolution limit of our suite of simulations (see Figure 5.2), we expect that the cosmic SFRD will be insensitive to the UV background.

While the cosmic SFRD is insensitive to the UV background, baryons in the form of underdense gas in the IGM are particularly susceptible to this radiation. This sensitivity is illustrated in Figure 5.5 where we show the evolution of γ and

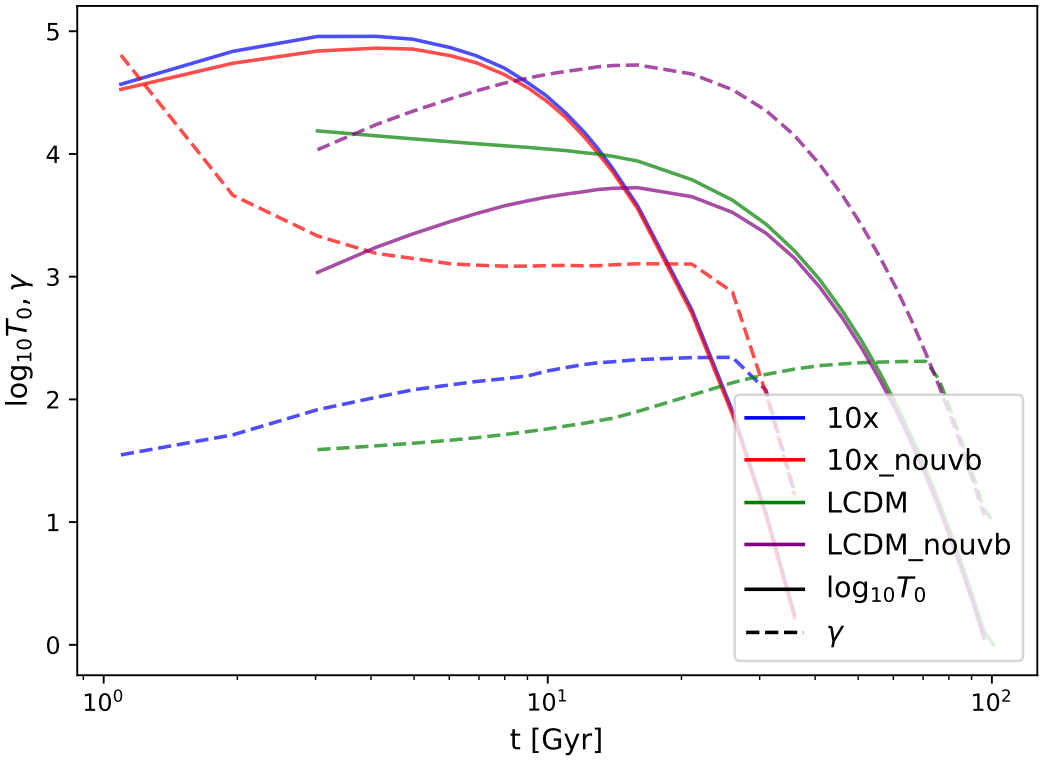

Figure 5.5 Evolution of γ and $\log_{10} \mathrm{T}_0$ across cosmic time for simulations with and without UV background. We use the same colours in Figure 5.4 for the different cosmologies. The state of the UV background in these simulations is also indicated in their names. While SFRDs do not depend on the UV background, the IGM is much more sensitive. Refer to Section 5.3.4 for further discussion.

$\log_{10} \mathrm{T}_0$ from Equation 4.7 against time for *10x* (blue), *10x_nouvb* (red), *LCDM* (green) and *LCDM_nouvb* (purple). See Sections 4.3.6 and 4.3.7 for definitions and methodology to extract the value of these parameters.

At late times when Λ is dominant, γ tends to zero as all the gas within the specified gas overdensity bins cools and approaches the CMB temperature floor set by Equation 4.6. This behaviour also explains the drop in T_0 regardless of the presence of UV background at late times. However, between the pairs of *10x* and *LCDM* simulations, the former hit the temperature floor earlier because of the increase in Λ. In short, the dominance of Λ is responsible for the similarity in the late time evolution of the IGM. At the same time, the scaling of Λ explains the slight deviation in the timing when the late time similarity is achieved.

On the other hand, the early time properties of the IGM are highly sensitive to the UV background. We first compare T_0 within the pair of corresponding simulations. Without a UV background, there is no source of heating which

lowers the value of T_0. This difference in T_0 diminishes with time for reasons explained before. Because Λ dominates earlier in *10x*, the difference of T_0 with and without UV background is significantly smaller than that of *LCDM*. Without a UV background in the simulation, the slope of the power-law fit to the IGM is consistently steeper than that with UV background among the pairs of simulations. Comparing *10x* and *LCDM*, the value and evolution of γ are very similar despite the difference in cosmology, suggesting that UV background plays a vital role in regulating the value. When we switch off the UV background, γ deviates significantly, further indicating that the UV background affects the IGM significantly.

To better illustrate the early time deviations between simulations of identical cosmology with and without a UV background, we overlay the power-law fit to the IGM in a volume-weighted distribution of gas temperature and density plot in Figure 5.6. Within each panel, the left and right plots are simulations of an identical cosmology with and without a UV background. Panels (a) and (b) correspond to simulations of *10x* cosmology at an early ($t \approx 1.95\,\mathrm{Gyr}$) and late time ($t \approx 26.05\,\mathrm{Gyr}$) respectively. Panels (c) and (d) are obtained from simulations with *LCDM* cosmology at an early ($t \approx 3.03\,\mathrm{Gyr}$) and late time ($t \approx 71.03\,\mathrm{Gyr}$) respectively.

The late time distribution of the gas temperature and overdensity is very similar within each cosmology regardless of the UV background as illustrated by panels (b) and (d). However, for simulations without a UV background, more gas is at the temperature floor, evident from the increased upper limit of overdensity. There is more cold gas because the source of heating is removed. On the other hand, panels (a) and (c) show significant differences between the pair of simulations at early times. Without the heating from the UV background, gas in the IGM can cool easily, hitting the temperature floor at an early time. Furthermore, there is a lack of a tight relation in the IGM of the left plots in both panels (a) and (c). Since UV radiation is an important process driving the formation of the tight power-law fit (McQuinn & Upton Sanderbeck, 2016), it will be absent in simulations without a UV background. In summary, the UV background significantly influences the evolution of the IGM, particularly at early times. The late time evolution of the simulated counter-factual universes will be dominated by Λ except in *EDS*, which we will discuss later. Therefore, there is a need to implement a self-consistent UV background in the simulations of counter-factual universes.

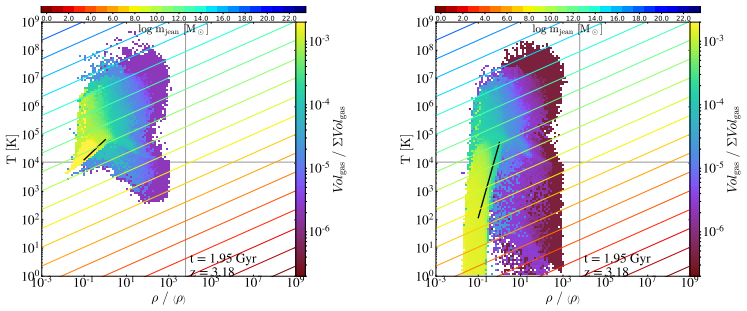

(a) *10x* (left) and *10x_nouvb* (right) $t \approx 1.95\,\mathrm{Gyr}$

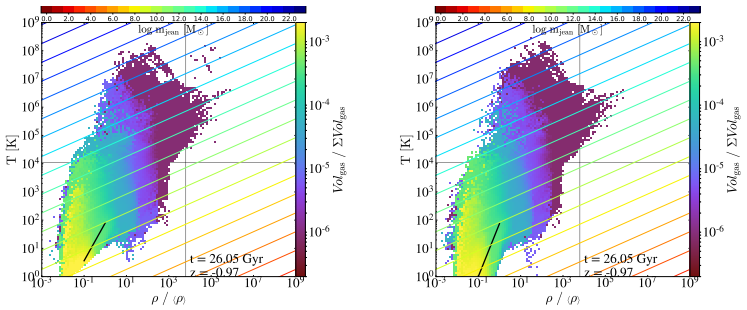

(b) *10x* (left) and *10x_nouvb* (right) $t \approx 26.05\,\mathrm{Gyr}$

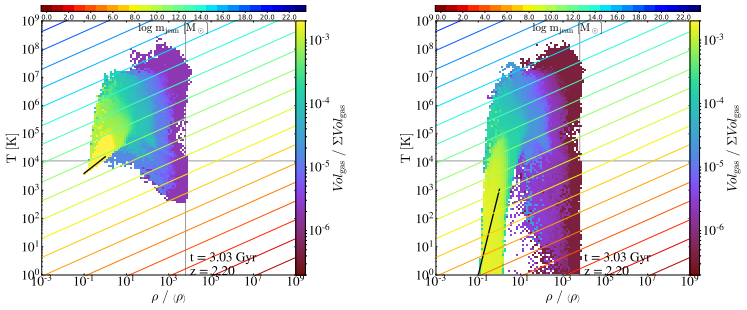

(c) *LCDM* (left) and *LCDM_nouvb* (right) $t \approx 3.03\,\mathrm{Gyr}$

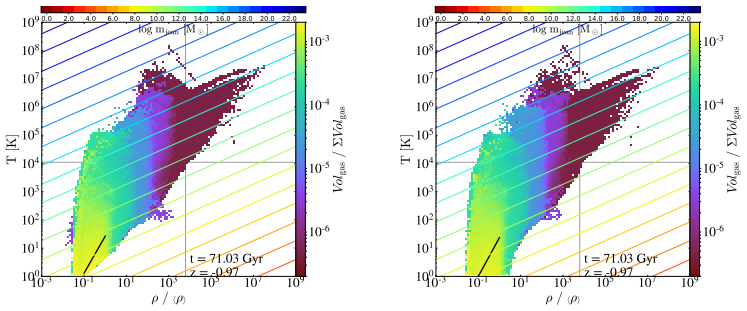

(d) *LCDM* (left) and *LCDM_nouvb* (right) $t \approx 1.95\,\mathrm{Gyr}$

Figure 5.6 Distribution of gas volume in bins of overdensity and temperature of the gas in the simulation volume at identical times. Within each pair, the left and right panels corresponds to simulations with and without UV background respectively. (a) and (b) correspond to the simulations within the *10x* cosmology while (c) and (d) are the simulations within the *LCDM* cosmology. Comparing the plots between each pair, it is clear that the impact of the UV background is most drastic at early times while the late time evolution are similar regardless of the UV background. Refer to Section 5.3.4 for detailed discussion.

5.3.5 UV background scaling

We will make the simple assumption that the UV background is dominated by young massive stars, whose short lifetime means that their abundance is directly proportional to the SFRD. Therefore, we will scale the UV background with the ratio of the SFRDs in each counter-factual universe to *LCDM* at identical times. We assume that at a particular time, the conditions of the different universes are identical to calculate the scaling

$$\frac{\Gamma_{\rm new}(t)}{\Gamma_{\rm LCDM}(t)} = \frac{\rm SFRD_{new}(t)}{\rm SFRD_{LCDM}(t)}, \tag{5.8}$$

where Γ is the photoheating rate from the UV background, subscripts 'new' and 'LCDM' represent counter-factual and *LCDM* cosmology respectively. We use time instead of redshifts to scale the UV background because the time associated with the redshift will vary for different cosmologies (see Equation 4.1).

According to our assumption, we have ignored any contribution from potential sources such as globular star clusters (Ricotti, 2004) or an early generation of black holes (Ricotti & Ostriker, 2004; Ricotti et al., 2005; Venkatesan et al., 2001). However, there is a lack of observations to support these proposed sources at the present moment (Meiksin, 2009). Quasars are the most probable alternative source to contribute to the UV background. However, the emissivity of quasars makes them sub-dominant in comparison to galaxies unless there is a significant number of very low luminosity AGNs (Meiksin, 2005; Bolton & Haehnelt, 2007; Srbinovsky & Wyithe, 2007). Therefore, we assume the UV background in counter-factual universes can be derived from Equation 5.8.

To obtain the ratio of SFRDs in different universes, we fit them with

$$\psi(z) = a\frac{(1+z)^b}{1+[(1+z)/c]^d}\ {\rm M_\odot\ year^{-1}\ cMpc^{-3}}. \tag{5.9}$$

where $a = 0.015, b = 2.7, c = 2.9, d = 5.6$ for the analytic fit to observations (see Equation 1.19). It is assumed that the SFRD from the simulations can be fitted with this double power-law in $(1 + z)$. We illustrate the goodness of the fit both visually and with the residuals in Figure 5.7. The different colours are consistent with previous figures that included all counter-factual universes. Overall, Equation 5.9 provides a reasonably good fit to the simulated data for

almost all counter-factual universes in Figure 5.7a. This is supplemented by the generally low values of residuals of SFRDs in Figure 5.7b. However, at specific times, the percentage difference increases above typical values of less than 0.5. If we refer to Figure 4.22, these times coincide with the turnaround in SFRD. In Chapter 4, we have established that this turnaround is not physical and most likely due to numerical limitations. Therefore, it is reasonable to ignore these data points.

The values of the fitted parameters of Equation 5.9 are summarised in Table 5.2. On top of these parameters, we also include the coefficient of determination or R-squared (R^2) value of the fit. It is calculated with

$$R^2 = \frac{\sum_{t=0}^{t} \left(\mathrm{SFRD}_{\mathrm{fit}}(t) - \overline{\mathrm{SFRD}}_{\mathrm{sim}}\right)^2}{\sum_{t=0}^{t} \left(\mathrm{SFRD}_{\mathrm{sim}}(t) - \overline{\mathrm{SFRD}}_{\mathrm{sim}}\right)^2} \tag{5.10}$$

where $\overline{\mathrm{SFRD}}_{\mathrm{sim}}$ denotes the mean of the SFRD from each simulation and the subscripts 'fit' and 'sim' refer to SFRD from our analytic fit and the simulation respectively. The purpose of this quantity is to provide a further quantitative measure of the goodness of fit in addition to Figure 5.7. The value of R^2 varies between zero and unity with higher values corresponding to a better fit. As we see in Table 5.2, counter-factual universes with scaled Λ can reproduce a similar trend in SFRD to our observed universe with R^2 value reaching as high as 0.99. *EDS* produced the lowest R^2 value of 0.911 among these simulations. Although it is still a good fit, the relatively lower value suggests that the simulated data can be better fitted with an equation other than Equation 5.9. On the other hand, universes with scaled σ_8 have much lower R^2 values. The value decreases with increasing α. Contrasting with simulations with scaled Λ, this proves again that scaling σ_8 does not mimic the effect of scaling Λ. Since there is little to no star formation across time in *s100x*, such a fit will not be appropriate and results in the radical values of the free parameters. Lastly, Equation 5.9 calculates the SFRD in terms of comoving volume, which has to be converted to physical volume in order to remove any dependency on cosmology.

Star formation history with scaled UV background

As a consistency check, we consider how the SFRDs in counter-factual universes might change after implementing the scaled UV background. Figure 5.4 pointed out that the SFRDs of *10x* and *LCDM* remains very similar with or without

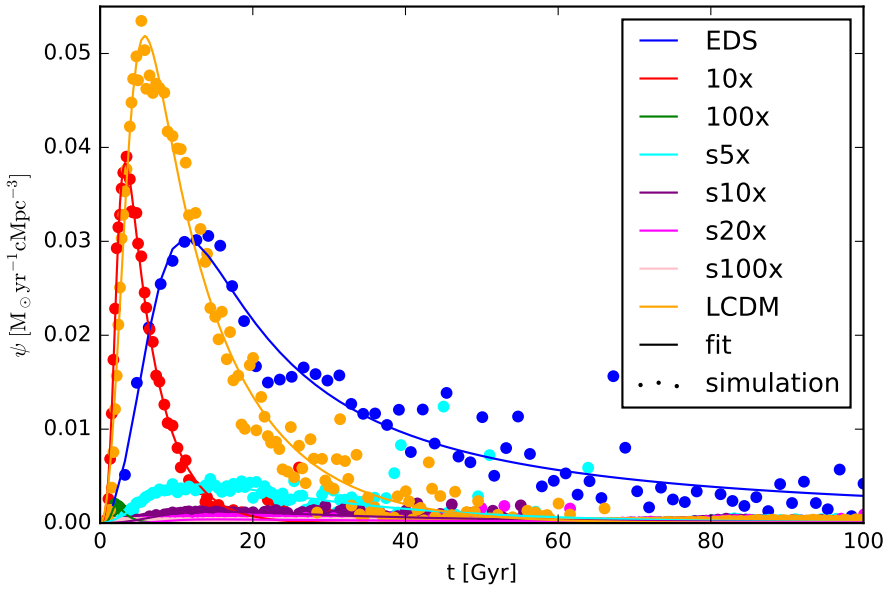

(a) Visual representation of fits

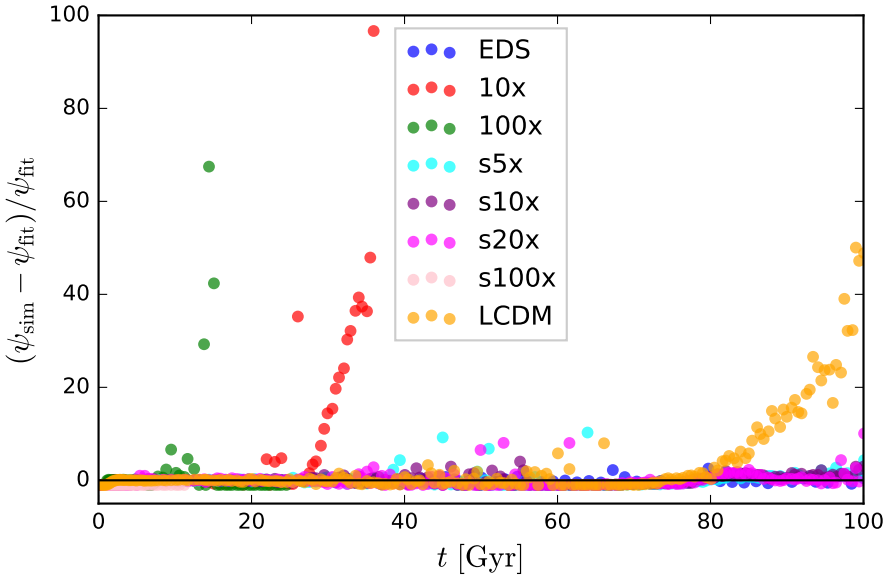

(b) Residuals of fits

Figure 5.7 Double power-law fit in $(1+z)$ of the SFRD obtained in both counterfactual and *LCDM* universes. The blue, red, green, cyan, purple, magenta, pink and orange lines and dots correspond to *EDS*, *10x*, *100x*, *s5x*, *s10x*, *s20x*, *s100x* and *LCDM* respectively. The residual is obtained as a ratio of the difference between the simulated and fitted SFRD to the fitted SFRD. In general, the fit is good in capturing the evolution of the SFRDs in different universes. However, there are significant deviations at specific times for certain simulations. The reason is discussed in Section 5.3.5.

Table 5.2 List of simulations in this Chapter with their reference name, the values of the best fit parameters of Equation 5.9 and their corresponding R^2 value. The goodness of fit varies significant between the two categories of the counter-factual universes. For universes with scaled Λ, the fit is much better than that of scaled σ_8 . Refer to Section 5.3.5 for more details.

Simulation setup list					
Reference name	a	b	c	d	R^2
LCDM	0.0259	1.56	2.35	4.70	0.983
EDS	0.0283	1.97	1.46	4.87	0.911
10x	0.0134	1.29	3.44	5.52	0.990
100x	0.000689	1.25	3.52	5.76	0.990
s5x	0.00508	0.740	1.53	3.46	0.519
s10x	0.00148	0.540	1.48	4.03	0.551
s20x	0.000425	0.311	1.46	6.49	0.165
s100x	1.21	−0.0575	1.05	309	0.0817

UV background. If we refer to Figure 5.7a, the relative SFRD of counter-factual universes to *LCDM* hints at the negligible impact of the scaled UV background on the SFRDs. At early times, the SFRDs of all counter-factual universes are similar or less than *LCDM*, which means that deviations in the photoheating rates in these universes will not be as extreme as switching the UV background off completely. At late times, even though the SFRD of the *EDS* cosmology is much higher than *LCDM*, the photoheating rates at these times are already low. Therefore, it is not likely any scaled UV background will be as extreme as removing the UV background in Section 5.3.4. As a result, the cosmic SFRD in simulations with scaled UV background is identical to those with the Haardt & Madau (2012) UV background model.

We have explained the limitation of resolution especially in the far future leading to a loss of haloes and even resulting in a turnaround in the cosmic SFRD (see 'Star formation history' under Section 4.3.7). As the onset of this adverse impact is dependent on the rate of expansion of the universe, it throws the credibility of the evolution of the SFRD in counter-factual universes into doubt. However, if we refer to Figure 5.7a, we show that the SFRDs in each universe do experience an evolution that can be fitted with a analytic fit of the same functional form by Madau & Dickinson (2014). From several data points with uncharacteristically large values in Figure 5.7b, we also show that the SFRDs in simulations with scaled Λ do exhibit a turnaround behaviour. The time when these points appear corresponds to the point where we have exceeded the resolution limit in the simulations, resulting in unphysical star formation (see

'Star formation history' under Section 4.3.7). Evident from the large residuals, our fit do not encompass this turnaround evolution. Therefore, we believe that we have a realistic SFRD in each of these counter-factual universes and our fit provided in Table 5.2 is able to describe the evolutions of the SFRD.

Intergalactic medium with scaled UV background

The sensitivity of the IGM to the UV background is then the main motivation for scaling the UV background in order to achieve a realistic evolution of the IGM in counter-factual universes. We show the differences between simulations with the default Haardt & Madau (2012) UV background (HM) and the scaled UV background (UVB) in Figure 5.8 given that the SFRD remains the same in each universe regardless of the UV background (see Section 5.3.5). We break down the analysis into universes with scaled Λ (panel a) and σ_8 (panel b).

In Figure 5.8a, we see that the scaled UV background does not impact the evolution of $\log_{10} T_0$. The solid lines (HM $\log_{10} T_0$) and dashed-dotted lines (UVB $\log_{10} T_0$) are indistinguishable from each other. At intermediate times, the dashed (HM γ) is consistently lower than the dotted lines (UVB γ), indicating that the temperature of the IGM gas of the simulations with the scaled UV background is more sensitive to its overdensity. The reduced heating from the scaled UV background makes cooling the dominant process, which is sensitive to density.

On the other hand, the IGM in the *EDS* simulation show an almost identical evolution regardless of the UV background. The only difference occurs in the value of $\log_{10} T_0$ before 20 Gyr when the SFRD reaches a peak. Before this time, the photoheating rates from the UVB is lower than HM because the SFRD of *EDS* is lower than that of *LCDM*. Therefore, the resulting value of UVB $\log_{10} T_0$ is slightly smaller than HM $\log_{10} T_0$. This slight difference is not significant enough to affect γ. Beyond this time, the HM photoheating rates are low, reducing the significance of any scaling of the SFRDs. Hence, the corresponding pairs of lines are identical, independent of the UV background.

Unlike Figure 5.8a, $\log_{10} T_0$ for the scaled σ_8 simulations varies significantly for the different UV backgrounds in Figure 5.8b. $\log_{10} T_0$ for simulations with a scaled UV background is consistently lower than its counterpart with the HM UV background. If we compare the SFRDs of *s5x*, *s10x*, *s20x* and *s100x* with *LCDM*, they are significantly lower translating into a weaker UV background.

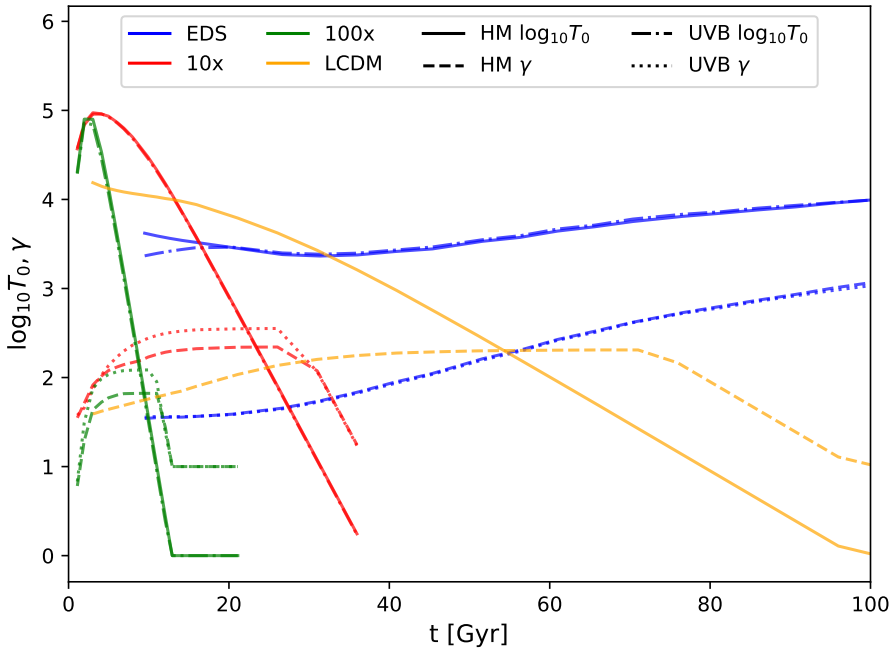

(a) Scaled Λ simulations

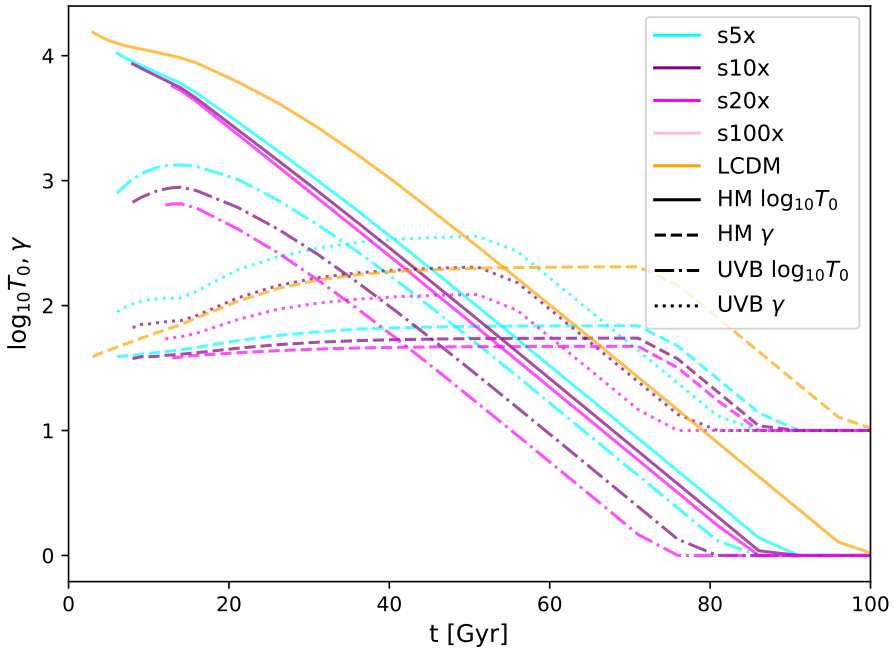

(b) Scaled σ_8 simulations

Figure 5.8 Comparison of the evolution of γ and $\log_{10} T_0$ across cosmic time for simulations with and without a scaled UV background. The various cosmologies are colour coded in a similar way as 5.7. The simulations are further categorised into those with the Haardt & Madau (2012) UV background (HM) in panel (a) and the scaled UV background (UVB) in panel (b). For different cosmologies, the extent of the impact of the scaled UV background varies. We discuss these differences in 'Intergalactic medium with scaled UV background' under Section 5.3.5.

This reduced heating rate also causes $\log_{10} T_0$ to reach the temperature floor and correspondingly, γ to approach a value of unity at a quicker pace. For the same reason, it increases γ in a way similar to Figure 5.8a. Therefore, simulations with a scaled UV background experience a slightly different evolution from its counterpart with the HM background. Moving forward, we will analyse the IGM with simulations of scaled UV background.

Removing the lines for simulations with the HM UV background, we present the evolution of the IGM associated with the various counter-factual universes in Figure 5.9. At the start of the simulations, $\log_{10} T_0$ for *10x* and *100x* is higher than *LCDM* for a short period of time. If we compare their SFRDs in Figure 5.7a, we find that the initial SFRDs for *10x* and *100x* are slightly higher than *LCDM*. This difference raises the initial heating rates, resulting in a higher $\log_{10} T_0$. It then falls rapidly because of a combination of much lower SFRD and a faster expansion as compared to *LCDM*. Within a short period, the gas in the IGM cools to the temperature floor. As a result, γ also flattens ($\gamma = 1$) quickly. The evolution of the IGM in *LCDM* over approximately 100 Gyr is essentially compressed into 40 Gyr for *10x* and even further into 20 Gyr for *100x*. We also observe a similar trend for simulations with scaled σ_8. A larger α translates to a lower σ_8, leading to less star formation, resulting in a lower heating rate from the UV background. Therefore, simulations with larger scaling on σ_8 experience a faster decline of $\log_{10} T_0$ towards zero and the flattening of γ.

In summary, α determines the speed at which T_0 approaches the temperature floor and γ flattens as the universe evolves. A higher α translates to these phenomena occurring at a faster rate. However, it is different for universes with scaled Λ and σ_8. For the former, Λ dominates the universe at different times. In our simulations where we scaled up Λ, the IGM starts off in a state that is comparable to *LCDM* but Λ soon dominates, causing a rapid drop in T_0 and flattening of γ. In the latter where σ_8 is scaled, it only changes the clustering of matter. Therefore, the initial point is already different with *LCDM* having a higher T_0 than the *s*α*x* simulations. The reduced clustering also leads to T_0 dropping to the temperature floor and γ flattening faster.

With these changes to the IGM, it is perhaps surprising to find that it has little to no effect on the SFRD. At late times when the universe is dominated by Λ and the UV background is insignificant, the gas in the IGM cools to the temperature floor regardless. At early times, we find that the absence of the UV background affects gas of low overdensity most significantly (see Figure 5.6),

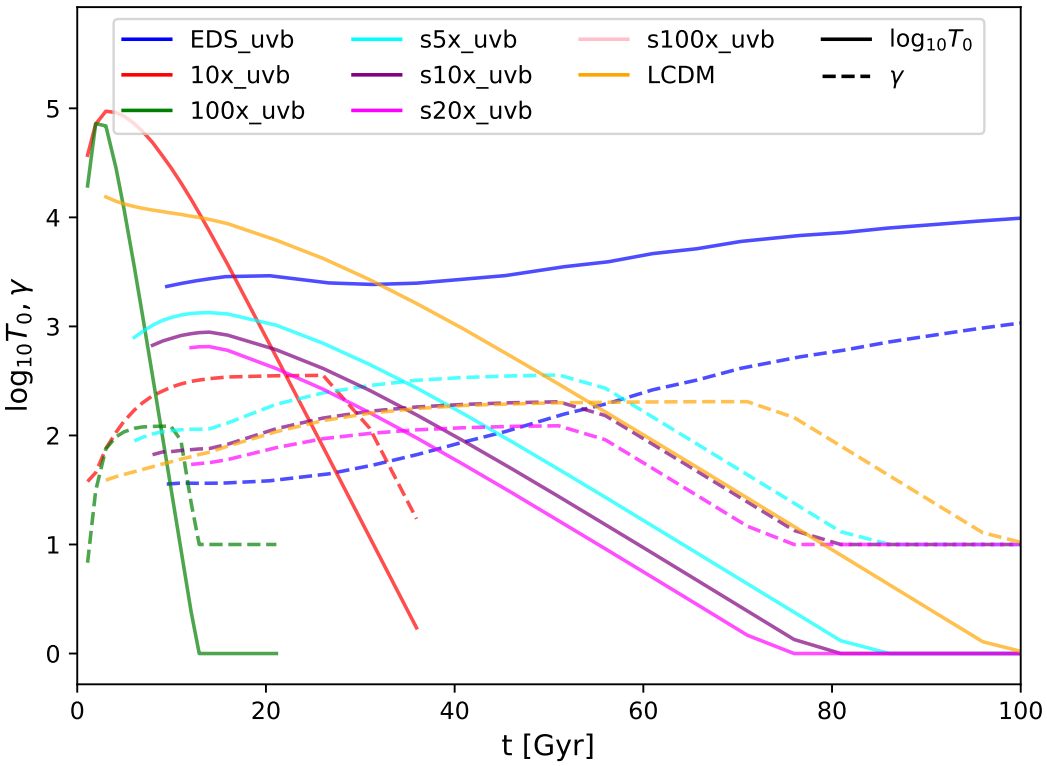

Figure 5.9 Evolution of γ and $\log_{10} T_0$ across cosmic time for simulations with scaled UV background. The various cosmologies are colour coded in a similar way as 5.7. The IGM evolves more drastically in a short period of time when we scale Λ. On the other hand, the IGM in *EDS* is consistently hotter beyond 40 Gyr. We discuss these differences in 'Intergalactic medium with scaled UV background' under Section 5.3.5.

which is much lower than the star formation threshold. Since switching off the UV background is the most extreme scenario and it did not affect the SFRD, we expect that scaling the UV background will have negligible effect on the SFRD as well.

5.3.6 Average metallicity of young stars

Since we are looking at the long term cosmic SFRD, it will be interesting to find out what is the source of star formation, especially at late times. Will the stars keep using the polluted gas in its vicinity to form more stars or will there be time for pristine gas from the IGM to mix? We investigate this by looking at how the average metallicity of young stars ($< 500\,\mathrm{Myr}$) evolves as a function of time in counter-factual universes. We plot the average metallicity as a ratio to the solar metallicity against time in Figure 5.10. Except for *EDS* and *s100x*, all other simulations exhibit a similar evolution in the average metallicity of the young stars. It increases, reaches a peak in metallicity, declines and finally starts to increase again. This trend can be explained by comparing the gas cooling time scale with the star formation time scale. If the former is shorter than the latter, the young stars will be of a lower metallicity or experiences a retarded growth in its metallicity. Sometimes, there are gaps in the line because there are no stars formed within the specified period at that snapshot.

We start by discussing the outliers to this general trend. The stars in *s100x* are consistently metal-poor or made from primordial gas. If we look at Figure 5.3, we see that this is a direct consequence of the almost non-existent star formation in this counter-factual universe. Without star formation, the gas is not polluted with metals from stellar feedback, allowing new stars to posses near-zero metallicity. On the other hand, with active star formation in *EDS*, the gas is continuously injected with new metals associated with feedback. Therefore, after the initial rise in metallicity, stars in *EDS* remains highly enriched with metals due to the consistently high SFR shown in Figure 5.3. However, it is important to note that the metallicities illustrated in Figure 5.10 are unusually high in comparison to observations. This difference can potentially be reduced if we employ the self-consistent chemistry network evolution offered by `Grackle`.

The general argument is that metallicity of the stars scales with the SFRD in the simulation. With the peak metallicity of stars coinciding with the peak of SFRD, the drop in metallicity is also attributed to the corresponding decline in

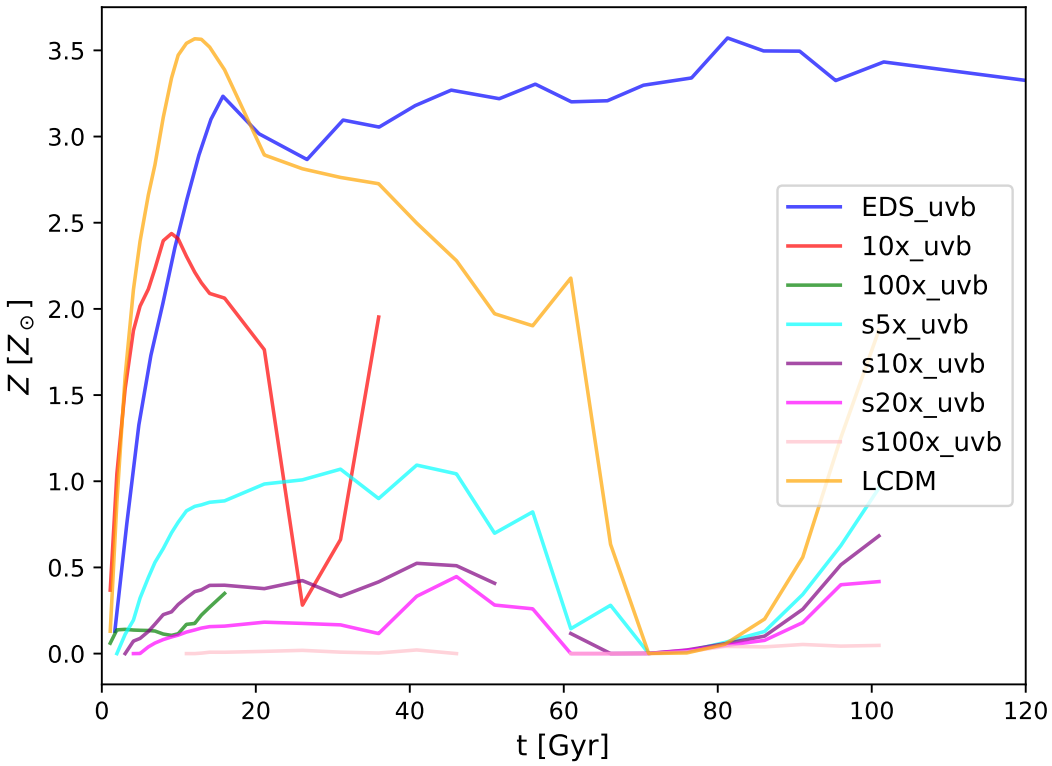

Figure 5.10 Evolution of the average metallicity of stars formed within 500 Myr of the specified time against time. The various cosmologies are colour coded in a similar way as 5.7. We find that the metallicity scales according SFRD. Therefore, they have a similar evolution to that shown in Figure 5.3. Refer to the discussion in Section 5.3.6.

SFRD. When the simulation is not actively forming stars, there is time for the fuel of star formation to mix with the fresh gas inflow from the IGM. Because of the difference in the gas cooling and star formation time scale discussed earlier, the metallicity of the young stars decreases. In other words, pristine gas from the filaments can lower the metallicity of the gas used, resulting in the new stars at late times to be of lower metallicity. The turnaround of metallicity at late times is, therefore, related to the turnaround in SFRD (see Section 5.3.3) when the star formation time scale is now shorter than the cooling time scale.

5.4 Asymptotic star formation efficiency

In this section, we look at how star formation differs between counter-factual universes in the context of anthropic reasoning. With our suite of simulations, we adopt a similar weights assignment of the counter-factual universes as proposed by Peacock (2007): the number of observers is proportional to the number of stars formed. In principle, this assignment generates the "measure problem": if the counter-factual universes are flat, they have infinite volume and so all contain infinite number of stars. Therefore, relative probabilities are apparently not well defined. The way to evade this problem is to follow Weinberg (1989) and argue for a flat prior in Λ since $\Lambda = 0$ is not a special point. This assumption gives the relative prior weight of a given member of the multiverse ensemble, and it is then reasonable to argue that the weight for that universe should be scaled in proportion to an appropriate measure. In his work, Peacock (2007) calculated this anthropic weight based on the collapse fraction, f_c. It is defined as the fraction of baryon mass in the universe that has collapsed into haloes of a critical mass near to that of the Milky Way, based on the fact that these haloes are observed to be the most efficient at converting their baryon content into stars. We extend this work by calculating the exact asymptotic star formation efficiency which is the ratio of the total stellar mass that can form to the total baryon mass available in the individual universe to form stars as $t \to \infty$. This quantity will provide a more direct link between the probability of observers and stellar mass in each universe.

In order to calculate the total stellar mass, we refer to the fits obtained for the counter-factual universes in Table 5.2. Since we are limited by computational resources, it is impossible to run all the simulations to infinite time. Therefore, we can only obtain the total stellar mass by integrating Equation 5.9 with the

fits we found to infinite time,

$$m_*(t \to \infty) = V \int_0^\infty \psi(z)\ dt, \tag{5.11}$$

where V is volume of the simulation in cMpc^3. Through the conversion

$$\frac{dz}{dt} = -\frac{\dot{a}}{a^2} = -\frac{H(z)}{a} \tag{5.12}$$

where each quantity is unique to its cosmology, we can then obtain the total stellar mass

$$m_*(t \to \infty) = V \int_{-1}^\infty \frac{\psi(z)}{H(z)(1+z)}\ dz, \tag{5.13}$$

where the limits reflect the infinite lifetime of the universes. We can then calculate the total amount of baryon mass that is available with

$$m_b = V \times 2.7755 \times 10^{11} \Omega_b\, h^2 \tag{5.14}$$

where the cosmological parameters are unique to each universe (Peacock, 1999). However, we should obtain the same amount of baryons in each counter-factual universe due to the scaling of the cosmological parameters (see Section 5.1). We then plot m_*/m_b against the scaling factor, α in Figure 5.11.

The exponential decay with increasing α is consistent for both f_c and m_*/m_b in Figure 5.11. It also tells us it is less likely to find observers in universes where α and consequently, Λ is large. Not only does structure formation occur at a slow pace (see Section 5.3.2), the collapse fraction and the asymptotic star formation efficiency is extremely low. On the other hand, with low α, we can get much higher conversion efficiency of baryons into stars as expected from the higher collapse fraction. Between $\alpha = 0$ and $\alpha = 1$, the relative weights differ by approximately 50%. In terms of m_*/m_b, universes with scaled Λ do not differ as significantly from universes with scaled σ_8 as compared with the behaviour we saw regarding their star formation history, metallicity and IGM.

From the decreasing weights with increasing α from the simulations of counter-factual universes, we can fit

$$f_c(\alpha) = \exp\left(-0.0769\alpha^{0.773} - 0.809\alpha^{0.205}\right) \tag{5.15}$$

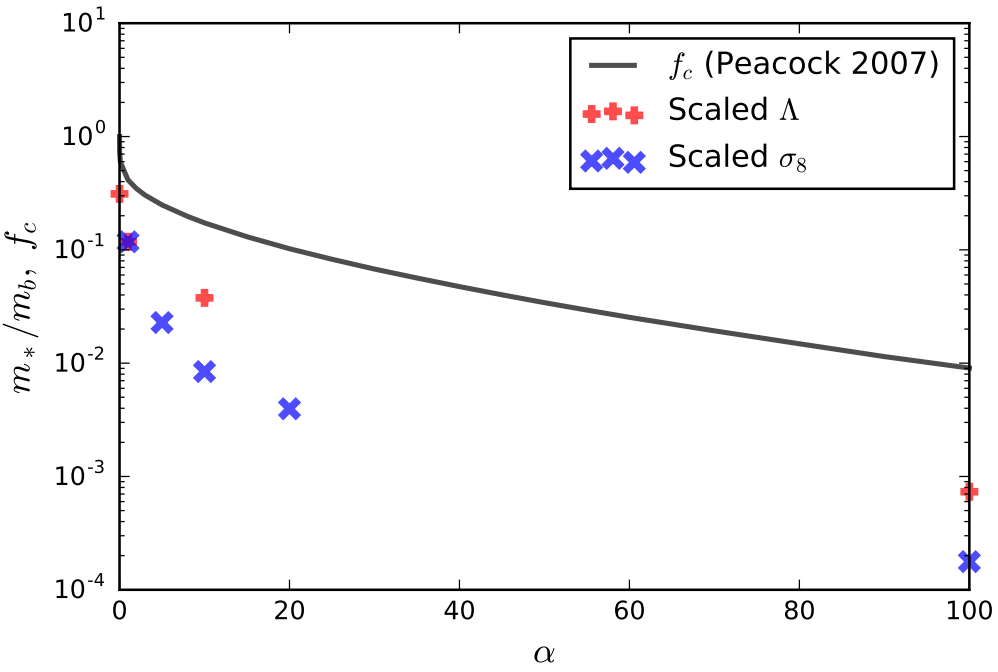

Figure 5.11 The collapse fraction from Peacock (2007) and asymptotic star formation efficiency as a function of the scaling factor, α. The solid line is the collapse fraction with the red pluses and blue crosses representing the asymptotic star formation efficiency from our scaled Λ and scaled σ_8 simulations. Essentially, the asymptotic star formation efficiency is an extension of the collapse fraction by considering baryonic processes such as feedback.

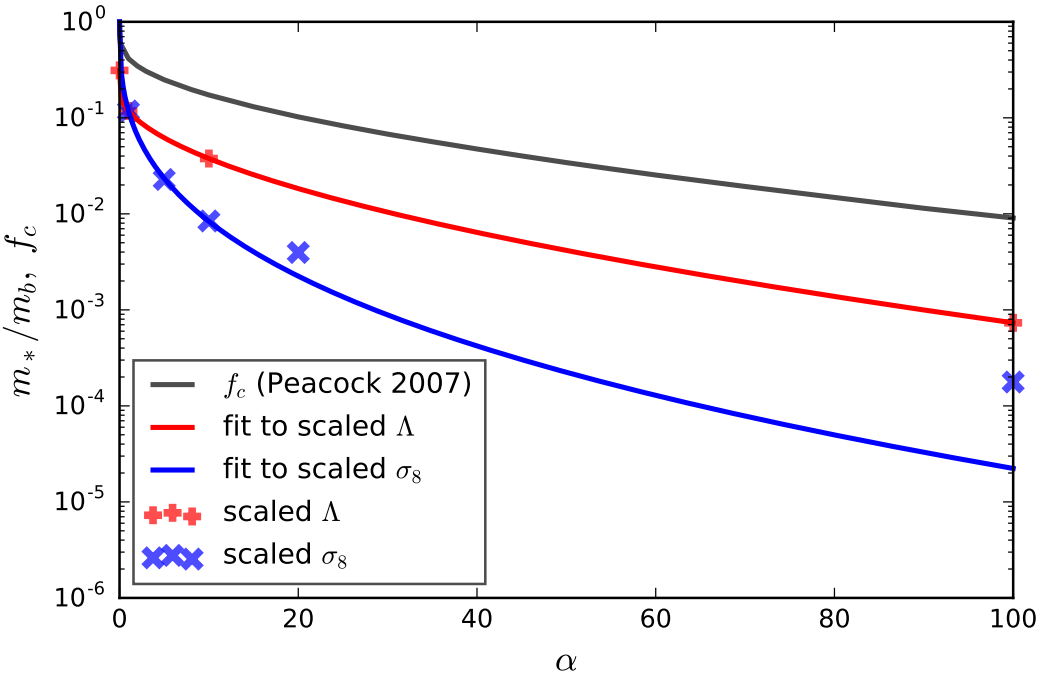

Figure 5.12 Fits to both the collapse fraction from Peacock (2007) and asymptotic star formation efficiency as a function of the scaling factor, α. The black line is the collapse fraction. The red pluses and blue crosses represent the asymptotic star formation efficiency from our scaled Λ and scaled σ_8 simulations respectively. The fits to these simulation results are of the same colour as the data points. We describe the fits to f_c with Equation 5.15 and the fits to m_*/m_b from our scaled Λ and scaled σ_8 simulations with Equations 5.16 and 5.18 respectively. The fits provide a useful mean to further understand the meaning of Figure 5.11.

perfectly to the collapse fraction from Peacock (2007). With the same functional form, we can fit

$$\frac{m_*}{m_b}(\alpha) = 0.312 \exp\left(-0.414\alpha^{0.556} - 0.560\alpha^{0.0478}\right), \tag{5.16}$$

to the asymptotic star formation efficiency from simulations with scaled Λ and

$$\frac{m_*}{m_b}(\alpha) = \exp\left(-1.070\alpha^{0.350} - 1.069\alpha^{0.350}\right), \tag{5.17}$$

which reduces to a single exponential decay,

$$\frac{m_*}{m_b}(\alpha) = \exp\left(-2.139\alpha^{0.350}\right), \tag{5.18}$$

to the asymptotic star formation efficiency from simulations with scaled σ_8. These fits are illustrated in Figure 5.12, allowing us to carry out further analysis.

With the fits to the decreasing m_*/m_b as α increases, we obtain a converging function as α approaches infinity, allowing us to calculate the percentage of observers residing in universes whose vacuum densities are no larger than ours ($\alpha \leq 1$). According to prediction by f_c (Peacock, 2007), approximately 9.6% of all possible observers live in such universe. This percentage almost double to 14.2% when we use the fit of the asymptotic star formation efficiency of universes with scaled Λ and even reaches 53.6%, a near six-fold increase when we apply the results from simulations with scaled σ_8. Furthermore, 50% of all observers can be found in universes with $\alpha \leq 13.5$, $\alpha \leq 8.29$ and $\alpha \leq 0.782$ according to Equations 5.15, 5.16 and 5.18 respectively. These values of α translates to $\Omega_\Lambda = 0.971$ for the collapse fraction calculations, $\Omega_\Lambda = 0.954$ and $\Omega_\Lambda = 0.662$ for the simulation with scaled Λ and σ_8 respectively. These values are consistent with the value of 0.9 from Efstathiou (1995). Our cosmological simulations of counter-factual universes with scaled σ_8 even reduces this median value such that it is much more consistent with observations. However, it is important to note that our fit in Equation 5.17 predicts a lower value of α than it should be, making it in excellent agreement with the observed value. It is a significant improvement over previous estimates. This prediction will be be further improved with the addition of metal-weighting, which reduces the weights of large α counter-factual universes (Barnes et al., 2018) because the reduced SFRD leads to fewer metals for planet formation (see Figure 5.10).

However, our result is in clear disagreement with Barnes et al. (2018). In the mentioned work, the authors reported a predicted (median) value of Λ to be 50 to 60 times larger than the observed value. Also, they conclude the percentage of observers residing in a universe with a value of Λ equal to or less than ours is approximately 2% based on a mass weighted measure. This measure is similar to the flat prior for the value of Λ but applied to the region where a given mass element is found. Essentially, it allows the use of star formation efficiency to predict the value of Λ. The authors concluded that the anthropic principle is not an appropriate explanation for the small value of Λ with these calculated values. This striking difference in our conclusions stems from the weight assignment to various counter-factual universes shown in Figure 5.13. We compare the results from our suite of simulations (blue and red lines) with previous work by Peacock (2007) (black line) and Barnes et al. (2018) (green dots) in a plot similar to the left panel of Figure 12 from Barnes et al. (2018). While it is clear that the blue, red and black lines will converge to zero as α approaches infinity, there is a lack of clear indication that the green dots will exhibit the same behaviour. If it does

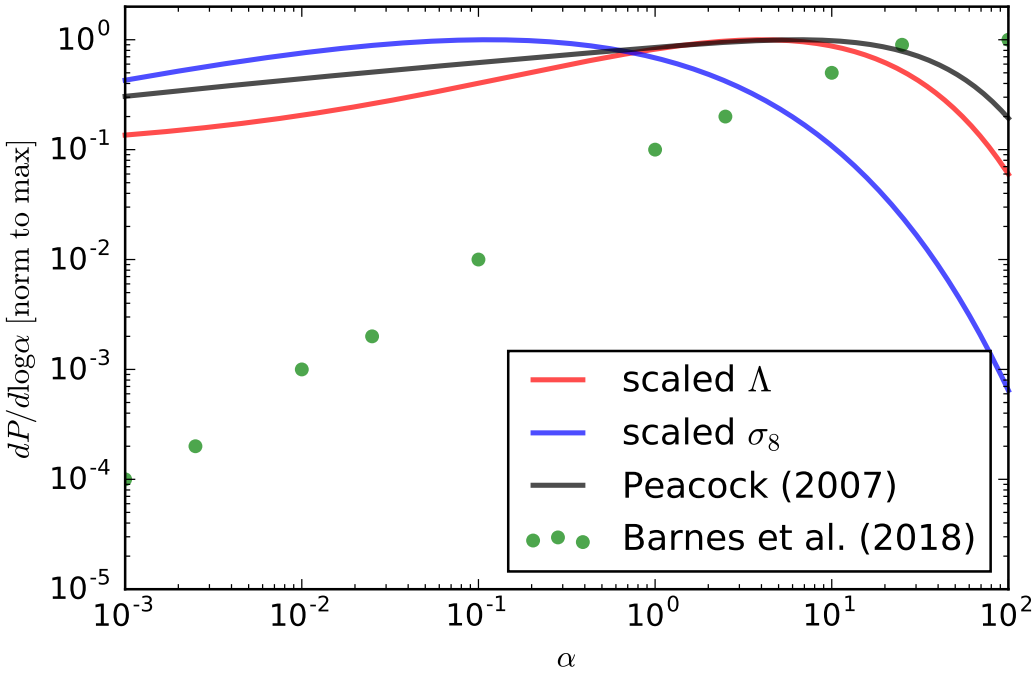

Figure 5.13 Relative probability per unit $\log \alpha$ from this work, Peacock (2007) and Barnes et al. (2018). The black, red and blue lines are the fits to the collapse fraction from Peacock (2007) with Equation 5.15, m_*/m_b from this work using Equations 5.16 and 5.18 respectively. The green dots are extracted from the left panel of Figure 12 from Barnes et al. (2018). The data from Barnes et al. (2018) suggests that more weight will be assigned to universes with larger value of Λ, resulting in the huge discrepancy about the applicability of the anthropic argument for the value of Λ concluded in the work presented in this figure.

not, most of the weight will be shifted to larger values of α, which explains the huge discrepancy between our results and those of Barnes et al. (2018). Our results do, however, illustrate a similar trend to the causal patch and diamond measures used in Barnes et al. (2018). Despite limitations with these measure as discussed by the authors, these can be independent predictions, supplementing our results to argue for the applicability of the anthropic principle to explain the observed value of Λ.

Furthermore, the cosmological volume in both sets of simulations differs significantly. In our counter-factual universes, we have been simulating them in a consistent volume of 71.94 cMpc as compared to 25 cMpc per side in Barnes et al. (2018). According to the HMF obtained (see Section 5.3.2), this disparity translates to a vastly different simulated halo mass range in the simulations. For example, in *10x*, the maximum halo mass simulated with the 25 cMpc cosmological box is approximately $10^{11.5}\,M_\odot$, which is less than $10^{12}\,M_\odot$, the

halo mass with the optimal star formation efficiency (Behroozi et al., 2019). Although the simulations in Barnes et al. (2018) have better mass resolution, which resolves lower mass haloes, the star formation efficiency in these haloes is not as high and they are likely affected by the UV background. Also, we have to take feedback into account when determining the star formation rate in the haloes. Therefore, it is possible that the star formation rates derived from their simulations is limited by the simulated cosmological volume. Based on all these comparisons, we believe the cosmological constant has a significant influence on the presence of observers in the multiverse setting and our suite of simulations has improved the applicability of the anthropic principle to explain the small observed value of Λ.

5.5 Summary and conclusions

In summary, we study the first suite of simulations using `Enzo` to simulate the evolution of counter-factual universes. We use the separate universe technique to obtain the initial conditions according to the scaling factor of Λ in ΛCDM cosmology. We also ran additional simulations where σ_8 is scaled to mimic the effect that scaling Λ has on the clustering of matter. We then analyse the impact of cosmology on the evolution of a range of properties including stellar masses, SFRDs, HMFs, tight power-law fit of the IGM and properties of gas and stars. In particular, we fit a double power-law (Madau & Dickinson, 2014) to the SFRDs of these counter-factual universes. By integrating to infinite time, we obtain the asymptotic star formation efficiency in these universes and extend the anthropic calculations made in Peacock (2007). We summarise our findings as follows:

- We scaled the cosmological parameters of our universe obtained from WMAP-9 to obtain a total of seven counter-factual universes. The initial conditions are then generated using `MUSIC` and evolved with `Enzo` to at least $t \approx 100\,\mathrm{Gyr}$ whenever possible. This length of time is necessary for Λ to dominate the evolution of the universes. Conversely, it also means that at early times, when Λ is not dominant, the evolution of these universes should be identical. This similarity allows us to check that the simulations were set up properly.
- The HMF of different universes is extremely sensitive to the scaling factor applied to Λ. A higher value of Λ allows it to become the dominant

component of the universe at an earlier time. As a result, the clustering of the dark matter is restricted. We see this effect clearly in the HMFs evolution with time. With a larger Λ, the mass of the most massive halo and the numbers of haloes across the mass range decreases. The cause is attributed to simulations hitting resolution issues earlier in universes expanding at a faster rate (see Section 5.3.2). In simulations with scaled σ_8, we find a less drastic effect of the HMFs, indicating that scaling σ_8 is not identical to scaling Λ. On the contrary, *EDS* does not encounter these issues because of the slower expansion.

- The star formation histories of the counter-factual universes are vastly different. They reach different peaks at different times. We find that a clearly defined peak in star formation is associated with the presence of Λ. The SFRD in *EDS* undergoes significant fluctuations as it reaches its maximum, illustrating the interplay between star formation and its feedback. Eventually, it declines but never quite reaches a zero star formation rate in the simulation. Since the cosmic SFRD differs significantly across universes, it raises doubts about using the same UV background across all simulations. Therefore, we implement a UV background that scales according to the ratio of its SFRD to *LCDM* at identical times.

- Due to the resolution limit of our simulations, the scaled UV background has a negligible effect on the SFRD. However, it does influence the evolution of the IGM. The temperature of the IGM decreases faster to the temperature floor in the simulations due to the reduced heating from the scaled UV background. At the same time, the temperature of the gas also loses sensitivity to its density at a similar quickened pace.

- We also find that the average metallicity of young stars scales with the SFRD. When the simulation is actively forming stars, the metallicity of the newly formed stars is high. The fuel for star formation is constantly enriched by feedback from the previously formed stars. Only when the SFRD declines, this reservoir of gas is then allowed to mix with the primordial gas entering the halo. This mixing reduces the average metallicity of the young stars at later times. Since star formation is always active in *EDS*, the gas is continuously enriched with metals from feedback, preventing any drop in the metallicity of the young stars.

- Lastly, we revisit the anthropic calculations of Peacock (2007) in more detail, extending the calculations of weights for members of the multiverse

ensemble. We assume that the prior on Λ is uniform in a small range around zero, consistent with Weinberg (1989). This assumption allows the counter-factual universes to be weighted by their asymptotic star formation efficiency. We find a similar exponential decay in the weights using this efficiency and the collapse fraction in Peacock (2007). Despite their differences in other properties, the star formation efficiency does not differ significantly between scaling Λ and σ_8 in the simulations.

This Chapter shows that if the probability of the existence of observers scales with the number of stars formed in the universe, then we will preferentially exist in universes with a small value of Λ. However, we have not considered the cases of negative vacuum densities in this study given that we have adopted the assumption of a uniform prior for the value of Λ around zero (Weinberg, 1989). Although the formation of haloes will be very efficient near the end of the lifetime of such universes, there is a question of whether star formation can cope with it. Since the densities and temperature are so high, cooling might be inhibited before the universe dies in the big crunch. Even if star formation is efficient, there might not be sufficient time for life to form. This scenario is different from the infinite lifetime of universes with positive Λ that we have simulated. As a future work, we will simulate universes with negative Λ in order to answer the questions we have posed about them. In conclusion, we do not yet possess the full picture, although indications of the applicability of the anthropic principle to explain the small observed value of Λ through cosmological simulations are positive.

Chapter 6

Conclusion and future work

This thesis set out to answer questions revolving around the cosmological constant, Λ. Introduced by Albert Einstein in 1915, it is the cause of the accelerated expansion of our universe. However, the value of Λ from quantum field theory is 120 orders of magnitude larger than the observed one. Many have tried to explain this small value using anthropic reasoning (Weinberg, 1987, 1989; Efstathiou, 1995; Peacock, 2007), suggesting that the universe is in its current state because of the need to be compatible with the observers residing in it (Carter, 1974). One of the assumptions of anthropic reasoning is a multiverse where there is an infinite number of universes that may be similar or different to ours. We have used cosmological simulations of both our universe and counter-factual universes to explore this concept, expanding on previous work with detailed galaxy formation models. The fundamental concepts and history of essential observations are summarised in Chapter 1.

In Chapter 2, we explained the methodology of various components of numerical simulations. These included the initial condition generator `MUSIC`, the simulation code `Enzo`, the chemistry and cooling library `Grackle`, `ROCKSTAR` halo finder and `yt` analysis toolkit. They each have their own role in enabling a cosmological simulation. In this work, we ran both cosmological volumes as well as zoom simulations, up to and beyond $z = 0$, in the standard ΛCDM and counter-factual universes. This wide range of parameter space allowed us to test the robustness of these codes and their ability to operate in previously unexplored regimes.

We first conducted an extensive parameter space exploration of the star formation and feedback prescription with a zoom simulation for a MW-sized halo in Chapter 3. The aim was to identify a combination in the vast space of possible feedback parameters that can reproduce the observed universe. Using a total of 71 zoom simulations, we calibrated our subgrid physics with the observational constraint of the baryonic makeup in a MW-sized halo from McGaugh et al. (2010). We found two sets of feedback parameters in two different star formation setups that can reproduce this baryon content. However, one of these setups (Setup 1) restricted star formation in the zoom simulation of dwarf galaxies, shifting our focus to the other setup (Setup 2). With a calibrated set of feedback parameters for Setup 2, we found that it can reproduce the baryonic composition of haloes of masses on top of the MW-sized halo, extending the effective range of halo mass to 10^{10} $M_{\odot}$ – 10^{12} $M_{\odot}$. This agreement is not reproduced with Setup 1, further justifying the use of Setup 2. Also, we conducted an exploratory study on the reproducibility of the results, concluding that operational differences in the implementation of the numerical code created an approximate average of 10% and 25% deviation in the stellar and baryon mass of the halo respectively.

Armed with a calibrated star formation and feedback prescription, we applied it to a cosmological box simulation in Chapter 4. This simulation was evolved into the future when Λ dominates the universe. In order to compare our results with previous work, we chose a resolution comparable to the simulation in Nagamine & Loeb (2004) that is evolved with a different code. After some modifications to `Enzo` and `Grackle`, we showed that the distributions of gas temperature and density in both our and Nagamine & Loeb (2004)'s simulations undergo a similar evolution as the universe evolves into the future, despite differences in the methodology of the simulation codes.

We then established numerical convergence with six other simulations with varying resolutions and subgrid physics. We showed that differences in these parameters affect specific details of the halo mass function (HMF), the intergalactic medium (IGM) and star formation history (SFH) in the simulations. The general evolution agreed between the simulations, even with these small differences. We found that `Enzo` and `Grackle` were challenged operationally in the far future, as a result of the nature of this relatively unexplored regime. We also identified another example of the cosmological 'coincidence problem' where photons at present are just sufficient to keep the IGM at its current mean temperature, evident from its prompt and sharp decline beyond $z = 0$.

Although the simulations produced a general evolution of the SFRD consistent with observations, the peak in our simulation SFRD was lower and delayed. This discrepancy arose because of the limited resolution of the simulations. At late times, we also identified a turnaround in the cosmic SFRD, contrary to the extrapolation of the analytic fit to the observations. Upon further investigation, we concluded that this feature is not physical and caused by the limitations of the simulations. One of the hints for this explanation is the absence of a turnaround in our simulation with the best spatial resolution. By integrating the SFRD from this simulation with respect to time from $z = 8$ to $z = -0.995$ or $t \approx 100\,\mathrm{Gyr}$, we obtained a 99% agreement between the total simulated and predicted stellar mass from the fit of observations. We also investigated the future evolution of several baryonic fractions of a MW-sized galaxy into the future with the zoom simulation from Chapter 3 and the cosmological volume simulation. Even though they had vastly different resolutions, the simulations produced a similar evolution of these properties into the future.

We then conducted simulations of counter-factual universes in Chapter 5. From the previous chapters, we are confident in the star formation and feedback prescription, the ability and limitations of the simulation code to realistically evolve the counter-factual universes. We simulated a total of seven counter-factual universes by scaling Λ directly or scaling σ_8 in a way that mimics a universe with scaled Λ. Through the comparison of the evolution of the HMFs, IGM and SFRDs of these simulations, we concluded that the different methods of scaling do not mimic each other. Direct scaling of Λ drastically affected the evolution of these properties because the universe expands rapidly on top of the reduced clustering from scaling σ_8.

As a result of the scaling of Λ, the SFRD evolved very differently in each counter-factual universe, suggesting that a Haardt & Madau (2012) UV background model cannot be applied universally. Therefore, we have to scale the UV background according to the ratio of SFRD in the counter-factual universe to the SFRD in ΛCDM universe. The scaled background had a negligible effect on the SFRD due to the limited resolution of our simulations. However, the evolution of the IGM is significantly altered. In general, increasing Λ reduced the SFRD across time. On the other hand, in EdS universe, the SFRD remained high for a more extended period before decreasing to zero. These differences scaled the UV background accordingly, causing the IGM temperature in universes with a larger Λ to drop faster.

We then fitted the time-varying SFRDs in each counter-factual universe with a double power-law fit that is similar to Madau & Dickinson (2014). By integrating these fits to infinite time, we derived the asymptotic star formation efficiency, which served as weights for members in the multiverse. These are similar to the weights derived from the collapse fractions in Peacock (2007). It is possible to do so because we assumed a flat prior distribution of Λ in a small range around zero (Weinberg, 1989). According to these weights, we concluded the probability to locate observers in a similar universe to ours had a near six-fold increase as compared to Peacock (2007). If we took the median value of Ω_Λ based on the probability of observers in different universes, we obtained a value that is consistent with Efstathiou (1995) and even closer to the observed value. Hence, with cosmological simulations, we supplemented the calculations in previous work with detailed galaxy formation models. The incorporation of baryonic processes increased the proportion of observers living in a universe with a cosmological constant that is equal or less than the observed value significantly, improving the applicability of the anthropic principle to explain the small observed value of Λ.

We have demonstrated the ability of the simulations to evolve and produce results consistent with our observable universe. However, we have neglected the effects of black holes. They exist in the centres of almost all galaxies (Kormendy & Richstone, 1995; Magorrian et al., 1998) and are responsible for heating gas, quenching star formation and exhausting the gas supply of the galaxies. We believe that these effects are most prominent in massive galaxies in order to replicate the sharp drop in the stellar mass function and create red and dead galaxies (Croton et al., 2006). While black holes do not affect the evolution of a MW-sized galaxy (see Chapter 3), it will affect the massive haloes in Chapters 4 and 5. If we look at the HMFs in these chapters, the mass of the haloes can reach approximately $10^{15}\,\mathrm{M}_\odot$. Using the seeding mechanism in Illustris (Vogelsberger et al., 2014) as an example, black hole seeds of mass $10^5\,h^{-1}\mathrm{M}_\odot$ are inserted in all haloes with mass above $5 \times 10^{10}\,h^{-1}\mathrm{M}_\odot$. The effects of black hole feedback will be most prominent in the *EDS* simulation of Chapter 5 containing the largest amount of massive haloes. With the increase in the number of massive haloes, the simulation universe will contain more black holes, resulting in an increase in feedback. Therefore, we expect the asymptotic star formation efficiency from the simulations of universes with low values of Λ to be reduced, likely with increasing severity as Λ decreases if black hole effects are included.

Resolution is always a key parameter that people look at to quantify the capability of a simulation. We do not want a simulation with an excessively high resolution because it is not optimising the usage of computational resources nor one with a poor resolution because the results will more than likely always show signs of hitting the resolution limit. As discussed extensively in Chapters 4 and 5, our suite of simulations is of lower resolutions, particular in the far future. The worsening spatial resolution due to the expansion of the universe proves to be an important issue to address if we wish the extend the validity of our results. Even before we consider this problem in the far future, we should look to improve our resolution in order to reproduce the analytical fit of the cosmic SFRD by Madau & Dickinson (2014). It is important because the UV background implemented in these simulations is derived from this fit. Alternatively, we can model the radiation transfer self-consistently to improve the agreement between the evolution in the SFRD and its resultant radiation background.

Lastly, we have been simulating counter-factual universes with `Enzo`. Within hydrodynamical simulations, there are other simulation codes such as `GADGET` (Springel et al., 2001) and `AREPO` (Springel, 2010). Each code has its advantages and disadvantages. If we are able to repeat this experiment with other codes, we can obtain a more complete understanding of the operational limits of simulating counter-factual universes and assign more accurate weights to different universes. We can even extend the work further by incorporating semi-analytic models in the analysis, e.g., Henriques et al. (2015). Since countless resources have been devoted to the improvement of simulations, we should be able to produce highly realistic simulations of counter-factual universes. Numerical experiments have allowed us to probe all aspects of the universe from the visible stars to the unseen dark matter. It is also the only tool that allows the exploration of other universes. There is no reason to think that it cannot be used to explain the value of the cosmological constant, Λ.

Bibliography

Abel T., Anninos P., Zhang Y., Norman M. L., 1997, New A, 2, 181

Agertz O., Kravtsov A. V., Leitner S. N., Gnedin N. Y., 2013, ApJ, 770, 25

Albrecht A., Steinhardt P. J., 1982, Physical Review Letters, 48, 1220

Allen S. W., Evrard A. E., Mantz A. B., 2011, ARA&A, 49, 409

Almgren A. S., Bell J. B., Lijewski M. J., Lukić Z., Van Andel E., 2013, ApJ, 765, 39

Anninos W. Y., Norman M. J., 1994, ApJ, 429, 434

Anninos P., Zhang Y., Abel T., Norman M. L., 1997, New A, 2, 209

Baade W., 1952, Trs. IAU, 8, 397

Babcock H. W., 1939, Lick Observatory Bulletin, 19, 41

Balbi A., et al., 2000, ApJ, 545, L1

Baldauf T., Seljak U., Senatore L., Zaldarriaga M., 2011, J. Cosmology Astropart. Phys., 10, 031

Barnes J., Hut P., 1986, Nature, 324, 446

Barnes L. A., et al., 2018, MNRAS, 477, 3727

Barreira A., Nelson D., Pillepich A., Springel V., Schmidt F., Pakmor R., Hernquist L., Vogelsberger M., 2019, arXiv e-prints,

Barrow J. D., Tipler F. J., 1986, The anthropic cosmological principle

Becker R. H., et al., 2001, AJ, 122, 2850

Behroozi P. S., Wechsler R. H., Wu H.-Y., 2013a, ApJ, 762, 109

Behroozi P. S., Wechsler R. H., Conroy C., 2013b, ApJ, 770, 57

Behroozi P., Wechsler R. H., Hearin A. P., Conroy C., 2019, MNRAS, p. 1134

Bennett C. L., et al., 2013, ApJS, 208, 20

Berger M. J., Colella P., 1989, Journal of Computational Physics, 82, 64

Bertschinger E., 2001, ApJS, 137, 1

Bigiel F., Leroy A., Walter F., Brinks E., de Blok W. J. G., Madore B., Thornley M. D., 2008, AJ, 136, 2846

Black J. H., 1981, MNRAS, 197, 553

Blanchard A., Valls-Gabaud D., Mamon G. A., 1992, A&A, 264, 365

Blumenthal G. R., Faber S. M., Primack J. R., Rees M. J., 1984, Nature, 311, 517

Bolton J. S., Haehnelt M. G., 2007, MNRAS, 382, 325

Bond J. R., Szalay A. S., 1983, ApJ, 274, 443

Booth C. M., Schaye J., 2009, MNRAS, 398, 53

Bouwens R. J., et al., 2012a, ApJ, 752, L5

Bouwens R. J., et al., 2012b, ApJ, 754, 83

Bryan G. L., Norman M. L., 1997, arXiv Astrophysics e-prints,

Bryan G. L., Norman M. L., 1998, ApJ, 495, 80

Bryan G. L., Norman M. L., Stone J. M., Cen R., Ostriker J. P., 1995, Computer Physics Communications, 89, 149

Bryan G. L., et al., 2014, ApJS, 211, 19

Carroll S. M., 2001, Living Rev. Rel., 4, 1

Carroll S. M., Press W. H., Turner E. L., 1992, ARA&A, 30, 499

Carter B., 1974, in Longair M. S., ed., IAU Symposium Vol. 63, Confrontation of Cosmological Theories with Observational Data. pp 291–298

Casimir H. B. G., 1948, Indag. Math., 10, 261

Cen R., 1992, ApJS, 78, 341

Cen R., Ostriker J. P., 1992, ApJ, 399, L113

Cen R., Ostriker J. P., 1999, ApJ, 514, 1

Cen R., Ostriker J. P., 2006, ApJ, 650, 560

Chaboyer B., Demarque P., Kernan P. J., Krauss L. M., 1996, Science, 271, 957

Cole S., 1991, ApJ, 367, 45

Cowsik R., McClelland J., 1973, ApJ, 180, 7

Crain R. A., et al., 2015, MNRAS, 450, 1937

Crocce M., Pueblas S., Scoccimarro R., 2006, MNRAS, 373, 369

Croton D. J., et al., 2006, MNRAS, 365, 11

Cucciati O., et al., 2012, A&A, 539, A31

Dahlen T., Mobasher B., Dickinson M., Ferguson H. C., Giavalisco M., Kretchmer C., Ravindranath S., 2007, ApJ, 654, 172

Dalla Vecchia C., Schaye J., 2012, MNRAS, 426, 140

Davé R., Hernquist L., Katz N., Weinberg D. H., 1999, ApJ, 511, 521

Davé R., et al., 2001, ApJ, 552, 473

Davis M., Efstathiou G., Frenk C. S., White S. D. M., 1985, ApJ, 292, 371

Dawoodbhoy T., et al., 2018, MNRAS, 480, 1740

Dekel A., Birnboim Y., 2006, MNRAS, 368, 2

Dekel A., Rees M. J., 1987, Nature, 326, 455

Deltete R. J., 1993, Perspectives on Science, 1, 285

Diemand J., Kuhlen M., Madau P., Zemp M., Moore B., Potter D., Stadel J., 2008, Nature, 454, 735

Dirac P. A. M., 1937, Nature, 139, 323

Doroshkevich A. G., Khlopov M. I., Sunyaev R. A., Szalay A. S., Zeldovich I. B., 1981, Annals of the New York Academy of Sciences, 375, 32

Dubois Y., Teyssier R., 2008, A&A, 477, 79

Earman J., 1987, American Philosophical Quarterly, 24, 307

Eddington A. S., 1930, MNRAS, 90, 668

Eddington A. S., 1933, The expanding universe

Efstathiou G., 1995, MNRAS, 274, L73

Efstathiou G., Davis M., White S. D. M., Frenk C. S., 1985, ApJS, 57, 241

Efstathiou G., Bond J. R., White S. D. M., 1992, MNRAS, 258, 1P

Einasto J., Saar E., Kaasik A., Chernin A. D., 1974, Nature, 252, 111

Einstein A., 1915, Sitzungsberichte der Königlich Preußischen Akademie der Wissenschaften (Berlin), Seite 844-847.,

Einstein A., 1917, Sitzungsberichte der Königlich Preußischen Akademie der Wissenschaften (Berlin), Seite 142-152.,

Einstein A., de Sitter W., 1932, Proceedings of the National Academy of Science, 18, 213

Eisenstein D. J., Hu W., 1999, ApJ, 511, 5

Ellis R. S., et al., 2013, ApJ, 763, L7

Enzo Collaboration 2018, Distributed Stellar Feedback, `https://enzo.readthedocs.io/en/latest/physics/star_particles.html#distributed-feedback`

Faber S. M., Jackson R. E., 1976, ApJ, 204, 668

Falgout R. D., Yang U. M., 2002, in Sloot P. M. A., Hoekstra A. G., Tan C. J. K., Dongarra J. J., eds, Computational Science — ICCS 2002. Springer Berlin Heidelberg, Berlin, Heidelberg, pp 632–641

Faucher-Giguère C.-A., Lidz A., Zaldarriaga M., Hernquist L., 2009, ApJ, 703, 1416

Ferland G. J., et al., 2013, Rev. Mexicana Astron. Astrofis., 49, 137

Freedman W. L., et al., 1994, Nature, 371, 757

Friedmann A., 1922, Zeitschrift fur Physik, 10, 377

Friedmann A., 1924, Zeitschrift fur Physik, 21, 326

Fujii Y., Nishioka T., 1991, Physics Letters B, 254, 347

Gavazzi R., Treu T., Rhodes J. D., Koopmans L. V. E., Bolton A. S., Burles S., Massey R. J., Moustakas L. A., 2007, ApJ, 667, 176

Genel S., et al., 2018, preprint, (arXiv:1807.07084)

Giodini S., et al., 2009, ApJ, 703, 982

Gnedin N. Y., 2000, ApJ, 535, 530

Gottloeber S., 1998, in Mueller V., Gottloeber S., Muecket J. P., Wambsganss J., eds, Large Scale Structure: Tracks and Traces. pp 43–46 (arXiv:astro-ph/9711312)

Governato F., et al., 2010, Nature, 463, 203

Griffen B. F., Ji A. P., Dooley G. A., Gómez F. A., Vogelsberger M., O'Shea B. W., Frebel A., 2016, ApJ, 818, 10

Gruppioni C., et al., 2013, MNRAS, 432, 23

Guth A. H., 1981, Phys. Rev. D, 23, 347

Haardt F., Madau P., 1996, ApJ, 461, 20

Haardt F., Madau P., 2012, ApJ, 746, 125

Hahn O., Abel T., 2011, MNRAS, 415, 2101

Hamilton J. C., 2014, Studies in the History and Philosophy of Modern Physics, 46, 70

Hamuy M., Phillips M. M., Suntzeff N. B., Schommer R. A., Maza J., Aviles R., 1996, AJ, 112, 2391

Hanany S., et al., 2000, ApJ, 545, L5

Heckmann O., 1931, Veroeffentlichungen der Universitaets-Sternwarte zu Goettingen, 2, 126.1

Heckmann O., 1932, Veroeffentlichungen der Universitaets-Sternwarte zu Goettingen, 2, 180.1

Heitmann K., Higdon D., White M., Habib S., Williams B. J., Lawrence E., Wagner C., 2009, ApJ, 705, 156

Henriques B. M. B., White S. D. M., Thomas P. A., Angulo R., Guo Q., Lemson G., Springel V., Overzier R., 2015, MNRAS, 451, 2663

Hockney R. W., Eastwood J. W., 1988, Computer simulation using particles

Hoekstra H., Hsieh B. C., Yee H. K. C., Lin H., Gladders M. D., 2005, ApJ, 635, 73

Hoffman Y., Ribak E., 1991, ApJ, 380, L5

Hollenbach D., McKee C. F., 1979, ApJS, 41, 555

Hoyle F., 1994, Home is where the wind blows. Chapters from a cosmologist's life.

Hoyle F., Sandage A., 1956, PASP, 68, 301

Hu W., 2000, ApJ, 529, 12

Hubble E., 1929, Proceedings of the National Academy of Science, 15, 168

Hui L., Gnedin N. Y., 1997, MNRAS, 292, 27

Humason M. L., Mayall N. U., Sandage A. R., 1956, AJ, 61, 97

Hummels C. B., et al., 2018, arXiv e-prints,

Jaffe A. H., et al., 2001, Physical Review Letters, 86, 3475

Jordan P., Pauli W., 1928, Zeitschrift fur Physik, 47, 151

Kapteyn J. C., 1922, ApJ, 55, 302

Kardashev N., 1967, ApJ, 150, L135

Katz N., Gunn J. E., 1991, ApJ, 377, 365

Katz H., et al., 2019, arXiv e-prints, p. arXiv:1905.11414

Keller B. W., Wadsley J. W., Wang L., Kruijssen J. M. D., 2019, MNRAS, 482, 2244

Kennicutt Jr. R. C., 1989, ApJ, 344, 685

Kennicutt Jr. R. C., 1998a, ARA&A, 36, 189

Kennicutt Jr. R. C., 1998b, ApJ, 498, 541

Kennicutt Jr. R. C., et al., 2007, ApJ, 671, 333

Khochfar S., Ostriker J. P., 2008, ApJ, 680, 54

Kim J.-h., et al., 2016, ApJ, 833, 202

Klypin A. A., Trujillo-Gomez S., Primack J., 2011, ApJ, 740, 102

Knollmann S. R., Knebe A., 2009, ApJS, 182, 608

Kolb E. W., Turner M. S., 1990, Front. Phys., 69, 1

Komatsu E., et al., 2009, ApJS, 180, 330

Kormendy J., Richstone D., 1995, ARA&A, 33, 581

Kragh H., 1996, Cosmology and controversy. The historical development of two theories of the universe

Krauss L. M., 1998, ApJ, 501, 461

Krauss L. M., Turner M. S., 1995, General Relativity and Gravitation, 27, 1137

Kravtsov A. V., 2013, ApJ, 764, L31

Lemaître G., 1931a, MNRAS, 91, 490

Lemaître G., 1931b, Nature, 127, 706

Lemaitre G., 1934, Proceedings of the National Academy of Science, 20, 12

Lenz W., 1926, Phys.Z, 27, 642

Li Y., Hu W., Takada M., 2014, Phys. Rev. D, 89, 083519

Linde A. D., 1982, Physics Letters B, 108, 389

Linde A. D., 1986, Modern Physics Letters A, 1, 81

Linder E. V., Cahn R. N., 2007, Astroparticle Physics, 28, 481

Lukić Z., Stark C. W., Nugent P., White M., Meiksin A. A., Almgren A., 2015, MNRAS, 446, 3697

Madau P., Dickinson M., 2014, ARA&A, 52, 415

Madau P., Ferguson H. C., Dickinson M. E., Giavalisco M., Steidel C. C., Fruchter A., 1996, MNRAS, 283, 1388

Madau P., Haardt F., Rees M. J., 1999, ApJ, 514, 648

Magnelli B., Elbaz D., Chary R. R., Dickinson M., Le Borgne D., Frayer D. T., Willmer C. N. A., 2011, A&A, 528, A35

Magnelli B., et al., 2013, A&A, 553, A132

Magorrian J., et al., 1998, AJ, 115, 2285

Mathews W. G., 1978, ApJ, 219, 413

McGaugh S. S., 2005, ApJ, 632, 859

McGaugh S. S., Schombert J. M., de Blok W. J. G., Zagursky M. J., 2010, ApJ, 708, L14

McKay M. D., Beckman R. J., Conover W. J., 1979, Technometrics, 21, 239

McQuinn M., 2016, ARA&A, 54, 313

McQuinn M., Upton Sanderbeck P. R., 2016, MNRAS, 456, 47

Meiksin A., 2005, MNRAS, 356, 596

Meiksin A. A., 2009, Reviews of Modern Physics, 81, 1405

Milne E. A., 1935, Relativity, gravitation and world-structure

Misner C. W., 1968, ApJ, 151, 431

Moore B., Ghigna S., Governato F., Lake G., Quinn T., Stadel J., Tozzi P., 1999, ApJ, 524, L19

More S., Kravtsov A. V., Dalal N., Gottlöber S., 2011, ApJS, 195, 4

Moster B. P., Naab T., White S. D. M., 2013, MNRAS, 428, 3121

Munshi D., Sahni V., Starobinsky A. A., 1994, ApJ, 436, 517

Nagamine K., Loeb A., 2004, New A, 9, 573

Nagamine K., Springel V., Hernquist L., 2004, MNRAS, 348, 435

Navarro J. F., White S. D. M., 1994, MNRAS, 267, 401

Navarro J. F., Frenk C. S., White S. D. M., 1996, ApJ, 462, 563

Nernst W., 1916, Verhandlungen der Deutschen Physikalischen Gesellschaft, 4, S

Norman M. L., Abel T., Bryan G., 1999, in Holt S., Smith E., eds, American Institute of Physics Conference Series Vol. 470, After the Dark Ages: When Galaxies were Young (the Universe at 2 ¡ Z ¡ 5). pp 58–62, doi:10.1063/1.58641

Oñorbe J., Garrison-Kimmel S., Maller A. H., Bullock J. S., Rocha M., Hahn O., 2014, MNRAS, 437, 1894

Oñorbe J., Hennawi J. F., Lukić Z., 2017, ApJ, 837, 106

O'Raifeartaigh C., O'Keeffe M., Nahm W., Mitton S., 2018, European Physical Journal H, 43

O'Shea B. W., Nagamine K., Springel V., Hernquist L., Norman M. L., 2005, ApJS, 160, 1

Oesch P. A., et al., 2013, ApJ, 773, 75

Okamoto T., Eke V. R., Frenk C. S., Jenkins A., 2005, MNRAS, 363, 1299

Omukai K., Tsuribe T., Schneider R., Ferrara A., 2005, ApJ, 626, 627

Oppenheimer B. D., Davé R., 2006, MNRAS, 373, 1265

Ostriker J. P., Cowie L. L., 1981, ApJ, 243, L127

Ostriker J. P., Peebles P. J. E., 1973, ApJ, 186, 467

Ostriker J. P., Steinhardt P. J., 1995, Nature, 377, 600

Ostriker J. P., Vishniac E. T., 1986, ApJ, 306, L51

Ostriker J. P., Peebles P. J. E., Yahil A., 1974, ApJ, 193, L1

Padmanabhan T., Narasimha D., 1992, MNRAS, 259, 41P

Peacock J. A., 1999, Cosmological Physics

Peacock J. A., 2007, MNRAS, 379, 1067

Peebles P. J. E., 1982, ApJ, 263, L1

Peebles P. J. E., 1984, ApJ, 284, 439

Peebles P. J. E., 1993, Principles of Physical Cosmology

Peeples M. S., et al., 2019, ApJ, 873, 129

Pen U.-L., 1997, ApJ, 490, L127

Perlmutter S., et al., 1999, ApJ, 517, 565

Petrosian V., 1974, in Longair M. S., ed., IAU Symposium Vol. 63, Confrontation of Cosmological Theories with Observational Data. pp 31–46

Petrosian V., Salpeter E., Szekeres P., 1967, ApJ, 147, 1222

Petrostan V., Salpeter E. E., 1970, Comments on Astrophysics and Space Physics, 2, 109

Phillips M. M., 1993, ApJ, 413, L105

Pierce M. J., Welch D. L., McClure R. D., van den Bergh S., Racine R., Stetson P. B., 1994, Nature, 371, 385

Pillepich A., et al., 2018, MNRAS, 473, 4077

Planck M., 1911, Verhandlungen der Deutschen Physikalischen Gesellschaft, 13, 138

Planelles S., Quilis V., 2010, A&A, 519, A94

Pritchard J. R., Furlanetto S. R., Kamionkowski M., 2007, MNRAS, 374, 159

Puchwein E., Bolton J. S., Haehnelt M. G., Madau P., Becker G. D., Haardt F., 2015, MNRAS, 450, 4081

Raymond J. C., Smith B. W., 1977, ApJS, 35, 419

Reddy N. A., Steidel C. C., 2009, ApJ, 692, 778

Rees M. J., Ostriker J. P., 1977, MNRAS, 179, 541

Ricotti M., 2004, in Lamers H. J. G. L. M., Smith L. J., Nota A., eds, Astronomical Society of the Pacific Conference Series Vol. 322, The Formation and Evolution of Massive Young Star Clusters. p. 509 (arXiv:astro-ph/0404305)

Ricotti M., Ostriker J. P., 2004, MNRAS, 352, 547

Ricotti M., Ostriker J. P., Gnedin N. Y., 2005, MNRAS, 357, 207

Riess A. G., et al., 1998, AJ, 116, 1009

Roberts M. S., Rots A. H., 1973, A&A, 26, 483

Roberts M. S., Whitehurst R. N., 1975, ApJ, 201, 327

Robertson H. P., 1955, PASP, 67, 82

Robertson B. E., Ellis R. S., Dunlop J. S., McLure R. J., Stark D. P., 2010, Nature, 468, 49

Robotham A. S. G., Driver S. P., 2011, MNRAS, 413, 2570

Rowan-Robinson M., 1968, MNRAS, 141, 445

Rubin V. C., Ford Jr. W. K., Thonnard N., 1978, ApJ, 225, L107

Rubin V. C., Ford Jr. W. K., Thonnard N., 1980, ApJ, 238, 471

Salcido J., et al., 2018, MNRAS, 477, 3744

Salmon J., 1996, ApJ, 460, 59

Sandage A., 1958, ApJ, 127, 513

Sandage A., 1961, ApJ, 133, 355

Sanders D. B., Mazzarella J. M., Kim D.-C., Surace J. A., Soifer B. T., 2003, AJ, 126, 1607

Sarazin C. L., White III R. E., 1987, ApJ, 320, 32

Schaye J., Theuns T., Rauch M., Efstathiou G., Sargent W. L. W., 2000, MNRAS, 318, 817

Schaye J., et al., 2010, MNRAS, 402, 1536

Schaye J., et al., 2015, MNRAS, 446, 521

Schenker M. A., et al., 2013, ApJ, 768, 196

Schiminovich D., et al., 2005, ApJ, 619, L47

Schmidt M., 1959, ApJ, 129, 243

Schmidt A. S., White S. D. M., Schmidt F., Stücker J., 2018, MNRAS, 479, 162

Scoccimarro R., 1998, MNRAS, 299, 1097

Seeliger H., 1898a, Popular Astronomy, 5, 474

Seeliger H., 1898b, Popular Astronomy, 5, 544

Seljak U., et al., 2005, Phys. Rev. D, 71, 103515

Sherwin B. D., Zaldarriaga M., 2012, Phys. Rev. D, 85, 103523

Sheth R. K., Tormen G., 2002, MNRAS, 329, 61

Shklovsky J., 1967, ApJ, 150, L1

Sijacki D., Springel V., Di Matteo T., Hernquist L., 2007, MNRAS, 380, 877

Silk J., 1968, ApJ, 151, 459

Simon J. D., Geha M., 2007, ApJ, 670, 313

Simpson C. M., Grand R. J. J., Gómez F. A., Marinacci F., Pakmor R., Springel V., Campbell D. J. R., Frenk C. S., 2018, MNRAS, 478, 548

Sirko E., 2005, ApJ, 634, 728

Smith S., 1936, ApJ, 83, 23

Smith B., Sigurdsson S., Abel T., 2008, MNRAS, 385, 1443

Smith B. D., Hallman E. J., Shull J. M., O'Shea B. W., 2011, ApJ, 731, 6

Smith B., O'Shea B. W., Voit G. M., Ventimiglia D., Skillman S. W., 2013, The Astrophysical Journal, 778, 152

Smith B. D., et al., 2017, MNRAS, 466, 2217

Smith M. C., Sijacki D., Shen S., 2018, MNRAS, 478, 302

Smoot G. F., et al., 1992, ApJ, 396, L1

Sorini D., Oñorbe J., Hennawi J. F., Lukić Z., 2018, ApJ, 859, 125

Springel V., 2010, MNRAS, 401, 791

Springel V., Hernquist L., 2003, MNRAS, 339, 289

Springel V., Yoshida N., White S. D. M., 2001, New A, 6, 79

Springel V., et al., 2008, MNRAS, 391, 1685

Srbinovsky J. A., Wyithe J. S. B., 2007, MNRAS, 374, 627

Starobinsky A., 1980, Physics Letters B, 91, 99

Stinson G., Seth A., Katz N., Wadsley J., Governato F., Quinn T., 2006, MNRAS, 373, 1074

Stone J. M., Norman M. L., 1992, ApJS, 80, 753

Storchi-Bergmann T., 2014, in Sjouwerman L. O., Lang C. C., Ott J., eds, IAU Symposium Vol. 303, The Galactic Center: Feeding and Feedback in a Normal Galactic Nucleus. pp 354–363 (arXiv:1401.0032), doi:10.1017/S174392131400091X

Sutherland R. S., Dopita M. A., 1993, ApJS, 88, 253

Takeuchi T. T., Yoshikawa K., Ishii T. T., 2003, ApJ, 587, L89

Tatekawa T., Mizuno S., 2007, J. Cosmology Astropart. Phys., 12, 014

Teyssier R., Moore B., Martizzi D., Dubois Y., Mayer L., 2011, MNRAS, 414, 195

Thacker R. J., Couchman H. M. P., 2000, ApJ, 545, 728

Tully R. B., de Marseille O., Fisher J. R., 1975, in Bulletin of the American Astronomical Society. p. 426

Turk M. J., Smith B. D., Oishi J. S., Skory S., Skillman S. W., Abel T., Norman M. L., 2011, ApJS, 192, 9

Turner M. S., White M., 1997, Phys. Rev. D, 56, R4439

Turner M. S., Steigman G., Krauss L. M., 1984, Physical Review Letters, 52, 2090

Valkenburg W., Villaescusa-Navarro F., 2017, MNRAS, 467, 4401

Venkatesan A., Giroux M. L., Shull J. M., 2001, ApJ, 563, 1

Viel M., Lesgourgues J., Haehnelt M. G., Matarrese S., Riotto A., 2005, Phys. Rev. D, 71, 063534

Vilenkin A., 1983, Phys. Rev. D, 27, 2848

Vogelsberger M., et al., 2014, MNRAS, 444, 1518

Voit G. M., 2005, Reviews of Modern Physics, 77, 207

Von Neumann J., Richtmyer R. D., 1950, Journal of Applied Physics, 21, 232

Wagner C., Schmidt F., Chiang C.-T., Komatsu E., 2015, MNRAS, 448, L11

Walker M. G., Mateo M., Olszewski E. W., Gnedin O. Y., Wang X., Sen B., Woodroofe M., 2007, ApJ, 667, L53

Walker M. G., Mateo M., Olszewski E. W., Peñarrubia J., Evans N. W., Gilmore G., 2009, ApJ, 704, 1274

Wang L., Dutton A. A., Stinson G. S., Macciò A. V., Penzo C., Kang X., Keller B. W., Wadsley J., 2015, MNRAS, 454, 83

Weinberg S., 1987, Physical Review Letters, 59, 2607

Weinberg S., 1989, Reviews of Modern Physics, 61, 1

Weinberg S., 2000, arXiv e-prints, pp astro–ph/0005265

White S. D. M., 1986, in Bulletin of the American Astronomical Society. p. 935

White S. D. M., Frenk C. S., 1991, ApJ, 379, 52

White S. D. M., Rees M. J., 1978, MNRAS, 183, 341

White S. D. M., Frenk C. S., Davis M., 1983, ApJ, 274, L1

Woit P., 2006, Not Even Wrong: The Failure of String Theory and the Search for Unity in Physical Law. Basic Books, `https://books.google.co.uk/books?id=pcJA3iOxKAUC`

Woltjer L., 1972, ARA&A, 10, 129

Woodward P., Colella P., 1984, Journal of Computational Physics, 54, 115

Wright E. L., et al., 1992, ApJ, 396, L13

Wyder T. K., et al., 2005, ApJ, 619, L15

Wyithe J. S. B., Dijkstra M., 2011, MNRAS, 415, 3929

Wyithe J. S. B., Loeb A., 2003, ApJ, 586, 693

Yamamoto K., Sugiyama N., Sato H., 1998, ApJ, 501, 442

Yoshida N., Sugiyama N., Hernquist L., 2003, MNRAS, 344, 481

Zel'Dovich Y. B., 1967, Soviet Journal of Experimental and Theoretical Physics Letters, 6, 316

Zel'dovich Y. B., 1968, Soviet Physics Uspekhi, 11, 381

Zel'dovich Y. B., 1970, A&A, 5, 84

Zeldovich I. B., Einasto J., Shandarin S. F., 1982, Nature, 300, 407

Zwicky F., 1933, Helvetica Physica Acta, 6, 110

de Bernardis P., et al., 2000, Nature, 404, 955

van Albada T. S., Bahcall J. N., Begeman K., Sancisi R., 1985, ApJ, 295, 305

van Leer B., 1977, Journal of Computational Physics, 23, 276